Surface Structuration of Metal-Organic Frameworks Using Tip-Based Lithographies

Carlos Carbonell Fdez.

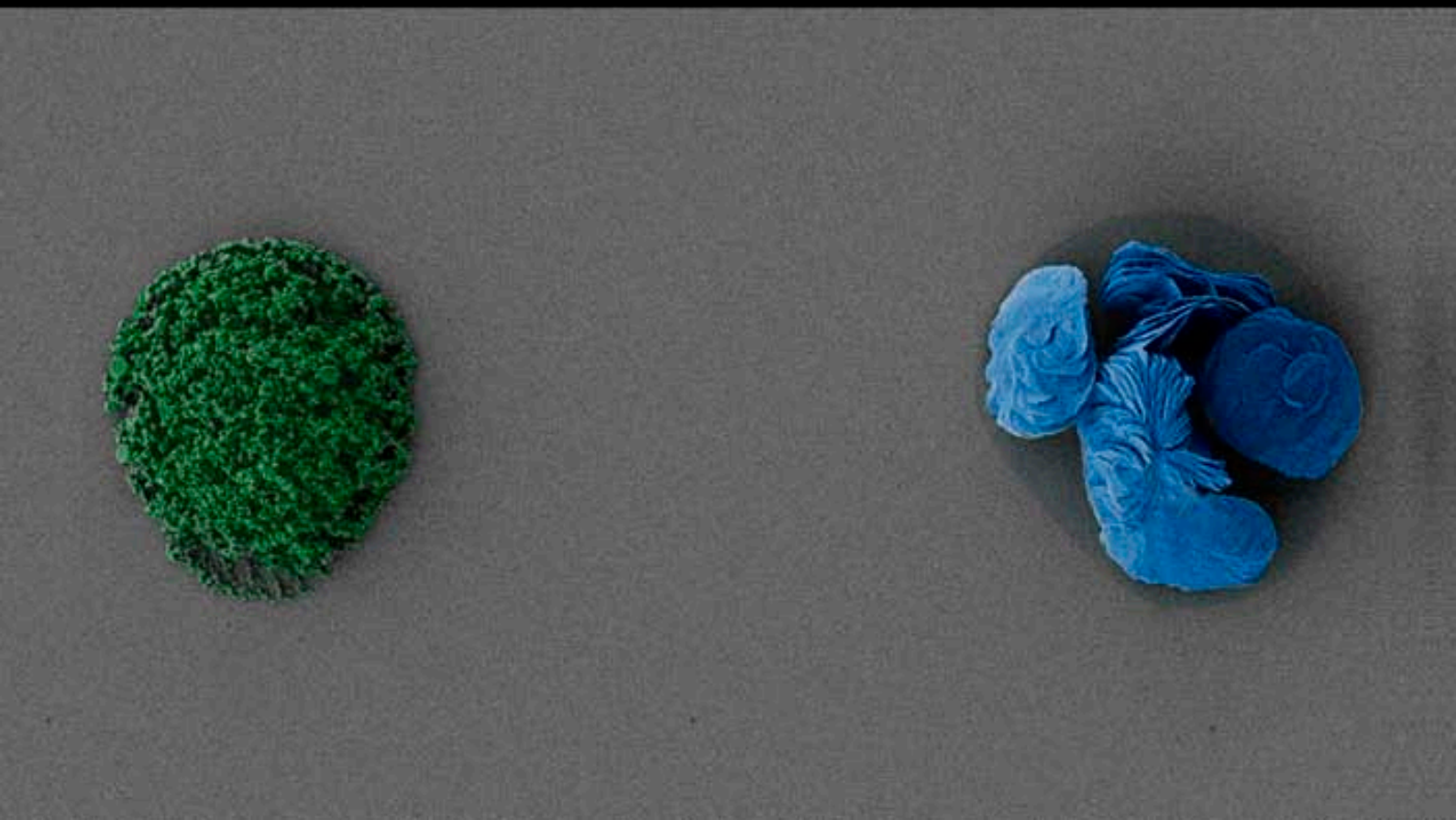

Universitat Autònoma de Barcelona

Surface Structuration of Metal-Organic Frameworks Using Tip-Based Lithographies

Carlos Carbonell Fernández

Tesi Doctoral

Doctorat en Ciència de Materials

Directors de la Tesi
Prof. Dr. Daniel Maspoch Comamala
Dr. Inhar Imaz Gabilondo

Tutor de la Tesi:
Prof. Dr. Jordi Pascual Gaínza

Institut Català de Nanociència i Nanotecnologia

Departament de Física – Facultat de Ciències

Memòria presentada per aspirar al grau de Doctor per Carlos Carbonell Fernández.

Carlos Carbonell Fernández

Prof. Dr. Daniel Maspoch
Investigador ICREA
Supramolecular Nanochemistry and Materials Group
Institut Català de Nanociència i Nanotecnologia

Dr. Inhar Imaz
Investigador Ramón y Cajal
Supramolecular Nanochemistry and Materials Group
Institut Català de Nanociència i Nanotecnologia

Prof. Dr. Jordi Pascual Gaínza
Catedràtic de Física Aplicada
Departament de Física
Universitat Autònoma de Barcelona

Bellaterra, 19 de setembre de 2014

The present PhD Thesis has been carried out at the Supramolecular Nanochemistry and Materials Group of the Catalan Institute of Nanoscience and Nanotechnology (ICN2) following the doctoral program in Materials Science of the Autonomous University of Barcelona. According to the decision of PhD Commission, this PhD Thesis is presented as a compendium of publications.

The publications are listed below in order of their appearance in the Thesis:

1) Arnau Carné, Carlos Carbonell, Inhar Imaz and Daniel Maspoch, Nanoscale Metal-Organic Materials, Chemical Society Reviews, November **2010**, 40, 291-305.

2) Carlos Carbonell , Inhar Imaz and Daniel Maspoch, Single-Crystal Metal-Organic Framework Arrays, Journal of the American Chemical Society, January **2011**, 133 (7), 2144–2147.

3) Carlos Carbonell, Kyriakos C. Stylianou, Jordi Hernando, Emi Evangelio, Sarah A. Barnett, Saju Nettikadan, Inhar Imaz and Daniel Maspoch, Femtolitre Chemistry assisted by microfluidic pen lithography, Nature Communications, June **2013**, 4:2173 doi: 10.1038/ncomms3173.

TABLE OF CONTENTS

Resumen

La presente Tesis Doctoral se ha dedicado al estudio, desarrollo e implementación de métodos para la síntesis y micro- nanoestructuración de materiales metal-orgánicos porosos (MOFs, Metal-Organic Frameworks) sobre superficies. La importancia en la estructuración de MOFs con alta resolución radica en la necesidad de su integración en microdispositivos, especialmente de tipo sensor.

En el primer capítulo se realiza una prospección bibliográfica sobre el estado del arte en MOFs, con una breve introducción histórica, las principales rutas sintéticas, propiedades y aplicaciones. Se introducen también los nano-MOFs (NMOFs) con sus particularidades tanto sintéticas como relativas a sus propiedades y aplicaciones. Este capítulo incluye el trabajo de revisión titulado "Nanoscale Metal-Organic Materials", Chemical Society Reviews (2010) donde se da una descripción extensa y más genérica sobre materiales Metal-Orgánicos.

El Capítulo 2 cita los objetivos generales y particulares de la presente Tesis Doctoral.

En el Capítulo 3 se introduce la nanoestructuración de MOFs en superficie y se desarrolla un nuevo método para nanoestructurar un MOF en particular (HKUST-1) sobre superficies con precisión nanométrica y al nivel de monocristales. Además de desarrollar un nuevo y versátil método para nanoestructurar HKUST-1 en superficies, se estudia cómo influye la funcionalización de la superficie sobre el crecimiento, nucleación y orientación cristalina. Los resultados de este capítulo se incluyen en el artículo "Single-Crystal Metal-Organic Framework Arrays", Journal of the American Chemical Society, (2011).

A partir del análisis de los resultados y problemáticas aparecidas en el capítulo anterior, en el Capítulo 4 se desarrolla una nueva aproximación que permite ampliar el abanico de MOFs viables para su estructuración. Así, en este capítulo se estudian las características de la nueva aproximación basada en combinar reactivos en volúmenes del orden de los femtolitros (10^{-15} l) utilizando una sonda de nanolitografía por microfluídica. Se demuestra la habilidad para realizar diferentes reacciones químicas y bioquímicas confinadas en dicho rango de volúmenes. Más adelante se demuestra la utilidad de la nueva aproximación para estructurar MOFs diferentes en un espacio micrométrico de una superficie realizando química combinatoria. Finalmente, se demuestra que dicha aproximación se puede utilizar para la detección combinatoria de posibles nuevos materiales, en nuestro caso se descubren dos nuevos bioMOFs. Los resultados de este trabajo se incluyen en el artículo "Femtolitre Chemistry assisted by microfluidic pen lithography" Nature Communications, (2013).

Abstract

The present PhD Thesis has been dedicated to the study, development and implementation of methods for the synthesis and nanostructuring of Metal-Organic Frameworks (MOFs) on surfaces. The importance in structuring MOFs with high resolution is the need for their integration into microdevices, especially sensors.

In the first chapter a literature survey on the state of the art in MOFs, with a brief historical introduction, the main synthetic routes, properties and applications is given. Nano-MOFs (NMOFs) are also introduced with both synthetic and properties and application characteristics. This chapter includes the review paper entitled "Nanoscale Metal-Organic Materials", Chemical Society Reviews (2010) where an extensive and more generic description of Metal-Organic material is developed.

Chapter 2 cites the general and specific objectives of this PhD thesis.

In Chapter 3 nanostructuring of MOFs on surfaces is introduced and a new method to nanostructure a particular MOF (HKUST-1) on surfaces with nanometer precision even at the level of single crystals is developed. In addition to developing a new and versatile method for HKUST-1 surface nanoestructure, we study how the surface functionalization influences on the growth, nucleation and crystal orientation. The results of this chapter are included in the article "Single-Crystal Metal-Organic Framework Arrays", Journal of the American Chemical Society, (2011).

From the analysis of the results and issues that appeared in the previous chapter, in Chapter 4 is developed a new approach that can extend the range of viable MOFs for structuring. Thus, in this chapter the characteristics of the new approach based on combining reagents in volumes on the order of femtoliters (10^{-15} l) using a nanolithography microfluidic probe is studied. It is demonstrated the ability to perform various confined chemical and biochemical reactions in this volume range. Also, the utility of the new approach to structure different MOFs in a space of a micrometer performing combinatorial chemistry surface is demonstrated. Finally, it is shown that this approach can be used for combinatorial detection of possible new materials, in our case two new bioMOFs are discovered. The results of this work are included in the article "Femtolitre Chemistry assisted by microfluidic pen lithography" Nature Communications, (2013).

Acknowledgements / Agradecimientos

Generalmente, uno escribe los agradecimientos cuando ya ha terminado la escritura del resto de capítulos y apartados de la Tesis. Llegados a este punto, lo único que a uno le apetece, más que agradecer, es maldecir a todas y cada una de las personas que orbitan en la esfera social personal. Dicho esto y medio-bromas aparte, el primer y mi más sentido agradecimiento se lo debo a mis padres. Gracias por haberme fecundado, alimentado, educado, orientado y animado a pesar de las dificultades y retos que os he supuesto. Particularmente, gracias a mi padre por haberme inculcado el interés por lo desconocido. Gracias mi hermano Sergio y a toda mi familia por apoyarme y por hacerme sentir especial.

En segon lloc, vull agrair al Institut Català de Nanociència i Nanotecnologia per brindar-me l'excel·lent oportunitat de créixer tant a nivell acadèmic com a nivell humà i especialment al meu tutor de carrera i de tesis, el Prof. Jordi Pascual, exdirector i co-fundador del ICN2 qui sempre ha estat un referent i font d'inspiració.

Agrair profundament als meus directors de Tesi i amics, el Prof. Daniel Maspoch i el Dr. Inhar Imaz, no només per la rigorosa direcció científica de la meva Tesi, també per la òptica critica i inconformista del vostre caràcter científic que se m'heu contagiat, la vostra confiança en la meva persona i el futur que m'heu ofert batallant al vostre costat per a participar en la construcció d'aquest projecte professional i científic, nanoUP. Agradecer también a Daniel Ruiz por aceptarme en su grupo y permitirme iniciar mi doctorado.

Durante el largo periodo de tiempo que ha durado el desarrollo de esta tesis, he tenido la oportunidad de trabajar con excelentes profesionales técnicos y científicos así como de viajar y colaborar con científicos de otras instituciones. Gracias a todos vosotros por haber hecho posible mi investigación; Jordi Hernando, gracias por tu disponibilidad y por compartir desinteresadamente tus inagotables conocimientos. Kyriakos thank you very much for your extremely accurate help in any apparently insignificant issue, for expressing your confidence in my scientific criteria but especially thanks for your friendship. Thanks to all the NanoInk people in Chicago, especially to Karen who helped me in all the personal things and accepted me in her house when I needed it, but also special thanks to Alexander, Donato and Saju. Gracias a Félix Zamora y Julio Gomez de la UAM. Muchas gracias a todo el personal del servei de microscòpia de la UAB donde he gastado tantas horas de mi vida doctoranda, gracias a Judith Orò del servei de microscopia del ICMAB y a Judith Linacero de la Plataforma de Nanotecnologia del Parc Cientific y gracias a Marcos Rosado por su asistencia, primero en el servei de microscopia de la UAB y después en el ICN2.

Por supuesto, tengo que agradecer a todos y cada uno de los miembros y exmiembros de nanoUP y personal cercano de otros grupos de ICN2, empezando por los que se fueron a lugares lejanos pero les sigo teniendo muy cerca; Marta Rubio y Cornelius Krull grandes compañeros y amigos. Gracias al clan de Sant Andreu, incluyendo a Xavi, Ivan y el exiliado Arnau, gracias a Jordi, Heng, Abraham y a Sonia, Nere, Luis Carlos, Elsa, Àngels, Emi, Mary, Ram y Sabina por aguantarme en mi periodo de technician y por pasarlo tan bien en tantos "eventos extra-

academicos". Un sentido agradecimiento también para nuestra ex-project manager Marta G., por tu gestión, comprensión y paciencia y por esas fantásticas inmersiones canarias y menos canarias que hemos compartido y seguro que seguiremos compartiendo. Gracias a Clara también por acompañarme en una etapa de este periodo transmitiéndome tu profunda sensibilidad.

Como no, quiero agradecer también a todos aquellos, que aunque menos relacionados con el desarrollo de este trabajo, vuestra contribución ha sido también importante, dada la necesidad de disfrutar del tiempo libre para aprovechar mejor el tiempo dedicado a la ciencia. Y en este grupo, el primero sin duda es mi gran amigo y psicólogo a efectos prácticos Álex, con quien además de disfrutar del tiempo libre, he gozado de intensas provocaciones intelectuales. Gracias a José (Largo), David M., David L. y Kiketo, gracias a Jordi H y Jeri. Gracias a mis compis montañeros del ICN2 y agregados Pablo G., Robert, Diana, James, Helena, Carla, Ariadna…

Acabando, quiero agradecer a Diana B. por darme el último impulso y por enseñarme a ser un poco más ambicioso, además de compartir la última etapa de mi agonía escribiente dándome su cariño y su apoyo.

Y ya por último, quiero rendir un especial homenaje a la que fue mi compañera de viaje durante 14 años, que tanto quise y con la que tanto aprendí. Aunque ya no está ella, siempre estará lo que imprimió en mi ser, contribuyendo en ser quien soy y por tanto, partícipe perruna de esta Tesis. Dedico mi Tesis a mi querida Nuska.

Chapter 1.
Introduction to Nanoscaled Metal-Organic Frameworks (NMOFs)

In this chapter, an introduction to nanoscaled Metal-Organic Frameworks is given. It summarizes the recently reported procedures to synthesize them as well as their properties and applications.

1. Metal-Organic Frameworks (MOFs)

1.1. From Coordination Polymers to MOFs

In 1704, a Berlin colour-maker named Diesbach made a mistake. He was attempting to create the known cochineal red lake pigment. The recipe was simple: iron sulphate and potash. However trying to save some money, one day he used contaminated potash with animal oil. When Diesbach mixed the contaminated potash with iron sulphate, instead of the expected strong red pigment, he obtained a very pale one. Then he concentrated it, but instead of the darker red pigment, he first got a purple and then, a deep blue solid. At this moment, Diesbach accidentally created the first synthetic blue pigment, Prussian Blue,[1] which was identified 273 years later as the first coordination polymer.

Indeed, despite being a valuable pigment used all over the world, the crystalline structure of Prussian Blue remained unknown until 1977.[2] Today, it is known that Prussian blue is a CP with a 3-D cubic structure built up from the connection of heterometallic centres by cyanide organic ligands, resulting in a mixed-valence polycyanide compound with a characteristic strong blue colour.

In the intervening years, little attention was paid to coordination polymers, in comparison to purely organic and inorganic materials, and only a few scattered structural studies were reported. At the end of 40s Powell and Rayner determined the structure of the Hofmann clathrate $[Ni(NH_3)_2(Ni(CN)_4]\cdot 2C_6H_6$,[3] and few years later, Ywamoto's group extended the description of related groups[4]. Remarkably, in 1959, a Japanese group determined the structure of [Cu(adiponitrile)]·NO_3, which was formed of six interpenetrating diamond networks.[5] The 1D chain structures of Ag(pyrazine)NO_3 and Cu(pyrazine)$(NO_3)_2$ were reported in 1966 and 1970,[6, 7] respectively.

It can be considered that the interest on coordination polymers really took off at the end of 70's. In 1977, Prof. A. F. Wells published a revolutionary paper in the journal monographs in crystallography,[8] which introduced for the first time the concept that inorganic crystal structures can be seen as networks by reducing them to well-defined nodes and connections. A short communication in 1989, and in a subsequent full paper in 1990,[9, 10] Prof. Robson adopted this approach to describe coordination polymers. He proposed that: "*a new and potentially extensive range of solid polymeric materials with unprecedented and possibly useful properties may be afforded by linking together centers with either a tetrahedral or an octahedral array of valencies by rod-like connecting units*". In this study, the structure of an open diamond-like network was first

described, in which tetrahedral Cu(I) centres and 4-connecting tetra(4-cyanophenyl)methane molecules were connected to form a solid in which the cationic framework represents only 1/3 of the crystal volume.

At that moment, nobody could imagine that this new concept would open a new world in the field of chemistry, materials science and nanotechnology. But only five years later, Prof. Yaghi confirmed the high potentiality of these pioneering studies. He reported the hydrothermal synthesis, of an extended network with formula Cu(4,4'-bpy)1.5·NO_3(H_2O) (where 4,4'-bpy is 4,4' bypiridine) which contains large rectangular channels filled by nitrate ions. He showed that these nitrates could be exchanged by other anions, demonstrating the accessibility of the channels and the first zeolite-like properties in a coordination polymer. In this study, Prof. Yaghi named this new compound as a Metal-Organic Framework (MOF).[11]

1.2. Definition of MOF

When Prof. Yaghi introduced the term of MOF, it was unpredictable the potential of this new generation of "hybrid" materials and the quantity of structures with different compositions, topologies and properties which will be reported during the next 20 years. However, the large number of publications concerning these new materials and the introduction of many terminologies to define them generated some confusion and misunderstanding. Indeed, since the middle of 90's, the new published compounds have been indistinctly termed as MOFs, coordination polymers, coordination networks, hybrid organic–inorganic materials and organic zeolite analogues.[12-16] To introduce some clarity and to define more clearly the different terminologies, some attempts have been made in the literature to elucidate their definitions.[17, 18] Finally, the International Union of Pure and Applied Chemistry (IUPAC) has published some provisional recommendations[19] defining a MOF as: *"a Coordination Compound continuously extending in 1, 2 or 3 dimensions through coordination bonds (Coordination Polymer or alternatively Coordination Network) with an open framework containing potential voids"*. And a coordination compound as: *"any compound that contains a coordination entity. A coordination entity is an ion or neutral molecule that is composed of a central atom, usually that of a metal, to which is attached a surrounding array of atoms or groups of atoms, each of which is called ligands"*.

1.3. MOFs - Infinite possibilities

The interest on MOFs is based on two key attributes: (i) their extremely large surface-areas given by its ultra-micro-porosity, the highest of any known materials; and (ii) the flexibility in which their structures and compositions can be varied, offering a diversity of pore shapes. Both attributes confer MOFs with potential for myriad applications. Most of these applications are obviously related to its ultra-high porosity (up to 7000 m^2/g) (**Figure 1**), and mainly includes their use in storage, separation and catalysis. A tasting of the performance of MOFs in these applications is given below. Also, the progresses made in the MOF field in terms of their synthesis, topologies and applications have today enveloped in many reviews. [20-34]

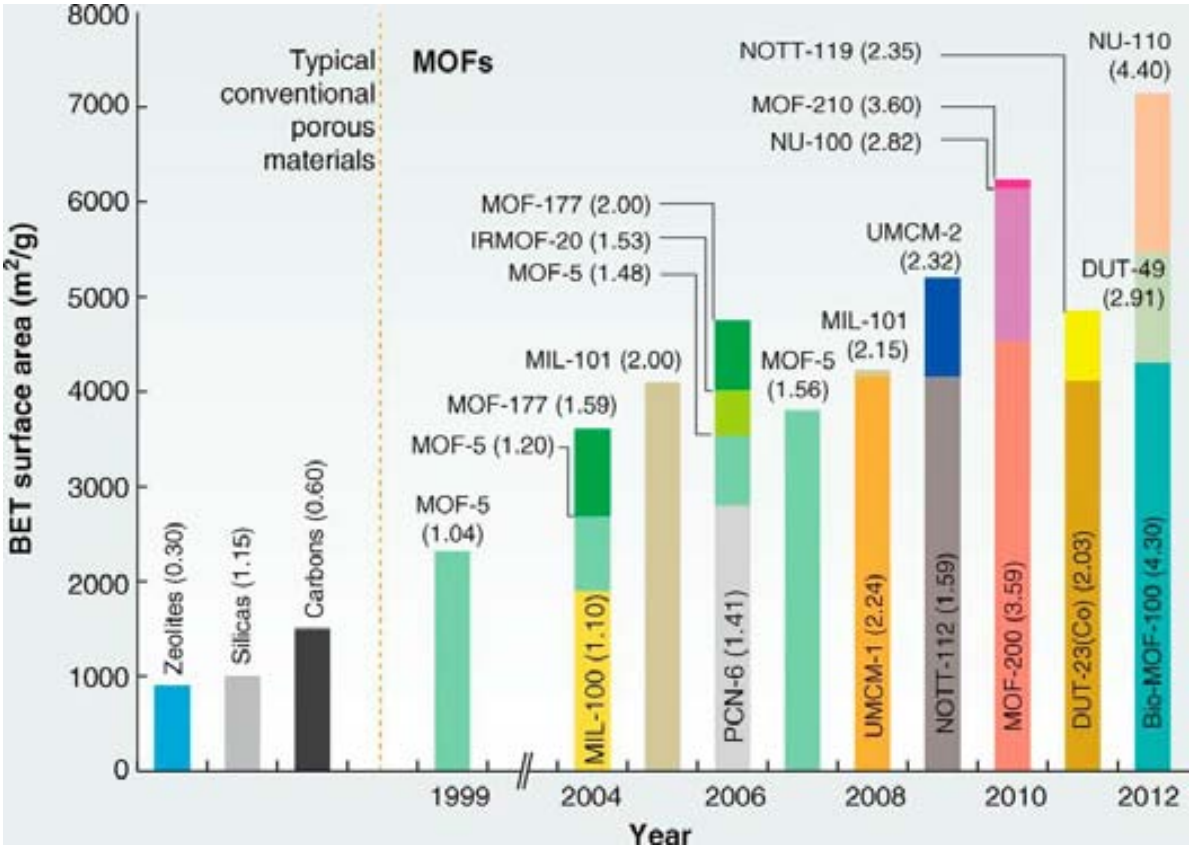

Figure 1. Progress in the synthesis of ultrahigh-porosity MOFs. Brunauer–Emmett–Teller (BET) surface areas of MOFs and typical conventional materials were estimated from gas adsorption measurements. The values in parentheses represent the pore volume (cm^3/g) of these materials. Adapted from reference 32.

1.4. Properties and Applications of MOFs

1.4.1. Gas storage and separation

The porous structure of MOFs enables them to be used as adsorbents of small molecules. However, this is only possible if guest species (such as solvents or unreacted reactants) located into the pores are removed after their synthesis. In 1997, the first indication of reversible adsorption in MOFs was provided by Kitagawa *et al.*, who studied the porosity of a 1D MOF with a general formula of $M_2(4,4'\text{-bpy})_3(NO_3)_4$ (where M is Co, Ni or Zn). They proved that this MOF could adsorb gas molecules (O_2, CH_4 and N_2) in its crevices at high pressure.[35] Permanent porosity of MOFs was further demonstrated in the layered zinc terephthalate $Zn_2(BDC)_4(H_2O)_2$ (nowadays known as MOF-2) by conducting N_2 gas isotherms at low pressures and temperatures.[12] A subsequent step forward in the development of MOFs as materials with gas storage properties was the synthesis of the first robust 3D MOF with formula $Zn_4O(BDC)_6$ (known as MOF-5).[36] MOF-5 exhibited a very high potential porosity of 63% of the volume of the unit cell and a surface area of 2320 m^2/g, which largely outperformed zeolites. First findings in gas sorption of MOFs and the increasing control in their synthesis motivated scientists to increase the porosity of these materials, reaching today the unprecedented aforementioned surface areas. (**Figure 1**)

Here, one of the strategies that allow increasing the pore volume of MOFs is based on their design using the reticular chemistry approach. This strategy is based on taking an existing MOF as a reference and replacing the original ligand by an expanded version of it (**Figure 2**). The topology and the SBU of the "parental" MOF are maintained, and therefore the pore volume is increased (**Figure 4**). In fact, this strategy has allowed for the preparation of MOFs with pore size larger than 20 Å, thereby entering to the world of "mesoporous materials".[37]

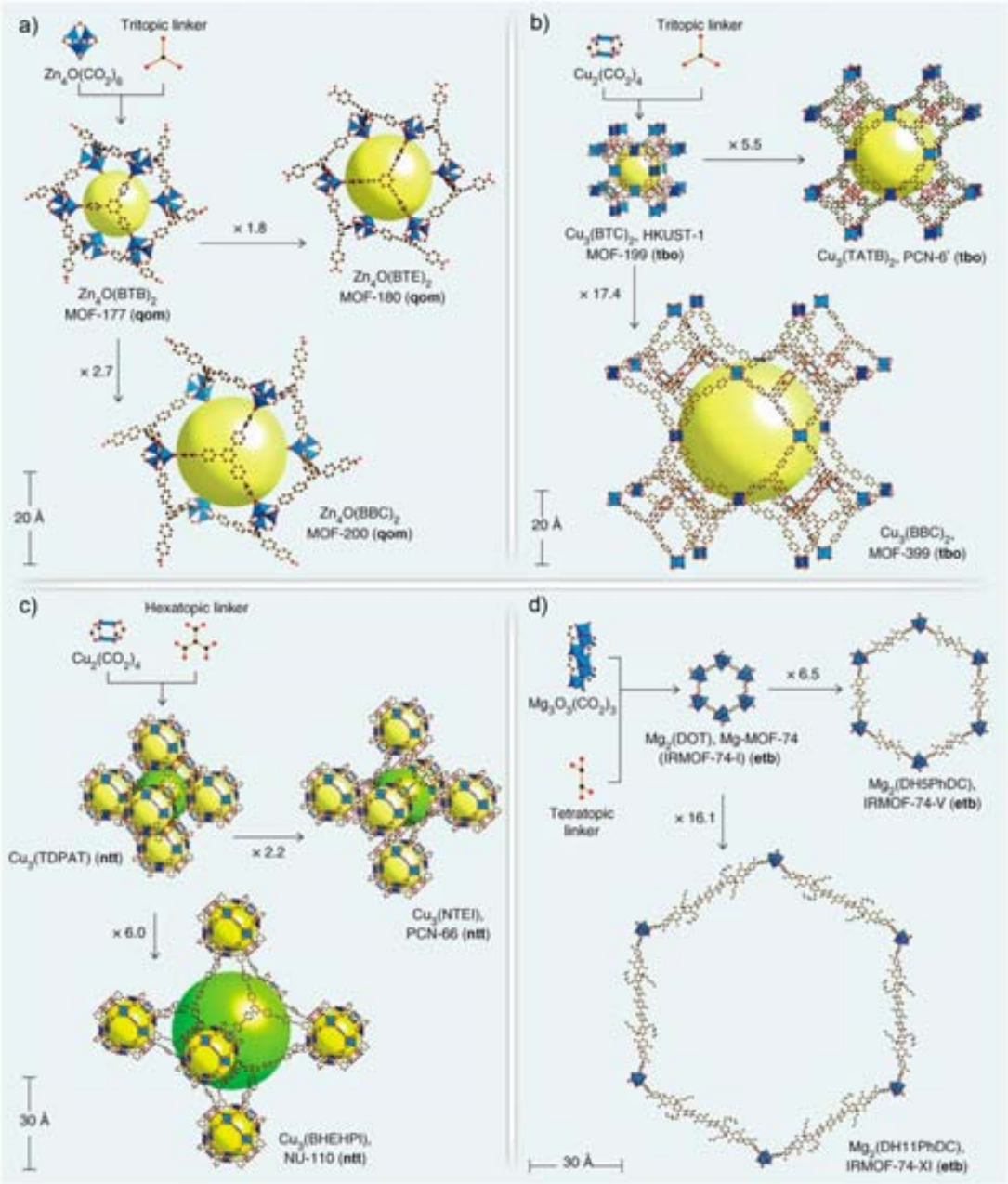

Figure 2. Isoreticular expansion of archetypical MOFs with different topologies. Adapted from reference [38].

This storage capacity soon raised interest among the scientists, expanding their interest for storing other gases. These gases mainly include H_2, CH_4 and CO_2, due to environmental reasons and economic factors related to energy costs. While H_2 and CH_4 can be used as alternative fuels, CO_2 sequestration is important to reduce the anthropogenic impact in the greenhouse effect. MOFs have shown high adsorption and storage capacities of these gases as is detailed next. In fact, their industrial potential for gas storage has been demonstrated due to their capacity to store gases exceeding the standard pressure-volume-temperature (PVT) curve of an empty tank; *i. e.* a tank filled

with a MOF can store higher amounts of gas than an empty tank at the same pressure.[39] An overview of the adsorption of these three gases is presented in the following sections.

1.4.1.1. H_2 adsorption

H_2 is an ideal carrier and is considered the future fuel due to its abundance, its high heat of adsorption (20 Mj/Kg of H_2 compared to 44.5 Mj/Kg of gasoline) and its non-polluting post combustion products (mainly water). However, its storage and transport present both safety and economic challenges. To date, storage of H_2 is based in chemisorption, which gives high storage capacity but slow release kinetic and poor reversibility. For instance, metal hydrides such as $LaNi_5H_{6.5}$ bind strongly to H_2 with a heat of adsorption reaching 200 KJ/mol. However, this high heat of adsorption makes H_2 release kinetically unfavourable and only possible at high temperatures (400 K).[40] As an alternative, MOFs offer physisorption which would ensure a reversible loading and release of H_2, demanding less energy input in the desorption than the current chemisorbents. Since physisorption has good correlation with the surface area, one of the main strategies to increase H_2 uptake is to increase the surface area of MOFs. For instance, low density MOFs made of carboxylate-based ligands such as $Cu_3L{\cdot}3H_2O$ (known as NU-100; where L is (1,3,5-tris[(1,3-carboxylic acid-5-(4-(ethynyl)phenyl))ethynyl]-benzene))[41] and $Zn_4O(BTE)_{4/3}(BPDC)$ (known as MOF-210; where BTE is 4,4',4''-(benzene-1,3,5-triyltris(ethyne-2,1-diyl))tribenzoic acid and BPDC is biphenyl-4,4′-dicarboxylic acid)[42] have shown a high H_2 adsorption of 9 % (wt%) at 56 bar and 77 K.

Structural features of the network can also have an impact on H_2 storage. Network catenation seems to have a positive effect in the H_2 storage, as demonstrated by the comparison of the H_2 adsorption of two otherwise isostructural MOFs with formula ($Cu_6(H_2O)_6(TATB)_4$) (known as PCN-6; where TATB is 4,4′,4′′-s-triazine-2,4,6-triyl-tribenzoate).[43] The catenated structure showed an uptake of 95 mg/g at 77 K and 50 bar, whereas the non-catenated structure had an uptake of 58 mg/g at the same conditions.

Also, exposition to open metal sites can increase enthalpy of adsorption for H_2. For example, the Ni(II) analogue of (M_2(DHTA)) (known as MOF-74; where DHTA is 2,5-dihydroxiterephtalic acid) presents an ordered arrangement of opened metal sites facing the 1D channels in its structure. This feature is responsible for its high enthalpy of H_2 adsorption, which results in high H_2 uptake, particularly at low pressures.[44] However, the promising storage capacities demonstrated by MOFs have only been achieved at low temperatures (77 K) so far, becoming negligible when the room temperature is

approached. For this reason, MOFs are still far from the targets (5.5 wt% at 233K) set for their practical application in H_2 storage.

1.4.1.2. CO_2 Sequestration

CO_2 is one of the main gases responsible for the anthropogenic effect of the greenhouse. It is released during combustion of fossil fuels and therefore, it is both technical and economical challenging to significantly cut its emission. One of the strategies consists in sequestrating it at the point of emission, avoiding its release to the atmosphere. However CO_2 is produced after combustion processes, it is present in complicated mixtures. In fact, in a typical post combustion exhaust, it only represents the 15% of the total mixture. Therefore, high selective adsorbents are required to sequestrate CO_2 from the gas mixture. But if the affinity of the adsorbent is too high, the energy required to remove the adsorbed CO_2 and regenerate the adsorbent increase, thereby resulting in an energy penalty for the sequestration of CO_2. For example, in the current technologies based on alkanolamine aqueous solutions, approximately 70% of the overall cost of CO_2 sequestration is attributed to the adsorbent regeneration.[45]

MOFs can contribute to address this over cost as their guest removal is less energy demanding while still achieving high selectivity for CO_2. Preferential adsorption for CO_2 can be achieved by two means: (i) size-based selectivity by which MOFs with small pores would allow only the diffusion of molecules up to a certain size into their pores (kinetic effect); and (ii) adsorptive selectivity arising from the difference in the affinity of the various components in the mixture to be adsorbed on the pore surface of the MOFs (thermodynamic parameter).[46] In regard to the kinetic-based selectivity, the small size of the molecules in the gas stream would require MOFs with very small pores. However, almost all MOFs with high surface areas and high storage capacities for CO_2 have pores with apertures larger than the CO_2 molecules, invalidating them for molecular sieving.

Therefore, the strategy based on differential heat of adsorption of the molecules composing the gas mixture seems to be the most promising. Here, the higher quadrupolar moment of CO_2 compared with the other gases (especially N_2 and O_2) opens the door to design MOFs with pore surfaces having higher affinity for CO_2.[47, 48] This affinity can be increased when unsaturated metal sites are decorating the pore wall. Unsaturated metal ions can act as a charge dense binding sites that induce the polarization of the adsorbed CO_2 and therefore, increase the selectivity for CO_2 over other gases less polarizable. Illustrative examples are the MOF-74 analogues, in which a strong interaction between the unsaturated Lewis metal sites decorating the pores and the CO_2

molecules is observed (**Figure 3**). This high interaction contributes to the high adsorption of 20 wt% CO_2 at 1 atm and 303 K of MOF-74 analogues.[49]

Introduction of basic Lewis moieties are also reported to be beneficial for CO_2 adsorption.[48] The amines with free electron pairs interact with the CO_2 quadruple increasing its heat of adsorption. For example, the diamine, N-dimethylethylenediamine (mmem) has been grafted in the Mn(II)-based MOF with formula $H_3[(Cu_4Cl)_3(BTTri)_8]$ (known as CuBTTri; where H_3BTTri is 1,3,5-tri(1H-1,2,3-triazol-4-yl)benzene) with exposed unsaturated metal sites, resulting in an increase of CO_2 heat of adsorption and in a higher selectivity.[50] The CO_2 adsorption reached 16 wt% at atmospheric pressure and 298 K. Here, tunnability of MOFs is a major advantage due to the ease incorporation of functional groups on the pore walls.

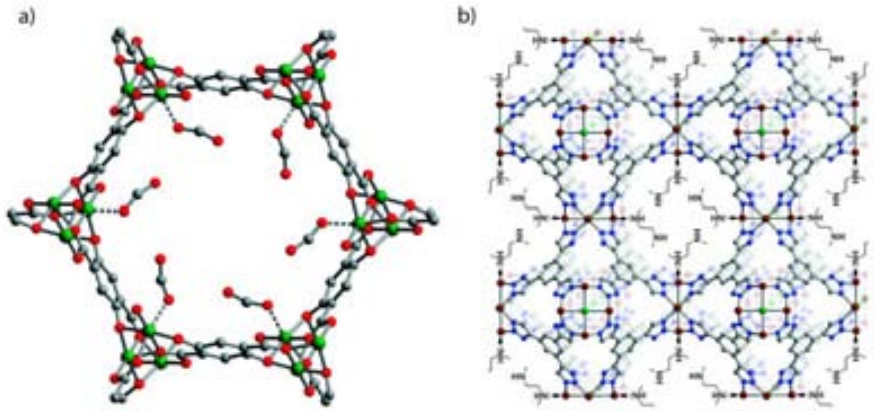

Figure 3. (a) Crystallographic structure of Ni-MOF-74 in which interaction of CO_2 with the unsaturated Ni(II) ions is shown by a doted line. (b) Illustration of the functionalization of Cu-BTTri through binding N,N-dimethylethylenediamine (mmen) to the open metal coordination sites to increase its CO_2 heat of adsorption. Adapted from reference 49.

1.4.1.3. CH_4 adsorption

In the last years, economic and environmental considerations have increased the interest in natural gases (NG), comprising mainly CH_4 as a fuel for **transportation** and especially, as a replacement for petrol (gasoline). From an environmental point of view, CH_4 delivers roughly twice the energy of coal with the same amount of CO_2 released. From an economical point of view, the price of natural gas has lived a spectacular recent drop in price due to deployment of inexpensive technologies for its recovery from shale.

The remaining challenge to use CH_4 as a source of energy is its mass- and volume-efficient storage at ambient temperature and its delivery. Currently, CH_4 is stored at very

high pressures (250 bar) in most natural gas powered vehicles. While it is suitable for large vehicles such as buses, this solution is less than satisfactory for cars. The Department of Energy (DOE) of United States estimated that a storage of 263 V/V is required for practical on board applications. Therefore, finding new alternative storing systems is today a priority.

In this sense, MOFs have shown excellent capabilities to store high amounts of CH_4 at low pressure compared to an empty tank. Hupp and co-workers recently reported a detailed comparison of CH_4 sorption capacities of a wide range of MOFs (**Figure 4**). Surprisingly, the archetypical $Cu_3(BTC)_2$ (known as HKUST-1; where BTC is 1,3,5-benzenetricarboxylic acid) exhibits the highest volumetric uptake, reaching 267 V/V storage at 65 bars and therefore, meeting the required target.[51] For comparison, an empty tank stores this amount of CH_4 at 255 bars. This high value is attributed to a combination of its high metal density which allows methane-metal interactions at low pressures, and of its small cages, which increase the methane-methane interactions at high pressure, favouring the cooperative adsorption. The combination of both effects explains why HKUST-1 outperforms MOFs with much larger surface areas.[52] This high methane storage capacity demonstrated by MOFs has attracted the attention of the chemical industry to use them as an on-board tank of CH_4 for vehicles. First prototypes of vehicles powered by CH_4 stored in a tank filled with a MOF have been yet developed by BASF.[53]

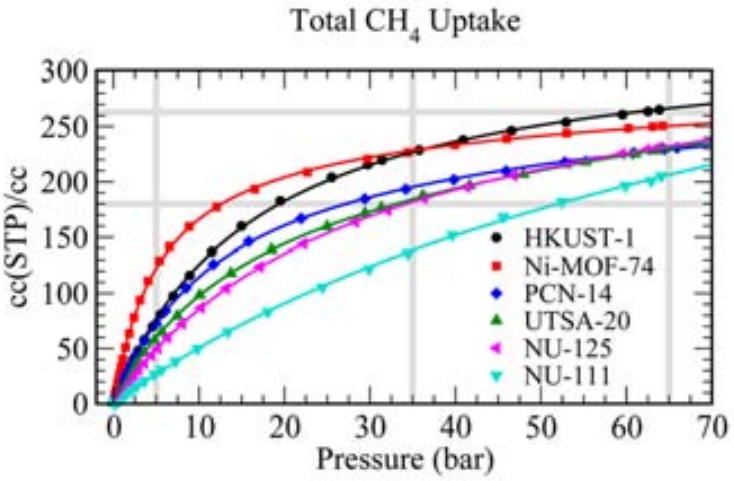

Figure 4. Comparison of the total volumetric and gravimetric uptakes for six iconic MOFs. The gray horizontal lines show the old and new Department of Energy (DOE) targets for volumetric methane storage. Adapted from reference 54.

1.4.1.4. Gas separation and purification

The preferential adsorptions of one gas over another can be exploited to purify or separate gas mixtures. One way of promoting gas selectivity is based on the relative size of the molecule compared to the pore (i.e. based on kinetics). Therefore, the ease of pore size tunning in MOFs can be used to prepare molecular sieving. For instance, $Zn(PhIm)_2$ (known as ZIF-7; where PhIm is benzimidazole) with an estimated pore size in between H_2 and CO_2 was used to separate mixtures of these gases.[55] The presence of metal open sites can also promote preferential interaction with gases depending on their chemical formulation (thermodynamic effect). Long *et al.* demonstrated the potential of this approach by studing the different hydrocarbon affinity towards unsaturated Fe(II) ions in the Fe-MOF-74 structure (**Figure 5**).[56] It was observed that the adsorption capacity increased with the unsaturation, being the most adsorbed gas acetylene. This selectivity can therefore be exploited to separate pure gases from naphtha cracker. In conclusion, both topology and functionality in the pores of MOFs can be exploited to resolve gas mixtures.

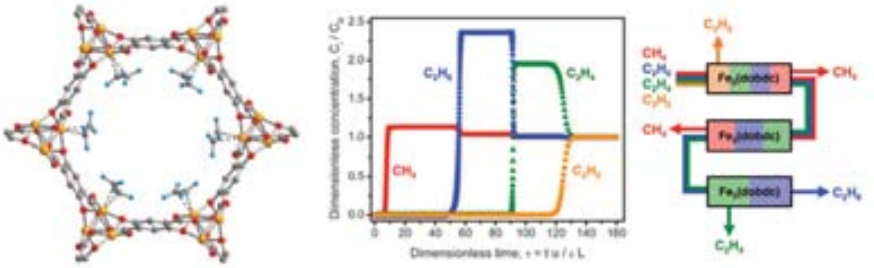

Figure 5. (Left) Structure of the complex Fe-MOF-74·acetylene determined by neutron powder diffraction, showing interactions between the triple bond and the Fe(II) ion. (Right) Breakthrough calculations for hydrocarbon mixtures. Adapted from reference 56.

1.4.2. Catalysis

MOFs share with zeolites several characteristics that make them attractive for catalysis. Some of these characteristics are their ordered arrangement of active centres (metallic ions and organic moieties), homogenous and tuneable pore size and chirality. However, their use as catalysts suffers from some drawbacks, including their low chemical stability in some solvents (especially water), low thermal stability and the fact

that the metal centres are fully coordinated in many structures, provoking a decrease of their catalytic activity.

Lewis acid sites are long reported as catalytically active for a myriad class of reactions, such as oxidations, condensations and alkylations. In fact, they have been extensively exploited in zeolites. Thus, one way of conferring acidity to the MOF is through the generation of open-metal sites. Open-metal centres in MOFs can be obtained by removing guest solvent molecules coordinated to these metal centres. For example, upon dehydration of HKUST-1, the water molecule coordinated to the Cu(II) ions is lost, changing the number of coordination of Cu(II) ions from 5 to 4. The formation of these metal open sites makes HKUST-1 an effective catalyst for acid catalysed reactions.[57] $Fe_3Cl(H_2O)_2O(NH_2\text{-}BDC)_3$ (known as MIL-101; where NH_2-BDC is 2-aminoterephtalic acid) has also shown good catalytic properties. As in the case of HKUST-1, it contains coordinated water molecules that can be removed upon dehydration giving rise to active metal sites. In addition, it can be synthesised with Cr(III) and Fe(III) ions, adding tuneability to its catalytic performance and it has very big pores and is thermally and chemically stable. All together make MIL-101 a good catalyst that showed its potential, for instance, in carbonyl cyanosilylation and oxidation reactions.[58-60]

The introduction of unsaturated metals in the structure is not the only approach to make catalytically active MOFs. Even if it is still rare, organic building blocks can also be used. For instance, Kitagawa *et al.* noted that the non-coordinated carbonyl oxygen found in the pillared Cu_2(pzdc)(pz) (where pzdc is pyrazine-2,3 dicarboxylate, and pz is pyrazine) had a strong basic Lewis character. This feature was exploited to strongly adsorb acetylene and promote its polymerization on the microporous channel.[61] In another example reported by Hasegawa *et al.,* the Lewis basic character of non-coordinated amines or amides were used to catalyse Knovenagel condensation reactions. In this case, the organic ligand used to prepare the MOF had two distinct moieties: three pyridine groups to coordinate Cd(II) ions and three amide groups that were responsible for the catalytic activity. This structure was effective in catalysing the Knovenagel reaction with small substrates, reaching conversions up to 98%.[62]

This approach is somehow challenging because it is difficult to prepare MOF structures with free reactive organic ligands located on the pore surfaces since they always tend to coordinate with metal ions. As an alternative, post-synthetic procedures can be employed to introduce functional organic groups into the MOF structure. These functional groups can be introduced by two different ways: (i) covalent modification of the organic linker; and (ii) by grafting molecules at coordinative vacancies in the metal

centre, as shown in **Figure 6.**[63] This last methodology was used to coordinate proline chiral molecules bearing a pyridine moiety to the open-metal site of Cr-MIL-101. This simple modification increased its performance in aldol reactions between aromatic aldehydes and ketones.[64]

MOFs can also present catalytic activity by incorporating guest active species. These species can be metal complexes, such as metalloporphyrins, polioxometalates or inorganic nanoparticles. One of the advantages of confining molecular complex catalysts in MOF cavities is that the catalytic system becomes heterogenous and therefore, the recovery of the catalyst becomes simpler. An example of that was provided by Eddaoudi *et al.*, who achieved the encapsulation of porphirines inside the cages of $In_1(HImDC)_2$ (where HImDC is 4,5-imidazoledicarboxylic).[65] Here, the porphyrin was incorporated during the synthesis of the MOF because its post-synthetic incorporation was not possible due to the small size of the channels compared to the porphyrin. Finally, the metalloporphyrin was synthesised by impregnating the porphyrin@MOF in a solution containing the metal ion. The MOF supported catalyst proved its activity and recyclability in oxidation of alkanes.

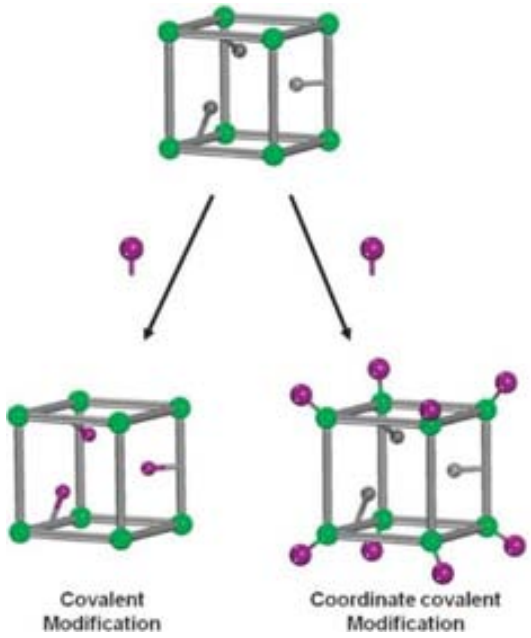

Figure 6. Schematic illustration showing the two existing strategies for the post synthetic modification of MOFs. Adapted from reference [63].

Another type of species that can be incorporated in MOFs are catalytic inorganic nanoparticles (INPs). MOFs can be excellent support materials for INPs because they have high surface areas and an excellent regularity of the cavities, which enables narrow size distributions of the embedded INPs. INPs are generally incorporated into MOFs by

first immersing the MOF into a solution containing the metal nanoparticle precursors (generally in their ionic form) or by gas phase loading when these precursors are volatile.[66] Then, a typical reduction reaction of the precursors adsorbed in the MOF is undertaken to form the INP inside its cavities. Thus, the MOF cavities become a template for the synthesis of the INPs.[67] To date, a great variety of INPs have been incorporated into MOFs, thereby allowing their use as heterogeneous catalysts for a wide range of reactions. For example, MOF-5 loaded with Pd NPs have shown good performance in the hydrogenation reaction of aromatic and aliphatic alkenes.[68] The use of MOFs loaded with INPs also enables size selective catalysis due to the tunnability of their pore size and shape. Thus, Fe-MIL-101 loaded with Pd nanoparticles showed good performance in the hydrogenation of ketones to alcohols. While conversions up to 100% were achieved for small ketones, no reaction was observed in the case of bulky ketones.[69]

Finally, chiral MOFs have also shown promising catalytic capacity for solid asymmetric catalysts. In fact, while zeolites outperform MOFs in Lewis acid catalysed reactions due to their superior thermal and hydrolytic stability, chiral catalysis in MOFs is unmatchable for zeolites due to their larger opened channels and richness in chiral structures. For example, the chiral MOF with formula $Cd_3Cl_6L_3$ (where L is (R)-6,6′-dichloro-2,2′-dihydroxy-1,1′-binaphthyl-4,4′-bipyridine) and post-synthetically functionalized with Ti(IV) complex showed excellent activity in the addition of alkylzinc on aromatic aldehydes converted to chiral secondary alcohols.[70] Interestingly, the enantiomeric excess of the reaction was dependent on the pore size, reaching up to 84% for the larger pores (**Figure 7**).[71] The use of enantiomers of salen-based complexes have also been reported to make chiral MOFs. Enantiopure Mn(II)-based salen complexes functionalized with carboxylates were used as building block for the synthesis of a chiral MOF, which was catalytically active for the epoxidation of olefins, reporting an impressive enantiomeric excesses of 92 (%).[72, 73]

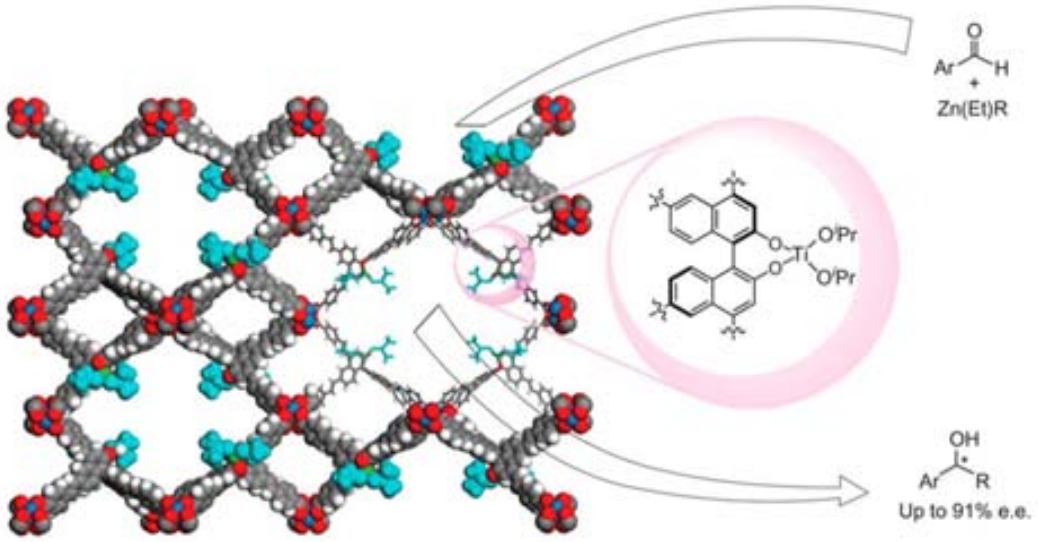

Figure 7. Schematic illustration of the homochiral [(BINOL-TC)Cu_2)] built up from the enantiopure binol tetracarboxylate and its asymmetric alkyl addition activity[71]

2. Nanoscaled MOFs (NMOFs)

Recently, there has been an increasing interest in the synthesis of MOFs at the submicrometer regime (100-1000 nm) and further down, to the nanoscale (1-100 nm). Analogously to other materials, NMOFs can show size-dependent properties which, if properly exploited, may expand the scope of these materials in numerous practical applications, including drug-delivery, contrast agents, sensor technology, functional membranes and thin-films, while opening up novel avenues to more traditional storage, separation, and catalysis applications. At this length scale, they can also be integrated on surfaces (see also chapter 3) for creating devices for sensing and electronic applications, among others. Because of all these potential advantages, in the last few years, huge efforts have been dedicated to prepare NMOFs and structuring them on surfaces. These advances on their structuration on surfaces will be discussed in Chapter 3. Because of their potential advantages, huge efforts have been recently dedicated to develop NMOFs synthetic methodologies and prospects which are discussed in the following section. NMOFs have been classified according to their dimensionality: 0-D (particles), 1-D (fibers, tubes, and rods), 2-D (sheets, thin films and membranes).

2.1. 0-D and 1-D NMOFs

2.1.1. Synthesis

There are two major strategies for synthesizing 0-D and 1-D nanoscale metal–organic materials: (i) confinement of the supramolecular assembly at nanoscopic locations by using emulsions or templates; and (ii) the controlled precipitation of NMOFs once they are formed tuning the synthetic parameters such as pH, temperature, concentration and applying microwave radiation or sonication and using capping agents.

2.1.1.1. Nanoscopic Confinement

(a) Emulsion confinement

Nanoemulsion is a suspension of small droplets, usually stabilized by a surfactant, with diameters ranging from 50 to 1000 nm, of one liquid in a second liquid in which the first will not mix. Because of these dimensions, these droplets can be used as "nanoreactors" to confine the self-assembly, nucleation and growth of NMOFs (**Figure 8**). Briefly, this approach usually consists of first dissolving each precursor in the solvent that will be dispersed. A water-in-oil, or reverse emulsion is then prepared from a surfactant, and the collisions between droplets containing those precursors or the application of an external stimulus, such as temperature, light or microwave radiation, spontaneously induce their polymerization, thus delimiting their growth inside the nanodroplet.

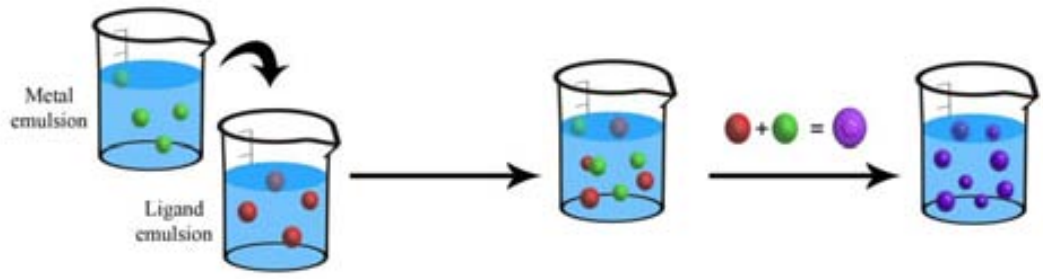

Figure. 8. Schematic representation of the microemulsion synthetic strategy for synthesizing 0- and 1-D NMOFs.

For example, by dissolving Prussian blue precursors in water, using this solution to create a water-in-oil emulsion and further exposing this emulsion to daylight, Mann *et al.* synthesized the first examples of NMOFs: Prussian blue cubic nanocrystals.[74] Since then,

emulsions have been successfully used to produce nanocrystals of heterometallic cyanometalates, Prussian Blue analogues using triazole instead of cyano groups and Gd(III)-based MOFs.

Besides the utility of their internal volume as "nanoreactors", nanodroplets of these emulsions have also the potential to be used as "soft templates" to prepare MOF-based nanoshells. In this case, the polymerization must be concentrated on the interface of the droplets by using, for example, a chemical affinity surfactant. Thus far, this strategy has been used by Wang *et al.*, who synthesized the first examples of Prussian blue nanoshells.[75] These shells were synthesized by preparing an oil-in-water emulsion with an organometallic surfactant terminated with pentacyano(4-(dimethylamino)pyridine)ferrate. Then, the addition of Fe(III) ions to the aqueous solution induced the coordinative polymerization between them and the surfactant, thereby creating a MOF-based shell on the interface of each droplet.

(b) Template confinement

Nanomaterials are also excellent candidates to be used as templates for fabricating NMOFs. In this methodology, a metal-organic polymer is deposited on the template by using a deposition technique, such as LbL deposition. This deposition, followed by the removal of this template using thermal or chemical techniques, can leave behind NMOFs that mimics the shape and size of this template.

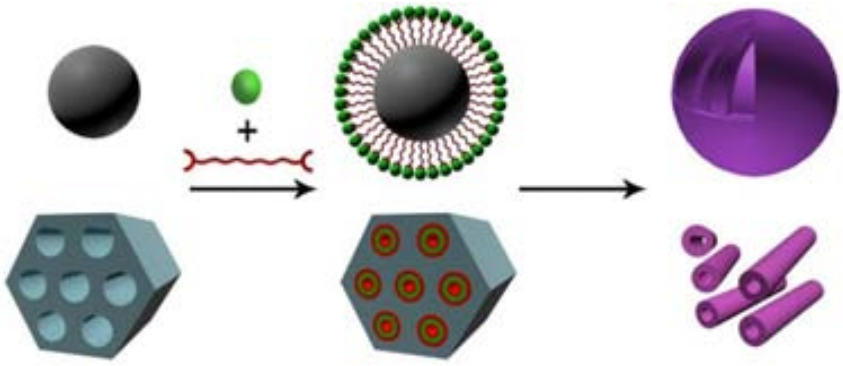

Figure 9. Schematic representation of the template confinement synthetic strategy for synthesizing 0-D and 1-D metal–organic nanostructures. Green ball represents the metal ion while red shape represents organic ligand.

In 2004, Hou *et al.* utilized alumina membranes as sacrificial templates for synthesizing Zr(IV)–phosphonate nanotubes.[76] In their methodology, a film of a MOF is initially deposited on the template by deposition (*e.g.* via layer-by-layer [LbL] deposition). Subsequent removal of the template via thermal or chemical techniques

leaves behind a structure that mimics the size and shape of the template. In a second and more recent example, a self-sacrificing template strategy was used to prepare nano-$[Cd_2(btc)_2(H_2O)_2]$ tubes.[77] First, nano-$[Cd_2(btc)_2(H_2O)_2]$ rods were synthesized using a combination of ultrasonic synthesis and vapor diffusion, with triethylamine as deprotonating base agent. After removal of excess of triethylamine from the crude reaction under continuous ultrasonic irradiation, the nanorods then served as templates. A new MOF phase was then formed on the surface of each nanorod, which were simultaneously dissolved or chemically etched to form well-defined tubes (inner diameter: 50 to 150 nm; outer diameter: 100 to 300 nm). Interestingly, a similar chemical etching methodology was used to prepare hollow nano-Prussian blue cubes (dimensions: *ca*. 50 nm).[78]

Using templates, 0-D NMOFs can be synthesized and, at the same time, self-assembled to form high-order structures or superstructures. This self-assembly can be done at the liquid/solid interfaces but also at liquid/air interfaces. Maspoch *et al.* have recently reported the synthesis of a wide range of hollow MOF superstructures by exploiting the special conditions that dictate precipitation and reaction during the drying of an aerosol droplet (see Figure 10 f).[79] Spray-drying method enables atomisation of MOF-precursor solutions into aerosol droplets that are used as individual reactors for MOF synthesis. In the proposed mechanism, the droplets suspended in a hot-air stream start to evaporate, and then the reactants diffuse to the droplet shell, where their concentration increases until reaching a critical level, at which point the MOF crystallises. During crystallisation, the mobility of the MOF nanocrystals is reduced and therefore, they become closely packed within the droplet shell. Interestingly, the resulting hollow MOF superstructures have a single thin layer of uniformly packed MOF nanocrystals, which hold together the structure. (**Figure 10**)

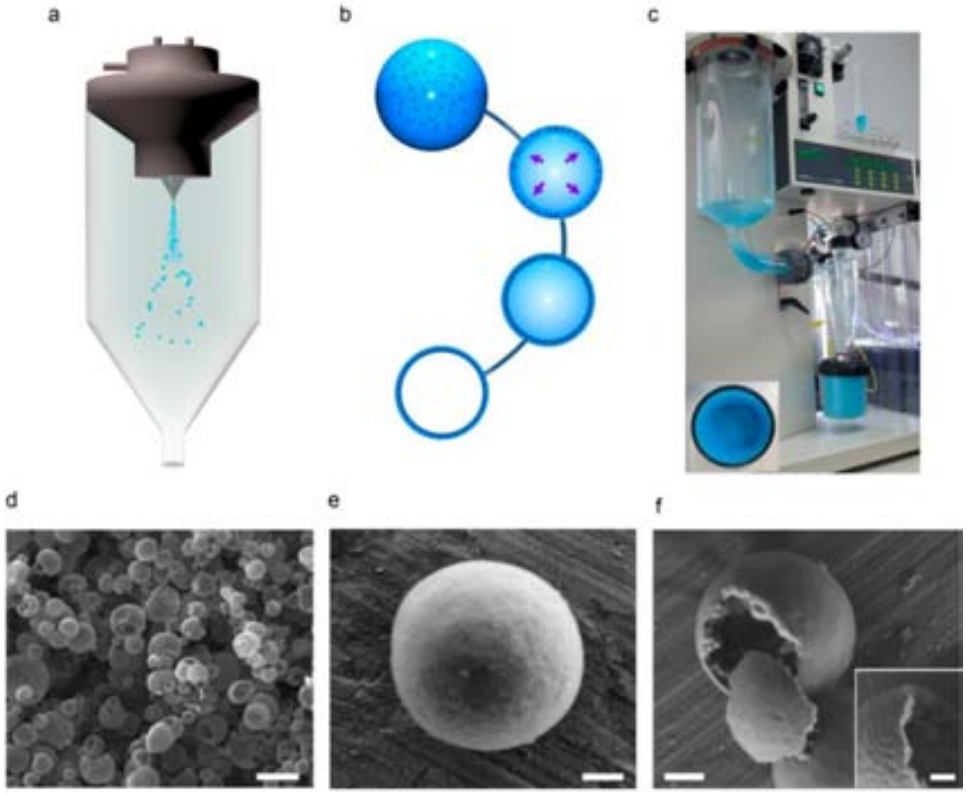

Figure 10. Spray-drying synthesis of spherical hollow HKUST-1 superstructures. a, Schematic illustration showing the spray-drying process used to synthesize HKUST-1 superstructures. **b**, Proposed spherical superstructure formation process, which implies the crystallization of nanoMOF crystals. **c**, Picture of the spray-dryer after its use to synthesize large amounts of blue HKUST-1 superstructures. **d-f**, Representative FESEM images that show a general view of the spherical HKUST-1 superstructures (**d**), a wall of a single HKUST-1 superstructure showing the assembly of nanoHKUST-1 crystals (**e**), and a mechanically broken hollow superstructure showing the internal cavity and the thickness of its wall (**f** and inset). The scale bars correspond to 5 ⌈m (**d**), 500 nm (**e,f**) and 200 nm (**f, inset**).

The versatility of this approach was proven by synthesizing hollow MOF superstructures that are composed of nanocrystals of HKUST-1, Cu-bdc,[45] NOTT-100,[46] MIL-88A,[47] MIL-88B,[47] MOF-14,[48] MOF-74 [M=Zn_{II}, Ni_{II} and Mg_{II}],[12] UiO-66,[49] ZIF-8, a Cu_{II} Prussian blue analogue,[6] MOF-5[50] or IRMOF-3.[51] In all cases, the superstructures retained the excellent sorption properties of the parent MOF. Moreover, it was proved that this method enables partial control of the size of HKUST-1 nanocrystals that form the superstructure walls, through tuning of spray-drying parameters (e.g., concentration and flow rate). Furthermore, it simultaneously enables synthesis and assembly of different types of NMOFs, paving the way to hollow MOF superstructures of greater structural complexity. In terms of potential applications, one advantage of the spray-drying approach is that it enables the combined precipitation/crystallization of different

species within a single droplet, which could be exploited to create advanced encapsulation systems in which an active molecule is entrapped within the MOF shell. As a proof of concept, our group entrapped sodium chloride crystals inside the HKUST-1 shell. Then, it was hypothesised that the rate of crystallisation inside the nebulised droplet is related to the relative mobility of the crystals and therefore, to their relative position in the final composite. Thus, sodium chloride crystals would crystallise before having their mobility reduced, whereas HKUST-1 reactants diffuse to the droplet shell, where they then crystallise. It was demonstrated that the hollow HKUST-1 shells could be used to encapsulate functional materials that would confer the final composite with added functionality, such as magnetism (encapsulation of iron oxide nanoparticles) or luminescence (encapsulation of sodium fluorescein). Finally, it was confirmed the efficacy of the resulting magnetic MOF composite superstructures for selective magnetic removal of pollutants (e.g., dibenzothiophene).

2.1.1.2. Controlled precipitation

A second family of methodologies that enable the synthesis of 0-D and 1-D NMOFs is based on mixing the precursors under certain reaction conditions that favor the fast nucleation (to increase the seed number) of MOF crystals. In most of the cases, these conditions involve the use of capping agents, microwave radiation, ultrasounds, temperature and pH modulators.

Among the most common approaches to inorganic nanoparticle synthesis is the use of stabilizing agents that cap particle growth and stabilize them to prevent them from aggregating. For example, gold nanoparticles are usually synthesized in the presence of weakly-bound coordinating ligands (*e.g.* citrate or tannic acid) or surfactants (*e.g.* PVP). Analogously, Tsuruoka *et al.*[80] and Horcajada *et al.*[81] have controlled the growth of nanoMOFs by adding coordination modulators, such as monocarboxylic acids, which act as capping agents by forming coordination bonds with the metal center of the MOF. Such modulators include the monocarboxylate ligands dodecanoic acid and acetic acid. Selective use of these reagents at different concentrations has enabled control over the size of HKUST-1 crystals from 20 nm to 1 μm.[82] Also, Cravillon *et al.* synthesized nano-ZIF-8 crystals (diameter: < 20 nm) using an excess of sodium formate and *n*-butylamine.[83] Both substances act as competitive modulating agents in the coordination equilibrium and the deprotonation equilibrium, respectively, during nucleation and growth. Apart from coordination modulators, excess reagents[84] or surfactants also can be used to control MOF crystal growth; this method also enables control over MOF shape and provides increased stability against agglomeration. As proof-of-concept, Nune *et al.*

employed the highly cationic surfactant poly(diallyldimethylammonium chloride) to prepare hexagonal nano-ZIF-8 crystals (diameter: 57 ± 7 nm).[85]

It is well known that, at high temperatures, solubility of precursors increases avoiding fast precipitation and causing crystallization. It is therefore a strategy generally used to produce bulk MOFs. However, if one controls certain reaction conditions, including solvent, surfactant, pH, temperature and time, solvothermal synthesis can be a very productive strategy for synthesizing a wide variety of NMOFs. For instance, Horcajada, Gref *et al.*, synthesized a series of NMOFs by mixing Fe(III) metal ions with a series of multitopic ligands, such as 1,4-benzenedicarboxylate (BDC), benzene-1,3,5-tricarboxylate (BTC), fumaric acid, etc., in a variety of solvents at temperatures usually above 100ºC allowing the synthesis on nano-MIL-88A, nano-MIL-89 and nano-MIL53 crystals smaller than 200 nm.[86] Also, Maspoch *et al.*[87] reported the synthesis of a colloidal suspension of a heterometallic NMOF for contrast agent applications, named nanoCAMOF-1 presenting uniform nanowires of 10 nm in diameter and 200 nm in length. The size control was achieved by simply adjusting the pH of the reaction.

The use of microwave radiation and ultrasounds can also be exploited for miniaturizing MOFs. Ni and Masel reported for the first time the use of microwave radiation to induce the precipitation of an already known MOF (IRMOF-1, 2 and 3) based on Zn(II) metal ions and BDC ligands at the nanometer scale.[88] This reaction consists of exposing a diethylformamide solution of both building blocks at 150 W for only 25 seconds. Similarly, sonochemical synthesis can lead to a homogenous nucleation and a substantial reduction in crystallization time. The well-known MOF-5 was miniaturized to 5-25 micrometres using this methodology.[89] And even more recently, nanoscale arrowheads NMOFs of Prussian blue analogues have been prepared by Wu *et al.* with the help of ultrasonic radiation.[90]

2.1.2. Properties and applications of 0-D and 1-D NMOFs

A wide range of promising properties can be obtained by taking advantage of the multiple inorganic and organic building blocks that can be combined to prepare NMOFs. One can use the intrinsic properties of either the organic or inorganic components. The ability of metal ions to interact with phonons and electrons, to show luminescence and strong absorptions and to have interesting magneto-optical properties makes NMOFs suitable as functional materials in devices. The organic components can also exhibit their own functionalities. For example, organic chromophores, radicals or biomolecules are excellent building units to prepare optical, magnetic and biocompatible nanoscale

materials. New properties also arise from the polymerization of both building blocks. This is the case of the tailorable porous structures constructed from the linkage of inorganic building units through multitopic organic ligands. All these properties can take advantage of the benefits of working at the nanometre length scale, thus opening novel avenues for developing NMOFs with astonishing properties and applications. Some of these can help to develop novel drug delivery systems, contrast agents, porous catalytic materials, gas storage materials, magnetic and optical nanomaterials, gels, etc. Recent great advances done towards these directions are summarized next.

2.1.2.1. Gas sorption and separation

Extensive research in this area has been done over the past 15 years.[91] Bulk MOFs exhibit diverse pore sizes and extremely high BET surface areas, and as such, can store many gases and absorb many functional molecules of different sizes (*e.g.* ferrocene[92] and myoglobin).[93] Although researchers have extensively explored these capabilities in bulk MOFs, chiefly driven by the great potential of these materials to soon replace fuel cells, very little work has been done on how the size and shape of nanoMOFs could influence the uptake or shape of the isotherm. Tanaka *et al.* did compare bulk crystals and nanocrystals of the flexible [Zn(ip)(bipy)] for methanol uptake at 293 K, finding comparable performance in the two cases, but the shape of each isotherm was different and the kinetics for the nanoMOFs were dramatically higher.[94] The same group also compared bulk crystals and nanocrystals of $[Cu_2(ndc)_2(dabco)]$, finding a greater total uptake of CO_2 and of N_2 (Figure 11).[80] In another study, Cho *et al.* showed that nanoMOF crystals constructed from In(III) and H_2bdc with different hexagonal shapes (rods, lumps and disks) exhibited almost identical isotherm shapes and uptakes (H_2 and CO_2 uptakes of 140 cm^3g^{-1} and 333 cm^3g^{-1}, respectively).[95]

The high separation capacity of MOFs is also being exploited for gas chromatography—namely, via integration of nanoMOFs into gas chromatography columns. For instance, a capillary coated with nano-MOF-5 crystals was tested for its efficacy in natural gas separation and benchmarked against a commercial Al_2O_3-based PLOT column.[96] Each column was run under its optimal operation conditions: albeit both columns separated all five components of natural gas (composition: 97.1% methane, 1.7% ethane, 0.7% propane, 0.2% isobutane, and 0.3% n-butane) with baseline resolution, the nano-MOF-5 column was 15% faster than the Al_2O_3 reference column.

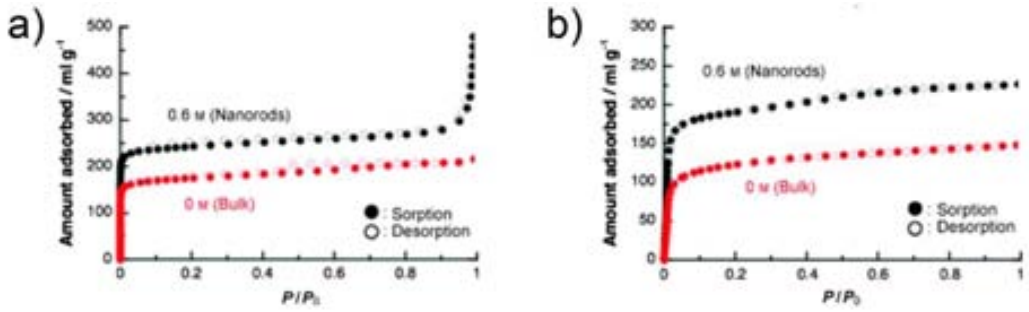

Figure 11. b) nitrogen at 77 K and c) carbon dioxide at 195 K for [{$Cu_2(ndc)_2(dabco)$}$_n$] bulk powders prepared without acetic acid (red) and nanorods prepared with 0.6 M acetic acid (black).

2.1.2.2. Drug delivery systems

MOFs exhibit many desired characteristics for their potential use as delivery platforms, including high surface areas and large pore sizes for encapsulation of drugs/active ingredients,[97, 98] intrinsic biodegradability, stability in water and physiologic media, and versatile functionality for post–synthetic grafting of drug molecules. One obvious application for NMOFs is as drug delivery systems.[99] In principle, there are two major strategies that one can use for NMOF-based delivery systems: i) the drugs (or other active ingredient) is adsorbed inside the porous NMOFs, which can then be delivered by diffusion or degradation under specific conditions and at desired locations for subsequent local release of the cargo; or the drug (or other active ingredient) serves as one of the building blocks of the NMOFs (in which it is incorporated as one of the main organic ligands or post-synthetically attached), which can then be delivered while the NMOFs are degraded under certain conditions. An excellent example of the first type of potential NMOF drug delivery systems was reported by Horcajada *et al.*, who showed the successful sorption of several antitumor or antiviral drugs, including busulfan, doxorubicin, azidothymidine triphosphate and cidofovir, into non-toxic Fe(III)-based nanoMOFs (MIL-100, MIL-101, MIL-53, and MIL-88; size: 50 to 350 nm) crystals.[99] Importantly, once all the adsorbed drugs had been incorporated into the porous structures, they could be released at different rates: doxorubicin and azidothymidine triphosphate adsorbed into nano-MIL-100 crystals were released after 3 and 5 days, respectively, whereas busulfan adsorbed into nano-MIL-53 crystals was released after 6 days.[100] Following the second approach, Taylor-Pashow *et al.* synthesized nano-amino-MIL–101–Fe crystals (diameter: 200 nm) in which Bodipy, a fluorescent analog of the

anticancer drug vinblastine, was grafted onto the NMOF through a covalent amine bond, with loading levels of up to 11% (w/w). Confocal microscopy of HT–29 cells that had been incubated with Bodipy–loaded nanocrystals revealed fluorescence inside the cells..[101] Additionally, a Pt(IV)-based drug, *c,c,t*–[$PtCl_2(NH_3)_2(Oet)O_2CCH_2CH_2CO_2H$] (ethoxysuccinato–cisplatin), was also grafted onto nano-amino-MIL–101 crystals, with an overall loading of 12.8% (w/w).[101]

2.1.2.3. Contrast agents.

NMOFs are excellent candidates to act as contrast agents because they can be composed of highly paramagnetic metals ions, such as Gd(III) and Mn(II), and their small sizes allow different biodistribution and opportunities beyond the conventional imaging of chemical agents such as theragnostics potentiality. Lin *et al.* have enormously contributed to demonstrate the efficiency of NMOFs to modify the relaxation times of the water protons in the surrounding medium when a magnetic field is applied. In such a context, Gd(III) based nanorods have shown exceptionally high longitudinal $R1$ and transverse $R2$ relaxativities of 35.8 s^{-1} and 55.6 s^{-1} per mM of Gd(III),[102] whereas nanoparticles built up from Gd(III) metal ions connected through benzenehexacarboxylate ligands have an impressive $R2$ relaxativity of 122.6 s^{-1} per mM of Gd(III).[103] More recently, Horcajada, Gref *et al.* contributed to this field by synthesizing a NMOF built up from Fe(III) metal ions connected through fumarate ligands that shows a R1 relaxativity of 50 s^{-1} per mM of Fe(III), which can be considered as sufficient for *in vivo* use (Fig. 5g-i).[86]

Maspoch *et al.*[87] recently showed that the macrocyclic DOPT can be used as a chelating ligand to create heterometallic NMOFs. In this study the relaxativity was studied in dependence of pH, temperature and magnetic field giving a maximum R1 of 15 s^{-1} per mM of Gd(III). This compound was found to be stable in physiological saline solution and cell culture media and non-cytotoxic.

Computed tomography (CT), another medical imaging technique, is based on X-ray attenuation by a specimen and can provide three-dimensional images with excellent spatial resolution. Standard contrast agents for CT contain elements with a high *Z number* (*e.g.* iodine, barium and bismuth), which can be incorporated in large amounts into nanoMOFs. As proof-of-concept, DeKrafft et *al.* fabricated nanoMOFs based on the associations of Zn(II) and Cu(II) ions with 2,3,5,6-tetraiodo-1,4-benzenedicarboxylic acid.[104] Compared to

commercial Iodoxanol, a clinically used iodinated contrast agent contains 49% (w/w) iodine; the nano-[Cu(I_4-bdc)(H_2O)$_2$]·2H_2O and nano-[Zn(I_4-bdc)(EtOH)$_2$]·2EtOH crystals both contained 63% (w/w) iodine. Based on their results, the authors affirmed that these nanoMOFs should be capable of delivering high payloads of iodine, potentially representing a new class of CT contrast agents that do not suffer from the inherent drawbacks of small-molecule agents.

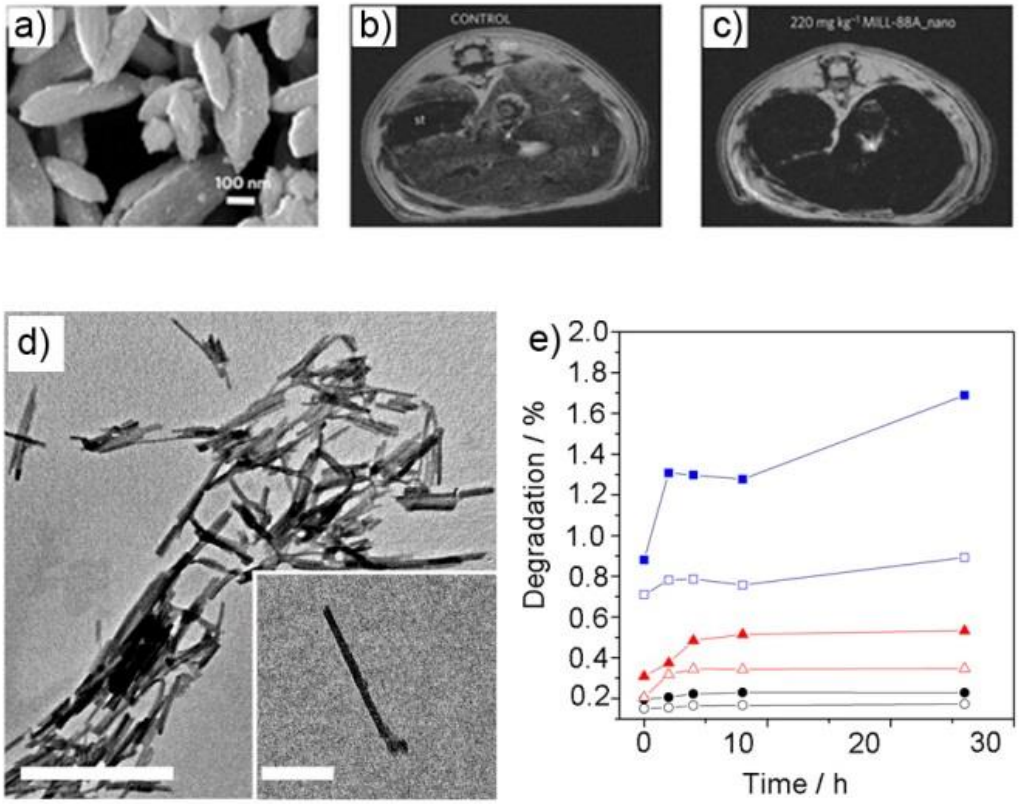

Figure 12. (a) Representative SEM image of nano-MIL-88A crystals. **(b)-(c)** MR images acquired with gradient-echo or spin-echo sequence of control (untreated) rats and of rats injected with nano-MIL-88A crystals (dosing: 220 mg kg^{-1}) in their liver, respectively. (d) TEM images of nanoCAMOF-1. Scale bars: 500 and 100 nm (inset). (e) Time dependence of the percentage of the total Gd(III) [filled symbols] and the maximum potential free Gd(III) [empty symbols] ions relative to the total Gd(III) content in nanoCAMOF-1 leached upon incubation in saline solution at pH = 4 (black circles), 7.4 (red triangles), and 9 (blue squares) and at 37.5 °C.

2.1.2.4. Catalysis

Nanocomposites comprising porous NMOFs and catalytic inorganic nanoparticles exhibit promising catalytic performance.[105] Lu et *al.* showed that Pt@ZIF-8 nanocomposites catalyzed the oxidation of CO at 130 °C, with a conversion of nearly

100% at 200 °C. The catalytic properties of Pt nanoparticles and the molecular sieving capability of the ZIF-8 matrix were combined and evaluated for liquid-phase hydrogenation two substrates: *n*-hexene and cis-cyclooctene. Pt@ZIF-8 nanocomposites catalyzed the hydrogenation of the linear *n*-hexene molecule, albeit with a low conversion presumably because of slow diffusion through the small pores (3.4 Å) of the nano-ZIF-8 crystals. Furthermore, the reusability of Pt@ZIF-8 nanocomposites as a catalyst for the hydrogenation of *n*-hexene was demonstrated by the observation of similar conversion efficiencies for consecutive runs (7.3%, 9.6% and 7.1% for the first, second and third runs, respectively). In contrast, no catalytic activity was observed for the sterically hindered substrate cys-cyclooctene, which is consistent with the small pore size of ZIF-8 (3.4 Å), but which also suggests the absence of Pt nanoparticles on the outer surface of the composite.[106]

2.2. Two-dimensional (2-D) NMOFs

The exotic mechanical, thermal, electronic, optical and chemical properties of graphene have recently inspired the study of other graphene-like 2D materials.[107] Interestingly, 2D layered MOFs (MOF nanosheets) can mimic graphene (**Figure 13a**). Although their development is in the early stages, the top-down (or *deconstruction*) method has been proposed as a promising strategy to fabricate them. This approach relies on the delamination or exfoliation of MOF nanosheets from bulk MOF crystals using ultrasonication irradiation or other methods. For instance, Li *et al.* fabricated MOF nanosheets via delamination of bulk MOF-2 crystals.[108] The delamination step was performed by dispersing dried MOF-2 crystals in acetone, and then subjecting them to ultrasonic radiation at room temperature (confirmed from the observation of the Tyndall effect) (**Figure 13b**). Sedimentation of the ultrasonicated suspension afforded a colloidal suspension of MOF-2 nanosheets. Figures 13c and 13d show representative SEM and AFM images, respectively, of the sheets. As observed in the images, the nanosheets had lateral dimensions of 100 to 1000 nm and a thicknesses of 0.7 to 6.0 nm (in agreement with the theoretical thickness of a single MOF-2 nanosheet: 0.7 nm). Similarly, Saines *et al.* obtained several Mn(II), Co(II) and Zn(II)-DMS MOF nanosheets by exfoliating the corresponding bulk MOF crystals.[109] In this case, the exfoliation was done via ultrasonication of an ethanolic colloidal suspension of the corresponding bulk MOF crystals. Importantly, some of the resulting nanosheets showed lateral dimensions close to 500 nm and unilamellar thicknesses around 1 nm. This approach has been also used by Xu *et al.*, who exfoliated the 2D layered structure of Cu-TCPP by a modular assembly

strategy.[110] With this process, a "modularization" step was used for the synthesis of highly crystalline "modules" with a nanostructure that can be conveniently assembled into a thin film in the following "assembly" step. This method affords MOF thin films (see Section 3), and it can be easily set up for different substrates at very high speed and with controllable thickness (**Figure 13 e-g**).

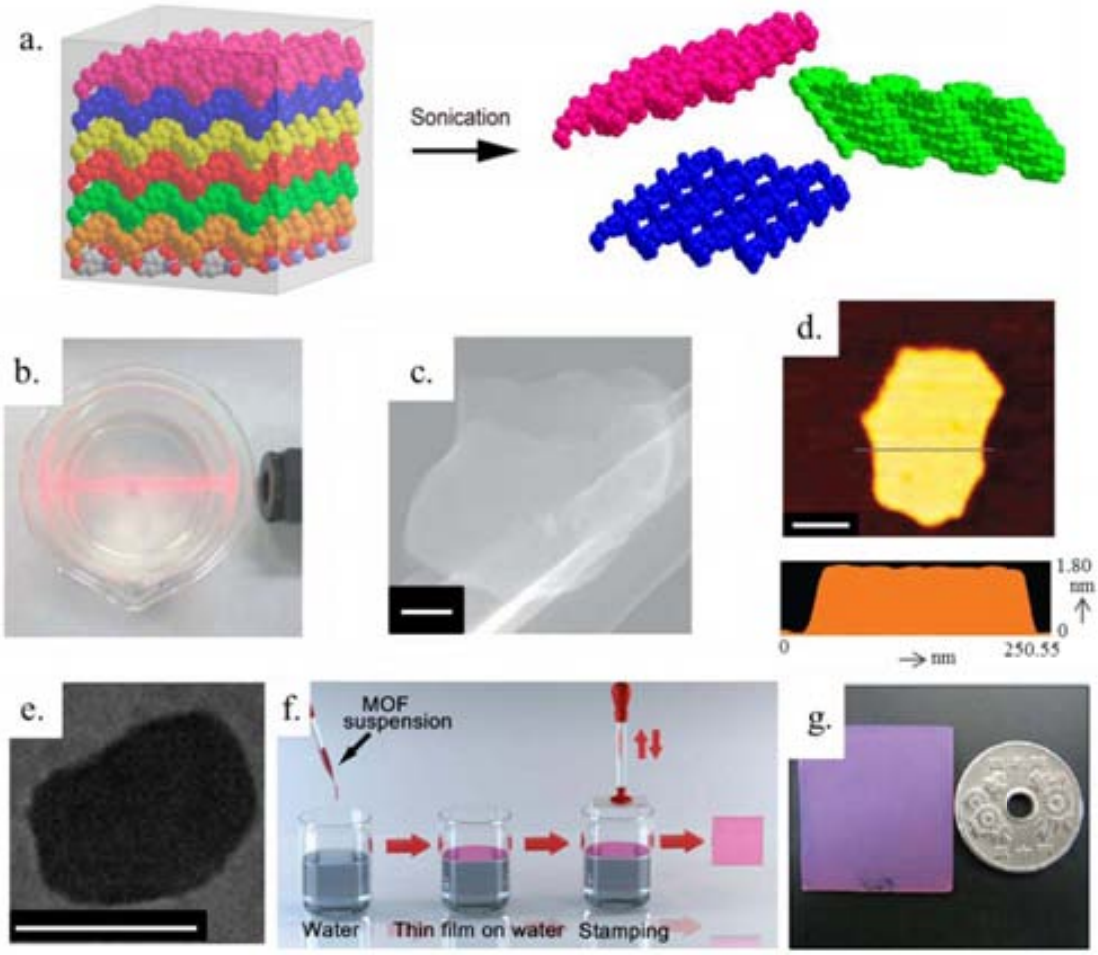

Figure 13: **(a)** Schematic illustration of the delamination process of a 2D bulk MOF (*e.g.* MOF-2) used for isolating MOF nanosheets. **(b)** Photograph of a colloidal suspension in acetone of MOF-2 nanosheets. The light beam was applied from the side to demonstrate the Tyndall effect. **(c)** Representative SEM image of MOF-2 nanosheets showing their morphology. Scale bar: 100 nm. **(d)** Depiction of an AFM image of a delaminated MOF-2 nanosheet (thickness: *ca.* 1.5 nm; lateral dimensions: 200 to 300 nm). Scale bar: 100 nm. **(e)** Representative TEM image of a single Cu–TCPP nanosheet. Scale bar: 200 nm. **(f)** Illustration of the assembly of MOF Cu–TCPP nanosheets to form a thin film. **(g)** Photograph of the MOF thin film created after 15 deposition cycles on a quartz substrate. Adapted from references 36 and 38.

2.3. NMOFs on Surfaces

Beyond the fabrication of discrete 0-D (nanoparticles), 1-D (nanorods, nanowires, …) and 2-D (nanosheets) NMOFs, another important challenge is to control the growth of these crystals directly on surfaces, thus creating functional NMOF-based membranes, thin films, or patterned surfaces. The fabrication of functional materials into appropriate devices will advance the development of important technologies arising from the need to rapidly process data[111, 112] to efficiently produce and store energy [113] and to improve human health through the early detection of diseases. [114-116]

Three principal strategies have been explored to fabricate NMOF membranes and thin films (Fig. 6): (i) the direct assembly and growth of NMOFs on surfaces; (ii) the use of Langmuir–Blodgett (LB) monolayer transfer technique; and (iii) the Liquid Phase Epitaxy (LPE) Layer by Layer (LbL) synthesis.

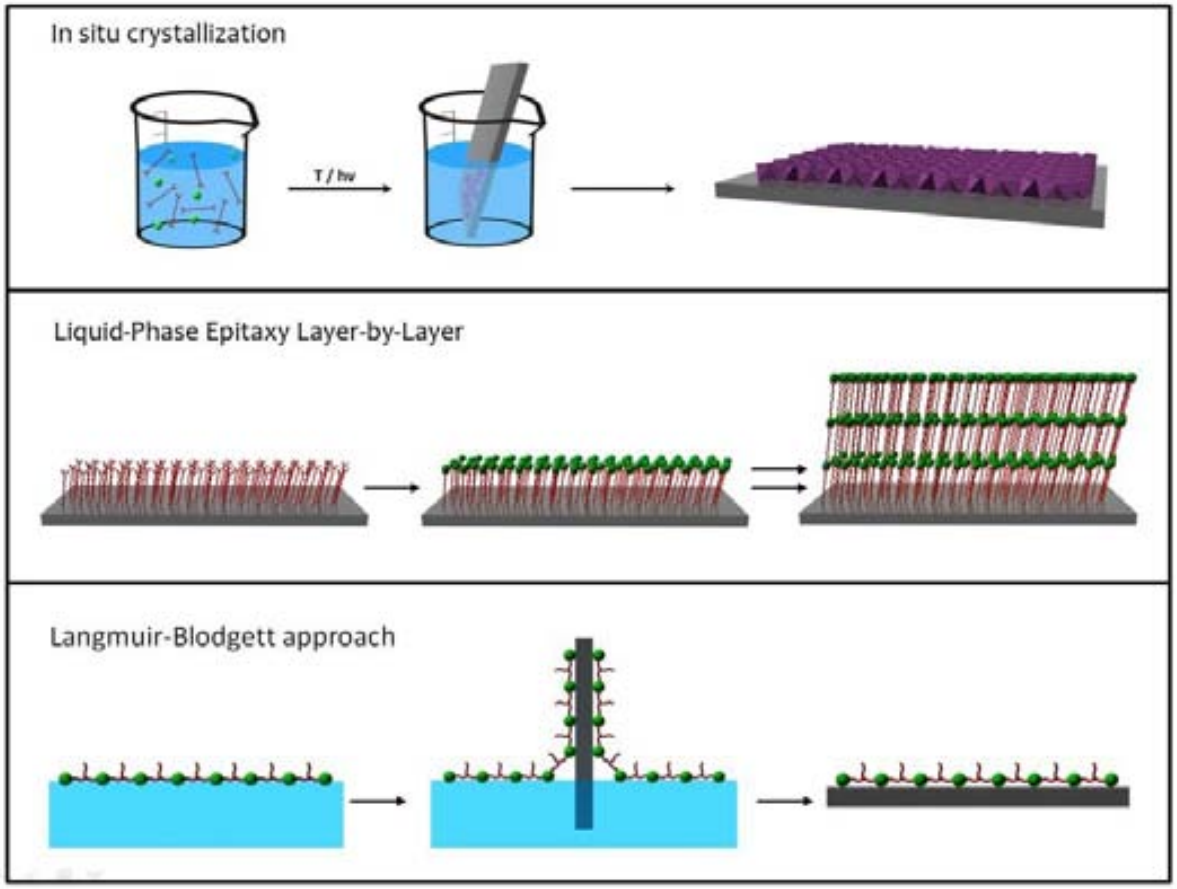

Figure 14. Schematic illustration of the three principal synthetic strategies used for preparing 2-D metal–organic nanomaterials, including the in situ crystallization, the layer-by-layer approach and the Langmuir–Blodgett approach.

2.3.1. Direct assembly and growth of NMOFs on surfaces

The most general strategy used for fabricating metal–organic thin films and membranes is the direct nucleation and growth of NMOFs on surfaces. (Figure 16) Initial efforts for growing these crystals on bare surfaces (e.g. SiO_2, Al_2O_3, Au, graphite, etc.) were based on immersing these substrates into a solution containing the precursors. Then, the NMOFs were grown on the surfaces by inducing their nucleation using methods analogous to those used for preparing 0-D and 1-D NMOFs, such as microwave radiation, temperature, etc. With these synthetic approaches, some metal–organic supports were successfully synthesized. However, most of the bare substrates inhibit the nucleation of NMOFs, and thus low crystal density is usually obtained.

A very promising solution to overcome this problem is the use of chemical affinity templates to promote the nucleation of NMOFs. Self-assembled monolayers (SAMs) are excellent candidates to act as such templates because they can be terminated with different functional groups that can direct the nucleation and growth of crystalline materials. SAMs are organic assemblies formed by the adsorption of molecular constituents from solution or the gas phase onto the surface of solids or in regular arrays on the surface of liquids (in the case of mercury and probably other liquid metals and alloys); the adsorbates organize spontaneously (and sometimes epitaxially) into crystalline (or semicrystalline) structures. The molecules or ligands that form SAMs have a chemical functionality, or "headgroup", with a specific affinity for a substrate; in many cases, the headgroup also has a high affinity for the surface and displaces adsorbed adventitious organic materials from the surface.[117] The case of the HKUST-1 system is especially appropriate to describe this phenomenon. Bein *et al.*[118] studied their nucleation and growth by immersing Au substrates previously functionalized with SAMs terminated with COOH–, OH– and CH3– groups into a solution containing Cu(II) metal ions and BTC ligands. Under the studied conditions, all terminated SAMs seemed to favour the nucleation, and therefore, increased the crystal density in comparison with bare Au surfaces. In addition, these authors also observed preferential crystal growth orientations depending on the terminal functional group of these SAMs. Indeed, the COOH-terminated SAM favoured orientation along the [100] direction and the formation of pyramid-like crystals, whereas the OH-terminated SAM favored the [111] orientation and led to the formation of octahedral crystals. The third surface terminated with CH3– groups did not favour any orientation. These results, even though are quite contradictory to latter exhaustive experiments performed by Fischer *et al.*,[119] confirm the importance of

SAMs for controlling not only the density of crystals (homogeneity) deposited on the surface but also their orientation.

More recently, the use of SAMs on surfaces has also shown to be important for selectively growing a certain MOF crystal phase in front of another. This is the case of MIL-88B, a MOF composed of Fe(III) metal ions connected through BDC ligands. Scherb *et al.* [120] demonstrated the preferential formation of crystals of this MOF by placing down a surface functionalized with a COOH-terminated SAM in a mother liquor solution containing both precursors. Surprisingly, even though the crystals formed in the solution corresponded to MIL-53, another MOF built up from Fe(III) metal ions connected through BDC ligands, the crystals that grew on the surface only corresponded to well-oriented MIL-88B crystals along the [001] direction. Also interesting is the work reported by Wöll *et al.*,[121] who controlled the formation of a non-interpenetrated phase of a MOF built up from the linkage of [Zn_4O] clusters through 4,4′-biphenyldicarboxylate ligands. Besides bulk synthetic methods lead to the interpenetrated phase, these authors proved to control the formation of the non-interpenetrated one on surfaces by using SAMs as templates and the LbL synthesis, opening new possibilities to synthesize new types of MOFs on surfaces not accessible by conventional methods.

In addition to the use of SAMs, other ways have been proposed to promote the homogeneous nucleation and growth of NMOFs on surfaces. One of the most interesting approaches is the use of seeds to induce a better crystallization. Similar to the growth of zeolitic membranes , Caro *et al.*[122] created a homogeneous and dense coating of imidazolate based MOFs (ZIF-7) on alumina supports by first dipping them into an aqueous polyethyleneimine dispersion of pre-synthesized ZIF-7 nanocrystals with dimensions of 30 nm. These seeded supports were then immersed vertically into a solution containing the ZIF-7 precursors and heated up to 100 °C using microwave for three hours to obtain a large scale ordered polycrystalline ZIF-7 thin films.

A previous chemical modification of the surface is also an important factor to be considered in order to increase the crystal density on surfaces. One possibility is the “formate” route reported by Caro *et al.*,[123] which consists of pre-oxidation of the surfaces with sodium formate treatment. With this oxidation, the nucleation of [$Mn(HCOO)_2$] was enhanced and rather dense coatings were obtained. Qiu *et al.* and De Vos *et al.* further proved this concept.[91, 124] According to these authors, the oxidation of metallic copper surfaces generates Cu(II) metal ions process, creating more surface nucleation points during the HKUST-1 synthesis, and therefore, enhancing the crystal density on those surfaces (Figure 15).

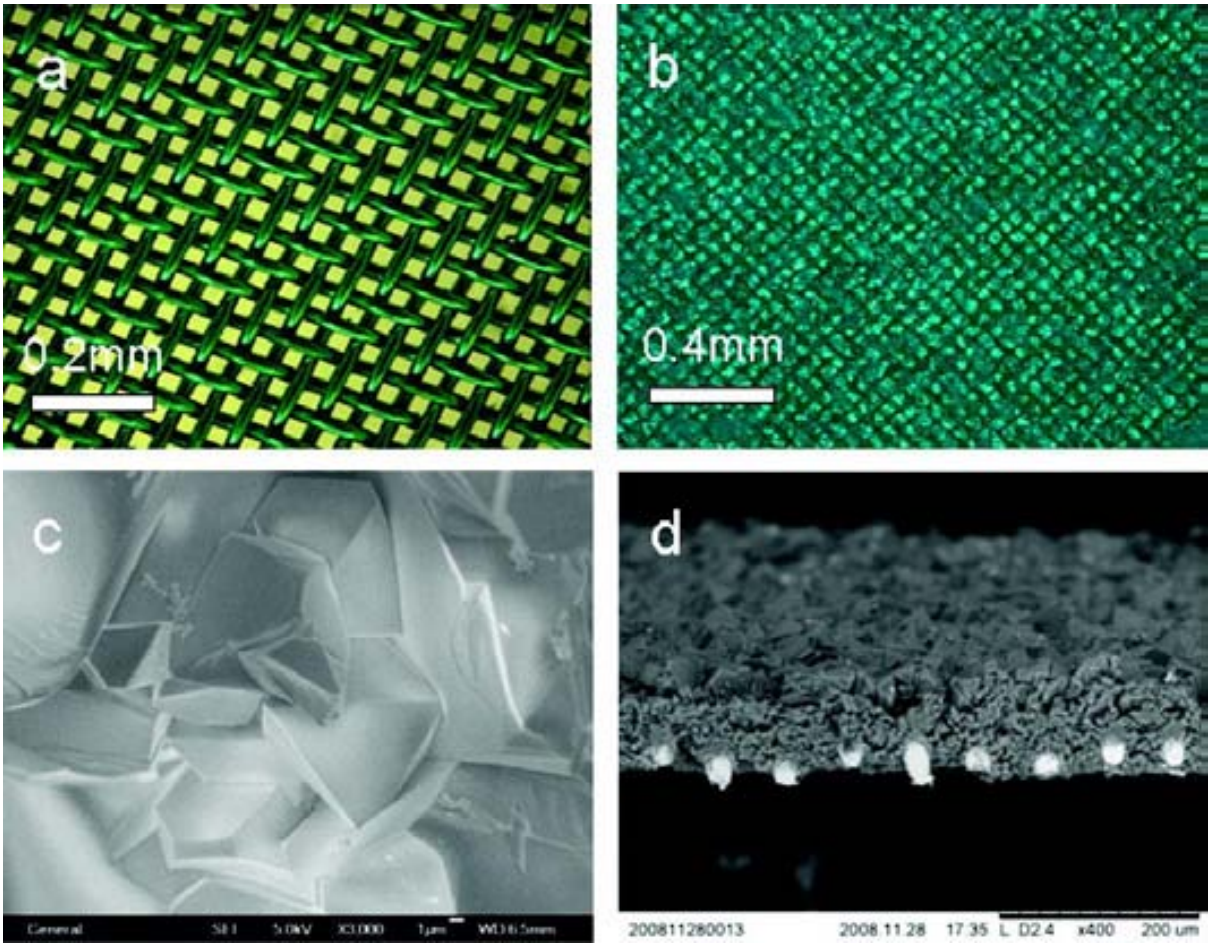

Figure 15. (a) Copper net and (b) net- net-supported HKUST-1 membrane; SEM image of (c) the surface and (d) the cross section of the membrane.

2.3.2. Liquid-Phase Epitaxy (LPE) synthesis

LPE is based on the stepwise Layer-by-Layer (LbL) adsorption of components from the liquid phase onto a surface (**Figure 14**). Typically, a SAM surface is alternatively immersed in the solution containing the metal ions and then in the solution of the organic ligands. Thus, the thickness of the MOF thin film can be controlled by the number of alternating cycles. For example, this methodology was used by Shekhah *et al.* to fabricate (100) and (111) oriented HKUST-1 films on -COOH and –OH terminated SAMs, respectively,[125] and non-interpenetrated MOF-508 films on –4,4′-bipyridil terminated SAMs.[121] LPE was also used by Arslan *et* al. for fabricating HKUST-1 thin films. However, in contrast to previous LPE procedures, the stock solutions of the reactants (copper(II) acetate and H_3btc) were deposited via spray-coating of surfaces

modified with (Au) SAMs, which enabled markedly faster deposition and consequently, faster fabrication of polycrystalline HKUST-1 films.[126]

2.3.3. Langmuir–Blodgett (LB) monolayer transfer technique

The Langmuir-Blodgett method relies on the formation and isolation of individual MOF layers, which are then sequentially transferred onto a substrate. Stacking of these layers by weak interactions leads to formation of the 3D MOF thin film. Makiura *et al.* reported the formation of the 2D layered [CoTCPP-py-Cu] network by spreading a chloroform/methanolic solution of the organic building blocks (Co(II)-TCPP and py) onto an aqueous solution of $CuCl_2$. The resulting NMOF layers were then deposited onto a Si substrate, and stacked via sequential LbL growth. The π–stacking interactions between the pendant pyridine groups, which are coordinated axially to the paddlewheels, led to generation of NAFS-1 films, the thickness of which could be controlled by controlling the number of stacked layers.[127]

Both aforementioned strategies, the LB technique and the LPE synthesis, can also be coupled for producing metal–organic thin films on solid supports.[127] Makiura, Kitagawa *et al.* recently reported the LbL growth of pre-formed metal–organic sheets using the LB technique. First, these layers were formed by spreading a chloroform/methanol solution of a Co(II) metalloporphyrin complex and pyridine onto an aqueous solution containing Cu(II) metal ions, and instantly transferred on a Si substrate. Sequential sheet formation and deposition on the same substrate allows the LbL stacking, thereby resulting in the generation of MOF thin films of any desired thickness.

2.3.4. Properties and applications of NMOFs on surfaces

The exceptional advantages and properties already exhibited by nanoscale 0-D and 1-D metal–organic materials can be integrated on surfaces for fabricating metal–organic functional thin films and membranes with a wide range of properties and applications. Their use can allow the fabrication of electronic or optoelectronic thin films, membranes with gas separation capabilities, new surface sensors, magnetic platforms, etc.

2.3.4.1. Gas sorption and separation

The exceptional porous characteristics already exhibited by bulk MOFs make them excellent components for creating metal–organic membranes or thin films with potential properties in gas separation, gas storage, fabrication of novel sensors, etc. However, even though the preparation of these 2-D metal–organic systems has attracted much research interest in the last years, only a few efficient membranes for gas separation have been reported. The first metal–organic membrane showing separation performance was reported by Qiu *et al.*[128] This membrane, which was created with nanoscale HKUST-1 crystals on an oxidized copper grid, showed a higher permeation flux and excellent permeation selectivity for H_2 in comparison with CO_2, N_2 and CH_4. This phenomenon can be explained by the size selectivity occurred on the HKUST-1 channels. Thus, the small H_2 molecule goes through the membrane more easily than CO_2, N_2, and CH_4. More recently, Caro et *al.* and Brown et *al.* prepared a series of improved nano-ZIF-8, nano-ZIF-7, nano-ZIF-90, and nano-ZIF-22 membranes that exhibited much better selectivities for H_2, by choosing nanoMOFs whose pore dimensions were close to the size of H_2.[122, 129-131] Non-oriented and oriented membranes constructed with NMOFs of zeolitic imidazolate frameworks showed a high H_2 selectivity favoured by a pore dimension of these nMOFs very similar to the size of H_2 (**Figure 15**). They also formed nano-ZIF-90 membranes on polymeric hollow-fiber supports to fabricate high-surface-area membrane modules. The gas separation factors, permeances and selectivities of the polymeric-supported nano-ZIF-90 membrane indicated that it should be able to separate liquid alkanes.[131]

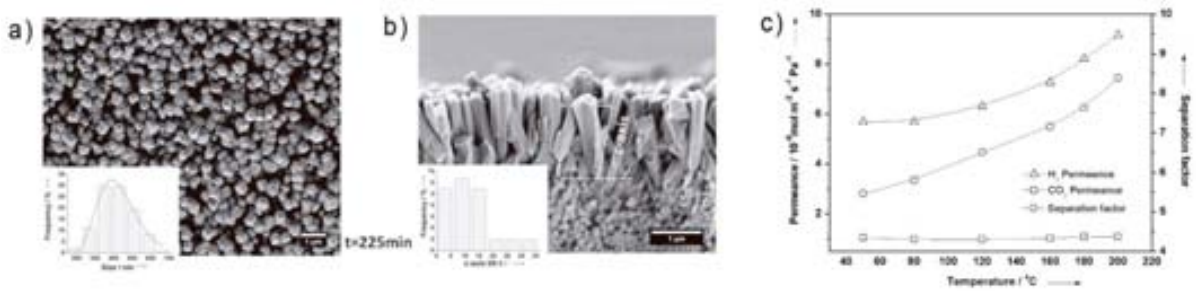

Figure 15. (a) SEM top views and (b) cross sections of the ZIF-7 membrane obtained after 225 minutes of microwave assisted secondary growth. (c) H2 and CO2 permeances from equimolar binary mixtures and H2/CO2 mixture separation factors of the c-out-of-plane oriented ZIF-7 membrane at different temperatures.

2.3.4.2. Sensors.

The combination of high porosity and physical properties certainly provides excellent conditions to use metal–organic thin films for sensing applications. Kreno et *al.* compared a bare sensor to a NMOF-modified version that contained an Ag nanoparticle array coated with nano-HKUST-1 crystals: the modified sensor showed a 14-fold signal enhancement for CO_2 sensing.[132, 133] These differences were attributed to the high capacity of the nano-HKUST-1 crystals to concentrate CO_2 within the MOF pores. Bein *et al.* reported the selective growth of HKUST-1 thin films on functionalized quartz - crystal microbalance (QCM) gold electrodes. This device was used to evaluate accurately the mass variations, making possible the detection of water adsorption when this thin film was exposed to atmospheres with different relative humidities.[134] More recently, Lu and Hupp constructed ZIF-8-based Fabry–Pérot devices that function as selective sensors for chemical vapours and gases. This sensor is based on the displacement of Fabry–Pérot interference peaks as a function of the exposure of the device to an analyte . The authors show the capabilities of such ZIF-8 based thin films to detect the presence of ethanol in the atmosphere. [140, 135]

2.3.4.3. Magnetic properties.

The interesting magnetic properties of metal–organic materials studied by the molecular magnetism field during the last decades can be certainly used to fabricate magnetic metal–organic thin films. The examples, however, are still scarce. An illustrative example is the work led by Bousseksou *et al.*, who fabricated NMOF thin films displaying a room temperature spin-crossover behavior with hysteresis (Fig. 8b). These authors demonstrated the formation of such thin films by stepwise synthesis of [Fe(pyrazine)[M(CN)$_4$]] (where M is Ni, Pd or Pt) on surfaces.

3. REFERENCES

1. K. A., *Bull. Hist. Chem.*, 2008, **33**, 7.
2. H. J. Buser, D. Schwarzenbach, W. Petter and A. Ludi, *Inorg. Chem.*, 1977, **16**, 2704-2710.
3. H. M. P. J. H. RAYNER, *Nature*, 1949, **163**.
4. T. Iwamoto, T. Nakano, M. Morita, T. Miyoshi, T. Miyamoto and Y. Sasaki, *Inorg. Chim. Acta*, 1968, **2**, 313-316.
5. Y. Kinoshita, I. Matsubara, T. Higuchi and Y. Saito, *B. Chem. Soc. Jpn.*, 1959, **32**, 1221-1226.
6. R. G. Vranka and E. L. Amma, *Inorg. Chem.*, 1966, **5**, 1020-1025.
7. A. Santoro, A. D. Mighell and C. W. Reimann, *Acta Crystallogr. B*, 1970, **26**, 979-984.
8. A. F. Wells, *Three-Dimensional Nets and Polyhedra*, Wiley, New York, 1977.
9. B. F. Hoskins and R. Robson, *J. Am. Chem. Soc.*, 1989, **111**, 5962-5964.
10. B. F. Hoskins and R. Robson, *J. Am. Chem. Soc.*, 1990, **112**, 1546-1554.
11. O. M. Yaghi and H. Li, *J. Am. Chem. Soc.*, 1995, **117**, 10401-10402.
12. H. Li, M. Eddaoudi, T. L. Groy and O. M. Yaghi, *J. Am. Chem. Soc.*, 1998, **120**, 8571-8572.
13. Y. Aoyama, in *Design of Organic Solids*, eds. E. Weber, Y. Aoyama, M. R. Caira, G. R. Desiraju, J. P. Glusker, A. D. Hamilton, R. E. Meléndez and A. Nangia, Springer Berlin Heidelberg, 1998, vol. 198, pp. 131-161.
14. P. J. Hagrman, D. Hagrman and J. Zubieta, *Angew. Chem. Int. Ed.*, 1999, **38**, 2638-2684.
15. B. Moulton and M. J. Zaworotko, *Curr. Opin. Solid St. M.*, 2002, **6**, 117-123.
16. S. L. James, *Chem. Soc. Rev.*, 2003, **32**, 276-288.
17. G. Férey, *Chem. Mater.*, 2001, **13**, 3084-3098.
18. C. Janiak, *Dalton Transactions*, 2003, 2781-2804.
19. S. R. Batten, N. R. Champness, X.-M. Chen, J. Garcia-Martinez, S. Kitagawa, L. Öhrström, M. O'Keeffe, M. Paik Suh and J. Reedijk, *Pure and Appl. Chem.*, 2013, **85**.
20. D. Bradshaw, S. El-Hankari and L. Lupica-Spagnolo, *Chem. Soc. Rev.*, 2014.
21. C. K. Brozek and M. Dinca, *Chem. Soc. Rev.*, 2014.
22. J. Canivet, A. Fateeva, Y. Guo, B. Coasne and D. Farrusseng, *Chem. Soc. Rev.*, 2014.
23. Y. J. Colon and R. Q. Snurr, *Chem. Soc. Rev.*, 2014.
24. A. U. Czaja, N. Trukhan and U. Muller, *Chem. Soc. Rev.*, 2009, **38**, 1284-1293.
25. P. Falcaro, R. Ricco, C. M. Doherty, K. Liang, A. J. Hill and M. J. Styles, *Chem. Soc. Rev.*, 2014.
26. S. Furukawa, J. Reboul, S. Diring, K. Sumida and S. Kitagawa, *Chem. Soc. Rev.*, 2014.
27. J. Liu, L. Chen, H. Cui, J. Zhang, L. Zhang and C.-Y. Su, *Chem. Soc. Rev.*, 2014.
28. A. Schneemann, V. Bon, I. Schwedler, I. Senkovska, S. Kaskel and R. A. Fischer, *Chem. Soc. Rev.*, 2014.
29. V. Stavila, A. A. Talin and M. D. Allendorf, *Chem. Soc. Rev.*, 2014.
30. T. Zhang and W. Lin, *Chem. Soc. Rev.*, 2014.
31. Z. Zhang and M. J. Zaworotko, *Chem. Soc. Rev.*, 2014.
32. M. Eddaoudi, D. B. Moler, H. Li, B. Chen, T. M. Reineke, M. O'Keeffe and O. M. Yaghi, *Acc. Chem. Res.*, 2001, **34**, 319-330.
33. J. L. C. Rowsell and O. M. Yaghi, *Micropor. Mesopor. Mat.*, 2004, **73**, 3-14.
34. A. Carné-Sánchez, I. Imaz, K. C. Stylianou and D. Maspoch, *Chem. Eur. J.*, 2014, **20**, 5192-5201.
35. M. Kondo, T. Yoshitomi, H. Matsuzaka, S. Kitagawa and K. Seki, *Angew. Chem. Int. Ed.*, 1997, **36**, 1725-1727.
36. H. Li, M. Eddaoudi, M. O'Keeffe and O. M. Yaghi, *Nature*, 1999, **402**, 276-279.
37. O. K. Farha, I. Eryazici, N. C. Jeong, B. G. Hauser, C. E. Wilmer, A. A. Sarjeant, R. Q. Snurr, S. T. Nguyen, A. Ö. Yazaydın and J. T. Hupp, *J. Am. Chem. Soc.*, 2012, **134**, 15016-15021.
38. H. Furukawa, K. E. Cordova, M. O'Keeffe and O. M. Yaghi, *Science*, 2013, **341**.
39. A. U. Czaja, N. Trukhan and U. Muller, *Chem. Soc. Rev.*, 2009, **38**, 1284-1293.
40. L. Schlapbach and A. Zuttel, *Nature*, 2001, **414**, 353-358.

41. O. K. Farha, A. Özgür Yazaydın, I. Eryazici, C. D. Malliakas, B. G. Hauser, M. G. Kanatzidis, S. T. Nguyen, R. Q. Snurr and J. T. Hupp, *Nat Chem*, 2010, **2**, 944-948.
42. H. Furukawa, N. Ko, Y. B. Go, N. Aratani, S. B. Choi, E. Choi, A. Ö. Yazaydin, R. Q. Snurr, M. O'Keeffe, J. Kim and O. M. Yaghi, *Science*, 2010, **329**, 424-428.
43. S. Ma, J. Eckert, P. M. Forster, J. W. Yoon, Y. K. Hwang, J.-S. Chang, C. D. Collier, J. B. Parise and H.-C. Zhou, *J. Am. Chem. Soc.*, 2008, **130**, 15896-15902.
44. J. L. C. Rowsell and O. M. Yaghi, *J. Am. Chem. Soc.*, 2006, **128**, 1304-1315.
45. R. S. Haszeldine, *Science*, 2009, **325**, 1644-1645.
46. K. Sumida, D. L. Rogow, J. A. Mason, T. M. McDonald, E. D. Bloch, Z. R. Herm, T.-H. Bae and J. R. Long, *Chem. Rev.*, 2011, **112**, 724-781.
47. H.-Y. Cho, D.-A. Yang, J. Kim, S.-Y. Jeong and W.-S. Ahn, *Catalysis Today*, 2012, **185**, 35-40.
48. Z. Zhang, Y. Zhao, Q. Gong, Z. Li and J. Li, *Chem. Comm.*, 2013, **49**, 653-661.
49. P. D. C. Dietzel, R. E. Johnsen, H. Fjellvag, S. Bordiga, E. Groppo, S. Chavan and R. Blom, *Chem. Comm.*, 2008, 5125-5127.
50. T. M. McDonald, D. M. D'Alessandro, R. Krishna and J. R. Long, *Chem. Sci.*, 2011, **2**, 2022-2028.
51. Y. Peng, V. Krungleviciute, I. Eryazici, J. T. Hupp, O. K. Farha and T. Yildirim, *J. Am. Chem. Soc.*, 2013.
52. T. A. Makal, J.-R. Li, W. Lu and H.-C. Zhou, *Chem. Soc. Rev.*, 2012, **41**, 7761-7779.
53. U. Mueller, M. Schubert, F. Teich, H. Puetter, K. Schierle-Arndt and J. Pastre, *J. Mater. Chem.*, 2006, **16**, 626-636.
54. Y. Peng, V. Krungleviciute, I. Eryazici, J. T. Hupp, O. K. Farha and T. Yildirim, *J. Am. Chem. Soc.*, 2013, **135**, 11887-11894.
55. Y.-S. Li, F.-Y. Liang, H. Bux, A. Feldhoff, W.-S. Yang and J. Caro, *Angew. Chem.*, 2010, **122**, 558-561.
56. E. D. Bloch, W. L. Queen, R. Krishna, J. M. Zadrozny, C. M. Brown and J. R. Long, *Science*, 2012, **335**, 1606-1610.
57. L. Alaerts, E. Séguin, H. Poelman, F. Thibault-Starzyk, P. A. Jacobs and D. E. De Vos, *Chem. Eur. J.*, 2006, **12**, 7353-7363.
58. J. Kim, S. Bhattacharjee, K.-E. Jeong, S.-Y. Jeong and W.-S. Ahn, *Chem. Comm.*, 2009, 3904-3906.
59. Y. K. Hwang, D.-Y. Hong, J.-S. Chang, H. Seo, M. Yoon, J. Kim, S. H. Jhung, C. Serre and G. Férey, *Applied Catalysis A: General*, 2009, **358**, 249-253.
60. A. Henschel, K. Gedrich, R. Kraehnert and S. Kaskel, *Chem. Comm.*, 2008, 4192-4194.
61. R. Matsuda, R. Kitaura, S. Kitagawa, Y. Kubota, R. V. Belosludov, T. C. Kobayashi, H. Sakamoto, T. Chiba, M. Takata, Y. Kawazoe and Y. Mita, *Nature*, 2005, **436**, 238-241.
62. S. Hasegawa, S. Horike, R. Matsuda, S. Furukawa, K. Mochizuki, Y. Kinoshita and S. Kitagawa, *J. Am. Chem. Soc.*, 2007, **129**, 2607-2614.
63. K. K. Tanabe and S. M. Cohen, *Chem. Soc. Rev.*, 2011, **40**, 498-519.
64. M. Banerjee, S. Das, M. Yoon, H. J. Choi, M. H. Hyun, S. M. Park, G. Seo and K. Kim, *J. Am. Chem. Soc.*, 2009, **131**, 7524-7525.
65. M. H. Alkordi, Y. Liu, R. W. Larsen, J. F. Eubank and M. Eddaoudi, *J. Am. Chem. Soc.*, 2008, **130**, 12639-12641.
66. S. Hermes, M.-K. Schröter, R. Schmid, L. Khodeir, M. Muhler, A. Tissler, R. W. Fischer and R. A. Fischer, *Angew. Chem. Int. Ed.*, 2005, **44**, 6237-6241.
67. M. Meilikhov, K. Yusenko, D. Esken, S. Turner, G. Van Tendeloo and R. A. Fischer, *Eur. J. Inorg. Chem.*, 2010, **2010**, 3701-3714.
68. M. Sabo, A. Henschel, H. Frode, E. Klemm and S. Kaskel, *J. Mater. Chem.*, 2007, **17**, 3827-3832.
69. J. Hermannsdörfer and R. Kempe, *Chem. Eur. J.*, 2011, **17**, 8071-8077.
70. C.-D. Wu, A. Hu, L. Zhang and W. Lin, *J. Am. Chem. Soc.*, 2005, **127**, 8940-8941.

71. L. Ma, J. M. Falkowski, C. Abney and W. Lin, *Nat Chem*, 2010, **2**, 838-846.
72. S.-H. Cho, B. Ma, S. T. Nguyen, J. T. Hupp and T. E. Albrecht-Schmitt, *Chem. Comm.*, 2006, 2563-2565.
73. F. Song, C. Wang, J. M. Falkowski, L. Ma and W. Lin, *J. Am. Chem. Soc.*, 2010, **132**, 15390-15398.
74. S. Vaucher, M. Li and S. Mann, *Angew. Chem. Int. Ed.*, 2000, **39**, 1793-1796.
75. G. Liang, J. Xu and X. Wang, *J. Am. Chem. Soc.*, 2009, **131**, 5378-5379.
76. S. Hou, C. C. Harrell, L. Trofin, P. Kohli and C. R. Martin, *Journal of the American Chemical Society*, 2004, **126**, 5674-5675.
77. R. Li, Y.-P. Yuan, L.-G. Qiu, W. Zhang and J.-F. Zhu, *Small*, 2012, **8**, 225-230.
78. M. Hu, N. L. Torad and Y. Yamauchi, *Eur. J. Inorg. Chem.*, 2012, **2012**, 4795-4799.
79. A. Carné-Sánchez, I. Imaz, M. Cano-Sarabia and D. Maspoch, *Nat Chem*, 2013, **5**, 203-211.
80. T. Tsuruoka, S. Furukawa, Y. Takashima, K. Yoshida, S. Isoda and S. Kitagawa, *Angew. Chem. Int. Ed.*, 2009, **48**, 4739-4743.
81. P. Horcajada, C. Serre, D. Grosso, C. Boissière, S. Perruchas, C. Sanchez and G. Férey, *Advanced Materials*, 2009, **21**, 1931-1935.
82. S. p. Diring, S. Furukawa, Y. Takashima, T. Tsuruoka and S. Kitagawa, *Chem. Mater.*, 2010, **22**, 4531-4538.
83. J. Cravillon, R. Nayuk, S. Springer, A. Feldhoff, K. Huber and M. Wiebcke, *Chem. Mater.*, 2011, **23**, 2130-2141.
84. J. Cravillon, C. A. Schröder, R. Nayuk, J. Gummel, K. Huber and M. Wiebcke, *Angew. Chem. Int. Ed.*, 2011, **50**, 8067-8071.
85. S. K. Nune, P. K. Thallapally, A. Dohnalkova, C. Wang, J. Liu and G. J. Exarhos, *Chem. Comm.*, 2010, **46**, 4878-4880.
86. P. Horcajada, T. Chalati, C. Serre, B. Gillet, C. Sebrie, T. Baati, J. F. Eubank, D. Heurtaux, P. Clayette, C. Kreuz, J.-S. Chang, Y. K. Hwang, V. Marsaud, P.-N. Bories, L. Cynober, S. Gil, G. Férey, P. Couvreur and R. Gref, *Nature Mat.*, 2010, **9**.
87. A. Carné-Sánchez, C. S. Bonnet, I. Imaz, J. Lorenzo, É. Tóth and D. Maspoch, *J. Am. Chem. Soc.*, 2013, **135**, 17711-17714.
88. Z. Ni and R. I. Masel, *J. Am. Chem. Soc.*, 2006, **128**, 12394-12395.
89. W.-J. Son, J. Kim, J. Kim and W.-S. Ahn, *Chem. Comm.*, 2008, 6336-6338.
90. S. Wu, X. Shen, B. Cao, L. Lin, K. Shen and W. Liu, *J. Mat. Sci.*, 2009, **44**, 6447-6450.
91. R. Ameloot, L. Stappers, J. Fransaer, L. Alaerts, B. F. Sels and D. E. De Vos, *Chem. Mater.*, 2009, **21**, 2580-2582.
92. Y. K. Park, S. B. Choi, H. Kim, K. Kim, B. H. Won, K. Choi, J. S. Choi, W. S. Ahn, N. Won, S. Kim, D. H. Jung, S. H. Choi, G. H. Kim, S. S. Cha, Y. H. Jhon, J. K. Yang and J. Kim, *Angew. Chem. Int. Ed.*, 2007, **46**, 8230-8233.
93. Y. Chen, V. Lykourinou, T. Hoang, L.-J. Ming and S. Ma, *Inorg. Chem.*, 2012, **51**, 9156-9158.
94. D. Tanaka, A. Henke, K. Albrecht, M. Moeller, K. Nakagawa, S. Kitagawa and J. Groll, *Nat Chem*, 2010, **2**, 410-416.
95. W. Cho, H. J. Lee and M. Oh, *J. Am. Chem. Soc.*, 2008, **130**, 16943-16946.
96. A. S. Münch, J. Seidel, A. Obst, E. Weber and F. O. R. L. Mertens, *Chem. Eur. J.*, 2011, **17**, 10958-10964.
97. P. Horcajada, C. Serre, M. Vallet-Regi, M. Sebban, F. Taulelle and G. Ferey, *Angew. Chem. Int. Ed.*, 2006, **45**, 5974-5978.
98. P. S. Wheatley, A. R. Butler, M. S. Crane, S. Fox, B. Xiao, A. G. Rossi, I. L. Megson and R. E. Morris, *J. Am. Chem. Soc.*, 2006, **128**, 502-509.
99. P. Horcajada, T. Chalati, C. Serre, B. Gillet, C. Sebrie, T. Baati, J. F. Eubank, D. Heurtaux, P. Clayette, C. Kreuz, J.-S. Chang, Y. K. Hwang, V. Marsaud, P.-N. Bories, L. Cynober, S. Gil, G. Ferey, P. Couvreur and R. Gref, *Nat Mater*, 2010, **9**, 172-178.

100. P. Horcajada, R. Gref, T. Baati, P. K. Allan, G. Maurin, P. Couvreur, G. Férey, R. E. Morris and C. Serre, *Chem. Rev.*, 2011, **112**, 1232-1268.
101. K. M. L. Taylor-Pashow, J. Della Rocca, Z. Xie, S. Tran and W. Lin, *J. Am. Chem. Soc.*, 2009, **131**, 14261-+.
102. W. J. Rieter, K. M. L. Taylor, H. An, W. Lin and W. Lin, *J. Am. Chem. Soc.*, 2006, **128**, 9024-9025.
103. K. M. L. Taylor, A. Jin and W. Lin, *Angew. Chem. Int. Ed.*, 2008, **47**, 7722-7725.
104. K. E. deKrafft, Z. Xie, G. Cao, S. Tran, L. Ma, O. Z. Zhou and W. Lin, *Angew. Chem. Int. Ed.*, 2009, **48**, 9901-9904.
105. C.-H. Kuo, Y. Tang, L.-Y. Chou, B. T. Sneed, C. N. Brodsky, Z. Zhao and C.-K. Tsung, *J. Am. Chem. Soc.*, 2012, **134**, 14345-14348.
106. G. Lu, S. Li, Z. Guo, O. K. Farha, B. G. Hauser, X. Qi, Y. Wang, X. Wang, S. Han, X. Liu, J. S. DuChene, H. Zhang, Q. Zhang, X. Chen, J. Ma, S. C. J. Loo, W. D. Wei, Y. Yang, J. T. Hupp and F. Huo, *Nat Chem*, 2012, **4**, 310-316.
107. A. K. Geim, *Science*, 2009, **324**, 1530-1534.
108. P.-Z. Li, Y. Maeda and Q. Xu, *Chem. Comm.*, 2011, **47**, 8436-8438.
109. P. J. Saines, M. Steinmann, J.-C. Tan, H. H. M. Yeung, W. Li, P. T. Barton and A. K. Cheetham, *Inorg. Chem.*, 2012, **51**, 11198-11209.
110. G. Xu, T. Yamada, K. Otsubo, S. Sakaida and H. Kitagawa, *J. Am. Chem. Soc.*, 2012, **134**, 16524-16527.
111. R. G. Baraniuk, *Science*, 2011, **331**, 717-719.
112. M. Wuttig and N. Yamada, *Nat Mater*, 2007, **6**, 824-832.
113. A. S. Arico, P. Bruce, B. Scrosati, J.-M. Tarascon and W. van Schalkwijk, *Nat Mater*, 2005, **4**, 366-377.
114. C. D. Chin, T. Laksanasopin, Y. K. Cheung, D. Steinmiller, V. Linder, H. Parsa, J. Wang, H. Moore, R. Rouse, G. Umviligihozo, E. Karita, L. Mwambarangwe, S. L. Braunstein, J. van de Wijgert, R. Sahabo, J. E. Justman, W. El-Sadr and S. K. Sia, *Nat Med*, 2011, **17**, 1015-1019.
115. P. Saá, J. Castilla and C. Soto, *Science*, 2006, **313**, 92-94.
116. D. Sidransky, *Science*, 1997, **278**, 1054-1058.
117. J. C. Love, L. A. Estroff, J. K. Kriebel, R. G. Nuzzo and G. M. Whitesides, *Chem. Rev.*, 2005, **105**, 1103-1170.
118. E. Biemmi, C. Scherb and T. Bein, *J. Am. Chem. Soc.*, 2007, **129**, 8054-8055.
119. D. Zacher, A. Baunemann, S. Hermes and R. A. Fischer, *J. Mater. Chem.*, 2007, **17**, 2785-2792.
120. C. Scherb, A. Schödel and T. Bein, *Angew. Chem. Int. Ed.*, 2008, **47**, 5777-5779.
121. O. Shekhah, H. Wang, M. Paradinas, C. Ocal, B. Schupbach, A. Terfort, D. Zacher, R. A. Fischer and C. Woll, *Nat Mater*, 2009, **8**, 481-484.
122. Y.-S. Li, F.-Y. Liang, H. Bux, A. Feldhoff, W.-S. Yang and J. Caro, *Angew. Chem. Int. Ed.*, 2010, **49**, 548-551.
123. M. Arnold, P. Kortunov, D. J. Jones, Y. Nedellec, J. Kärger and J. Caro, *Eur. J. Inorg. Chem.*, 2007, **2007**, 60-64.
124. H. Guo, G. Zhu, I. J. Hewitt and S. Qiu, *Journal of the American Chemical Society*, 2009, **131**, 1646-1647.
125. O. Shekhah, H. Wang, D. Zacher, R. A. Fischer and C. Wöll, *Angew. Chem. Int. Ed.*, 2009, **48**, 5038-5041.
126. H. K. Arslan, O. Shekhah, J. Wohlgemuth, M. Franzreb, R. A. Fischer and C. Wöll, *Advanced Functional Materials*, 2011, **21**, 4228-4231.
127. R. Makiura, S. Motoyama, Y. Umemura, H. Yamanaka, O. Sakata and H. Kitagawa, *Nat Mater*, 2010, **9**, 565-571.
128. H. Guo, G. Zhu, I. J. Hewitt and S. Qiu, *J. Am. Chem. Soc.*, 2009, **131**, 1646-1647.
129. Y.-S. Li, H. Bux, A. Feldhoff, G.-L. Li, W.-S. Yang and J. Caro, *Adv. Mater.*, 2010, **22**, 3322-3326.
130. A. Huang, W. Dou and J. Caro, *J. Am. Chem. Soc.*, 2010, **132**, 15562-15564.

131. A. J. Brown, J. R. Johnson, M. E. Lydon, W. J. Koros, C. W. Jones and S. Nair, *Angew. Chem. Int. Ed.*, 2012, **51**, 10615-10618.
132. L. E. Kreno, J. T. Hupp and R. P. Van Duyne, *Analytical Chemistry*, 2010, **82**, 8042-8046.
133. S. Achmann, G. Hagen, J. Kita, I. Malkowsky, C. Kiener and R. Moos, *Sensors*, 2009, **9**, 1574-1589.
134. E. Biemmi, A. Darga, N. Stock and T. Bein, *Micropor. Mesopor. Mat.*, 2008, **114**, 380-386.
135. G. Lu and J. T. Hupp, *J. Am. Chem. Soc.*, 2010, **132**, 7832-7833.

PUBLICATION 1.

Nanoscale Metal-Organic Materials

Arnau Carné, Carlos Carbonell, Inhar Imaz and Daniel Maspoch

Chem Soc. Rev., **2011**, 40, 291-305

View Article Online / Journal Homepage / Table of Contents for this issue
Dynamic Article Links

Chem Soc Rev

Cite this: *Chem. Soc. Rev.*, 2011, **40**, 291–305

www.rsc.org/csr

TUTORIAL REVIEW

Nanoscale metal–organic materials

Arnau Carné, Carlos Carbonell, Inhar Imaz and Daniel Maspoch*

Received 15th July 2010
DOI: 10.1039/c0cs00042f

Metal–organic materials are found to be a fascinating novel class of functional nanomaterials. The limitless combinations between inorganic and organic building blocks enable researchers to synthesize 0- and 1-D metal–organic discrete nanostructures with varied compositions, morphologies and sizes, fabricate 2-D metal–organic thin films and membranes, and even structure them on surfaces at the nanometre length scale. In this *tutorial review*, the synthetic methodologies for preparing these miniaturized materials as well as their potential properties and future applications are discussed. This review wants to offer a panoramic view of this embryonic class of nanoscale materials that will be of interest to a cross-section of researchers working in chemistry, physics, medicine, nanotechnology, materials chemistry, *etc.*, in the next years.

Introduction

Miniaturization to the nanometre scale regime is a very prolific strategy for the development of new materials with novel and often enhanced properties compared to traditional materials, opening up avenues for technological and biomedical applications in many areas, including drug-delivery, catalysis, diagnostics, solar cells, *etc*. To date, most nanoscale materials are either purely organic or inorganic in composition. However, architectures created from the supramolecular assembly of organic and inorganic components are rapidly growing as a very attractive alternative class of nanoscale materials.

Centre d'Investigació en Nanociencia i Nanotecnologia (CIN2, ICN-CSIC), Esfera UAB, 08193 Bellaterra, Spain. E-mail: daniel.maspoch.icn@uab.es; Fax: +34 93 581 4747

But, *why do we need another class of nanoscale materials?* Traditional metal–organic materials are a fascinating family of solids created from the supramolecular association of inorganic, such as metal ions and metal–organic or inorganic clusters, and organic building blocks, including organic molecules, biomolecules and organic polymers.[1] These bulk materials, in which both types of building blocks are assembled through metal coordination, hydrogen bonding, electrostatic interactions or π–π stacking, have the potential to be tailored to show adjustable structures, compositions and properties. As a consequence, they show promise for an impressive number of applications in gas storage, drug-delivery, diagnostics, sensing, catalysis, ion exchange or separation, magnetism, optics, *etc*. However, metal–organic materials in the form of traditional bulk crystalline materials do not always fulfill all specific needs for these applications. Depending upon

Arnau Carné

Arnau Carné Sánchez was born in Manresa (Catalonia, Spain) in 1985. He received his BSc degree in Chemistry at Universitat de Barcelona (UAB) in 2008. In 2009, he got his MSc in Environmental Diagnostics and Management from Cranfield University (UK). He is currently pursuing a PhD in Chemistry at the CIN2 (ICN-CSIC) under the supervision of Dr Daniel Maspoch and Dr Inhar Imaz in the field of metal–organic nanomaterials with special interest in developing new synthetic methodologies.

Carlos Carbonell

Carlos Carbonell (Barcelona, Spain, 1975) studied Technical Chemist Engineering (2002), Materials Engineering (2004) and obtained his MSc in Nanotechnology (2008) at the Universitat Autònoma de Barcelona. After working for 7 years at the industry, he started his PhD in 2009 at the CIN2 (ICN-CSIC) under the supervision of Dr Daniel Maspoch, leader of the Supramolecular Nanochemistry & Materials Group. His current field of interest includes the synthesis and patterning of metal–organic materials assisted by soft nanolithographic techniques, such as Dip-Pen Nanolithography.

the intended application, these materials require to be not only fabricated as bulk crystalline solids, but also miniaturized at the nanometre length scale and immobilized at specific locations on surfaces.

For example, nanoscopic dimensions are typically required to provide materials of sufficiently small sizes for their internalization into cells, and this limits the applications of metal–organic materials as delivery vehicles, diagnostics, *etc.* But nanoscale metal–organic materials combine these small dimensions with the possibility to design architectures with well-defined and uniform sizes and morphologies, to disperse them in aqueous media or other solvents, and to efficiently coat them for improving their biocompatibility or recognition capabilities. Of particular interest is also the fact that nanomaterials have higher surface areas than their macroscopic counterparts. This property can strongly influence or even improve the catalytic, ion exchange, separation, sensing and sorption properties of these metal–organic materials, which, in turn, can be dependent on their sizes and shapes. A similar situation occurs with some physical properties. It is well known that unique physical properties emerge when at least one dimension of a material is reduced to the nanometre scale. Thus, nanoscale metal–organic materials are also expected to hold highly desirable size-dependent optical, electrical and magnetic properties.

It is obvious, then, that by scaling them down to the nanometre length scale, the scope of metal–organic materials will be expanded. But, *how they can be prepared at the nanometre length scale*? Like their macroscopic counterparts, they can be basically prepared by using "bottom-up" synthetic methodologies based on self-assembly processes; however, assembly of both inorganic and organic building blocks needs now to be controlled at the nanometre scale. For this, there are two major strategies. One involves a set of synthetic methodologies that induce the controlled precipitation of self-assembled supramolecular metal–organic polymers once they are formed. To date, these methodologies include the use of poor solvents, microwaves, ultrasounds or thermal conditions. The second strategy consists of confining the supramolecular assembly at specific locations. For example, self-assembly processes can be confined into droplets by using micro- or nanoemulsion techniques. Or they can be precisely controlled on the surface of substrates, liquids, membranes or other nanostructures, which act as templates, by using deposition techniques, such as layer-by-layer (LbL) synthesis, Langmuir–Blodgett, *etc.* A specific case that fits in this second strategy is the use of techniques for their nanostructuration on surfaces. In fact, the growth and positioning control on surfaces of these materials is crucial to start to conceive their integration on supports for the fabrication of complex surface sensors, separation membranes, drug-delivery platforms and catalysts.

The miniaturization of metal–organic materials down to the nanometre length scale is therefore a unique opportunity to develop a new class of highly tailorable nanoscale materials that combine the rich diversity of compositions, structures and properties of classical metal–organic materials with the obvious advantages of nanomaterials. Note that we use the term metal–organic material here to include materials with extended metal–organic structures, crystalline or not, that are built up from the supramolecular assembly of inorganic (metal ions and metal–organic or inorganic clusters) and organic building blocks (organic ligands, polymers, and biomolecules). And the term nanoscale includes these materials with at least one dimension between 1 and 100 nm, although some representative examples with sizes comprised between 100 and 1000 nm have also been included due to their size-dependent characteristics and properties. Therefore, these nanoscale materials have been classified according to their dimensionality: 0-D (particles), 1-D (fibers, tubes, and rods), and 2-D (thin films and membranes). In this review, we describe the recent advances made on the synthesis, growth and nanostructuration of this class of materials, their potential properties and applications, and illustrate their future expectations.

Inhar Imaz

Inhar Imaz was born in Hendaia (Basque Country, France) in 1978. He received his PhD in Materials Science from the Université Bordeaux I in 2005, where he studied the formation of heterometallic metal–organic architectures from tetrahedral building blocks. He joined the CIN-2 (ICN-CSIC) centre in 2005 as a Postdoctoral fellow. At present, he is an associate professor under the "Ramón y Cajal" program at the Institut Català de Nanotecnologia. His research is focused on the design, the synthesis and the study of novel nanostructured metal–organic materials. He is exploring new synthetic methodologies, new properties and new applications of supramolecular nanomaterials.

Daniel Maspoch

Daniel Maspoch was born in L'Escala (Catalonia, Spain) in 1976. He received his BSc degree in Chemistry from Universitat de Girona, and he earned his PhD in Materials Science at the Universitat Autònoma de Barcelona and at the Institut de Ciencia de Materials de Barcelona. After postdoctoral work in Prof. Chad A. Mirkin's group at Northwestern University, he moved to the Centre d'Investigació en Nanociència i Nanotecnologia (ICN-CSIC), thanks to the Ramón y Cajal Program financial support. His group is working on controlling the supramolecular assembly of (bio)molecules, metal ions and nanoscale building blocks at the nanometre scale.

0- and 1-D metal–organic nanomaterials

Synthesis

There are two major strategies for synthesizing 0-D and 1-D nanoscale metal–organic materials (Fig. 1): (i) confinement of the supramolecular assembly at nanoscopic locations by using emulsions or templates; and (ii) the controlled precipitation of self-assembled metal–organic polymers once they are formed, thanks to the use of poor solvents, microwave radiation, ultrasounds or temperature.

Nanoemulsion is a suspension of small droplets, usually stabilized by a surfactant, with diameters ranging from 50 to 1000 nm, of one liquid in a second liquid in which the first will not mix. Because of these dimensions, these droplets can be used as "nanoreactors" to confine the self-assembly, nucleation and growth of metal–organic nanostructures. Briefly, this approach usually consists of first dissolving each precursor in the solvent that will be dispersed. A water-in-oil, or reverse, emulsion is then prepared from a surfactant, and the collisions between droplets containing those precursors or the application of an external stimulus, such as temperature, light or microwave radiation, spontaneously induce their polymerization, thus delimiting their growth inside the nanodroplet. For example, by dissolving Prussian blue precursors in water, using this solution to create a water-in-oil emulsion and further exposing this emulsion to daylight, Mann *et al.* synthesized the first examples of nanoscale metal–organic frameworks (NMOFs): Prussian blue cubic nanocrystals.[2] Since then, emulsions have been successfully used to produce nanocrystals of heterometallic cyanometalates, Prussian Blue analogues using triazole instead of cyano groups and Gd(III)-based MOFs.

Besides the utility of their internal volume as "nanoreactors", nanodroplets of these emulsions have also the potential to be used as templates to prepare metal–organic nanoshells. In this case, the polymerization must be concentrated on the interface of the droplets by using, for example, a chemical affinity surfactant. Thus far, this strategy has been used by Wang *et al.*, who synthesized the first examples of Prussian blue nanoshells.[3] These shells were synthesized by preparing an oil-in-water emulsion with an organometallic surfactant terminated with pentacyano(4-(dimethylamino)-pyridine)ferrate. Then, the addition of Fe(III) ions to the aqueous solution induced the coordinative polymerization between them and the surfactant, thereby creating a metal–organic shell on the interface of each droplet.

Nanomaterials are also excellent candidates to be used as templates for fabricating metal–organic nanostructures. In this methodology, a film of a supramolecular metal–organic polymer is deposited on the template by using a deposition technique, such as LbL deposition. This deposition, followed by the removal of this template using thermal or chemical techniques, can leave behind a metal–organic nanostructure that mimics the shape and size of this template. Martin *et al.* reported a brilliant example that illustrates how powerful can this approach be.[4] The LbL growth of a film composed of Zr(IV) metal ions and diorganophosphonate ligands on the pores of an alumina membrane, followed by the removal of this membrane using phosphoric acid, allowed the fabrication of highly uniform metal–organic nanotubes.

A second family of methodologies that enable the synthesis of 0-D and 1-D metal–organic nanostructures is based on mixing the precursors under certain reaction conditions that favor the fast nucleation (to increase the seed number)

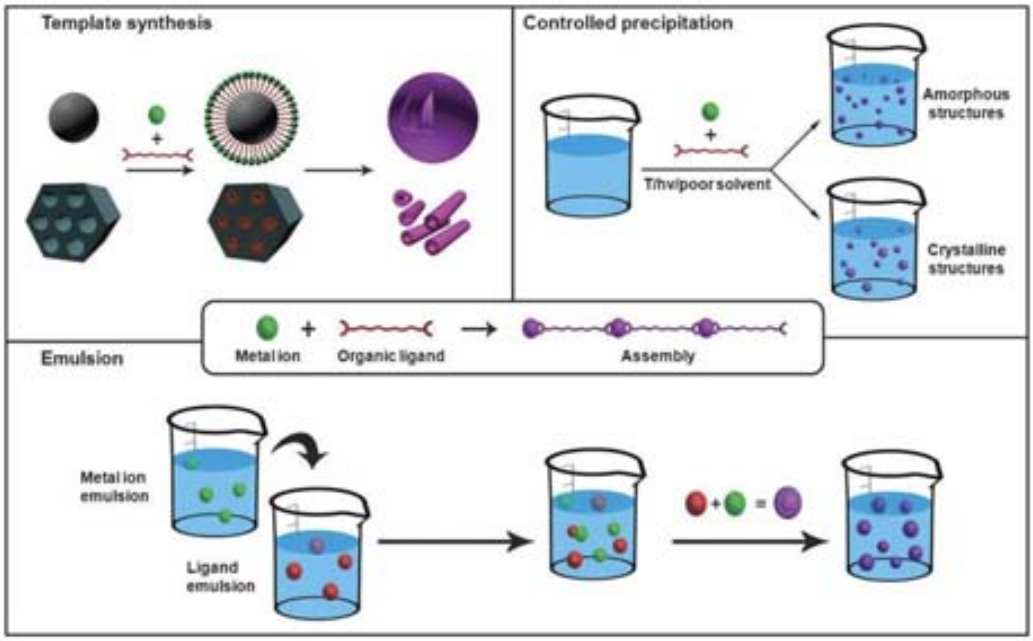

Fig. 1 Schematic representation of the principal synthetic strategies used for synthesizing 0- and 1-D metal–organic nanostructures using conventional coordination chemistry, including the LbL growth on templates, the controlled precipitation of metal–organic nanostructures and the microemulsion techniques.

of self-assembled metal–organic polymers. In most of the cases, these conditions involve the use of microwave radiation, ultrasounds or temperature. For example, it is well known that at high temperatures, solubility of precursors increases avoiding fast precipitation, and allows crystallization to occur. It is therefore a strategy generally used to produce bulk crystalline metal–organic materials. However, if one controls certain reaction conditions, including solvent, surfactant, temperature and time, solvothermal synthesis can be a very productive strategy for synthesizing a wide variety of NMOFs. Some of them were recently reported by Horcajada, Gref *et al.*, who synthesized a series of NMOFs by simply mixing Fe(III) metal ions with a series of multitopic ligands, such as 1,4-benzenedicarboxylate (BDC), benzene-1,3,5-tricarboxylate (BTC), fumaric acid, *etc.*, in a variety of solvents at temperatures usually above 100 °C.[5]

The use of microwave radiation and ultrasounds can also be exploited for miniaturizing MOFs. Ni and Masel reported for the first time the use of microwave radiation to induce the precipitation of an already known MOF (IRMOF-1, 2 and 3) based on Zn(II) metal ions and BDC ligands at the nanometre scale.[6] This reaction consists of exposing a diethylformamide (DEF) solution of both building blocks at 150 W for only 25 seconds. Similarly, sonochemical synthesis can lead to a homogenous nucleation and a substantial reduction in crystallization time. The well-known MOF-5 was miniaturized at the micrometre scale using this methodology.[7] And even more recently, nanoscale arrowheads NMOFs of Prussian blue analogues have been prepared by Wu *et al.* with the help of ultrasonic radiation.[8]

However, one of the most extensive approaches used so far for preparing metal–organic nanostructures is based on the use of poor solvents to induce the fast precipitation of metal–organic polymers. This strategy can be divided into two well-established synthetic methodologies: (i) self-assembly takes place in a solution in which the synthesized metal–organic polymers are not soluble, and therefore, the poor solvent is the initial solution used to mix the building blocks; and (ii) the use of an external poor solvent to precipitate the metal–organic polymers previously synthesized in the initial solution, and therefore, the poor solvent is an external one. Wang *et al.* and Oh and Mirkin simultaneously developed both synthetic methodologies.[9,10] The first authors exploited the insolubility of a coordination polymer built up from Pt(IV) metal ions and *p*-phenylenediamine in water to produce monodisperse spherical particles.[9] On the other hand, Oh and Mirkin first prepared a coordination polymer constructed from Zn(II), Cu(II) or Ni(II) metal ions and a carboxylate-functionalized binaphthyl bis-metallotridentate Schiff base (BMSB) in pyridine, and this polymer was then precipitated in the form of amorphous spherical infinite coordination particles (ICPs) by addition of a poor solvent, such as ether or pentane.[10] The versatility of this method has been proven by preparing a wide range of spherical amorphous ICPs, multi-shaped NMOFs and even nanoscale fibers.

Shapes and sizes

Even though we are in the early stages of their development,[11,12] the abovementioned synthetic methodologies have already facilitated the preparation of several metal–organic nanostructures, ranging from 0-D amorphous ICPs and crystalline NMOFs (with multiple shapes) to 1-D rod-like crystals, fibers and tubes (Fig. 2). In most of the cases, their preparation has allowed researchers to continuously improve these synthetic methodologies, thus starting to understand some of the reaction conditions that one needs to modify in order to control their

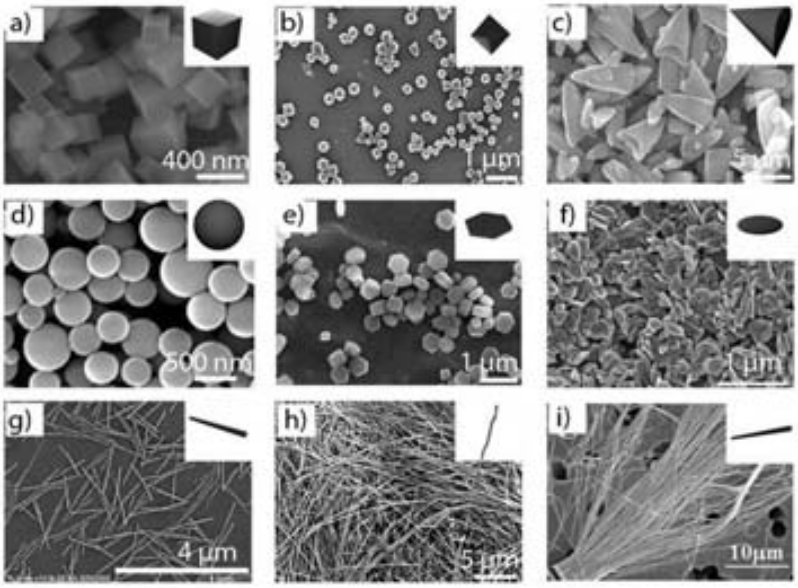

Fig. 2 Representative SEM images and their corresponding schematic figures of 0- and 1-D metal–organic nanostructures showing the wide diversity of morphologies obtained so far: (a) cubic particles, (b) octahedral particles, (c) arrow-like particles, (d) spheres, (e) hexagonal lumps, (f) plate-like particles, (g) rods, (h) fibers, and (i) tubes. (© The American Chemical Society, Springer and Wiley Interscience, reprinted with permission).

shapes and sizes. To date, the choice of the synthetic strategy as well as the corresponding reaction conditions seems crucial to prepare a certain type of nanostructure with precise control over its shape and size.

This is the case of amorphous spherical ICPs that have exclusively been prepared by using methods based on fast precipitation induced by poor solvents. This strategy provides further control on the size of the colloidal spheres through modifications in the reaction conditions. There are three known parameters that can be tuned in order to control their diameter. The first one is the characteristics of the poor solvent, such as the polarity. Oh and Mirkin reported that, under identical reaction conditions, the use of pentane as the poor solvent leads to Zn(II)–BMSB spherical ICPs with larger diameters (780 ± 230 nm) than the ones obtained using more polar diethyl ether (190 ± 60 nm).[10] The second parameter is the rate of addition of the poor solvent. Generally, larger spheres are obtained by decreasing the addition speed of the poor solvent in the reaction mixture. Finally, the third condition is the concentration of the reactants, which is inversely related to the diameter of the spheres. Maspoch *et al.* demonstrated that the diameter of ICPs built up from the connection of Zn(II) metal ions through bis(imidazole-1-ylmethyl)benzene (Bix) ligands was controlled from 130 ± 14 nm to 1050 ± 83 nm by decreasing the concentration of both Zn(II) metal ions and Bix components from 1×10^{-1} M to 5×10^{-3} M.[13]

Crystalline NMOFs are generally synthesized by using emulsions, solvothermal and sonochemical synthesis, poor solvents and microwave-assisted synthesis. In most of these strategies, the size and shape of the resulting NMOFs are closely dependent on the type of solvent, the nature, concentration and stoichiometry of the precursors, and the specific reaction conditions used in each one of these methodologies, such as the applied temperature in solvothermal synthesis, the microwave radiation intensity in microwave-assisted synthesis, *etc.*

There are several examples where the solvent has an effect on the shape and size of NMOFs. Jung and Oh found that cubic NMOFs built up from Zn(II) metal ions and metallosalen (MS) ligands were prepared with different sizes by performing identical solvothermal reactions under different DMSO/DMF mixtures.[14] Here, DMSO/DMF mixtures in proportions 1 : 1, 1 : 2, and 2 : 1 led to cubes with an average size of 308 ± 36 nm, 600 ± 94 nm, and 4860 ± 780 nm, respectively. The synthesis of NMOFs is also dependent on the nature, concentration and stoichiometry of the reactants. For example, Ni and Masel reported how the dimensions of cubic Zn(II)–BDC NMOFs prepared through microwave-assisted synthesis are reduced by decreasing the concentration of either Zn(II) metal ions or BDC ligands.[6]

Of special interest are the specific conditions, such as the temperature, the microwave radiation and the surfactant, used on these synthetic methodologies because they are excellent parameters to control for tailoring NMOFs. Among them, nanoemulsions are interesting because it is possible to tailor their droplet sizes, and therefore, the NMOFs sizes by controlling the composition of these emulsions, such as the relative composition of the surfactant, the oil phase and the aqueous phase. Lin *et al.* took advantage of this to prove that the dimensions (both diameter and length) of Gd(III)–BDC nanorods can be tailored by simply changing the water to surfactant molar ratio.[15] In solvothermal synthesis, the reaction temperature can also affect the dimensions of the produced NMOFs. This dependence was confirmed by Jung and Oh, who reported that smaller cubic Zn(II)–MS NMOFs are generated at lower reaction temperatures.[14] While cubes with dimensions of 166 ± 15 nm were obtained at 80 °C, an increase of the temperature up to 120 °C afforded bigger cubes with dimensions of 308 ± 36 nm.

The use of surfactants in methods based on fast precipitation is a further factor to be considered because they can play a critical role not only to control the morphology of NMOFs but also to increase their stability, avoiding agglomeration. For example, Thallapally *et al.* have recently highlighted the importance of using poly(diallyldimethylammonium chloride) as the surfactant to prepare hexagonally-shaped NMOFs built up from the connection of Zn(II) metal ions through imidazolate ligands.[16] The use of other surfactants did not result in the formation of these NMOFs. However, surfactants are not the only type of substances that can help researchers to control the NMOFs shape. Like in purely inorganic nanomaterials, organic ligands also show promise for acting as blocking agents, which can control the growth rate of NMOFs in certain directions. Oh *et al.* enormously contributed to prove this concept.[17] These authors reported that hexagonal rod-like In(III)–BDC NMOFs synthesized by solvothermal synthesis can be tuned to hexagonal lumps or disks by simply adding certain amounts of pyridine to the reaction solution.

Besides the formation of ICPs and NMOFs, there are other attractive nanoscale 1-D metal–organic materials: nanofibers and nanotubes.[18] To date, most of the metal–organic nanofibers have been prepared by using fast precipitation methods. Maspoch *et al.* reported the fabrication of chiral nanofibers by adding a solution of aspartate (Asp) ligands into a solution of Cu(II) metal ions.[19] Here, the length of these fibers was controlled by adjusting the addition rate of Asp solution, which is again inversely related to the length of the nanofibers produced. A mixture of both solutions by using a very slow diffusion led to very long (up to one centimetre) nanofibers, whereas a fast mixture decreased this length up to tens of micrometres. Nanotubes are also a very attractive type of nanoscale materials, but only one example made up from metal ions and organic ligands has been reported so far. As stated above, Martin *et al.* utilized alumina membranes as templates for synthesizing Zn(IV)–phosphonate nanotubes through a LbL synthesis.[4] This is a very versatile synthetic methodology, and it will certainly allow the preparation of more metal–organic nanotubes in the near future, opening the door to control their outside diameter and length by selecting the diameter of the pores and the thickness of the alumina membrane, respectively, whereas the pore size and the wall thickness can be controlled by the number of inorganic/organic layers deposited on the pore wall of the template.

Hierarchical metal–organic superstructures

Like pure inorganic nanomaterials, the research on metal–organic nanostructures has recently started to be extended to

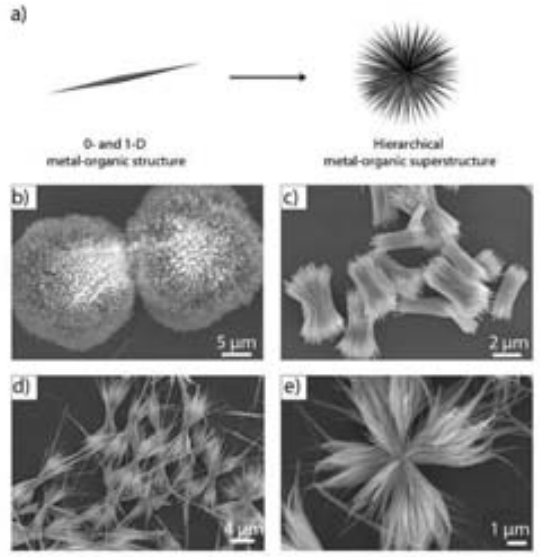

Fig. 3 (a) Scheme illustrating the formation of hierarchical metal–organic superstructures. (b–e) SEM images of representative hierarchical metal–organic structures: (b) urchin-like, (c) bundle-like, (d) sheaf-like, and (e) flower-like superstructures. (© The American Chemical Society and The Royal Society of Chemistry, reprinted with permission).

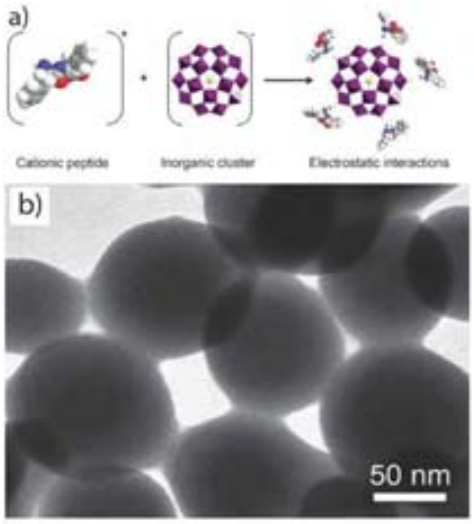

Fig. 4 (a) Scheme illustrating the formation of nanospheres through the supramolecular assembly (electrostatic interactions) between a cationic peptide and an anionic inorganic cluster. (b) SEM image of these spheres (© Wiley Interscience, reprinted with permission).

the assembly of ICPs or NMOFs into ordered hierarchical superstructures that are able to exhibit a rich range of complex architectures (Fig. 3a). For example, Zhang *et al.* demonstrated the formation of sheaf-, flower-, wheatear-, straw-, bundle-, urchin- and butterfly-like hierarchical architectures from connecting Eu(III), Tb(III) or Ce(III) metal ions through BTC ligands under simple fast precipitation methods (Fig. 3).[20] Among other functionalities, hierarchical superstructures can combine micro- and mesoporosity, thus having important prospects in industrial processes, such as catalysis, absorption, *etc.* Qiu *et al.* reported a versatile methodology based on the use of micelles as supramolecular templates for synthesizing hierarchically MOFs based on Cu(II) metal ions linked by BTC ligands.[21] One of the most important features of these materials is that they exhibit micro- and mesoporous structures with tunable adsorption capabilities.

Metal–organic nanostructures constructed from supramolecular non-coordination bonds

The diversity of 0-D and 1-D metal–organic nanostructures can be further expanded by using electrostatic interactions, hydrogen bonds, π–π stacking and van der Waals interactions as the main driving forces for the assembly of the organic and inorganic building blocks. The synthetic methodologies are not so different from those explained above. For example, hybrid spheres of about 150 nm in diameter were assembled from electrostatic interactions between cationic dipeptides and anionic polyoxometalate (POM) clusters by simply mixing both building blocks in the appropriate solvent (Fig. 4).[22] The fact that these interactions are weak makes these spheres to be easily disassembled by applying an external stimulus, such as pH (charge neutralization) and temperature. Thus, the sensitivity of electronic interactions to external stimuli could be of interest when thinking of controlled release of guest molecules or any other systems that require triggered disassembly. Based on the same approach, anionic POM clusters were electrostatically assembled with the cationic surfactant dimethyldioctadecylammonium bromide to yield nanostructures with different morphologies depending on the solvents used.[23]

It is known that polyion-neutral diblock copolymers self-assemble into nanoparticles when mixed with an oppositely charged polyelectrolyte in what can be termed complex coacervate core micelles. Particles thus synthesized are stabilized due to the electroneutral segments of the diblock polymer. Stuart *et al.* followed this approach to assemble a cationic organic polymer with a pre-synthesized coordination polymer with negative charge in its coordination center into nanospheres of about 50 nm in diameter.[24] Therefore, a reversible system such as a coordination polymer replaces a conventional polyelectrolyte conferring to the final system more versatility and sensitivity to external stimuli.

Another class of materials held entirely by non-coordination supramolecular interactions is those based on Pt–Pt interactions. It was found that square planar Pt^{II} self-assembles into 1-D structures through $Pt^{II}\cdots Pt^{II}$ interactions.[25]

Properties and applications

A wide range of promising properties can be obtained by taking advantage of the multiple inorganic and organic building blocks that can be combined to prepare nanoscale metal–organic materials. One can use the intrinsic properties of either the organic or inorganic components. The ability of metal ions to interact with phonons and electrons, to show luminescence and strong absorptions and to have interesting magneto-optical properties makes metal–organic materials suitable as functional materials in devices. The organic

components can also exhibit their own functionalities. For example, organic chromophores, radicals or biomolecules are excellent building units to prepare optical, magnetic and biocompatible nanoscale materials. New properties also arise from the polymerization of both building blocks. This is the case of the tailorable porous structures constructed from the linkage of inorganic building units through multitopic organic ligands. All these properties can take advantage of the benefits of working at the nanometre length scale, thus opening novel avenues for developing nanomaterials with astonishing properties and applications. Some of these can help to develop novel drug delivery systems, encapsulating matrices, contrast agents, porous catalytic materials, gas storage materials, magnetic and optical nanomaterials, gels, *etc.* Recent great advances have been made towards these directions.

Drug delivery systems. The development of nanoscale drug delivery metal–organic systems has been tackled by incorporating those drugs using different strategies: (i) drugs are one of the building blocks of the metal–organic structure; (ii) drugs are encapsulated inside a metal–organic matrix; and (iii) drugs are adsorbed in porous NMOFs. The three approaches have been recently tested. Lin *et al.* used the precipitation approach induced by a poor solvent to synthesize nanospheres built up from the coordination of a Pt(IV) based anticancer drug and Tb(III) metal ions (Fig. 5a–c).[26] The same authors also proved the postsynthetic covalent attachment of drugs in porous NMOFs built up from Fe(III) metal ions and 2-aminoterephthalic acid.[27] The free amino groups on the porous NMOFs were used to covalently interact with an ethoxysuccinato-cisplatin pro-drug activated with 1,1-carbonyldiimidazole. For the second strategy, Maspoch *et al.* proved that ICPs composed of Zn(II) metal ions linked by Bix ligands possess the ability to encapsulate a wide range of active species, including drugs such as doxorubicin (DOX), SN-38, camptothecin and daunomycin, within their amorphous matrix.[28] Horcajada, Gref *et al.* have recently developed the last strategy.[5] These authors used synthesized porous NMOFs composed of Fe(III) metal ions and different dicarboxylate ligands (*e.g.* BDC or BTC) to load a wide variety of antitumoral drugs, such as DOX, busulfan, cidofovir and azidothymidine triphosphate. The loading was achieved by soaking these porous NMOFs in saturated drug solutions. Interestingly, in all these cases, the successful design of the drug delivery system was confirmed by proving the controlled and progressive release of the encapsulated drug as well as their *in vitro* anticancer efficacies; thus opening the way to start considering the use of metal–organic nanostructures as novel drug delivery systems.

Encapsulating matrices. Amorphous metal–organic spheres can *in situ* encapsulate active species by previously incorporating them in the precursor solution (Fig. 5d–f). Since this discovery,[13] the classes of amorphous spheres that can be used as capsules have been extended. Kimizuka *et al.* fabricated ICPs able to encapsulate fluorescent dyes, metal nanoparticles and proteins.[29] In this case, the coordination polymer was created by connecting Gd(III) metal ions through adenosine 5′-monophosphate nucleotide. Encapsulation properties are not restricted to ICPs, and recently, electrostatic spheres composed of peptides and POMs have been used to encapsulate organic dyes.[22]

Contrast agents. Nanoscale metal–organic materials are excellent candidates to act as contrast agents because they

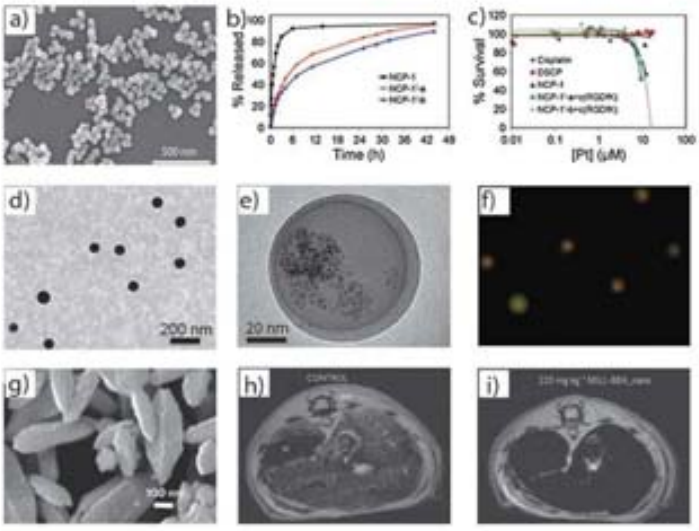

Fig. 5 Representative applications for the nanoscale supramolecular 0- and 1-D metal–organic structures. (a–c) Drug delivery systems. (a) Metal–organic nanospheres built up from the coordination of a Pt(IV) based anticancer drug and Tb(III) metal ions. (b) Drug release profile obtained by plotting %Pt released against time and (c) its *in vitro* cytotoxicity assay curves for HT-29 cells obtained by plotting the %cell viability against the Pt concentration of various samples. (d–f) Encapsulating systems. (d) TEM image of amorphous metal–organic ZnBix spheres. (e) TEM image of magnetic iron oxide nanoparticles encapsulated into ZnBix spheres. (f) Fluorescence optical image of fluorescein and quantum dots encapsulated into ZnBix spheres. (g–i) Contrast agents. (g) SEM image of metal–organic nanoparticles of $[FeO(H_2O)_2Cl(fumarate)_3]$ (MIL-88A). (h) Magnetic resonance images of control rats and (i) rats injected with 220 mg kg^{-1} of MIL-88A nanoparticles (© Wiley Interscience, The American Chemical Society and The Nature Publishing Group, reprinted with permission).

can be composed of highly paramagnetic metals ions, such as Gd(III) and Mn(II), and their small sizes allow different biodistribution and opportunities beyond the conventional imaging of chemical agents. Lin *et al.* have enormously contributed to demonstrate the efficiency of NMOFs to modify the relaxation times of the water protons in the surrounding medium when a magnetic field is applied. In such a context, Gd(III) based nanorods have shown exceptionally high longitudinal $R1$ and transverse $R2$ relaxivities of 35.8 s^{-1} and 55.6 s^{-1} per mM of Gd(III),[15] whereas nanoparticles built up from Gd(III) metal ions connected through benzene-hexacarboxylate ligands have an impressive $R2$ relaxivity of 122.6 s^{-1} per mM of Gd(III).[30] More recently, Horcajada, Gref *et al.* contributed to this field by synthesizing a NMOF built up from Fe(III) metal ions connected through fumarate ligands that shows a $R1$ relaxivity of 50 s^{-1} per mM of Fe(III), which can be considered as sufficient for *in vivo* use (Fig. 5g–i).[5]

Catalytic properties. Self-assembly of catalytic active metals into nanoparticles is a promising route towards a more efficient *heterogeneous catalysis* due to the possibility to increase the concentration of active sites. Sweigart *et al.* used the precipitation approach to assemble Rh based metal–organic catalysts and Al(III) metal ions into nanospheres.[31] Their nanostructuration increased the concentration of catalytic active sites, enhancing the stereoselective polymerization of phenylacetylene. In addition, the catalytic performance of these metal–organic nanocatalysts was dependent on their size. As expected, smaller spheres were more active than the bigger ones.

Gas sorption properties. Materials with a high capacity of gas sorption are gaining interest due to the need to store and handle new environmentally friendly fuels or remove green house gases. Because of the excellent properties exhibited by bulk porous MOFs, their nanoscopic counterparts are expected to exhibit interesting, novel and even improved gas sorption properties. This is the case of a NMOF built up from Zn(II) metal ions connected through isophthalate and 4,4′-bipyridyl ligands.[32] These porous nanocrystals reported by Groll *et al.* showed adsorption capacities almost identical to their bulk counterparts, but the shapes of the sorption isotherms differed significantly and the adsorption kinetics increased dramatically. The CO_2 and H_2 sorption properties of nanoscale metal–organic structures have also started to be investigated. Oh *et al.* successfully synthesized NMOFs based on In(III) metal ions and BDC ligands that showed a H_2 and CO_2 uptake of 140 $cm^3\ g^{-1}$ and 333 $cm^3\ g^{-1}$, respectively.[17] And Thallapally *et al.* have recently described a reversible uptake and release of CO_2 in an imidazolate NMOF with 35% of weight capacity at 30 bar.[16]

Optical properties. Luminescent coordination 5 nm-in-diameter nanoparticles were prepared by Mallah *et al.* by controlling the growth of the already known coordination polymer based on Tb(III) or Eu(III) metal ions and BDC ligands with poly(vinyl pyrrolidone).[33] Among them, the Eu(III)-based nanoparticles showed an intense red emission, remaining stable for at least 20 hours. The fact that the size of these particles did not exceed 10 nm together with their water dispersibility makes them interesting for biological applications. A different approach was followed by Loh *et al.* to prepare optically active nanofibers.[34] Two chromophores with good overlap between their respective emission and absorption bands were self-assembled into a 1-D nanostructured metal–organic polymer giving rise to a light harvesting antenna that transforms UV radiation into red radiation. Interestingly, the harvesting effect was only observed in the self-assembled system. This comes to prove that if the right building blocks are assembled into nanostructured metal–organic polymers, it is possible then to achieve interactions between functional molecules that otherwise would be impossible.

Magnetic properties. The family of Prussian blue nanoparticles has shown fascinating superparamagnetic properties.[35] In addition to these properties, spin crossover materials are perhaps the most attractive materials because thermal hysteresis takes place at room temperature in most of the cases. These materials undergo changes in their spin configuration from low spin to high spin due to external stimuli, such as temperature or light radiation. This usually implies a change in the magnetic properties, and therefore, it is of great interest for electronic devices, switches and memory devices. Coronado *et al.* made the first step to demonstrate that 10 nm-in-diameter coordination nanoparticles with the formula $[Fe(Htrz)_2(trz)(BF_4)]$ (where trz is a triazole derivative) retain their spin crossover properties.[36] Soon after, Ruiz-Molina *et al.* further proved that spherical ICPs can possess bistable spin crossover properties by polymerizing the electroactive complex with the general formula [Co (3,5-dbsq)(3,5-dbcat)(N–N)] (where 3,5-dbsq and 3,5-dbcat are, respectively, the semiquinonate radical and catecholate forms of 3,5-di-*tert*-butyl-1,2-benzoquinone) with the bitopic linker Bix.[37] More recently, interesting spin crossover properties have also been seen in NMOFs with the formula $[Fe(pz)Pt(CN)_4]$ (where pz is pyrazine) prepared by Gaspar, Real *et al.*[38]

Sensors. It is well known that the supramolecular interaction of external species in the structures of metal–organic materials can induce changes in their physical properties. This ability, together with the high surface areas that can be functionalized to recognize specific substances and the porous structures that can selectively adsorb species provide excellent characteristics to metal–organic structures for being used as novel sensors at the nanometre length scale. Thus far, however, not many sensors based on these structures have been reported. Oh and Mirkin demonstrated the ion-exchange capabilities of fluorescent Zn(II) based ICPs.[39] After exposing these spheres to Cu(II) metal ions, the cation-exchange reaction between Cu(II) and Zn(II) metal ions induced the disappearance of the fluorescence properties of these ICPs. Interestingly, the cation-exchange was faster for smaller ICPs, confirming the faster response that nanoscale sensors offer. Even though the detection response is not related to the NMOF, Lin *et al.* have recently reported an illustrative example of the potentiality of these structures to be functionalized for creating novel sensors.[40] Eu-doped NMOFs

composed of Gd(III) metal ions linked by BDC ligands were first coated with a silica shell, and then functionalized with a silylated Tb–EDTM monoamide derivative. The resulting nanoparticles were exposed to 2,2′-dipyridylamine (DPA), which constitutes up to 15% of the spores' dry mass. Upon excitation at 278 nm, the NMOFs only gave Eu luminescence because the complex Tb–EDTM is not luminescent. However, as DPA was added to the dispersion, the Tb luminescence became clearly visible owing to the formation of the complex Tb–EDTM–DPA. These modified NMOFs can therefore be used as sensors for anthrax and other bacterial spores.

Templates. As shown in Fig. 2, nanoscale metal–organic structures can exhibit a wide range of morphologies and functionalities. Thus, these materials show promise to be used as templates, transferring their complex morphologies to other materials, such as metal oxides, or acting as functional supports for synthesizing other nanoscale materials. With this concept, Oh *et al.* used a sub-1 μm, hexagonal, rod-shaped In(III) based NMOF to prepare hexagonally shaped hollow and non-hollow In_2O_3 rods by a simple calcination of the polymeric precursor.[41] The resulting In_2O_3 nanomaterials maintained the original morphology of the precursor MOFs. It is interesting to note that NMOFs also show promise for being used as templates to grow inorganic nanoparticles in their pores. Among others, Fischer *et al.* have enormously contributed to prove this application, showing the generation of Pd, Cu and Au nanoparticles in MOF-5 crystals by first loading the appropriate precursors in their porous structures and treating the resulting crystals with hydrogen gas.[42]

Other bioapplications. The use of bioorganic molecules expands the range of applications of metal–organic structures due to their assumed higher biocompatibility. Chmelewski *et al.* further expanded this range by using metal–organic fibers as scaffolds for cell culture.[43] Through smart peptide design, metal coordination nodes, such as nitrilotriacetic acid, histidine and bipyridyl, were incorporated into a peptide sequence. This allowed synthesizing collagen–metal frameworks that self-assembled into fibrous materials upon addition of transition metals (Zn(II), Cu(II), Ni(II) and Co(II)) able to adopt 3-D metal–organic scaffold for cell culture. Due to the nature of the interaction that holds these fibers, their assembly could be easily reverted by adding EDTA, which made more facile the cell recovering.

2-D metal–organic nanomaterials

Beyond the fabrication of discrete 0-D and 1-D nanostructures, another important challenge is to control the growth of these structures directly on surfaces, thus creating functional membranes, thin films, or devices based on these materials. The control of the supramolecular assembly of inorganic and organic building blocks on surfaces is especially of interest to fully exploit the exceptional adsorption properties of metal–organic materials, and create new functional surfaces for applications in electronic, sensing or photonics. An excellent review on this topic has also recently been published by Fischer *et al.*[44]

Synthesis

Chronologically, three principal strategies have been explored to fabricate metal–organic membranes and thin films (Fig. 6): (i) the LbL synthesis; (ii) the use of Langmuir–Blodgett (LB)

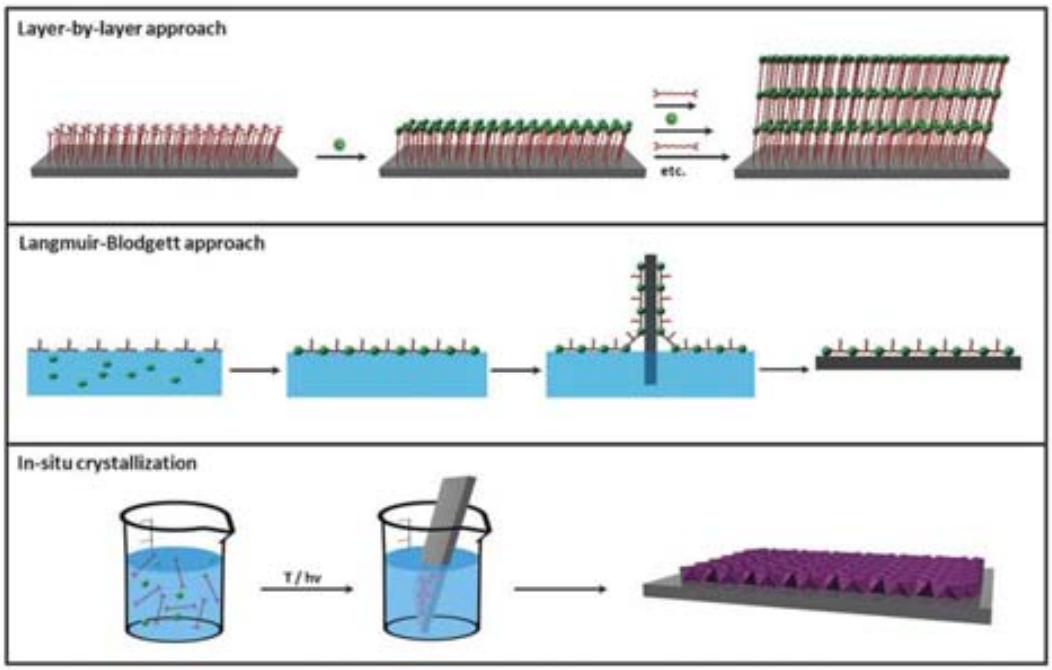

Fig. 6 Schematic illustration of the three principal synthetic strategies used for preparing 2-D metal–organic nanomaterials, including the layer-by-layer approach, the Langmuir–Blodgett approach and the *in situ* crystallization.

monolayer transfer technique; and (iii) the direct assembly and growth of metal–organic nanostructures on surfaces.

Initial efforts to fabricate nanoscale metal–organic surfaces began at the end of 80s decade with the use of the LbL synthesis (Fig. 6). The LbL synthesis is a well-known strategy that allows the step-by-step growth of hybrid organic–inorganic layers on surfaces by sequentially exposing them to solutions of both organic and inorganic building blocks. This approach was first used by Mallouk *et al.* in 1988 to fabricate an hybrid material composed of multilayers of Zr(IV) metal ions and 1,10-decanebisphosphonate (DBP) on a Si surface.[45] In this case, after an initial functionalization of the Si substrate with a phosphonate-terminated monolayer, the substrate was exposed alternatively to aqueous solutions of $ZrOCl_2$ and DBP. By repeating this process eight times, eight layers of Zr–DBP with a height of 13.6 nm (1.7 nm per layer) were fabricated. However, these adsorption steps can in principle be repeated as many times as desired in order to produce multilayer metal–organic films. The sequential dipping can be automated, and films containing more than 100 layers can be grown. Using the LbL synthesis, inorganic–organic multilayers composed of a wide variety of metal ions (*e.g.* Hf(IV), Ce(IV), Cu(II), *etc.*) and organic ligands (*e.g.* different types of diphosphonates, mercaptohexadecanoic acid, *etc.*) have nowadays been prepared on different surfaces (*e.g.* gold, silicon, *etc.*).

Beyond the stepwise coordination of metal ions and organic ligands, ultra thin metal–organic assemblies can also be grown with the electrostatic LbL self-assembly (ELSA) method. This methodology is based on the subsequent deposition of species with opposite charges on the surface. Generally, the inorganic species are anionic inorganic clusters or complexes (*e.g.* POMs), 2-D inorganic materials (*e.g.* clays and Zr(IV) phosphonates) and inorganic nanoparticles (*e.g.* gold nanoparticles). And the vast majority of organic species are oppositely charged organic polymers or large molecules. An illustrative example is the multilayer films of molybdenum oxide reported by Kunitake *et al.*[46] In this case, the inorganic species was the anionic POM $[Mo_8O_{26}]$, whereas poly-(allylamine hydrochloride) (PAH) was the cationic organic polymer. Alternate electrostatic adsorption cycles of both building blocks on a polymeric surface resulted in films with uniform thicknesses and extremely smooth surfaces.

A second general approach for fabricating nanoscale 2-D metal–organic materials is the LB technique (Fig. 6). LB is a well-known technique that allows the organization of organic molecules on air/liquid interfaces, creating ultra thin layers that can be further deposited on surfaces. To our knowledge, Nagel and Oertel first used this technique to fabricate coordination polymer monolayers on an air/water interface.[47] This process usually consists of four steps: (i) a multitopic organic ligand is first functionalized with alkyl chains to allow their organization on the air/water interface; (ii) small volume of a solution of the organic ligand is spread on the surface of an aqueous solution containing the metal ion; (iii) an interfacial coordination reaction occurs between the metal ions in the aqueous subphase and the organic ligands once they are spread or self-organized on the air/water interface; and (iv) the created ultrathin coordination polymer layers are transferred to a flat solid support by immersing the substrate through the compressed layer. Among others, Yuan and Liu followed these steps to fabricate chiral metal–organic monolayers. Initially, the naphtha[2,3]imidazole ligand was functionalized with a long alkyl chain. A chloroform solution of this ligand was then spread on pure water containing Ag(I) metal ions. Immediately, metal–organic monolayers were formed through an *in situ* coordination between both species, transferring them on mica.[48]

Both general strategies, the LB technique and the LbL synthesis, can also be coupled for producing metal–organic thin films on solid supports.[49] Makiura, Kitagawa *et al.* recently reported the LbL growth of pre-formed metal–organic sheets using the LB technique. First, these layers were formed by spreading a chloroform/methanol solution of a Co(II) metalloporphyrin complex and pyridine onto an aqueous solution containing Cu(II) metal ions, and instantly transferred on a Si substrate. Sequential sheet formation and deposition on the same substrate allows the LbL stacking, thereby resulting in the generation of MOF thin films of any desired thickness.

The last general strategy so far used for fabricating metal–organic thin films and membranes is the direct nucleation and growth of NMOFs on surfaces. Initial efforts for growing these crystals on bare surfaces (*e.g.* SiO_2, Al_2O_3, Au, graphite, *etc.*) were focused on a strategy based on immersing these substrates into a solution containing the precursors. Then, the NMOFs were grown on the surfaces by inducing their nucleation using methods analogous to those used for preparing 0-D and 1-D NMOFs, such as microwave radiation, temperature, *etc.* With these synthetic approaches, some metal–organic supports were successfully synthesized. However, most of the bare substrates inhibit the nucleation of NMOFs, and thus low crystal density is usually obtained.

A very promising solution to overcome this problem is the use of chemical affinity templates to promote the nucleation of NMOFs. Self-assembled monolayers (SAMs) are excellent candidates to act as such templates because they can be terminated with different functional groups that can direct the nucleation and growth of crystalline materials. The case of the HKUST-1 system is especially appropriate to describe this phenomenon. Bein *et al.* studied their nucleation and growth by immersing Au substrates previously functionalized with SAMs terminated with COOH–, OH– and CH_3– groups into a solution containing Cu(II) metal ions and BTC ligands.[50] Under the studied conditions, all terminated SAMs seemed to favor the nucleation, and therefore, increased the crystal density in comparison with bare Au surfaces. In addition, these authors also observed preferential crystal growth orientations depending on the terminal functional group of these SAMs. Indeed, the COOH-terminated SAM favored orientation along the [100] direction and the formation of pyramid-like crystals, whereas the OH-terminated SAM favored the [111] orientation and led to the formation of octahedral crystals. The third surface terminated with CH_3– groups did not favor any orientation. These results, even though are quite contradictory to latter exhaustive experiments performed by Fischer *et al.*,[51] confirm the

importance of SAMs for controlling not only the density of crystals (homogeneity) deposited on the surface but also their orientation.

More recently, the use of SAMs on surfaces has also shown to be important for selectively growing a certain MOF crystal phase in front of another. This is the case of MIL-88B, a MOF composed of Fe(III) metal ions connected through BDC ligands.[52] Scherb *et al.* demonstrated the preferential formation of crystals of this MOF by placing down a COOH-terminated SAM in a mother liquor solution containing both precursors. Surprisingly, even though the crystals formed in the solution corresponded to MIL-53, another MOF built up from Fe(III) metal ions connected through BDC ligands, the crystals that grew on the surface only corresponded to well-oriented MIL-88B crystals along the [001] direction. Also interesting is the work reported by Wöll *et al.*,[53] who controlled the formation of a non-interpenetrated phase of a MOF built up from the linkage of $[Zn_4O]$ clusters through 4,4′-biphenyldicarboxylate ligands. Besides bulk synthetic methods lead to the interpenetrated phase, these authors proved to control the formation of the non-interpenetrated one on surfaces by using SAMs as templates and the LbL synthesis, opening new possibilities to synthesize new types of MOFs on surfaces not accessible by conventional methods.

In addition to the use of SAMs, other ways have been proposed to promote the homogeneous nucleation and growth of NMOFs on surfaces. One of the most interesting approaches is the use of seeds to induce a better crystallization. Similar to the growth of zeolitic membranes, Caro *et al.* created a homogeneous and dense coating of imidazolate based MOFs (ZIF-7) on alumina supports by first dipping them into an aqueous polyethyleneimine dispersion of pre-synthesized ZIF-7 nanocrystals with dimensions of 30 nm.[54] These seeded supports were then immersed vertically into a solution containing the ZIF-7 precursors and heated up to 100 °C using microwave for three hours to obtain a large scale ordered polycrystalline ZIF-7 thin films.

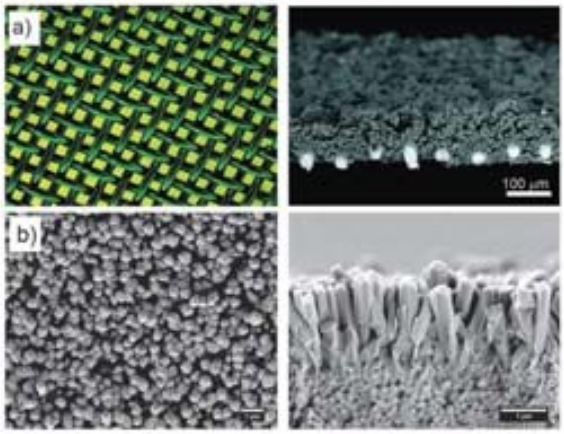

Fig. 7 (a) Optic micrographs of the copper net (left) and the net-supported HKUST-1 membrane (right). (b) SEM top (left) and cross-section (right) views of ZIF-7 membranes obtained after microwave assisted secondary growth (© Wiley Interscience and American Chemical Society, reprinted with permission).

A previous chemical modification of the surface is also an important factor to be considered in order to increase the crystal density on surfaces. One possibility is the "formate" route reported by Caro *et al.*,[55] which consists of pre-oxidation of the surfaces with sodium formate treatment. With this oxidation, the nucleation of $[Mn(HCOO)_2]$ was enhanced and rather dense coatings were obtained. Qiu *et al.* and De Vos *et al.* further proved this concept.[56,57] According to these authors, the oxidation of metallic copper surfaces generates Cu(II) metal ions process, creating more surface nucleation points during the HKUST-1 synthesis, and therefore, enhancing the crystal density on those surfaces (Fig. 7a).

Properties and applications

The exceptional advantages and properties already exhibited by nanoscale 0-D and 1-D metal–organic materials can be integrated on surfaces for fabricating metal–organic functional thin films and membranes with a wide range of properties and applications. Their use can allow the fabrication of electronic or optoelectronic thin films, membranes with gas separation capabilities, new surface sensors, magnetic platforms, *etc.*

Electronic and optoelectronic properties. The use of POMs to fabricate thin films is specially promising due to their ability to act as an electron reservoir, thereby giving rise to colored mixed-valence state species while retaining their structural integrity. Kurth, Volkmer *et al.* reported the formation of electrochromic thin films composed of multilayers of $[Eu(H_2O)P_5W_{30}O_{110}]^{12}$, which exhibit reversible electrochemical behavior accompanied by a large electrochromic response, PAH and poly(styrenesulfonate) (Fig. 8a).[58] Because the properties of POM clusters are fully maintained in the multilayers, their LbL structuration on surfaces allows the fabrication of highly stable and reversible electrochromic films with high optical contrast (transparent to blue). In addition to electrochromic films, other electronic devices based on metal–organic thin films have also been reported. Nishihara *et al.* reported the formation of redox multilayer films of Fe(II) metal ions and terpyridine (tpy) derivative ligands on gold electrodes.[59] Using similar organic ligands, Rampi *et al.* fabricated highly conductive 40 nm long molecular wires based on Fe(II) or Co(II) metal ions.[60] More recently, a very important step has also been done for the fabrication of nanoscale devices based on optoelectronic multilayer systems. Dong *et al.* described the metal–organic thin film formation on the surface of multiwall carbon nanotubes.[61] This thin film was created from the assembly of transition metal ions and tpy ligands. The authors demonstrated that an effective photoinduced charge transfer was induced under irradiation, which increased by addition of bilayers.

Gas separation properties. The exceptional porous characteristics already exhibited by bulk MOFs make them excellent components for creating metal–organic membranes or thin films with potential properties in gas separation, gas storage, fabrication of novel sensors, *etc.* However, even though the preparation of these 2-D metal–organic systems has attracted much research interest in the last years, only a few efficient membranes for gas separation have been reported.

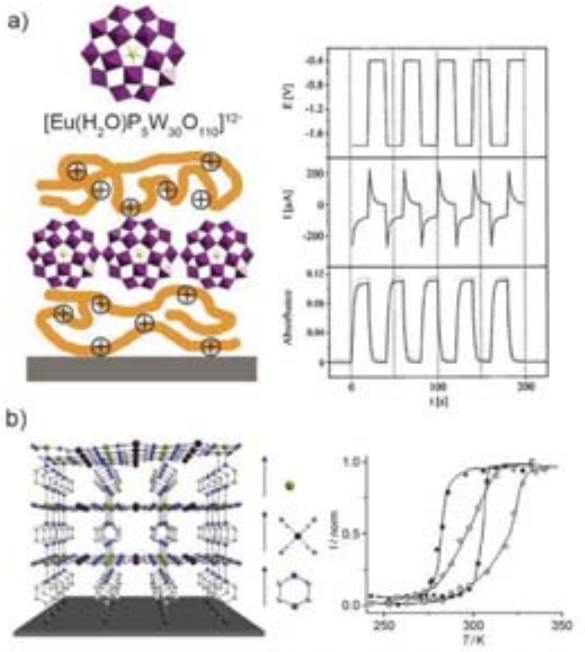

Fig. 8 (a) Schematic representation of the LbL film formation from the association of Eu–POM and a cationic polymer, and potential (Pt electrode), current, and absorbance at 700 nm of the LbL-coated ITO electrode during subsequent double-potential steps between ±0.4 and ±1.8 V. (b) Schematic drawing of the sequential assembly of [Fe(pyrazine){M(CN)$_4$}] (M = Ni, Pd, or Pt) films and the temperature dependence of the normalized Raman intensity ratio (I(norm) = I(1025 cm^{-1})/I(1230 cm^{-1})) for [Fe(pyrazine){Pt(CN)$_4$}] powder (■) and film samples (○) upon cooling and heating confirming the spin transition in LbL films (© Wiley Interscience, reprinted with permission).

The first metal–organic membrane showing separation performance was reported by Qiu *et al.*[56] This membrane, which was created with nanoscale HKUST-1 crystals on an oxidized copper grid, showed a higher permeation flux and excellent permeation selectivity for H_2 in comparison with CO_2, N_2 and CH_4. This phenomenon can be explained by the size selectivity occurred on the HKUST-1 channels. Thus, the small H_2 molecule goes through the membrane more easily than CO_2, N_2, and CH_4. However, the best gas selectivity exhibited for metal–organic membranes was recently reported by Caro *et al.*[54,62] Non-oriented and oriented membranes constructed with NMOFs of zeolitic imidazolate frameworks showed a high H_2 selectivity favored by a pore dimension of these NMOFs very similar to the size of H_2 (Fig. 7b).

Sensors. The combination of high porosity and physical properties certainly provides excellent conditions to use metal–organic thin films for sensing applications. Bein *et al.* reported the selective growth of HKUST-1 thin films on functionalized quartz-crystal microbalance (QCM) gold electrodes. This device was used to evaluate accurately the mass variations, making possible the detection of water adsorption when this thin film was exposed to atmospheres with different relative humidities.[63] More recently, Lu and Hupp constructed ZIF-8-based Fabry–Pérot devices that function as selective sensors for chemical vapors and gases. This sensor is based on the displacement of Fabry–Pérot interference peaks as a function of the exposure of the device to an analyte. The authors show the capabilities of such ZIF-8 based thin films to detect the presence of ethanol in the atmosphere.[64]

Magnetic properties. The interesting magnetic properties of metal–organic materials studied by the molecular magnetism field during the last decades can be certainly used to fabricate magnetic metal–organic thin films. The examples, however, are still scarce. An illustrative example is the work led by Boussekson *et al.*, who fabricated metal–organic thin films displaying a room temperature spin-crossover behavior with hysteresis (Fig. 8b).[65] These authors demonstrated the formation of such thin films by stepwise synthesis of [Fe(pyrazine){M(CN)$_4$}] (where M is Ni, Pd or Pt) on surfaces.

Nanostructuration of metal–organic structures on surfaces

Control over the growth, orientation and positioning of metal–organic materials on surfaces is crucial to start to conceive the integration of these materials on supports for the fabrication of complex surface sensors, separation membranes, drug-delivery platforms and catalysts. There are three potential strategies to achieve this control at the nanometre scale length (Fig. 9): (i) the use of SAM features as chemical affinity templates to selectively control the nucleation and growth of metal–organic materials on them; (ii) the use of lithographic techniques to directly deliver or confine small volumes of the reaction solution containing the precursors, seeds or NMOFs at specific locations of a surface; and (iii) the growth of nanoscale metal–organic materials at specific locations of a surface by locally applying an external factor, such as temperature, addition of an external solvent, *etc.*, that induces their nucleation.

As stated above, it is well known that SAMs terminated with the appropriate functional group are able to coordinate with metal ions. One can then imagine to use patterned SAM features to control the positioning of the nucleation and growth of NMOFs. This approach starts with the fabrication of SAM features on surfaces by using conventional lithographic techniques, such as μ-contact printing (μCP) or photolithography. The NMOFs are then selectively grown on these features by exposing the surfaces to the precursor solution under optimum conditions or using the LbL synthesis. Fischer *et al.* first proved this concept by controlling the growth of MOF-5 crystals on square-like COOH-terminated SAM features of 40 × 40 μm fabricated by μCP (Fig. 10a–c).[66] After patterning these features, the remaining Au surface was passivated with a CF_3-terminated SAM in order to prevent the nucleation of MOF-5 in non-specific regions. The substrate was immersed into the mother solution, and this system was heated at 75 °C for 72 h. Interestingly, excellent adsorption properties of the resulting MOF-5 microarrays were successfully confirmed by exposing them to vapors of [(η^5-C_5H_5)Pd(η^3-C_3H_5)]. Using this method, Fischer's group also fabricated MOF-5 and HKUST-1 microarrays on

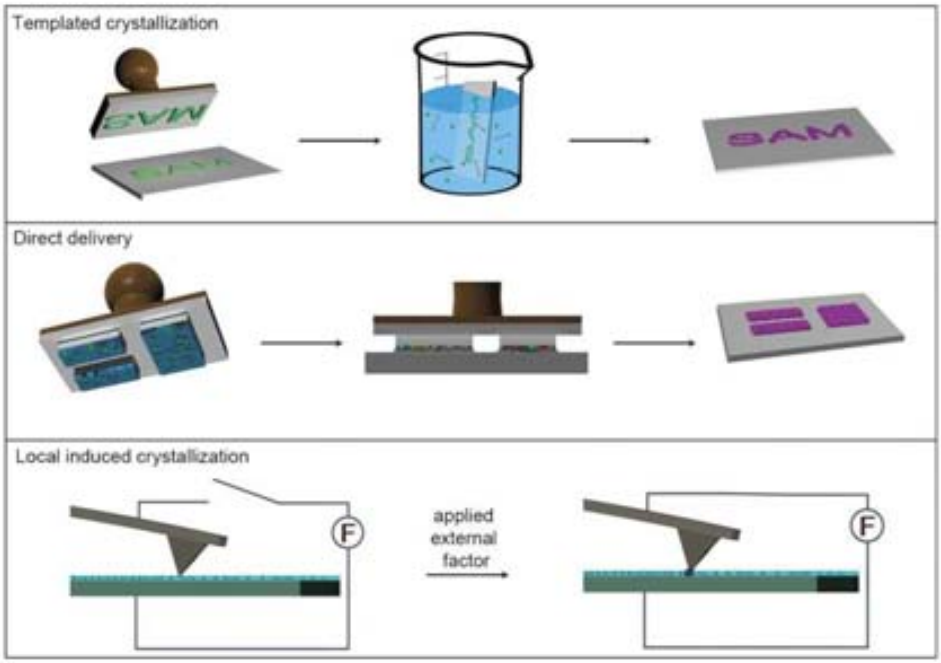

Fig. 9 Schematic illustration of the three principal fabrication strategies used for structuring metal–organic nanostructures on surfaces at the nanometre length scale, including the templated crystallization, the direct delivery and the local induced crystallization.

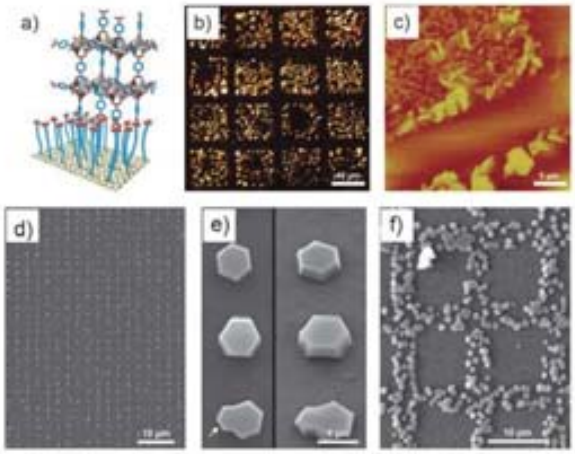

Fig. 10 (a–c) Arrays of MOF-5 crystals. (a) Schematic illustration of the concept of anchoring a typical MOF-5 building unit to a COOH-terminated SAM. (b) Optical microscope and (c) AFM images of a selectively grown film of MOF-5 on a patterned SAM of 16-mercaptohecadecanoic acid on a Au surface. The MOF-5-coated squares are 40 × 40 μm, and the crystals are about 100–500 nm in size. (d–f) Arrays of HKUST-1 crystals fabricated by LCW. (d) Large view and (e) details of individual crystals viewed from above (left) and at a 35° angle (right). The arrow indicates intergrowths caused by a second nucleation. (f) Square-like membrane structure composed of HKUST-1 crystals (© The American Chemical Society and Wiley Interscience, reprinted with permission).

alumina and silica surfaces.[51] In this case, however, the SAM features were patterned with standard photolithographic techniques.

In addition to immersing the pre-structured surface into the precursor solution, the LbL synthesis can also be localized on these SAM templates, thus controlling the positioning of the created metal–organic multilayers. For instance, Wöll *et al.* fabricated HKUST-1 crystalline microarrays on Au surfaces by using the LbL synthesis on COOH-terminated SAM features generated by μCP.[67] Similarly, Boom *et al.* fabricated a metal–organic multilayer pattern by sequentially immersing a glass surface, in which a template consisting of 5 μm OH-terminated SAM lines spaced from each other by 40 μm was created using photopatterning, into solutions of Pt(II) metal ions and 1,4-bis[2-(4-pyridyl)ethenyl]benzene ligands.[68]

Even though the use of SAM features is the most extended approach, recent advances have been made in using lithographic techniques for delivering small volumes of the precursor solution on surfaces, thus directly controlling the location in which the metal–organic structure is positioned or grown. Thus far, precursor solutions have been successfully patterned through different lithographic techniques, including the lithographically controlled wetting (LCW), microtransfer molding (μTM) and micromolding in capillaries (MIMIC). De Vos *et al.* controlled the synthesis of HKUST-1 crystals at the single-crystal level on glass substrates through LCW (Fig. 10d–f).[69] In this method, a polydimethylsiloxane (PDMS) stamp was initially coated with a DMSO solution containing Cu(II) metal ions and BTC ligands. This stamp was then placed in contact with the glass surface; in this manner, capillary forces drove the liquid to distribute only under the protrusions of the stamp. As the solvent evaporated, the nucleation of HKUST-1 crystals took place under these protrusions, and therefore, the grown crystals were formed in a pattern reproducing the motif of the stamp. Similarly,

Vieu *et al.* used μTM to transfer a colloidal solution containing coordination polymer nanoparticles on glass surfaces.[70] It is interesting to note that the resulting nanoparticle structures with dimensions up to 300 nm kept their inherent spin crossover properties. Stamps were also used by Park *et al.* to structure a coordination polymer on glass surfaces using MIMIC.[71] Continuous channels were formed when a PDMS stamp was brought into conformal contact with a solid substrate. These authors used the capillary action to fill the channels with a pyridine solution of a pre-formed coordination polymer composed of Zn(II) metal ions and 4,4′-di(4-pyridyl)cyanostilbene. The selective removal of pyridine by its absorption on the capillary walls drove to the formation while structuration of this coordination polymer.

Conclusions and perspectives

Although at the embryonic stage of their development, the recent advances made on this field, as shown in this review above, assure a brilliant future for this novel type of nanoscale materials. In this review, the advances on the early synthesis of metal–organic nanomaterials up to the initial studies of their properties and potential applications have been discussed. Along the way, there have been a number of achieved "milestones", including the preparation of the first discrete nanostructures with varied compositions, sizes and shapes, the controlled growth of metal–organic thin films and membranes, new fabrication routes for nanostructuring them in pre-designed features on surfaces, the discovery of interesting structural (*e.g.* porosity, encapsulation capabilities, ion-exchange, *etc.*) and physical (*e.g.* electronic, magnetism, *etc.*) properties, and the exploration of promising biological-related applications, including drug delivery, bioimaging, sensing, *etc.*

However, these studies are just the tip of the iceberg. The advantages of metal–organic nanomaterials are their high tailorability in terms of compositions, internal structures, morphologies, dimensions and properties, making possible their rational design for any specific application. A major challenge is then to develop novel methodologies and better understand the existing ones to fully exploit the limitless number of possible formulations, sizes and shapes of these materials. As an example of this issue is the possible local induced crystallization approach that shows promise for fabricating and structuring these materials on surfaces (Fig. 9). This strategy has not yet been explored. There is however no doubt that this route as well as other synthetic methodologies (*e.g.* microfluidics, supercritical conditions, vapour deposition, *etc.*) and lithographic techniques (*e.g.* Dip-Pen Nanolithography, Fountain-Pen Lithography, *etc.*) will be implemented in the next years, expanding the variety of synthesized metal–organic nanomaterials. In the same context, the fundamental understanding of how metal–organic nanomaterials are formed is crucial to begin to conceive of using these methods for controlling the fabrication of nanoscale metal–organic materials with desired properties.

Aside from the development of synthetic routes, there are other challenges which will focus the interest of researchers. One of them is the use of bio-related molecules as new building-blocks. Another direction of development is foreseen in the functionalization of these materials with functional species. Like their inorganic counterparts, this capability is particularly interesting for biological applications because it should allow the biocompatibilization and cell-specific targeting of these nanoscale materials. This future research, which will involve researchers of many different fields, will certainly expand the scope of properties and applications for nanoscale metal–organic materials up to their use for practical applications.

Acknowledgements

This work was supported by projects VALTEC08-2-003 and MAT2009-13977-C03. D. M. and I. I. thank the Ministerio de Ciencia y Tecnología for respective RyC and JdC contracts. A. C. and C. C. thank the Generalitat de Catalunya and the Institut Català de Nanotecnologia (ICN) for research fellowships.

Notes and references

1 Special issue on metal–organic framework materials. *Chem. Soc. Rev.* 2009, **38**, 1201.
2 S. Vaucher, M. Li and S. Mann, *Angew. Chem., Int. Ed.*, 2000, **39**, 1793.
3 G. D. Liang, J. T. Xu and X. S. Wang, *J. Am. Chem. Soc.*, 2009, **131**, 5378.
4 S. F. Hou, C. C. Harrell, L. Trofin, P. Kohli and C. R. Martin, *J. Am. Chem. Soc.*, 2004, **126**, 5674.
5 P. Horcajada, T. Chalati, C. Serre, B. Gillet, C. Sebrie, T. Baati, J. F. Eubank, D. Heurtaux, P. Clayette, C. Kreuz, J.-S. Chang, Y. K. Hwang, V. Marsaud, P.-N. Bories, L. Cynober, S. Gil, G. Férey, P. Couvreur and R. Gref, *Nat. Mater.*, 2010, **9**, 172.
6 Z. Ni and R. I. Masel, *J. Am. Chem. Soc.*, 2006, **128**, 12394.
7 W. J. Son, J. Kim and W. S. Ahn, *Chem. Commun.*, 2008, 6336.
8 S. K. Wu, X. P. Shen, B. S. Cao, L. Lin, K. C. Shen and W. Liu, *J. Mater. Sci.*, 2009, **44**, 6447.
9 X. P. Sun, S. J. Dong and E. K. Wang, *J. Am. Chem. Soc.*, 2005, **127**, 13102.
10 M. Oh and C. A. Mirkin, *Nature*, 2005, **438**, 651.
11 W. Lin, W. J. Rieter and K. M. L. Taylor, *Angew. Chem., Int. Ed.*, 2009, **48**, 650.
12 A. M. Spokoyny, D. Kim, A. Sumrein and C. A. Mirkin, *Chem. Soc. Rev.*, 2009, **38**, 1218.
13 I. Imaz, J. Hernando, D. Ruiz-Molina and D. Maspoch, *Angew. Chem., Int. Ed.*, 2009, **48**, 2325.
14 S. Jung and M. Oh, *Angew. Chem., Int. Ed.*, 2008, **47**, 2049.
15 W. J. Rieter, K. M. L. Taylor, H. Y. An, W. L. Lin and W. Lin, *J. Am. Chem. Soc.*, 2006, **128**, 9024.
16 S. K. Nune, P. K. Thallapally, A. Dohnalkova, C. Wang, J. Liu and G. J. Exarhos, *Chem. Commun.*, 2010, **46**, 4878.
17 W. Cho, H. J. Lee and M. Oh, *J. Am. Chem. Soc.*, 2008, **130**, 16943.
18 J. K.-H. Hui and M. J. Maclachlan, *Coord. Chem. Rev.*, 2010, **254**, 2363.
19 I. Imaz, M. Rubio-Martinez, W. J. Saletra, D. B. Amabilino and D. Maspoch, *J. Am. Chem. Soc.*, 2009, **131**, 18222.
20 K. Liu, H. You, G. Jia, Y. Zheng, Y. Huang, Y. Song, M. Yang, L. Zhang and H. Zhang, *Cryst. Growth Des.*, 2010, **10**, 790.
21 L.-G. Qiu, T. Xu, Z.-Q. Li, W. Wang, Y. Wu, X. Jiang, X.-Y. Tian and L.-D. Zhang, *Angew. Chem., Int. Ed.*, 2008, **47**, 9487.
22 X. H. Yan, P. L. Zhu, J. B. Fei and J. B. Li, *Adv. Mater.*, 2010, **22**, 1283.
23 A. Nisar, Y. Lu and X. Wang, *Chem. Mater.*, 2010, **22**, 3511.
24 Y. Yan, N. A. M. Besseling, A. de Keizer, A. T. M. Marcelis, M. Drechsler and M. A. C. Stuart, *Angew. Chem., Int. Ed.*, 2007, **46**, 1807.
25 W. Lu, V. A. L. Roy and C.-M. Che, *Chem. Commun.*, 2006, 3972.
26 W. J. Rieter, K. M. Pott, K. M. L. Taylor and W. B. Lin, *J. Am. Chem. Soc.*, 2008, **130**, 11584.

27 K. M. L. Taylor-Pashow, J. D. Rocca, Z. Xie, S. Tran and W. Lin, *J. Am. Chem. Soc.*, 2009, **131**, 14261.
28 I. Imaz, M. Rubio, L. García, F. García, D. Ruiz-Molina, J. Hernando, V. Puntes and D. Maspoch, *Chem. Commun.*, 2010, **46**, 4737.
29 R. Nishiyabu, C. Aime, R. Gondo, T. Noguchi and N. Kimizuka, *Angew. Chem., Int. Ed.*, 2009, **48**, 9465.
30 K. M. L. Taylor, A. Jin and W. Lin, *Angew. Chem., Int. Ed.*, 2008, **47**, 7722.
31 K. H. Park, K. Jang, S. U. Son and D. A. Sweigart, *J. Am. Chem. Soc.*, 2006, **128**, 8740.
32 D. Tanaka, A. Henke, K. Albrecht, M. Moeller, K. Nakagawa, S. Kitagawa and J. Groll, *Nat. Chem.*, 2010, **2**, 410.
33 N. Kerbellec, L. Catala, C. Daiguebonne, A. Gloter, O. Stephan, J. C. Bunzli, O. Guillou and T. Mallah, *New J. Chem.*, 2008, **32**, 584.
34 X. Zhang, Z. K. Chen and K. P. Loh, *J. Am. Chem. Soc.*, 2009, **131**, 7210.
35 L. Catala, F. Volatron, D. Brinzel and T. Mallah, *Inorg. Chem.*, 2009, **48**, 3360.
36 E. Coronado, J. R. Galán-Mascaros, M. Monrabal-Capilla, J. García-Martínez and P. Pardo-Ibáñez, *Adv. Mater.*, 2007, **19**, 1359.
37 I. Imaz, D. Maspoch, C. Rodriguez-Blanco, J. M. Pérez-Falcón, J. Campo and D. Ruiz-Molina, *Angew. Chem., Int. Ed.*, 2008, **47**, 1857.
38 I. Boldog, A. B. Gaspar, V. Martínez, P. Pardo-Ibañez, V. Ksenofontov, A. Bhattacharjee, P. Gütlich and J. A. Real, *Angew. Chem., Int. Ed.*, 2008, **47**, 6433.
39 M. Oh and C. A. Mirkin, *Angew. Chem., Int. Ed.*, 2006, **45**, 5492.
40 W. J. Rieter, K. M. L. Taylor and W. Lin, *J. Am. Chem. Soc.*, 2007, **129**, 9852.
41 W. Cho, Y. H. Lee, H. J. Lee and M. Oh, *Chem. Commun.*, 2009, 4756.
42 S. Hermes, M.-K. Schröter, R. Schmid, L. Khodeir, M. Muhler, A. Tissler, R. W. Fischer and R. A. Fischer, *Angew. Chem., Int. Ed.*, 2005, **44**, 6237.
43 M. M. Pires, D. E. Przybyla and J. Chmielewski, *Angew. Chem., Int. Ed.*, 2009, **48**, 7813.
44 D. Zacher, O. Shekhah, C. Wöll and R. A. Fischer, *Chem. Soc. Rev.*, 2009, **38**, 1418.
45 H. Lee, L. J. Kepley, H. G. Hong and T. E. Mallouk, *J. Am. Chem. Soc.*, 1988, **110**, 618.
46 I. Ichinose, H. Tagawa, S. Muzuki, Y. Lvov and T. Kunitake, *Langmuir*, 1998, **14**, 187.
47 J. Nagel and U. Oertel, *Thin Solid Films*, 1998, **327–329**, 495.
48 J. Yuan and M. Liu, *J. Am. Chem. Soc.*, 2003, **125**, 5051.
49 R. Makiura, S. Motoyama, Y. Umemura, H. Yamanaka, O. Sakata and H. Kitagawa, *Nat. Mater.*, 2010, **9**, 565.
50 E. Biemmi, C. Scherb and T. Bein, *J. Am. Chem. Soc.*, 2007, **129**, 8054.
51 D. Zacher, A. Baunemann, S. Hermes and R. A. Fischer, *J. Mater. Chem.*, 2007, **17**, 2785.
52 C. Scherb, A. Schödel and T. Bein, *Angew. Chem., Int. Ed.*, 2008, **47**, 5777.
53 O. Shekhah, H. Wang, M. Paradinas, C. Ocal, B. Schüpbach, A. Terfort, D. Zacher, R. A. Fischer and C. Wöll, *Nat. Mater.*, 2009, **8**, 481.
54 Y.-S. Li, F.-Y. Liang, H. Bux, A. Feldhoff, W.-S. Yang and J. Caro, *Angew. Chem., Int. Ed.*, 2010, **49**, 548.
55 M. Arnold, P. Kortunov, D. J. Jones, Y. Nedellec, J. Kärger and J. Caro, *Eur. J. Inorg. Chem.*, 2007, 60.
56 H. Guo, G. Zhu, I. J. Hewitt and S. Qiu, *J. Am. Chem. Soc.*, 2009, **131**, 1646.
57 R. Ameloot, L. Stappers, J. Fransaer, L. Alaerts, B. F. Sels and D. E. De Vos, *Chem. Mater.*, 2009, **21**, 2580.
58 S. Liu, D. G. Kurth, H. Möhwald and D. Volkmer, *Adv. Mater.*, 2002, **14**, 225.
59 Y. Nishimori, K. Kanaizuka, M. Murata and H. Nishihara, *Chem.–Asian J.*, 2007, **2**, 367.
60 N. Tuccitto, V. Ferri, M. Cavazzini, S. Quici, G. Zhavnerko, A. Licciardello and M. A. Rampi, *Nat. Mater.*, 2009, **8**, 41.
61 Y. Pan, B. Tong, J. Shi, W. Zhao, J. Shen, J. Zhi and Y. Dong, *J. Phys. Chem. C*, 2010, **114**, 8040.
62 Y.-S. Li, H. Bux, A. Feldhoff, G.-L. Li, W.-S. Yang and J. Caro, *Adv. Mater.*, 2010, **22**, 3322.
63 E. Biemmi, A. Darga, N. Stock and T. Bein, *Microporous Mesoporous Mater.*, 2008, **114**, 380.
64 G. Lu and J. T. Hupp, *J. Am. Chem. Soc.*, 2010, **132**, 7832.
65 S. Cobo, G. Molnar, J.-A. Real and A. Bousseksou, *Angew. Chem., Int. Ed.*, 2006, **45**, 5786.
66 S. Hermes, F. Schroder, R. Chelmowski, C. Woll and R. A. Fischer, *J. Am. Chem. Soc.*, 2005, **127**, 13744.
67 O. Shekhah, H. Wang, S. Kowarik, F. Schreiber, M. Paulus, M. Tolan, C. Sternemann, F. Evers, D. Zacher, R. A. Fischer and C. Wöll, *J. Am. Chem. Soc.*, 2007, **129**, 15118.
68 M. Altman, A. D. Shukla, T. Zubkov, G. Evmenenko, P. Dutta and M. E. van der Boom, *J. Am. Chem. Soc.*, 2006, **128**, 7374.
69 R. Ameloot, E. Gobechiya, H. Uji-i, J. A. Martens, J. Hofkens, L. Alaerts, B. F. Sels and D. E. D. Vos, *Adv. Mater.*, 2010, **22**, 2685.
70 C. Thibault, G. Molnár, L. Salmon, A. Bousseksou and C. Vieu, *Langmuir*, 2009, **26**, 1557.
71 Y. You, H. Yang, J. W. Chung, J. H. Kim, Y. Jung and S. Y. Park, *Angew. Chem., Int. Ed.*, 2010, **49**, 3757.

Chapter 2.
Objective of the Thesis

The main objective of this thesis work consists on the development of a new strategy to grow miniaturized MOFs on specific places of surfaces with the highest resolution as possible. Based on the exploitation of Tip-Based Nanolithographic techniques (Dip-Pen Nanolithography, Fluidic Enhanced Molecular Transfer Operation among others) we expect to obtain a way to localize and confine the formation and growth of different MOFs over surfaces. To achieve this main objective, different partial objectives have been designed:

- Control the positioning and growth of HKUST-1 archetypical MOF over different functionalized surfaces.

- Study the effect of the different solvents and reaction conditions as well as the nucleation, growth and orientation of the HKUST-1 crystals.

- Expand the scope of the strategy to growth different MOFs through a consecutive addition of building blocks in a two steps methodology.

- Optimize the procedure to discover new materials in a combinatorial high throughput approach.

Chapter 3. Structuration of HKUST-1 Metal-Organic Framework Crystals on Surfaces

In order to materialise the potentiality of Metal-Organic Frameworks (MOFs) it becomes necessary to build up an entire technological structure which must allow controlling the formation and positioning of MOFs in the micro-nanoscale on surfaces. In this chapter, a new versatile approach to pattern Metal-Organic Frameworks (MOFs) crystals, at surfaces even at the single-crystal level through Scanning Probe Lithography techniques, will be described.

1. Micro-nanopatterning of MOFs on surfaces

One could say that the importance of a material depends on the role that it plays in our everyday life or the potential impact that can have in the technological progress. This potentiality not only depends on the physical-chemical properties but also on its availability and on the ability to have it in the correct shape, position and conditions, of course everything under affordable costs. To put an example, carbon nanotubes (CNTs) have unusual and interesting properties such us extraordinary thermal and electrical conductivity and the highest specific strength of known materials but nevertheless, the longest reported CNT has only 20 cm, far away from the 100.000 km required to build a "space elevator". [1]

But, for science and technology, the most intriguing challenges appear within the discovery of these exceptional materials with extreme particular properties, stimulating the development of applications and also new ways to optimize its obtaining methods (synthesis, extraction, purification…) Some of the trending scientific topics for the last years, following this criteria, has been CNTs, nanomaterials in general and in the chemistry field; Metal-Organic Frameworks, flowing into a massive scientific investment and effort. In this last case, the development of new tools or protocols to control the growth, orientation and positioning of MOFs on surfaces is crucial to conceive its integration on supports for their application in storage, separation and catalysis but specially in electronics and sensing. An illustrative example presented by Falcaro [2], of a complex microfluidic MOF based device is shown in Figure 1, where the multifunctional MOF can act as a separator, catalyst and reservoir on a single microchip.

Recently, some strategies have been introduced to achieve this control at the micro- nanometre scale length. In this chapter, a brief introduction is given to contextualise the state of the art on the control over the surface structuration of MOFs. What we considered the most relevant strategies are summarized on: (i) the use of SAM features as chemical affinity templates to selectively control the nucleation and growth of metal–organic materials on them (*Figure 2*); (ii) the use of stamp based lithographic techniques to directly deliver or confine small volumes of the reaction solution containing the precursors, seeds or NMOFs at specific locations of a surface (*Figure 4*); (iii) the heterogeneous seeding with microparticles delivered into prefabricated patterned surface (Figure 6); (iv) electrochemical approach (Figure 7) and (v) the combination of different lithographic techniques to position pre-synthesized MOFs (Figure 8).

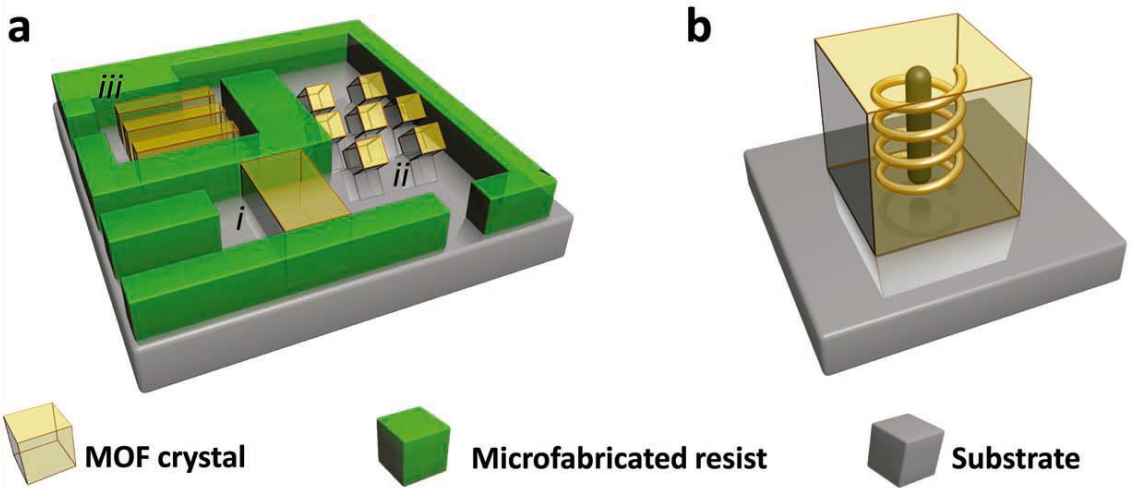

Figure 1. a) Perspective of a microfluidic circuit exploiting metal organic frameworks (MOFs) for different tasks (e.g. separation/gating (i), catalysis (ii) and chemical delivery (iii)) in a single lab-on-a-chip. b) Illustration of a microreactor obtained by fabricating controlled functional nanostructures inside a single ultra-porous MOF crystal. For example here the MOF (yellow cube) provides a molecular sieve allowing specific molecules to react with a catalytic core (grey cylinder) which undergoes a reaction at localised temperatures applied from an external field induced by a lithographed metallic coil via magnetic or electric induction.

1.1. SAM features as chemical template

As stated above, it is well known that SAMs terminated with the appropriate functional group are able to coordinate with metal ions. One can then imagine using patterned SAM features to control the positioning of the nucleation and growth of NMOFs. This approach starts with the fabrication of SAM features on surfaces by using conventional lithographic techniques, such as μ-contact printing (μCP) or photolithography. The NMOFs are then selectively grown on these features by exposing the surfaces to the precursor solution under optimum conditions or using the LbL synthesis (Figure 2.). Fischer *et al.* first proved this concept by controlling the growth of MOF-5 crystals on square-like COOH-terminated SAM features of 40 × 40 μm fabricated by μCP (Figure 3.)[3]

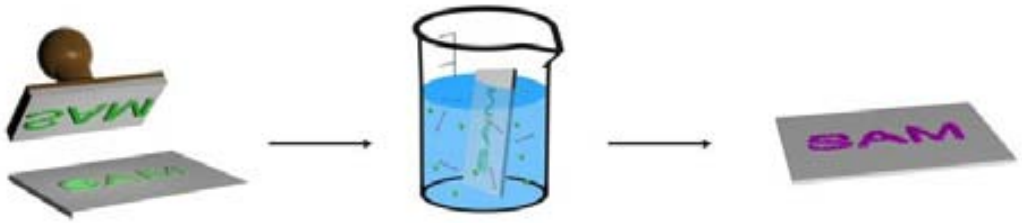

Figure 2. Schematic illustration of the template crystallization strategy used for structuring metal–organic frameworks on surfaces.

After patterning these features, the remaining Au surface was passivated with a CF3-terminated SAM in order to prevent the nucleation of MOF-5 in non-specific regions. The substrate was immersed into the mother solution, and this system was heated at 75 °C for 72 h. Interestingly, excellent adsorption properties of the resulting MOF-5 microarrays were successfully confirmed by exposing them to vapors of [(η5-C_5H_5)Pd(η3-C_3H_5)]. Using this method, Fischer's group also fabricated MOF-5 and HKUST-1 microarrays on alumina and silica surfaces.[4] In this case, however, the SAM features were patterned with standard photolithographic techniques.

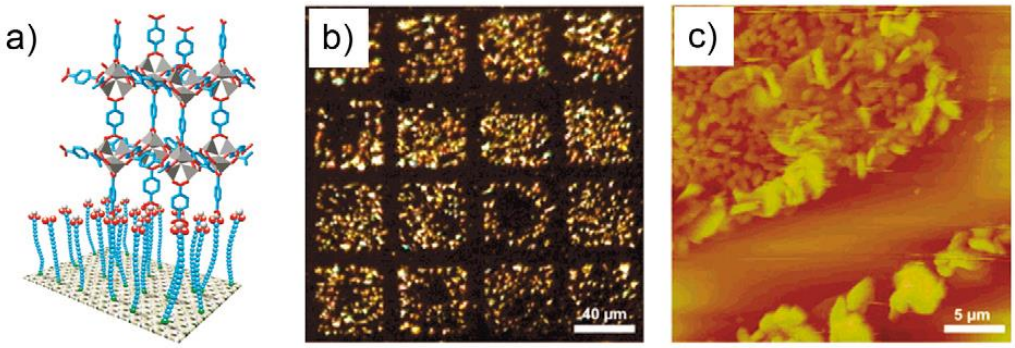

Figure 3. (a–c) Arrays of MOF-5 crystals. (a) Schematic illustration of the concept of anchoring a typical MOF-5 building unit to a COOH-terminated SAM. (b) Optical microscope and (c) AFM images of a selectively grown film of MOF-5 on a patterned SAM of 16-mercaptohecadecanoic acid on a Au surface. The MOF-5-coated squares are 40 × 40 µm, and the crystals are about 100–500 nm in size.

In addition to immersing the pre-structured surface into the precursor solution, the LbL synthesis can also be localized on these SAM templates, thus controlling the positioning of the created metal–organic multilayers. For instance, Wöll et al. fabricated HKUST-1 crystalline microarrays on Au surfaces by using the LbL

synthesis on COOH-terminated SAM features generated by μCP.[5] Similarly, Boom et al. fabricated a metal–organic multilayer pattern by sequentially immersing a glass surface, in which a template consisting of 5 μm OH-terminated SAM lines spaced from each other by 40 μm was created using photopatterning, into solutions of Pt(II) metal ions and 1,4-bis[2-(4-pyridyl)ethenyl]benzene ligands.[6]

1.2. Stamp based lithography

Even though the use of SAM features is the most extended approach, recent advances have been made in using stamp based lithographic techniques to directly deliver or confine small volumes of the reaction solution containing the precursors, seeds or NMOFs at specific locations of a surface, thus directly controlling the location in which the metal–organic structure is positioned or grown.

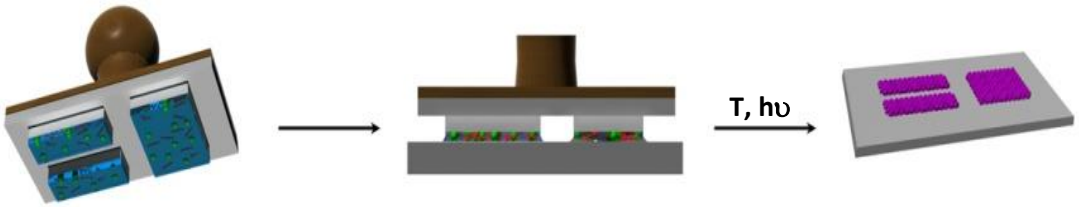

Figure 4. Schematic illustration of the direct delivery fabrication strategy used for structuring metal–organic frameworks on surfaces.

Thus far, precursor solutions have been successfully patterned through different lithographic techniques, including the lithographically controlled wetting (LCW), microtransfer molding (μTM) and micromolding in capillaries (MIMIC). De Vos et al. controlled the synthesis of HKUST-1 crystals at the single-crystal level on glass substrates through LCW (Figure 5.).[7] In this method, a polydimethylsiloxane (PDMS) stamp was initially coated with a DMSO solution containing Cu(II) metal ions and BTC ligands. This stamp was then placed in contact with the glass surface; in this manner, capillary forces drove the liquid to distribute only under the protrusions of the stamp. As the solvent evaporated, the nucleation of HKUST-1 crystals took place under these protrusions, and therefore, the grown crystals were formed in a pattern reproducing the motif of the stamp. Similarly, Vieu et al. used μTM to transfer a colloidal solution containing coordination polymer nanoparticles on glass surfaces.[8] It is interesting to note that the resulting nanoparticle structures with dimensions up to 300 nm kept their inherent spin crossover properties. Stamps were also used by Park et al. to structure a coordination polymer on glass

surfaces using MIMIC .[71] Continuous channels were formed when a PDMS stamp was brought into conformal contact with a solid substrate. These authors used the capillary action to fill the channels with a pyridine solution of a pre-formed coordination polymer composed of Zn(II) metal ions and 4,4′-di(4-pyridyl)cyanostilbene. The selective removal of pyridine by its absorption on the capillary walls drove to the formation while structuration of this coordination polymer.

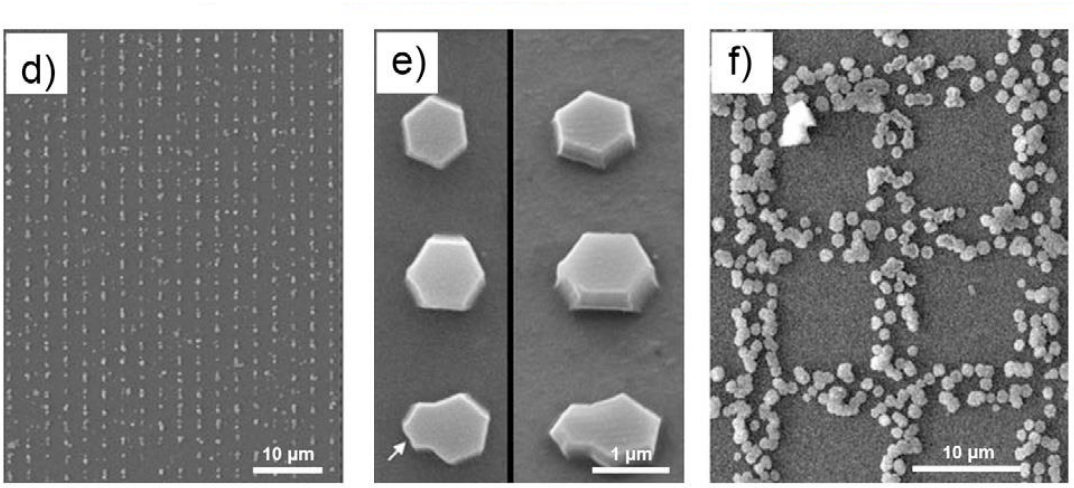

Figure 5. (d–f) Arrays of HKUST-1 crystals fabricated by LCW. (d) Large view and (e) details of individual crystals viewed from above (left) and at a 35° angle (right). The arrow indicates intergrowths caused by a second nucleation. (f) Square-like membrane structure composed of HKUST-1 crystals.

1.3. Heterogeneous seeding

Falcaro et al. [9] and Buso et al.[10] reported a novel class of α-hopeite microparticles as effective nucleating seeds for the fast formation of MOF-5, which show several advantages over functionalized silica particles. Named Desert Rose Microparticles (DRMs), these seeds form spontaneously within the starting MOF-5 precursor solution when Pluronic F-127 is added. Overall, the growth kinetics of MOF-5 in the presence of the DRMs is three times faster than the traditional solvothermal approach. The micrometre size DRMs can be effectively isolated from the precursor solution and used as seeds to induce localized MOF growth on a variety of substrates. MOF formation on DRM seeds is independent of both the substrate surface chemistry and the substrate geometry. The authors successfully grew MOF-5 crystals on flat silicon and alumina substrates, and also on more complex 3D geometries, by controlling the location of the micron seeds. (Figure 6) The 3D geometries were achieved using a commercial resist SU-8 membrane previously lithographed with arrays of vertical microchannels using Deep X-Ray

Lithography. DRMs were introduced inside each one of the lithographed channels, and the whole assembly was immersed in a MOF-5 precursor solution. MOF-5 crystals were observed to preferentially form inside the channels throughout the thickness of the membrane.

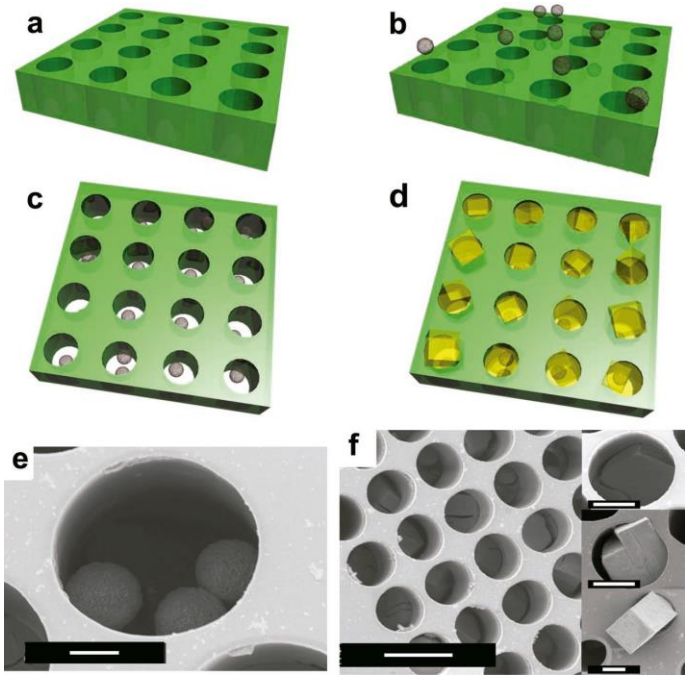

Figure 6. a–d) Schematics and e–f) SEM images of the protocol used to spatially manipulate MOF-5 formation using DRMs in pre-defined positions on a lithographed substrate. a) X-ray lithography was used to pattern a membrane with a uniform distribution of wells on a commercial resist (SU-8) layer. b) Drops of a DRM/DMF solution were pipetted onto the lithographed substrate. c) The substrate was vacuum dried to draw the DRMs into the lithographed wells. d) The DRM seeded substrate was then placed into a MOF-5 growing medium to generate MOF formation within the wells. e) SEM of DRMs positioned in the wells of a SU-8 lithographed membrane after vacuum drying (scale bar, 10 μm); the wells are 40 μm in diameter and 100 μm deep (scale bar, 100 μm). f) MOF-5 crystal growth within several lithographed wells after 5 h reaction time at 95 °C in the MOF-5 growing solution (scale bar, 50 μm). Insets show crystals emerging from a well at various growth stages (scale bar, 20 μm).

1.4. Electrochemical approach

Electrochemical investigations of Cu- and Zn-MOFs were first reported in 2007[11] using an electrochemical based MOF synthesis approach proposed by BASF.[12] In 2009 Ameloot et al. showed that an external electric field can be used to induce the growth of MOFs in particular locations in order to fabricate MOF patterns on a substrate.[13] Although it is possible to synthesize a variety of different porous frameworks, the authors used the well-known MOF structure called HKUST-

1 synthesized in 1999 by Chui at al.[14] This MOF is a copper based porous hybrid crystalline material where the Cu^{2+} cations are coordinated by a tricarboxylic ligand (1,3,5-benzenetricarboxylic acid, BTC) known as $Cu_3(BTC)_2$.

Using voltage in the 2.5–25V range, a copper electrode (anode) releases metal ions into solution containing the BTC ligand and methyltributylammonium methyl sulfate (MTBS) electrolyte. The high density of copper ions close to the electrode induces the formation of MOF crystals preferentially in this anodic region. Interestingly, nucleation is less likely to occur on top of the already formed crystals, and hence agglomeration or stacking of crystals is avoided. The bare metal area naturally provides a higher concentration of metal ions and the nucleation and growth of MOF crystals is enhanced in such areas, as depicted in Figure 7. As a consequence, a continuous coating of MOF can be prepared. Films with thickness in the 1 to 20 μm range were obtained with a height variation measured within 50 and 20% respectively; the thicker the film, the better the control of the thickness while the roughness of the coating depends on the crystal size distribution.

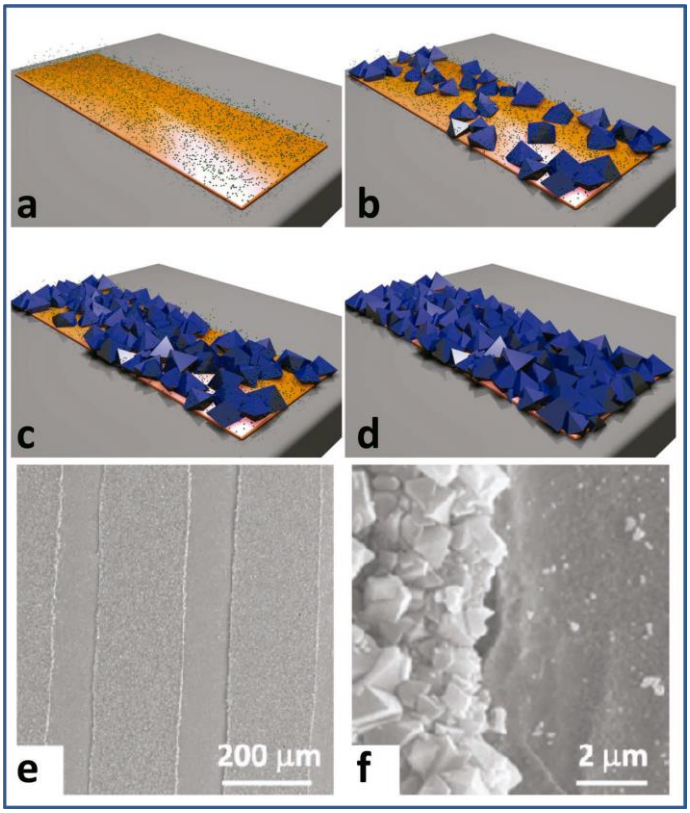

Figure 7. a–d) Schematic of the lithographic approach involving the electrodeposition technique to deposit $Cu_3(BTC)_2$ MOF (HKUST-1) on copper substrates developed by Ameloot et al.[13] (a) Using copper as an anode (orange substrate), the Cu cations (small, green dots) are released by the metal and concentrate close to the electrode. b) The ligand (BTC) in solution can react with the metal cations growing the MOF crystals (blue) where the probability that the reaction will occur is higher (anode). c) Over time the metal precursor density remains higher where the anode remains bare,

hence allowing for the porous crystal growth on these metal regions. d) Using this mechanism, it is possible to grow highly dense MOF crystals in selected areas. e) The microscopy measurements performed on the patterned regions and f) detail showing the preferential growth of $Cu_3(BTC)_2$MOFs on copper. Both images reproduced with permission.[13] Copyright 2009, ACS.

1.5. Presynthesized MOFs positioning

The combination of different microfabrication steps to pattern presynthesized MOFs represents the last approach by Paolo Falcaro and colleagues.[15] They demonstrate a versatile approach for fabricating MOF films, which could potentially be incorporated into devices using a generic patterning methodology applicable to all types of MOF. They use a facile protocol to pattern MOF films by combining ultraviolet lithography, hot pressing and pre-formed submicrometre-sized MOF crystals. The imprinting and lithographic processes are independent of each other and the resolution of the resulting patterned films depends on the size of the MOF crystals. The combination of these techniques can be used to achieve structural control of the resulting MOF films and does not affect their chemical functionality. This patterning protocol is in principle suitable for miniaturized catalytic, sensing, luminescent and biomedical devices, and is also scalable.

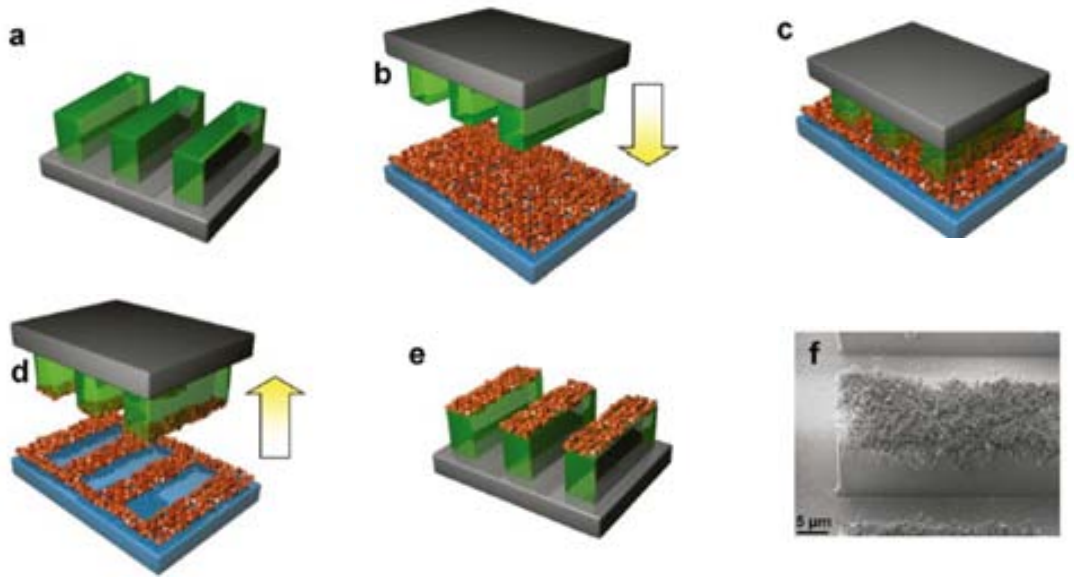

Figure 8. Schematic of the imprinting process. (a) A UV lithographed film of SU-8 photoresist is prepared, (b) The patterned SU-8 fi lm is pressed (c) onto a pre-prepared MOF fi lm obtained from a colloidal solution heated at 95 ° C. (d) After 2 minutes, the two fi lms are separated, (e) leaving behind a patterned thin fi lm MOF surface. (f) SEM image of an NH 2 -MIL-53(Al) MOF pattern.

2. Our Results: Structuration of HKUST-1 single crystals on surfaces

2.1. HKUST-1 (MOF-199) archetypical system for proof-of-concept

HKUST-1 (from the initials of the Hong Kong University of Science and Technology) is undoubtedly one of the most famous metal-organic framework materials. It was described for the first time by Orpen *et al.* in 1999 (HKUST university).[14] Obtained by the association of benzenetricarboxylic acid and copper ions, the HKUST-1 Metal-Organic Framework is composed of dimeric cupric units, in a "paddlewheel" coordination mode bridged by trimesic ligand through carboxylate groups. The framework is electrically neutral; the 12 carboxylate oxygens from the two TMA ligands bind to four coordination sites for each of the three Cu ions of the formula unit. Each metal completes its coordination sphere with a solvent molecule. A view down the [100] direction of the cubic cell of HKUST-1 reveals; 1-nm-size channels that consist on squares with 9.5 Å of edge and 13.3 Å of diagonal. These nanochannels intersect to provide a 3D connected network of pores. A view through the cell body diagonal [111] reveals a honeycomb arrangement of large hexagonal-shaped windows, each composed of a ring of six metal dimers and six trimesate groups, which measure 18.6 Å between opposite vertices. These windows are cross sections of the "cavities" formed at the intersection of the three orthogonal sets of channels. The high porosity indicated by the crystal structure and confirmed by absorptions measurements (the BET specific surface area is around 1500 $m^2.g^{-1}$ depending on the desolvation conditions) attracted the interest of many research groups and the HKUST-1 MOFs has been the centre of many different studies concerning potential applications such as catalysis, gas selectivity among others. The characteristic shape of the crystals is octahedral, making it an easy way to predict the formation by simply optical or electron microscopy (Figure 9. c). Furthermore, the soft and flexible conditions that lead to the formation of the HKUST-1, make this MOF the perfect candidate for most phenomenological and fundamental studies about the formation of MOFs. Thus HKUST-1 has been used in many cases as proof of concept to discover novel synthetic methodologies, to study the MOF formation among other.

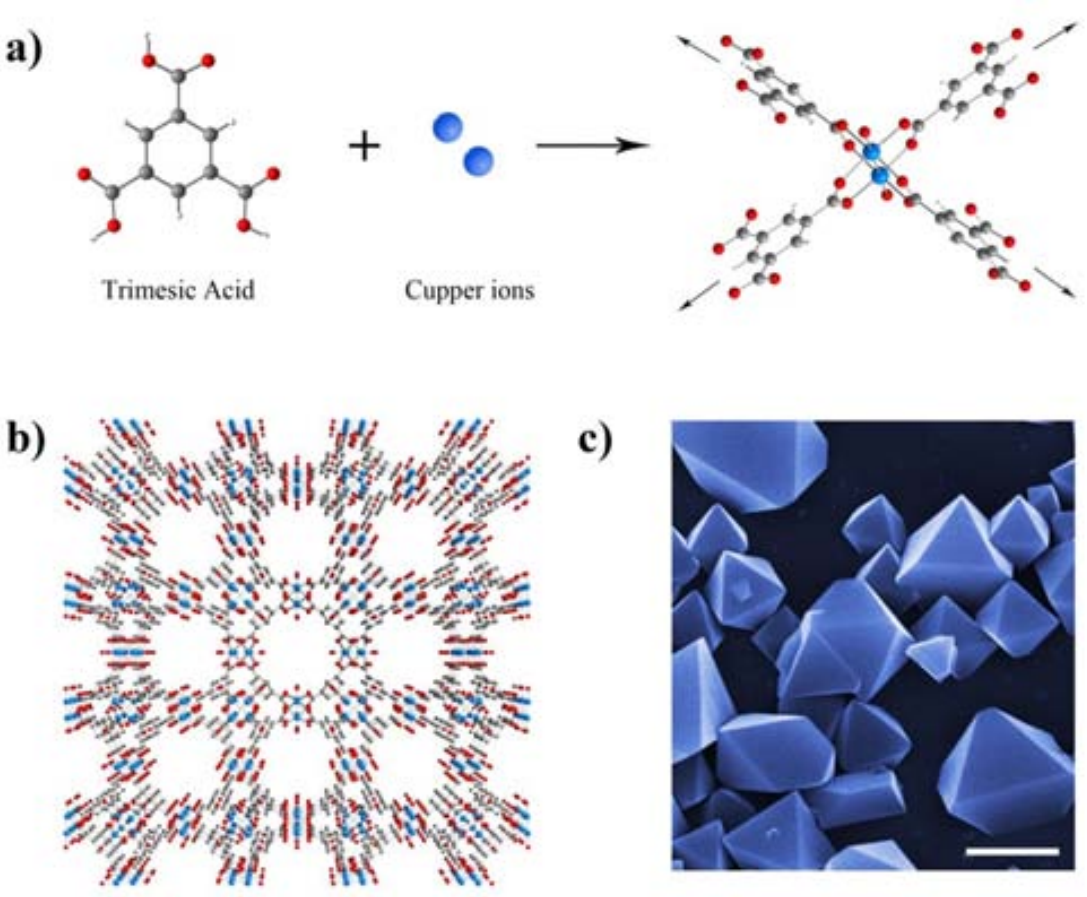

Figure 9. a). Dicopper(II) tetracarboxylate building blocks for HKUST-1. Key distances are Cu-Cu; 2.628(2) Å, Cu-OCO; 1.952(3) Å, and Cu-OH_2, 2.165(8) Å (number in parentheses is the estimated standard deviation of the final significant digit). b). viewed down the [100] direction, showing nanochannels with four fold symmetry. c) SEM colored image of HKUST-1 octahedral microcrystals bulk synthesized. Scale bar represents 10 um.

2.2. Fluidic Enhanced Molecular Transfer Operation (FEMTO)

The Nano eNabler System (Bioforce, USA), described as a Benchtop Molecular Printer is a commercial multifunctional surface patterning platform for dispensing attoliter to femtoliter volumes of liquids onto a wide variety of surfaces. The design is based on the Bioforce proprietary Fluidic Enhanced Molecular Transfer Operation (FEMTO) process [16]. Equipped with a 2 X-Y mobile axis platform to puck the substrate, giving 20 nm stage resolution and 50 x 50 mm^2 of patterning area in front of the 90 x 90 um^2 available with a conventional PZT based scanner. A part from the 2 X-Y axis platform, an interesting feature is the Z piezo-actuator which allows movements 40 μm along Z axis during the lithography, which will allow working with low spring constant cantilevers. A too weak spring does not pull off the substrate as required during withdraw step, as the meniscus makes the pen(s) stick to the surface if not enough withdraw distance is applied. Surface contact force is controlled via an optical lever detection system similar by those employed by an AFM.

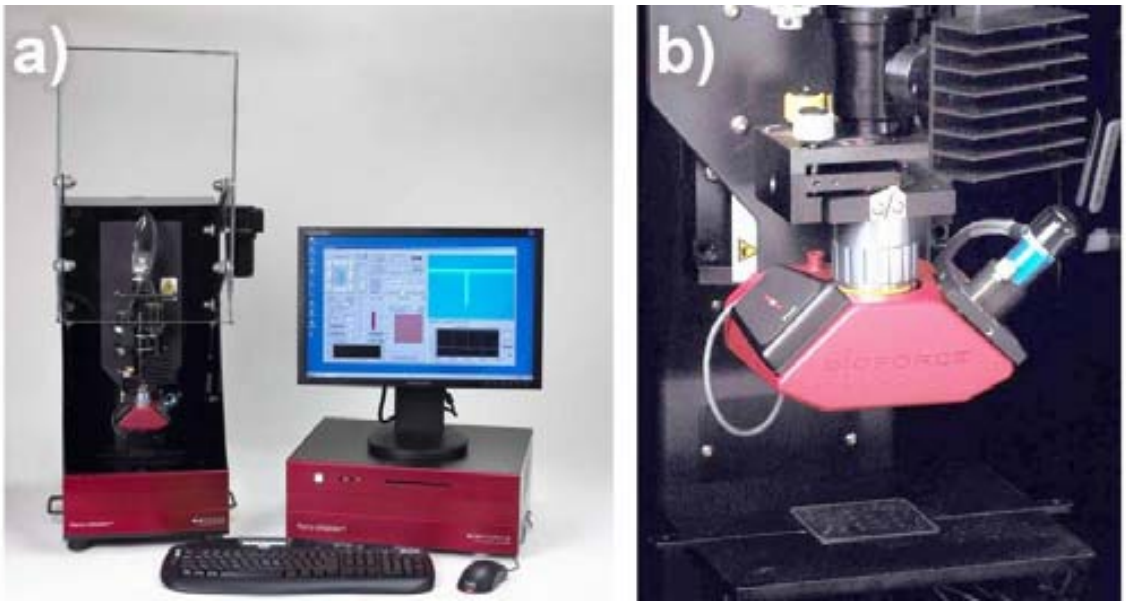

Figure 10. a) Setup of eNabler system (Bioforce). B) Detail of the head of the system showing the laser detector at left, laser emitter at right and the microscope objective in the middle.

2.3. Writing tools for FEMTO

The most remarkable distinctive feature of FEMTO is the microfluidic based writing tool which allows the reproducible dispensing of femtolitre droplets of certain liquids during long times. Surface Patterning Tool (SPT), is a microcantilever device in which a microchannel connects the tip to a reservoir that contains the liquid. (Figure 32.). This reservoir can be filled with a micropipette and the liquid flows by capillary effect along the cantilever. The minimum spot size will be limited by its gap at the edge of the cantilever.

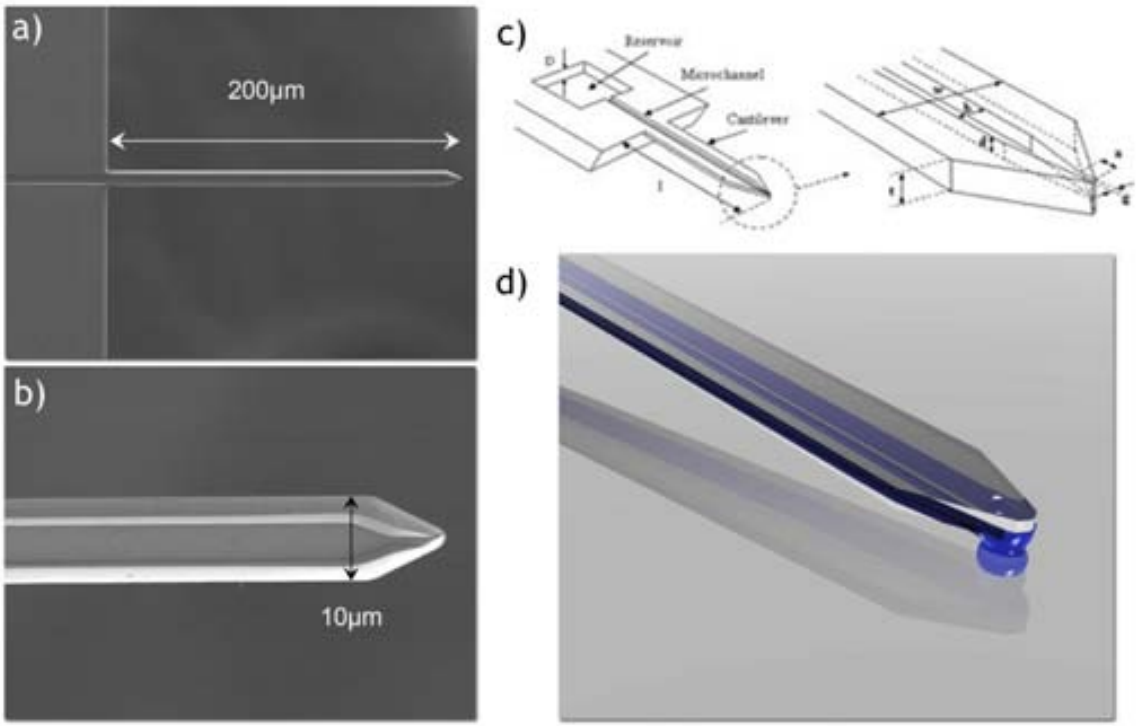

Figure 11. a,b) Representative FESEM images of the microfluidic pen. c) Schematic illustration of the microfluidic pen used in MPL. d) Representation of the droplet contact diameter for different dwell times. e) Thresholded merged optical microscopy images of the corresponding patterned droplets. Distance between droplets equals 35 µm.**c,d**,

2.4. Writing process

One of the critical aspects to create patterns and to promote reactions on liquids in the micrometre size range is the control of the integrity of deposited droplet during the time and on the surface. In the micrometre size range, droplets are considered to present spherical cape geometry defined by the contact angle between the liquid and the surface. (Figure 12.) The contact angle of a droplet depends on the thermodynamic equilibrium between the three involved phases, liquid – vapour (gas) – solid following the Young-Laplace equation (*Equation 1.)*. The line describing these triple interphase is called three phase line tension. Due to evaporation, contact angle presents a wide variety of values, from the maximum value (advancing contact angle) to the minimum one (receding contact angle).

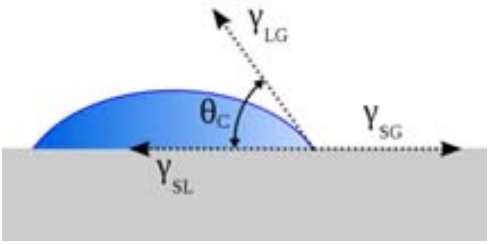

Figure 12. Esqueme showing the 3 phases thermodynamic equilibrium.

$$\cos\vartheta = \frac{\gamma_{sv}-\gamma_{sl}}{\gamma_{lv}}$$ ***Equation 1.*** Young-Laplace equation

Where γ_{sv} is the surface energy between solid and vapour, γ_{sv} is the surface energy between solid and liquid and γ_{sv} is the surface energy between liquid and vapour. The control over the thermodynamic equilibrium and so, the control over the droplet shape can be achieved by modifying some of the three phases, for example, increasing polarity of solvent, increasing pressure of vapour during lithography and modifying the wettability of the surface. Therefore, controlled atmosphere conditions and surfaces with different functionalities bearing to different wettabilities of our ink solution will allow us to study not only the influence of the droplet shape, but also, the influence of the surface chemistry on the crystal growth and orientation and the effect of the solvent evaporation rate in reaction yield.

Thus, due to the capital importance of the control of the droplet shape and evaporation the HKUST patterning exeperiment were performed under different synthetic conditions and on a series of Self-Assembled Monolayers (SAMs) surfaces bearing different functionalities, which vary the contact angle between the precursor solutions and the surface. (Figure 13.)

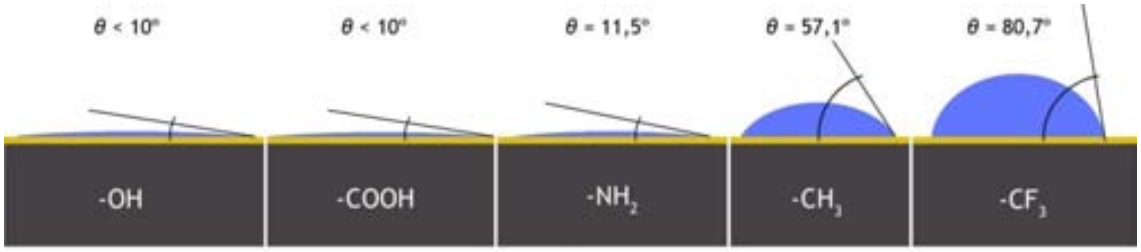

Figure 13. Representation of the droplet shapes over the different functionalized gold substrates depending on the contact angles measured for a DMF based solution.

In order to study the writing process we patterned arrays of droplets of water/glycerol (7:3) varying the dwell time. The SiN/SiO surface of the SPT has to be activated (increase the polarity) by exposure to a reactive atmosphere (Ozone or Plasma) in order to allow the fluid to flow by capillarity. When the SPT is not activated, the fluid remains in the reservoir. Nevertheless, once the SPT is activated, the liquid delivered on the reservoir wets the whole surface of the chip including out of the reservoir. In a certain way, the reservoir only acts to allow a bit more ink solution to fit in, but not to confine it.

After filling the reservoir with 1–1.5 µl, the liquid solution flows by capillarity to the edge of the cantilever through the microchannel. Then, the cantilever is mounted in the FEMTO holder and slowly approached to the surface until making contact outside the interest area. The cantilever is in the focal plane and we move the stage up to determine the surface position. It is useful to take two references: the every time narrower cantilever shadow and the every time more focused surface. Once reached the surface, the ink solution is deposited over the SiO_2 surface with a certain variable flow until reaching a maximum particular volume depending on the dwell time (see figure 14). As we can see in the figure 3.14 the diameter of the deposited droplets depends directly on the dwell time, reaching a maximum which depends on the liquid, the treatment of the SPT (time and power) and the treatment of the surface and the ambient conditions. The presence of a continuous feed through the microchannel offers the most remarkable advantage; allows the deposition of regular/equal droplet volume, for a particular dwell time, unless reservoir is empty. It has been shown then that the writing mechanism is highly dependent to the **flow rate** on the microchannel (liquid-channel interaction, capillary action), the **liquid-substrate** interaction and of course, intrinsic features of liquid and environment.

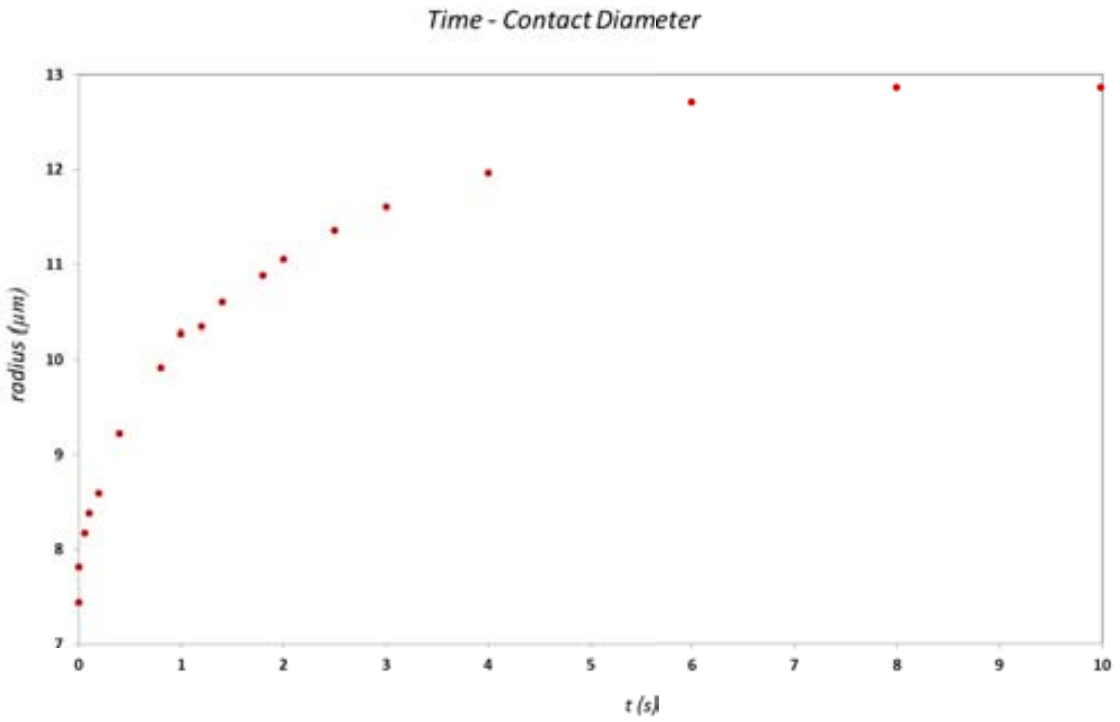

Figure 14. Representation of the droplet contact diameter for different dwell times (0.001, 0.002, 0.06, 0.1, 0.2, 0.4, 0.8, 1, 1.2, 1.4, 1.8, 2, 2.5, 3, 4, 6, 8, 10 s) from the patterning of a mixture water-glycerol (5:1) on a SiO_2 surface.

Surface Patterning Tools, not only offers the possibility to pattern reproducible and large arrays of atto- to femtolitre droplet volumes, the programming procedure of Enabler (Bioforce) is also very accessible and versatile. For example, DPN instruments programming are based on setting an origin coordinates and afterwords entering the values of relative distances, dwell times and movements from it, defining rows and columns of dots, contact times and clear spaces. If you want to do a complex pattern is necessary to introduce the values of every single particular row or column, in comparison, eNabler programming system consists in a graphical environment showing an array of selectable dots, permitting its use as a selectable pixel matrix. However, some disadvantages have also been found in FEMTO instrument ant writing tools. The lack of any levelling system makes impossible working with multitip arrays.

2.5. Preparation of materials

Preparation of DMSO based HKUST-1 precursor solution

A solution 5 mmol (1.18 g) of cupric nitrate hemipentahidrate $Cu(NO_3)_2 \cdot 2.5H_2O$ and 2.76 mmol (0.58 g) of trimesic acid (TMA) in 4.55 ml of DMSO (5 g)was prepared by vigorous stirring the mixture for 10 minutes. After that time, the solution was filtered with a 1 μm porous filter, obtaining our ink solution.

Functionalization of Gold Substrates

1x1 cm SiO_2 pieces were inmersed in piranha acid mixture solution (7:3 v/v solution of H_2SO_4 and H_2O_2; both from Panreac, Spain) for 30 min, rinsed with copious amounts of MilliQ water and dried with pressurized air. **Caution: piranha acid is a strong oxidizer and a strong acid. It should be handled with extreme care, as it reacts violently with most organic materials.** Prior to evaporation, substrates were exposed to Plasma cleaning (PVA Tepla PS210, Germany) at 200W for 20 s. The clean substrates were then mounted in a substrates holder adapted to the e-beam evaporator (AJA international, USA). Cr or Ti (≈ 5 nm) layer were first evaporated as adhesion layer. Then a 35nm gold layer was evaporated.

For the different functionalizations, a 1mM solution in Ethanol of the corresponding thiol (see table) was prepared. Gold substrates were then immersed in the thiol solution for 10 minutes. After the SAM formation time, substrates were kindly rinsed with alternated MiliQ water and Absolute Ethanol for 3 consecutive times. To confirm the adequate functionalization, contact angle was measured with a Contact Angle Analyser (Easy Drop Standard, Krüs) by depositing 1 μL droplet of the DMSO based ink solution on the different functionalized gold surfaces:

Functionality, Thiol	***Contact Angle (θ)***
-COOH, Mercaptohexadecanoic Acid (MHA)	< 10º
-OH, Mercaptoundecanol (MUOL)	17.6 ± 2.35º
$-NH_2$, Aminoundecanethiol (AUT)	28.9 ± 2.40º
$-CH_3$, Octadecanethiol (ODT)	83.0 ± 0.33º
$-CF_3$, Perfluorodecanethiol (PFDT)	100.7 ± 0.29º

Table 1. Functionality and measured contact angle of the DMSO based ink solution in the corresponding thiolated gold surface.

2.6. Size does matter

When our highly concentrated solution containing $Cu(NO_3)_2 \cdot 2.5H_2O$ (1.170 g) and H_3btc (0.580 g) in pure dimethylsulfoxide (DMSO, 4.55 ml) is kept in a closed vial, the solution remains transparent indefinitely. When instead of a closed vial we keep the solution in an open vial, it can be observed the formation of few HKUST-1 crystals close to the solution-glass-air interphase, but principally it can be observed the crystallization of the separated constituents either in this region or in the bulk solution. Nevertheless, when a macroscopic droplet of this solution is delivered over a surface, a higher yield formation of HKUST-1 crystals is observed on the area close to the three phase line tension of the droplet (Figure 12), so in the solid-liquid-gas/vapour interphase, but only the separated reagents crystallize on the bulk volume of the droplet. This was verified by PXRD (Figure 15. d). This observation motivated us to use this solution conditions and study what will happen with this system when the line tension is as closer as possible to the whole volume, in other terms, when miniaturizing the droplet size.

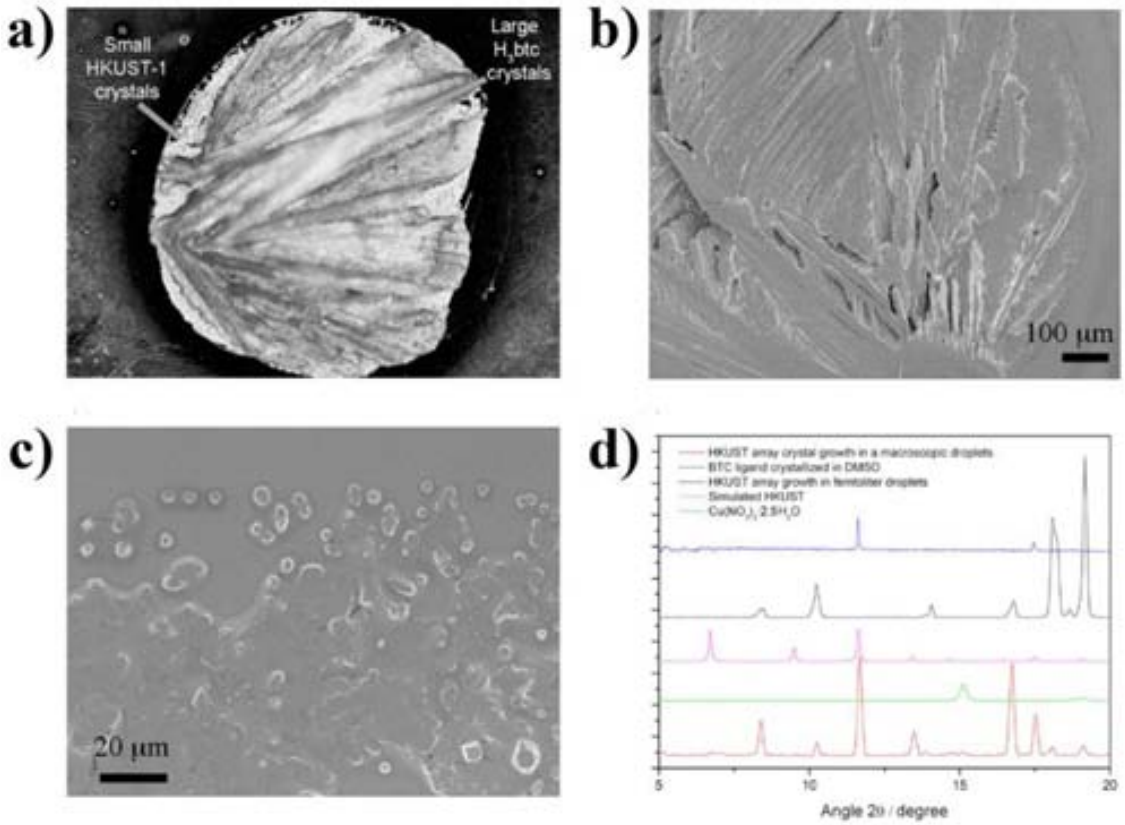

Figure 15. Control experiments performed on large DMSO precursor droplets on CF_3-terminated SAMs. (a) Optical microscope image of one of these droplets after DMSO evaporation. (b) FESEM image showing the precursor crystals. (c) FESEM image showing the HKUST-1 crystals. Note the presence of crystals with different orientation.(d) XRPD data.

2.7. Patterning of HKUST-1

In a typical experiment a SPT-10 was directly charged with the DMSO based ink solution by the addition of 2 μL of the filtered solution into the SPT reservoir, extracting the liquid excess with the same pipette. Different droplet arrays (15x15 and 10x10 dots) were patterned over surfaces functionalized with AUT, ODT and PFDT SAMs [figure 16]. All patterning was done with an Enabler Bioforce System (BioForce, USA) at room temperature and minimum dwell time of 0.01 s. taking a total array patterning time of less than 2 minutes. The fabricated arrays were then placed into ambient conditions for 24 hours until the DMSO was completely evaporated to form HKUST-1 crystals.

The different arrays of materials obtained on three different functionalities (NH_2, CH_3 and CF_3) keeped during 24 hours in ambient conditions were further compared (see Figure 16) using FeSEM.

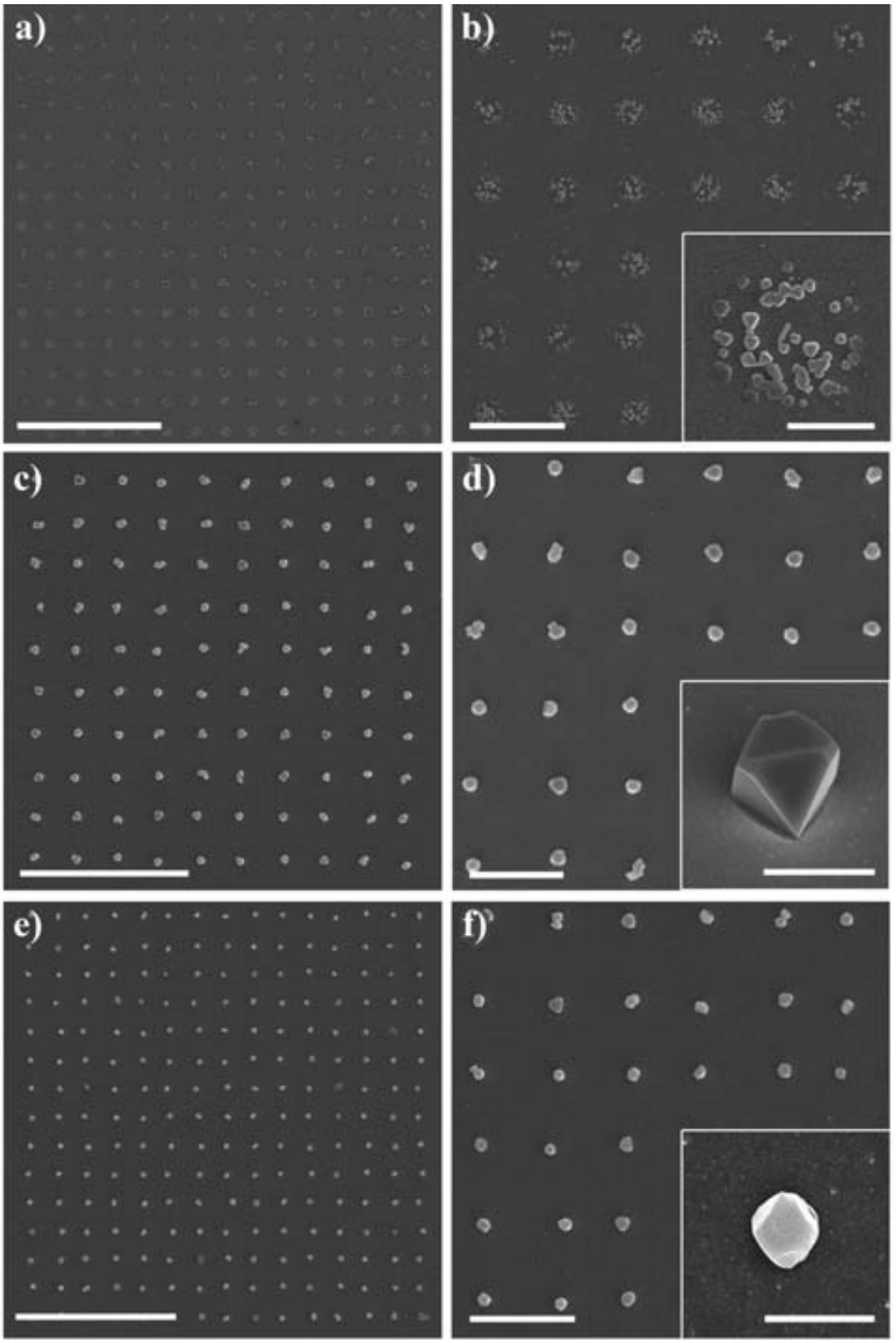

Figure 16. FESEM images of the HKUST-1 arrays fabricated on (a,b) NH_2-, (c,d) CH_3- and (e,f) CF_3-terminated SAMs on gold substrates. Scale bars represent 40 μm (a,c,e), 10 μm (b,d,f), and 2 μm for the inset images.

The FeSEM characterization shows clearly (i) a very homogeneous writing process without condensation phenomena or impurities formation (ii) a surface dependent MOF nucleation and crystallization.

Figure 3.16 a-b shows an array of 15x15 islands (8 μm separated) of HKUST-1 crystallites grown over amino (NH_2) terminated SAM. The estimated volume delivered is around 20 fL calculated following the equation 3.2. and the measured contact angle of 28.9º. The islands are of 3 μm in diameter and are constituted by homogeneous crystallites of around 200nm of edge dimensions. It appears in this case that, due to the quite high wettability of the $-NH_2$ surface, the deposited droplet spread, leading to different nucleation points from where different crystallites growth.

$$V = \frac{\pi \cdot r_b^3}{3} \cdot \frac{2 - 3 \cdot \cos\vartheta + cos^3\vartheta}{sin^3\vartheta} \qquad \textit{Equation 2.}$$

Where r_b is the contact radius and ϑ, the contact angle in deg.

The number of nucleation points is reduced when the contact area between the droplet and the surface is reduced. The Figure 16 c-d shows an array of 10x10 single crystals (10 μm separated) of HKUST-1 grown over CH_3 terminated SAM. Estimated volume delivered around 18 fL calculated following the equation 3.2. and the measured contact angle of 83.0º and edge dimensions of around 2 μm. After 24 h ambient conditions, the FeSEM images show the presence of one or two single crystals in each dot, the size of each crystal approximates 2 μm.

Reducing the wettability of our DMSO precursor solution by creating a CF_3 SAM, lower quantities of liquid are deposited on surfaces, and consequently smaller droplets are formed for a same dwell time. The delivered droplets volume is reduced to around 10 fL calculated following the equation 2. and the measured contact angle of 100.7º. The size of the single crystals formed after 24h in ambient conditions has been divided by two compared to those formed on $-CH_3$ functionalized surface; the size turns around 1 μm. (Figure 16 e-f)

According to the previous experiment, it is clear that the crystal growth is directly connected to the polarity of the surface: A less wettable surface attracts less liquid from the tip as demonstrates the evolution of droplets volume (-NH_2, -CH_3, -CF_3) and consequently the number and the size of the crystals can be reduced. Beyond the influence of the contact angle of the surface, the flowing of the liquid along the microchannel can also affect the liquid delivery on the surface.

2.8. Characterization of the HKUST-1 arrays

To provide further evidence of the formation of HKUST-1 crystals on surfaces using this direct-write pen-type lithographic approach we first performed Energy Dispersive X-ray (EDX) microanalysis of a HKUST-1 single crystal grown on a CH_3-terminated SAM gold substrate.

But the most relevant characterization technique for crystalline materials without a doubt is X-Ray diffraction (XRD). So we evaluated the possibility to characterise by XRD For this purpose, we estimated the size of the needed array to obtain XRD signal in about 1 mm^2, and we configured the difractometer to perform a gracing incidence measurement, similar to that usually carried out to characterise crystalline thin films or depositions. In this measurement, X-Ray beam, is irradiated with a very low incidence angle to ensure that interfere with the amount of material required to obtain signal, note that the material is distributed like a thin low density film.

To this aim, we prepared an HKUST-1 array consisting of 150x150 droplets of DMSO precursor solution spaced 8 μm apart (total area = 1.2 mm^2) on NH_2- and CF_3-terminated SAM gold substrates (Figure 17 and 18). Note that this large pattern took more than 3 hours while was performed with a unique 1.5 μL charge of the ink solution. After 48 h. the array was mounted on a microscope slide and characterized by X-Ray Grazing Incidence.

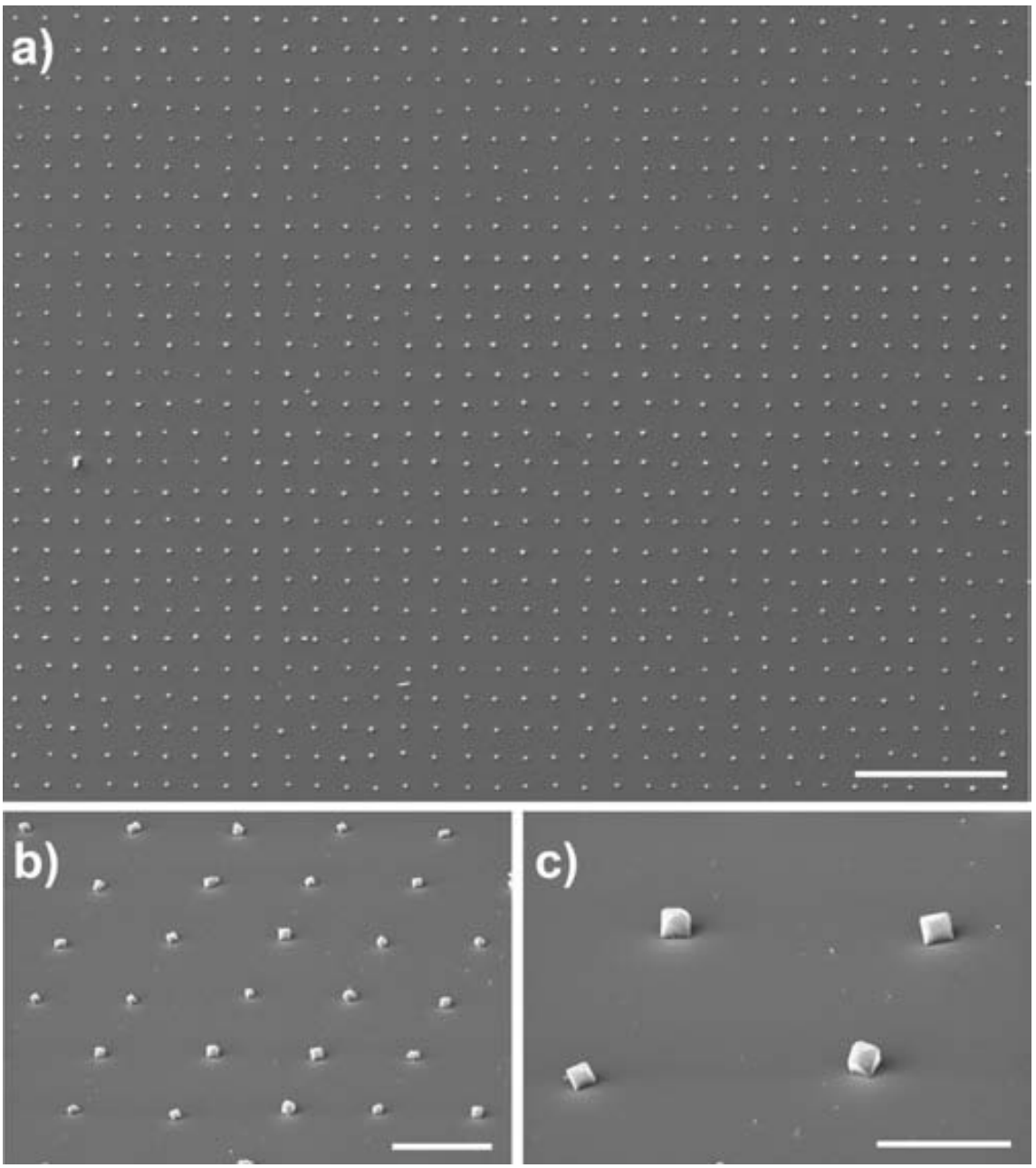

Figure 17. FESEM images of HKUST-1 arrays fabricated on CH_3-terminated SAMs on gold substrates. (a) The word "MOFs" fabricated with HKUST-1 single crystals and (b) a magnification image of the letter "M". (c,d) Single-crystal HKUST-1 array composed of crystals with edge dimensions of 550±100 nm. Scale bars represent 100 μm (a), 2 μm for inset image in (b), 40 μm (c), 5 μm (d) and 500 nm for the inset image in (d).

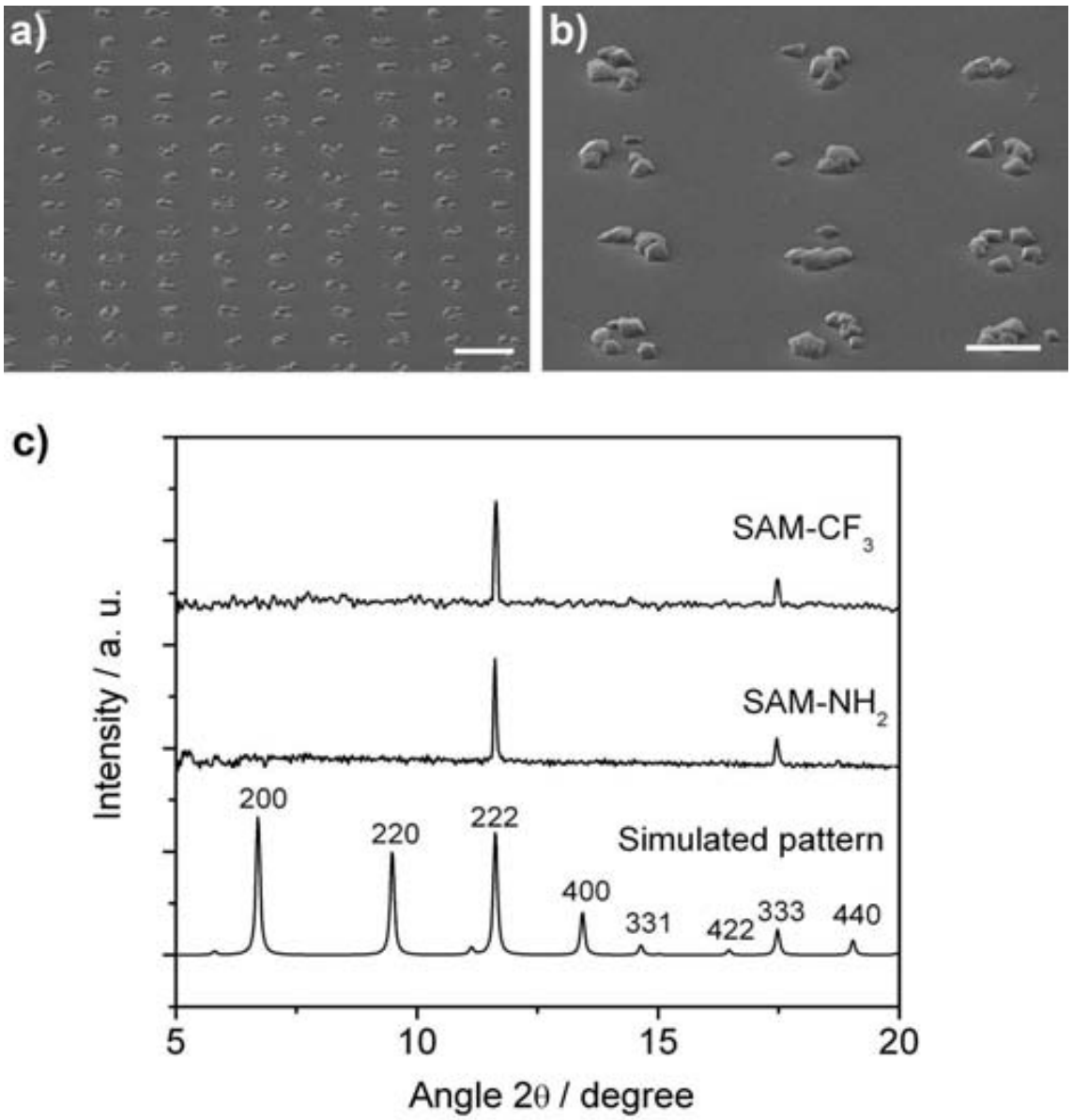

Figure 18. **a-b)** SEM images of the extended HKUST-1 array (150x150 dots, total area = 1.2 mm²) fabricated on a NH2-terminated SAM. Scale bars represent 10 μm (a) and 4 μm (c). **c)** XRD patterns (background corrected) of the HKUST-1 arrays fabricated on the CF3- and NH2-terminated SAMs, compared with the simulated XRD of HKUST-1.

The XRD data shown in Figure 18c clearly demonstrates not only the formation of HKUST-1 crystals but also a crystal growth orientation preference along the [111] direction for both NH_2- and CF_3-terminated SAMs. This is in accordance with the FeSEM images that show that the crystals are positioned over the faces of the octahedral crystal. It is interesting to note that Wöll *et al.* and Bein *et al.* also observed identical orientation preference in their crystallization methodologies on OH- and COOH-terminated SAMs, respectively.[6,14] However, the same authors did not observed crystal growth orientation on hydrophobic SAMs,[14] which is in fact

achieved in the HKUST-1 arrays fabricated by the pen-type lithographic technique, as further confirmed by the SEM images.

2.9. Combined functionalities bearing to complex patterns.

The different experiments performed show that HKUST-1 crystals can be synthesized and grown using soft lithography techniques. The high control offered by the technique is confirmed by the fact that the number and crystal size of the resulting HKUST-1 can be modulated through the wettability of the surface. This high versatility and control offers the possibility to create complex structures on surface that presents areas with different wettabilities and consequently areas with different crystals growth. For this First, an AUT SAM pattern array was prepared, delivering droplets of a 1 mM AUT solution in acetonitrile/glycerol (70/30) at 70% RH. Patterns consist of 3x3 droplets with contact diameters of 10 μm placed 40 μm apart on a gold substrate. (Figure 19) Once the so called map is obtained and after the 15 minutes needed to form the AUT SAM on the contact area of the droplets, the substrate is removed from the holder and washed several times with ethanol and water miliQ. The exposed gold regions of the substrate were then passivated with PFDT by immersing the substrate in a 1 mM PFDT ethanol solution for 10 minutes, obtaining a double functionalized surface.

The substrate was mounted again on the holder and positioned and oriented at the same position than initially. A new SPT was then charged with Ink Solution 2 and an array consisting of 9x9 droplets spaced 10 μm apart, were then fabricated, onto the AUT dot array area, with the origin in the first AUT dot localized with the help of the picture-map. As shown in Figure 1b, the resulting array is formed by 81 droplets of which 9 match up the NH_2-terminated dots (as marked by dash circles in Figure 1b) and the other are directly patterned on the CF_3-terminated SAM. The diameter of the droplets is estimated to be around 5 μm and 3 μm for the ones placed on the NH_2- and CF_3-terminated SAMs, respectively. The above results confirm that DMSO precursor droplets spread out more on the NH_2-terminated SAMs than on the non-polar CF_3-terminated SAMs once patterned using identical conditions (dwell time = 0.001 s, humidity = 35% and room temperature). HKUST-1 crystals were formed after exposing the patterned droplet arrays on the SAMs gold substrates at room temperature for 24 hours. Figure 19 c shows field-emission SEM (FESEM) images of the HKUST-1 array resulting from the evaporation of the 9x9 DMSO precursor droplet array. Interestingly, well-shaped octahedral crystals of HKUST-1 were grown in the contact areas between all FEMTO-delivered droplets and SAMs. However, all 9 droplets placed on the NH_2-terminated dots yield

multiple crystals with edge dimensions ranging from 300 nm to 750 nm, whereas the remaining droplets placed on the CF_3-terminated SAM yield single HKUST-1 crystals with edge dimensions comprised between 800 nm and 1.2 μm.

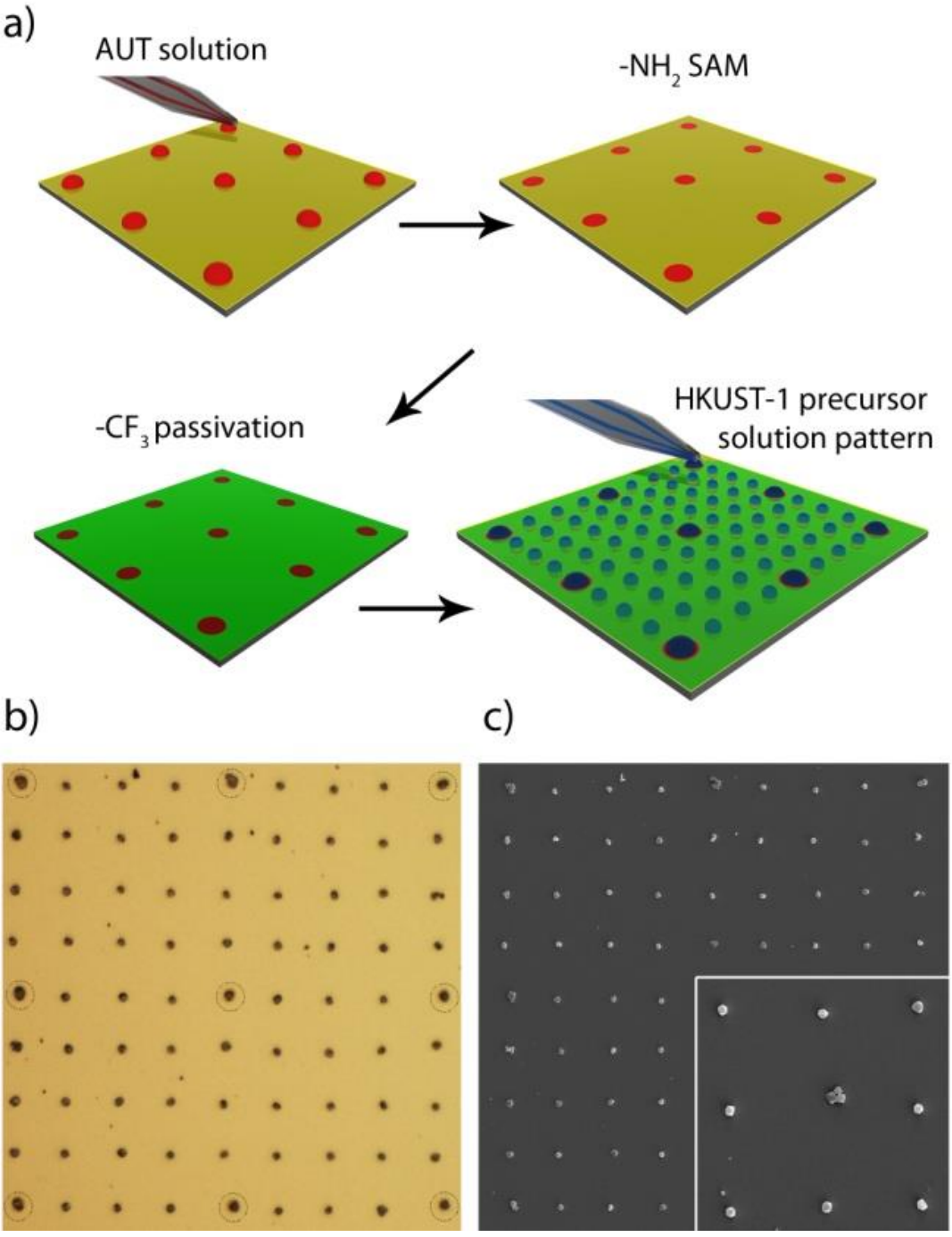

Figure 19. (a) Schematic illustration of the process followed for fabricating the 9x9 droplet array on a gold substrate previously patterned with a 3x3 AUT dot array and passivated with PFDT. (b) Optical microscopy image of the 9x9 droplet array, in which each droplets is spaced apart 10 μm. Dash circles mark the 9 droplets placed on each AUT dots. (c) FESEM image of the resulting HKUST-1 array. The inset shows a magnification area of this array, in which the central dot corresponds to multiple HKUST-1 crystals grown in a droplet placed on the AUT SAM and the other 8 corresponds to single HKUST-1 crystals grown in 8 droplets placed on the PFDT SAM.

The terminal group on the top of the SAMs, and therefore, the contact angle between the precursor droplet and the surface are again critical for the number and the dimensions of HKUST-1 crystals grown within each droplet, opening up the possibility to create single-crystal HKUST-1 arrays on surfaces with low wettability. For example, CH_3- and CF_3-terminated SAMs, where the droplets remain stuck, turned out to be ideal for single crystal growth within each droplet. The average edge dimension of each single crystal grown within each droplet placed on ODT and PDFT SAMs is 1.4 ± 0.3 μm and 0.9 ± 0.2 μm, respectively. As previously observed, identical droplets placed on NH_2-terminated SAMs tend to spread out, which results in a higher nucleation density and formation of multiple smaller crystals (edge dimensions: 100-400 nm) within each droplet.

2.10. Position and size control.

Another parameter to play with, in order to control the patterning regards the plasma treatment of the SPT which strongly influences on the volume of the droplet placed on a surface. For longer treatments, the surface of the SPT turns more polar, allowing polar liquids to flow better through the microchannels, and consequently, depositing larger volumes of liquid. On the contrary, when this treatment time is shorter, the volume of the droplet deposited is reduced. Following this strategy, we fabricated a 20x20 single-crystal HKUST-1 array on an ODT SAM using a SPT treated with plasma for 30 seconds instead of 15 minutes. As seen in Figure 20 c-d, the single HKUST-1 crystals size was reduced until of 550 ± 100 nm.

This fabrication methodology can also be used to precisely control the location in which a single MOF crystal wants to be grown. For example, 400 single crystals of HKUST-1 were grown on a CH_3-terminated SAM in such a way that forms the word “MOFs” (Figure 20 a-b).

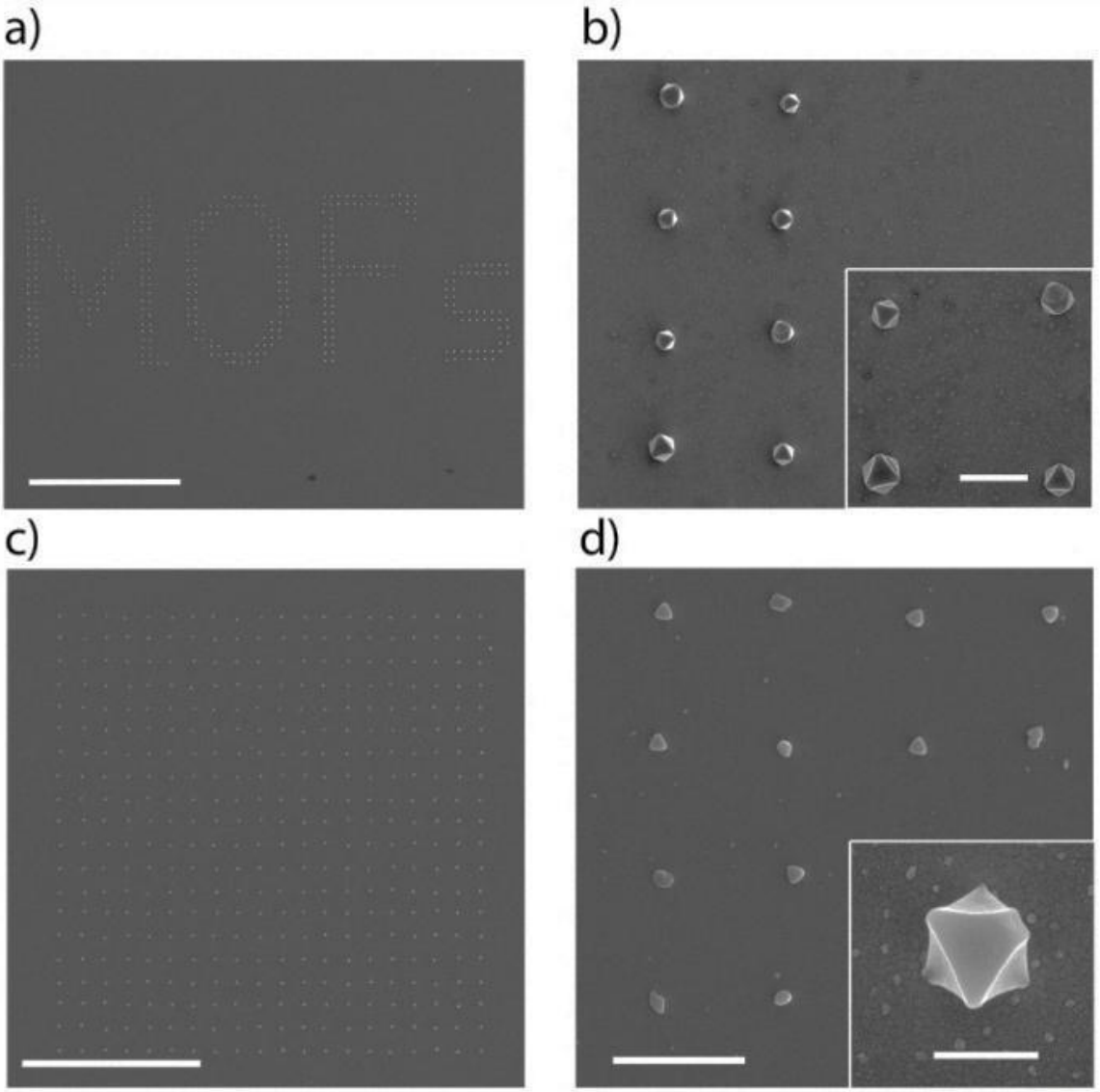

Figure 20. FESEM images of HKUST-1 arrays fabricated on CH_3-terminated SAMs on gold substrates. (a)The word "MOFs" fabricated with HKUST-1 single crystals and (b) a magnification image of the letter "M". (c,d) Single-crystal HKUST-1 array composed of crystals with edge dimensions of 550±100 nm. Scale bars represent 100 μm (a), 2 μm for inset image in (b), 40 μm (c), 5 μm (d) and 500 nm for the inset image in (d).

3. References

1. R. Zhang, Y. Zhang, Q. Zhang, H. Xie, W. Qian and F. Wei, *ACS Nano*, 2013, **7**, 6156-6161.
2. P. Falcaro, D. Buso, A. J. Hill and C. M. Doherty, *Adv. Mater.*, 2012, **24**, 3153-3168.
3. S. Hermes, F. Schröder, R. Chelmowski, C. Wöll and R. A. Fischer, *J. Am. Chem. Soc.*, 2005, **127**, 13744-13745.
4. D. Zacher, A. Baunemann, S. Hermes and R. A. Fischer, *Journal of Materials Chemistry*, 2007, **17**, 2785-2792.
5. O. Shekhah, H. Wang, S. Kowarik, F. Schreiber, M. Paulus, M. Tolan, C. Sternemann, F. Evers, D. Zacher, R. A. Fischer and C. Wöll, *J. Am. Chem. Soc.*, 2007, **129**, 15118-15119.
6. M. Altman, A. D. Shukla, T. Zubkov, G. Evmenenko, P. Dutta and M. E. van der Boom, *J. Am. Chem. Soc.*, 2006, **128**, 7374-7382.
7. R. Ameloot, E. Gobechiya, H. Uji-i, J. A. Martens, J. Hofkens, L. Alaerts, B. F. Sels and D. E. De Vos, *Adv. Mater.*, 2010, **22**, 2685-2688.
8. *Langmuir*, 2009, **26**, 1557-1560.
9. P. Falcaro, A. J. Hill, K. M. Nairn, J. Jasieniak, J. I. Mardel, T. J. Bastow, S. C. Mayo, M. Gimona, D. Gomez, H. J. Whitfield, R. Riccò, A. Patelli, B. Marmiroli, H. Amenitsch, T. Colson, L. Villanova and D. Buso, *Nat Commun*, 2011, **2**, 237.
10. D. Buso, A. J. Hill, T. Colson, H. J. Whitfield, A. Patelli, P. Scopece, C. M. Doherty and P. Falcaro, *Crystal Growth & Design*, 2011, **11**, 5268-5274.
11. A. Doménech, H. García, M. T. Doménech-Carbó and F. Llabrés-i-Xamena, *The Journal of Physical Chemistry C*, 2007, **111**, 13701-13711.
12. A. U. Czaja, N. Trukhan and U. Muller, *Chemical Society Reviews*, 2009, **38**, 1284-1293.
13. R. Ameloot, L. Stappers, J. Fransaer, L. Alaerts, B. F. Sels and D. E. De Vos, *Chemistry of Materials*, 2009, **21**, 2580-2582.
14. S. S.-Y. Chui, S. M.-F. Lo, J. P. H. Charmant, A. G. Orpen and I. D. Williams, *Science*, 1999, **283**, 1148-1150.
15. C. M. Doherty, G. Grenci, R. Riccò, J. I. Mardel, J. Reboul, S. Furukawa, S. Kitagawa, A. J. Hill and P. Falcaro, *Adv. Mater.*, 2013, **25**, 4701-4705.
16. J. Xu, M. Lynch, J. Huff, C. Mosher, S. Vengasandra, G. Ding and E. Henderson, *Biomedical Microdevices*, 2004, **6**, 117-123.

PUBLICATION 2.

Single-Crystal Metal-Organic Framework Arrays

Carlos Carbonell, Inhar Imaz and Daniel Maspoch

J.Am.Chem.Soc., **2011**, 133, 2144-2147

JACS
JOURNAL OF THE AMERICAN CHEMICAL SOCIETY

COMMUNICATION

pubs.acs.org/JACS

Single-Crystal Metal−Organic Framework Arrays

Carlos Carbonell, Inhar Imaz, and Daniel Maspoch*

CIN2(ICN-CSIC), Catalan Institute of Nanotechnology, Esfera UAB, 08193 Bellaterra, Spain

Supporting Information

ABSTRACT: A novel, versatile pen-type lithography-based methodology was developed to control the growth of HKUST-1 crystals on surfaces by direct delivery of femtoliter droplets containing both inorganic and organic building block precursors. This approach shows that through the use of surfaces with low wettability it is possible to control the crystallization of a single submicrometer metal−organic framework crystal at a desired location on a surface.

Scheme 1. Schematic Illustration of the Fabrication of Single-Crystal MOF Arrays by Using Direct-Write FEMTO

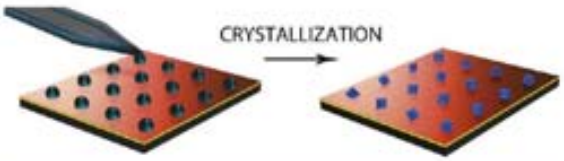

Metal−organic frameworks (MOFs) represent an emerging class of crystalline inorganic−organic hybrid materials that are receiving considerable attention because they offer a wide range of potential applications, such as gas storage, catalysis, separation, sensing, and drug delivery.[1] Depending upon the intended application, one wants to be able to fabricate such frameworks as bulk crystalline solids, miniaturize them at the micro- or nanometer scale,[2] or control their deposition on surfaces.[3] In the last case, the control of their growth, orientation, and/or positioning on the surface will be crucial in starting to conceive the integration of these MOFs on supports for the fabrication of complex surface sensors, separation membranes, drug-delivery platforms, and catalysts.[4] In fact, the patterning of other functional materials, such as nanoparticles, organic polymers, biological entities, etc., has expanded their applications in a wide range of areas from microelectronics to optics, microanalysis to sensors, and magnetic systems to cell biology.[5]

Previous studies have shown that MOFs such as MOF-5,[6] HKUST-1,[7] MOF-508,[8] and ZIF-7[9] can be grown as crystalline thin films on surfaces by first functionalizing them with self-assembled monolayers (SAMs) or using presynthesized seeds. With the use of SAMs, Fischer and co-workers further demonstrated that MOF-5 crystals could be selectively grown on 40 μm × 40 μm COOH-terminated SAM features fabricated by microcontact printing.[6] More recently, Wöll and co-workers[10] used these COOH-terminated SAM templates to grow layer-by-layer HKUST-1 crystals, whereas De Vos and co-workers[11] controlled their growth on specific locations of a surface using the lithographically controlled wetting technique. In this communication, we report a novel on-surface MOF growth strategy that uses a wet lithographic technique for direct delivery of femtoliter droplets containing both inorganic and organic building block precursors, which after their reaction and droplet evaporation allows the fabrication of arrays of submicrometer HKUST-1 crystals on alkanethiol-modified gold surfaces.

Pen-type lithography techniques, such as fluidic-enhanced molecular transfer operation (FEMTO),[12] dip-pen nanolithography (DPN),[13] and fountain-pen lithography (FPL),[14] allow the transfer of desired substances onto surfaces at the micro- and nanometer length scale through a scanning probe microscopy (SPM) probe or cantilever that dispenses femtoliter droplets of a solution containing these species. Thus, one could imagine their use to deliver droplets of a solution containing the organic and inorganic building blocks needed to build up a desired MOF onto specific regions of a surface. Once these droplets were positioned on the surface, the formation and crystallization of MOFs could be confined within each deposited droplet by controlling its evaporation and/or using external conditions such as microwave radiation or high temperature (Scheme 1). Following this strategy, we show herein that the controlled delivery of droplets containing a solution of Cu(II) ions and trimesic acid (H_3btc) onto surface-modified gold substrates leads to the fabrication of arrays of HKUST-1[15] single crystals. This versatile strategy allows us to control the miniaturization and positioning of HKUST-1 crystals even at the single-crystal level on supports, enabling the creation of any desired pattern in a given experiment without the need for prefabricated stamps.

In a typical experiment, the inking solution was obtained by mixing $Cu(NO_3)_2 \cdot 2.5H_2O$ (1.170 g) and H_3btc (0.580 g) in pure dimethyl sulfoxide (DMSO, 5 g). Next, a commercially available surface patterning tool (SPT, BioForce USA) that had been cleaned with plasma for 15 min (UV/Ozone Procleaner, BioForce, USA) was directly charged with this solution by the addition of a microdroplet of the filtered solution into the reservoir of the SPT with a micropipet. The tip was brought into contact with surfaces functionalized with SAMs made of 11-mercapto-1-undecanol (MUOL), 16-mercaptohexadecanoic acid (MHA), 1-aminoundecanethiol (AUT), 1-octadecanethiol (ODT), or 1*H*,1*H*,2*H*,2*H*-perfluorodecanethiol (PFDT) to fabricate arrays of droplets of this solution over the substrate. All of the patterning was done with an Enabler Bioforce System (BioForce USA) at room temperature using a minimum dwell time of

Received: January 10, 2011
Published: January 31, 2011

dx.doi.org/10.1021/ja2002428 | J. Am. Chem. Soc. 2011, 133, 2144–2147

Journal of the American Chemical Society COMMUNICATION

0.001 s. The fabricated arrays were then placed into ambient conditions for 24 h until the DMSO was completely evaporated to form HKUST-1 crystals, as confirmed by energy-dispersive X-ray spectroscopy (EDX; Figure S2 in the Supporting Information), X-ray diffraction (XRD), and scanning electron microscopy (SEM).

A series of SAM surfaces bearing different functionalities that vary the contact angle between the DMSO precursor solution and the surface (functionalities and measured contact angles: $-OH$, $<10°$; $-COOH$, $17.6 \pm 2.35°$; $-NH_2$, $28.9 \pm 2.40°$; $-CH_3$, $83 \pm 0.33°$; $-CF_3$, $100.7 \pm 0.29°$) were systematically studied first to determine the behavior of the droplets placed on these surfaces. Under the conditions studied, CH_3- and CF_3-terminated SAMs proved to be ideal for the fabrication of well-defined droplet arrays, whereas these arrays could not be fabricated on the OH- and COOH-terminated SAMs. When a droplet was placed on a OH- or COOH-terminated SAM, it spread completely. In contrast, the same droplet left on a CH_3- or CF_3-terminated SAM remained stuck in its place. The contact angle was then critical for droplet array formation. At low contact angles, the droplets tended to spread out completely once they were placed on the surface because the affinity and wettability of the solution on the surface was very high, thus preventing the formation of droplet arrays. This behavior was observed for both MUOL and MHA SAMs. However, as the contact angle between the solution and the surface increased, the affinity and spread diameter of the droplets decreased. This tendency could be observed for the AUT SAM, in which the patterned droplets also tended to spread out partially but not completely, thus allowing their structuration with a spread diameter larger than for the ODT and PFDT SAMs.

The tendency of the droplets to remain more stuck on surfaces with low wettability was further proven by fabricating a droplet array on a surface modified with NH_2- and CF_3-terminated SAMs (Figure 1a). Initially, we used FEMTO to generate patterns of AUT consisting of nine dots with diameters of 10 μm spaced 40 μm apart on a gold substrate. The exposed gold regions of the substrate were passivated with PFDT. FEMTO was then used to fabricate a 9×9 array of droplets of the DMSO precursor solution spaced 10 μm apart onto the AUT dot array area. As shown in Figure 1b, the resulting array contained 81 droplets, of which nine matched up the NH_2-terminated dots (as marked by the dashed circles in Figure 1b) and the others were directly patterned on the CF_3-terminated SAM. The diameters of the droplets were estimated to be around 5 and 3 μm for the ones placed on the NH_2- and CF_3-terminated SAMs, respectively. The above results confirm that DMSO precursor droplets spread out more on the NH_2-terminated SAMs than on the nonpolar CF_3-terminated SAMs when patterned using identical conditions (dwell time = 0.001 s, humidity = 35%, room temperature).

HKUST-1 arrays were fabricated by exposure of the patterned droplet arrays on the SAM-modified gold substrates at room temperature for 24 h. Figure 1c shows field-emission SEM (FESEM) images of the HKUST-1 array resulting from the evaporation of the 9×9 DMSO precursor droplet array. Interestingly, well-shaped octahedral crystals of HKUST-1 were grown in the contact areas between all of the FEMTO-delivered droplets and the SAMs. However, all nine droplets placed on the NH_2-terminated dots yielded multiple crystals with edge dimensions ranging from 300 to 750 nm, whereas the remaining droplets placed on the CF_3-terminated SAM yielded single

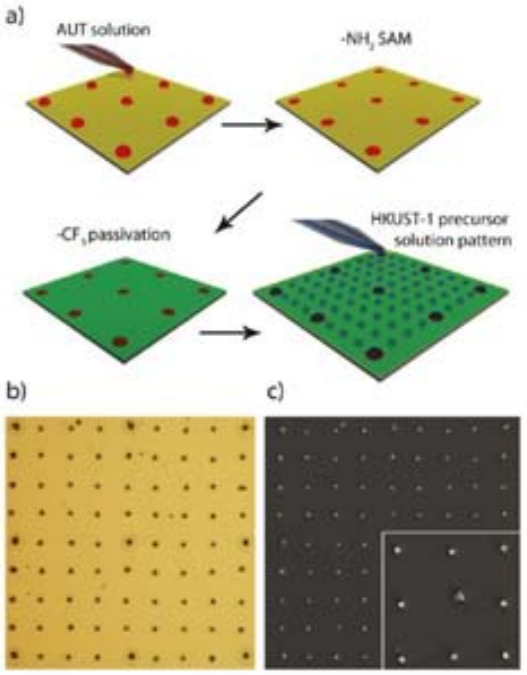

Figure 1. (a) Schematic illustration of the process followed for fabricating the 9×9 droplet array on a gold substrate previously patterned with a 3×3 AUT dot array and passivated with PFDT. (b) Optical microscopy image of the 9×9 droplet array, in which the droplets were spaced apart by 10 μm. Dashed circles mark the nine droplets placed on AUT dots. (c) FESEM image of the resulting HKUST-1 array. The inset shows a magnified area of this array in which the central dot corresponds to multiple HKUST-1 crystals grown in a droplet placed on the AUT SAM and the other eight correspond to single HKUST-1 crystals grown in droplets placed on the PFDT SAM.

HKUST-1 crystals with edge dimensions between 800 nm and 1.2 μm. The terminal group on the top of the SAMs, and therefore, the contact angle between the precursor droplet and the surface were again critical in determining the number and dimensions of the HKUST-1 crystals grown within each droplet, opening up the possibility of creating single-crystal HKUST-1 arrays on surfaces with low wettability. For example, CH_3- and CF_3-terminated SAMs, where the droplets remain stuck, turned out to be ideal for single-crystal growth within each droplet (Figure 2c–f). The average edge dimensions of the single crystals grown within the droplets placed on the ODT and PDFT SAMs were 1.4 ± 0.3 and 0.9 ± 0.2 μm, respectively. As previously observed, identical droplets placed on NH_2-terminated SAMs tended to spread out, resulting in a higher nucleation density and the formation of multiple smaller crystals (edge dimensions 100–400 nm) within each droplet (Figure 2a,b).

To provide further evidence of the formation of HKUST-1 crystals on surfaces using this direct-write pen-type lithographic approach, we first fabricated a 150×150 HKUST-1 array consisting of dots spaced 8 μm apart (total area = 1.2 mm^2) on NH_2- and CF_3-terminated SAM-modified gold substrates (Figure 3a and Figures S4 and S5) and characterized the dots using XRD. The XRD data shown in Figure 3b clearly demonstrate not only the formation of HKUST-1 crystals but also a crystal growth orientation preference along the [111] direction for both the NH_2- and CF_3-terminated SAMs. It is interesting to

dx.doi.org/10.1021/ja2002428 | J. Am. Chem. Soc. 2011, 133, 2144–2147

Journal of the American Chemical Society COMMUNICATION

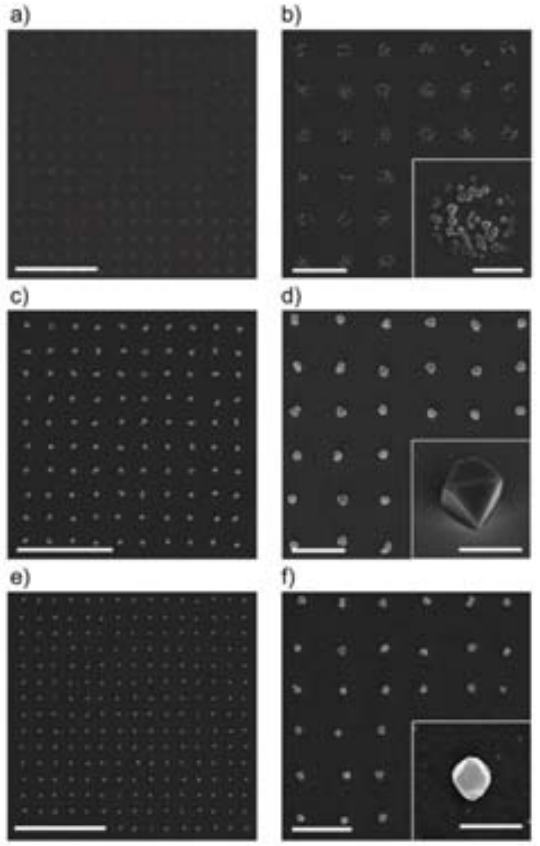

Figure 2. FESEM images of the HKUST-1 arrays fabricated on (a, b) NH_2-, (c, d) CH_3-, and (e, f) CF_3-terminated SAMs on gold substrates. Scale bars represent (a, c, e) 40 μm, (b, d, f) 10 μm, and (insets) 2 μm.

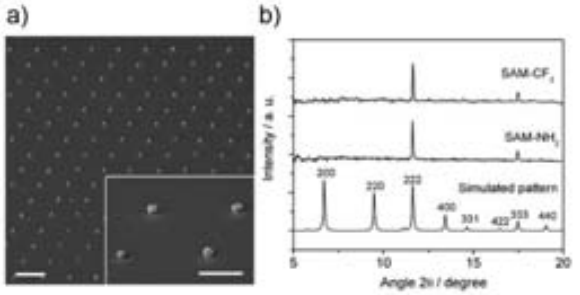

Figure 3. (a) SEM images of a large HKUST-1 array (1.2 mm^2) fabricated on CF_3-terminated SAMs on gold substrates. Scale bars represent 10 and 4 μm for the main and inset images, respectively. (b) XRD patterns (background-corrected) for the HKUST-1 arrays fabricated on the CF_3- and NH_2-terminated SAMs, compared with a simulated XRD pattern for HKUST-1.

note that Wöll and co-workers[7] and Bein and co-workers[16] also observed an identical orientation preference in their crystallization methodologies on OH- and COOH-terminated SAMs, respectively. However, the same authors did not observe crystal growth orientation on hydrophobic SAMs,[14] which was in fact achieved in the HKUST-1 arrays fabricated by the pen-type lithographic technique, as further confirmed by the SEM images (Figure 3a inset).

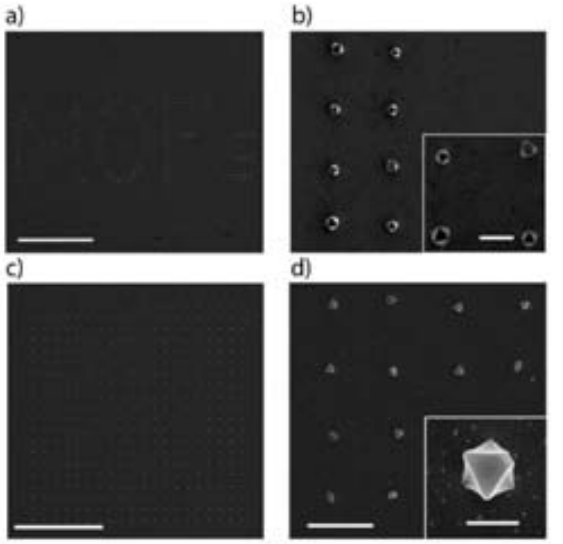

Figure 4. FESEM images of HKUST-1 arrays fabricated on CH_3-terminated SAMs on gold substrates. (a) The word "MOFs" fabricated with HKUST-1 single crystals and (b) a magnification image of the letter "M". (c, d) Single-crystal HKUST-1 array composed of crystals with edge dimensions of 550 ± 100 nm. Scale bars represent (a) 100 μm, (inset of b) 2 μm, (c) 40 μm, (d) 5 μm, and (inset of d) 500 nm.

Miniaturization of the delivered droplets was also essential for the formation of pure HKUST-1 crystals. Consistent with this conclusion, in control experiments, a mixture of H_3btc, $Cu(NO_3)_2 \cdot 2.5H_2O$, and nonoriented HKUST-1 crystals was obtained from the evaporation of large DMSO precursor droplets (droplet diameter ≈ 1 mm) on CF_3-terminated SAMs, as confirmed by optical microscopy, FESEM, and powder XRD (see Figure S6).

This fabrication methodology can also be used to precisely control the location at which a single MOF crystal is grown. For example, 400 single crystals of HKUST-1 were grown on a CH_3-terminated SAM in such a way that the word "MOFs" was formed (Figure 4a,b). In addition, for a certain dwell time, it is well-known that the time plasma treatment of the SPT strongly influences the volume of the droplet placed on a surface. For longer treatments, the surface of the SPT turns more polar, allowing polar liquids to flow better through the microchannels and consequently resulting in the deposition of larger volumes of liquid. On the contrary, when this time treatment is shorter, the volume of the droplet deposited can be reduced. Following this strategy, we fabricated a 20 × 20 single-crystal HKUST-1 array on an ODT SAM using an SPT treated with plasma for 30 s instead of 15 min. As Figure 4c,d shows, the single HKUST-1 crystals grown within each droplet were smaller, showing an average edge dimension of 550 ± 100 nm.

In summary, we have reported a novel, versatile pen-type lithography-based approach for growing HKUST-1 crystals on supports and shown that through the use of surfaces with low wettability it is possible to control the growth of a submicrometer single crystal at a desired location on a surface. Since many functional MOFs have been synthesized, it is likely that this approach can be generalized for controlling the growth of many MOFs at the single-crystal level on several surfaces (see Figure S7). Such capabilities will expand the scope of application for

MOFs in sensors, magnetic and electronic devices, etc., where such control opens new opportunities to integrate them in specific locations of devices. In addition, with our results, one can start to conceive of the generation of combinatorial MOF arrays through delivery of droplets that differ in composition, pH, etc. Once achieved, such parallel fabrication would provide the advantages, for example, of larger libraries for screening the synthesis of novel MOFs.

■ ASSOCIATED CONTENT

Supporting Information. Experimental details and EDX and FESEM images of HKUST-1 arrays on different surfaces. This material is available free of charge via the Internet at http://pubs.acs.org.

■ AUTHOR INFORMATION

Corresponding Author
daniel.maspoch.icn@uab.es

■ ACKNOWLEDGMENT

This work was supported by Projects VALTEC08-2-0003. D.M. and I.I. thank the MICINN for RyC Contracts. C.C. thanks the ICN for a research contract. The authors thank the Servei de Microscopia of the PCB and UAB as well as Pablo García for XRD measurements. We also acknowledge Prof. Laura M. Lechuga for the use of Nano eNabler system.

■ REFERENCES

(1) (a) Kitagawa, S.; Kitaura, R.; Noro, S. i. *Angew. Chem., Int. Ed.* **2004**, *43*, 2334–2375. (b) Férey, G. *Chem. Soc. Rev.* **2008**, *37*, 191–214. (c) Rosi, N. L.; Eddaoudi, M.; Vodak, D. T.; Eckert, J.; O'Keeffe, M.; Yaghi, O. M. *Science* **2003**, *300*, 1127–1129. (d) Czaja, A. U.; Trukhan, N.; Muller, U. *Chem. Soc. Rev.* **2009**, *38*, 1284–1293. (e) Maspoch, D.; Ruiz-Molina, D.; Veciana, J. *Chem. Soc. Rev.* **2007**, *36*, 770–818.

(2) (a) Spokoyny, A. M.; Kim, D.; Sumrein, A.; Mirkin, C. A. *Chem. Soc. Rev.* **2009**, *38*, 1218–1227. (b) Lin, W.; Rieter, W.; Taylor, K. *Angew. Chem., Int. Ed.* **2009**, *48*, 650–658. (c) Carné, A.; Carbonell, C.; Imaz, I.; Maspoch, D. *Chem. Soc. Rev.* **2010**, *40*, 291–305.

(3) (a) Zacher, D.; Shekhah, O.; Wöll, C.; Fischer, R. A. *Chem. Soc. Rev.* **2009**, *38*, 1418–1429. (b) Zacher, D.; Baunemann, A.; Hermes, S.; Fischer, R. A. *J. Mater. Chem.* **2007**, *17*, 2785–2792.

(4) (a) Allendorf, M. D.; Houk, R. J. T.; Andruskiewicz, L.; Talin, A.; Pikarsky, J.; Choulury, A.; Gall, K. A.; Hesketh, P. J. *J. Am. Chem. Soc.* **2008**, *130*, 14404–14405. (b) Li, S.-S.; Bux, H.; Feldhoff, A.; Li, G.-L.; Yang, W.-S.; Caro, J. *Adv. Mater.* **2010**, *22*, 3322–3326. (c) Biemmi, E.; Darga, A.; Stock, N.; Bein, T. *Microporous Mesoporous Mater.* **2008**, *114*, 380–386. (d) Lu, G.; Hupp, J. T. *J. Am. Chem. Soc.* **2010**, *132*, 7832–7833. (e) Cobo, S.; Molnar, G.; Real, J.-A.; Bousseksou, A. *Angew. Chem., Int. Ed.* **2006**, *45*, 5786–5789.

(5) (a) Fan, S.; Chapline, M. G.; Franklin, N. R.; Tombler, T. W.; Cassell, A. M.; Dai, H. *Science* **1999**, *283*, 512–514. (b) Chen, C. S.; Mrksich, M.; Huang, S.; Whitesides, G. M.; Ingber, D. E. *Science* **1997**, *276*, 1425–1428. (c) Sirringhaus, H.; Kawase, T.; Friend, R. H.; Shimoda, T.; Inbasekaran, M.; Wu, W.; Woo, E. P. *Science* **2000**, *290*, 2123–2126. (d) Huang, Y.; Duan, X.; Wei, Q.; Lieber, C. M. *Science* **2001**, *291*, 630–633. (e) Kasemo, B. *Curr. Opin. Solid State Mater. Sci.* **1998**, *3*, 451–459.

(6) Hermes, S.; Schröder, F.; Chelmowski, R.; Wöll, C.; Fischer, R. A. *J. Am. Chem. Soc.* **2005**, *127*, 13744–13745.

(7) Shekhah, O.; Wang, H.; Zacher, D.; Fischer, R.; Wöll, C. *Angew. Chem., Int. Ed.* **2009**, *48*, 5038–5041.

(8) Shekhah, O.; Wang, H.; Paradinas, M.; Ocal, C.; Schupbach, B.; Terfort, A.; Zacher, D.; Fischer, R. A.; Wöll, C. *Nat. Mater.* **2009**, *8*, 481–484.

(9) Li, Y. S.; Liang, F. Y.; Bux, H.; Feldhoff, A.; Yang, W. S.; Caro, J. *Angew. Chem., Int. Ed.* **2010**, *49*, 548–551.

(10) Shekhah, C.; Wang, H.; Kowarik, S.; Schreiber, F.; Paulus, M.; Tolan, M.; Sternemann, C.; Evers, F.; Zacher, D.; Fischer, R. A.; Wöll, C. *J. Am. Chem. Soc.* **2007**, *129*, 15118–15119.

(11) Ameloot, R.; Gobechiya, E.; Uji-i, H.; Martens, J. A.; Hofkens, J.; Alaerts, L.; Sels, B. F.; De Vos, D. E. *Adv. Mater.* **2010**, *22*, 2685–2688.

(12) Vengasandra, S. G.; Lynch, M.; Xu, J.; Henderson, E. *Nanotechnology* **2005**, *16*, 2052–2055.

(13) Piner, R. D.; Zhu, J.; Xu, F.; Hong, S.; Mirkin, C. A. *Science* **1999**, *283*, 661–663.

(14) Reese, M. O.; van Dam, R. M.; Scherer, A.; Quake, S. R. *Genome Res.* **2003**, *13*, 2348–2352.

(15) Chui, S. S.-Y.; Lo, S. M.-F.; Charmant, J. P. H.; Orpen, A. G.; Williams, I. D. *Science* **1999**, *283*, 1148–1150.

(16) Biemi, E.; Scherb, C.; Bein, T. *J. Am. Chem. Soc.* **2007**, *129*, 8054–8055.

(Supporting Information)

Single-Crystal Metal-Organic Framework Arrays

Carlos Carbonell, Inhar Imaz, Daniel Maspoch*

Centre d'Investigació en Nanociència i Nanotecnologia (CIN2, ICN-CSIC),

Campus UAB, 08193 Bellaterra, Spain.

E-mail: daniel.maspoch.icn@uab.es

S1. Materials and Characterization

The reagents $Cu(NO_3)_2 \cdot 2.5H_2O$, trimesic acid, 11-mercapto-1-undecanol (MUOL), 16-mercaptohexadecanoic acid (MHA), 1-aminoundecanethiol (AUT), 1-octadecanethiol (ODT) and 1H,1H,2H,2H-perfluorodecanethiol (PFDT) were obtained from Sigma-Aldrich Co. High purity DMSO was purchased from ROMIL. Polycrystalline Au films were prepared by electronbeam evaporation of 10 nm of Ti on SiOx followed by 40 nm of Au at a rate of 1 $Å \cdot s^{-1}$ and a base pressure of around $1x10^{-7}$ Torr. All patterning experiments were performed using a commercially available Enabler Bioforce System (BioForce, USA). Surface Patterning Tool (SPT, BioForce, USA) were used for patterning. The SPTs were cleaned with plasma for 15 minutes (UV/Ozone ProcleanerTM, BioForce, USA) before their use. Scanning electron microscopy (SEM) images were collected on a SEM (ZEISS EVO MA10) at acceleration voltages of 20 kV and on a Field Emission SEM (Strata DB235, FEI Company) at acceleration voltages of 5-20 kV. The X-ray EDX microanalysis was performed on an Oxford Instruments INCA Energy SEM system, which performs the elemental qualitative and quantitative analyses. XRD measurements were performed with a X'Pert PRO MRD Panalytical diffractometer especially configured for in-plane diffraction.

Figure S2. Energy-dispersive X-ray Spectroscopy (EDX) microanalysis of a HKUST-1 single crystal grown on a CH_3-terminated SAM gold substrate.

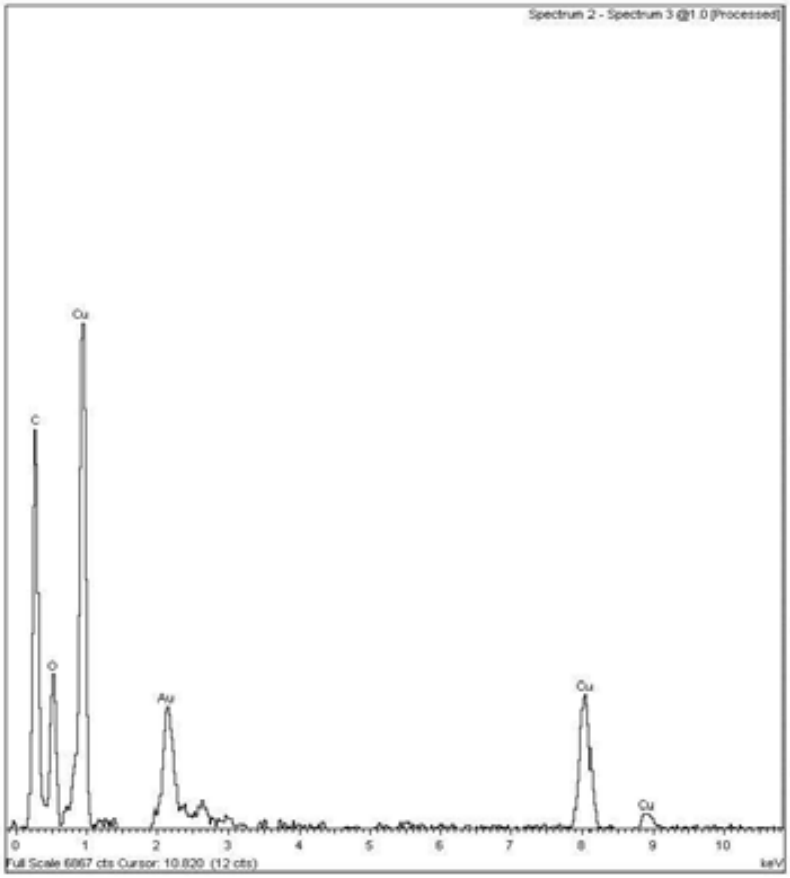

Figure S3. FESEM images of a single-crystal HKUST-1 array fabricated over gold functionalized with CH_3-terminated SAM. Scale bars represent 10 μm (a) and 1 μm (c).

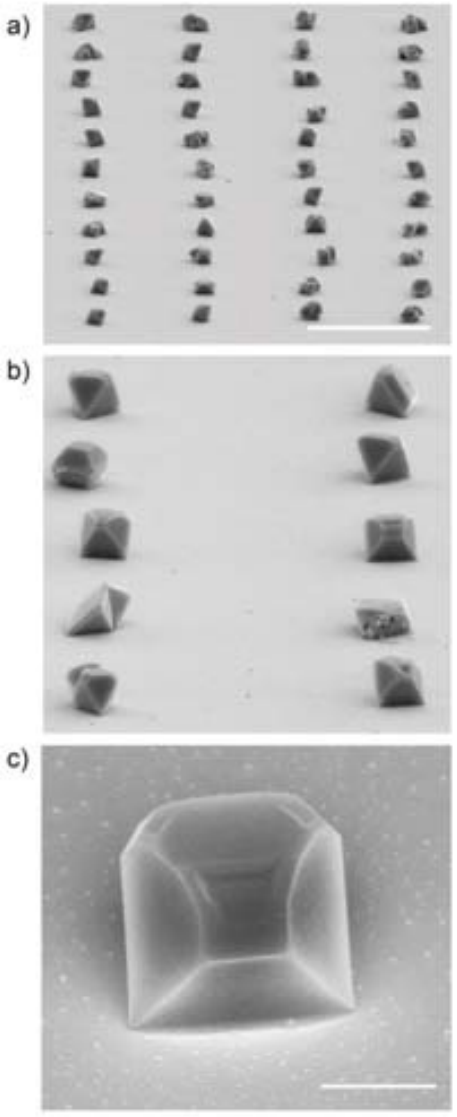

Figure S4. SEM images of the extended HKUST-1 array (150x150 dots, total area = 1.2 mm^2) fabricated on a CF_3-terminated SAM. Scale bars represent 40 μm (a), 8 μm (b) and 4 μm (c).

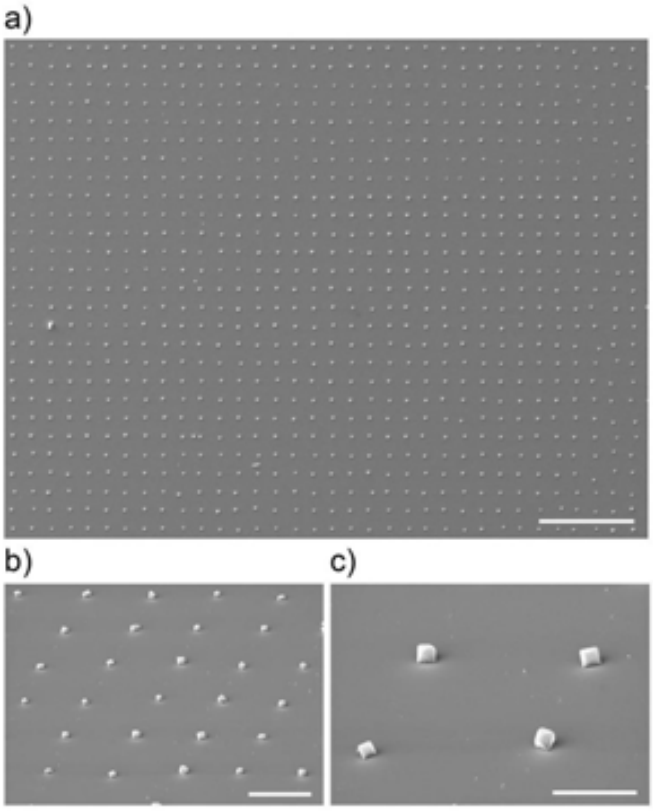

Figure S5. SEM images of the extended HKUST-1 array (150x150 dots, total area = 1.2 mm^2) fabricated on a NH_2-terminated SAM. Scale bars represent 10 μm (a) and 4 μm (c).

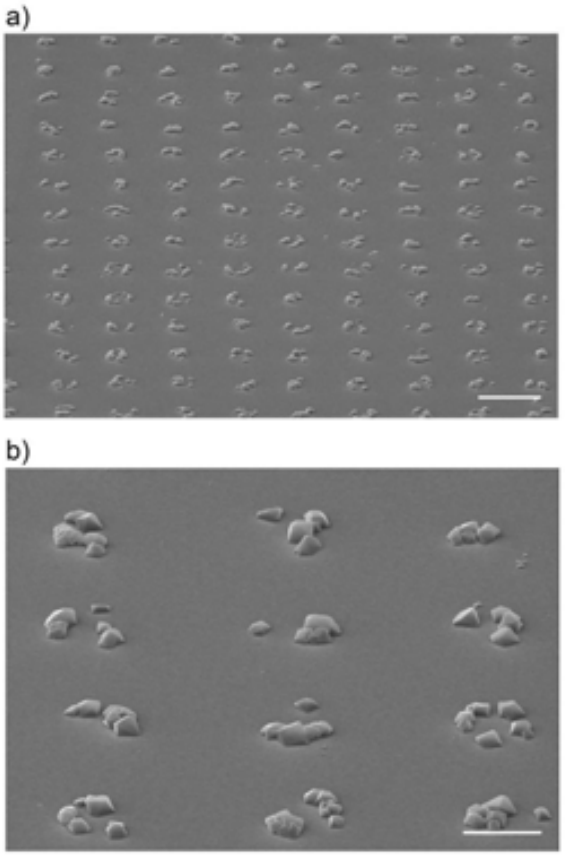

Figure S6. Control experiments performed on large DMSO precursor droplets on CF_3-terminated SAMs. (a) Optical microscope image of one of these droplets after DMSO evaporation. (b) FESEM image showing the precursor crystals. (c) FESEM image showing the HKUST-1 crystals. Note the presence of crystals with different orientation. (d) XRPD data.

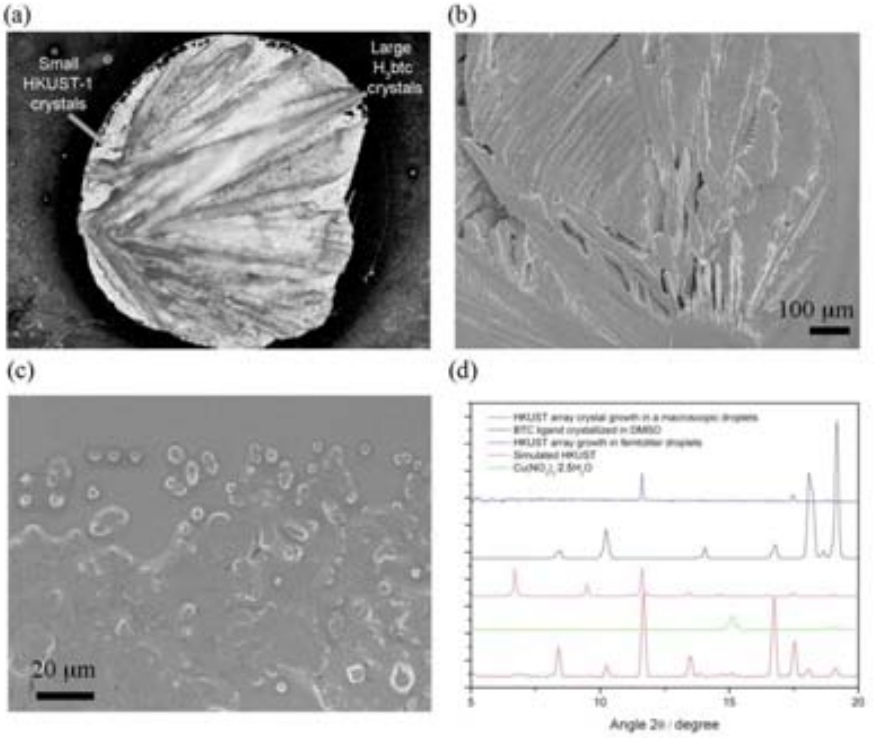

Figure S7. FESEM images of an HKUST-1 array fabricated on glass previously functionalized with a NH_2-terminated silane SAM. Scale bars represent 10 μm (a,b), 5 μm (c) and 1 μm (d).

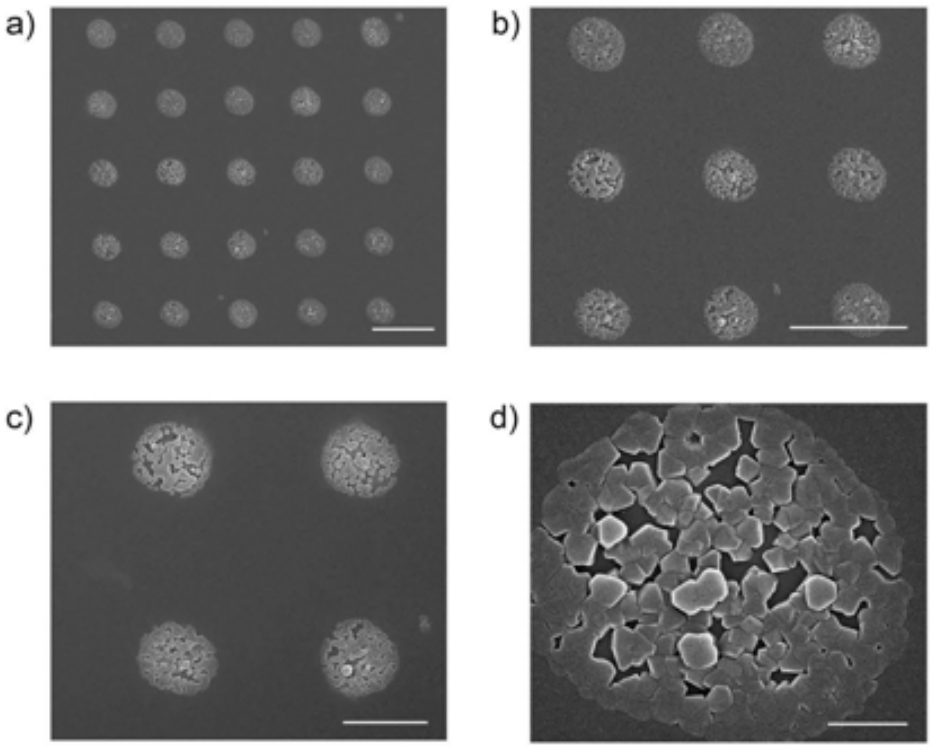

Chapter 4.
Femtolitre Chemistry assisted by Microfluidic-Pen Lithography for the Combinatorial Synthesis and Positioning of MOFs

In this chapter we introduce a new and versatile approach that will allow us to perform combinatorial chemistry in the femtolitre regime, from the biological or basic chemical approach to the complex coordination NMOFs synthesis, always under high precision location control.

1. Femtolitre chemistry

The ability to carry out chemical reactions at volumes from femtolitres (10^{-15} litres) to attolitres (10^{-18} litres) offers a wide variety of research opportunities in biology, chemistry, pharmacy or materials science. There are many advantages of working at this scale.

Femtoliter is the range of single cells and organelles volume; the study of the reactions of cellular biochemistry will be more accurate and realistic in this volume. It is of vital importance a detailed knowledge of the reactions that take place inside the cells, inside organelles and between them. Obtaining information about reaction kinetics of the biochemistry that take place inside the cell is crucial to our understanding of cellular function and dysfunction.[1-3]

It is also the scale where mixing rate of reagents occurs faster than reaction rate.[4] To measure the rate of reaction between two chemical species, they must to be mixed much faster than the reaction rate – otherwise, only the mixing rate is observed. Rapid enough mixing is difficult, especially for the many important liquid-phase and biological reactions with millisecond or shorter-time-scale dynamics. Two reactants in a quiescent liquid mix by diffusion with a timescale: $\tau = L2/D$, where L is the length over which diffusion must take place and D is the diffusion coefficient. With typical values of D being 10^{-9} seconds or less for large molecules, mixing by diffusion is slow. When L is reduced to micrometers, diffusive mixing times can be reduced to less than 10 μs without the necessity to induce turbulence. This phenomenon is also important to obtain highly homogenous micro- nanostructures, which represents another clear advantage for femtolitre chemistry.

Working with these volumes is also interesting because implies an environmental and economic optimization. If one expects to screen the reaction of a reagent with a library of thousands of other reagents and thousands of proportions, is better to be able to miniaturise the lab, otherwise, thinking on beakers or mL vials, it would be necessary a huge space to perform so many reactions. This problem was addressed with the invention of microarray technologies which are based on the combinatorial chemistry of picoliter droplets, mainly delivered through inkjet printers or robotics. This technic has been mainly used in genomics where robotic machines arrange minuscule amounts (tipically pico- to nanoliters) of hundreds or thousands of gene sequences on a single microscope slide. According to the National Human Genome Research Institute, in 2011 there was a database of 40000 gene sequences that researchers could use for this purpose. Microarray

technologies are still in an order of magnitude over the femtoliter scale. New technologies become necessary to reduce the size of micro to submicro and nanoarrays.

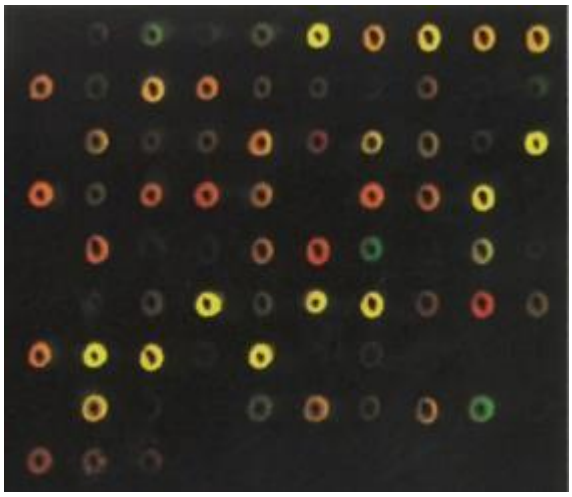

Figure 1. Example of microarray data. Microarray analysis can be performed to assess differences in gene expression between two different samples. After isolating nucleic acids from the two samples, one sample is labeled with a dye that fluoresces green, and the other sample is labeled with a dye that fluoresces red. The samples are combined in equal amounts and hybridized to the array. Each spot on a microarray contains a specific gene sequence. When the array is scanned, green or red spots indicate expression of the gene in only one sample, and yellow spots indicate expression of the gene in both samples. Adapted from ref 5.

But not everything are advantages, of course, there are also many difficulties of working at the femtoliter scale; droplets in ambient conditions practically evaporate instantaneously and there are not many tools to manipulate these volumes among others.

At these ultrasmall dimensions, control over chemical reactions has been achieved by two main approaches: (i) micromachining techniques, mainly microfluidics and femtoliter wells[6-9], and (ii) self-enclosed volume elements, including vesicles, micelles and droplets stabilized in an immiscible solvent[10-15].

As introduced in Chapter 1, MOFs are the ultimate designer materials. The number of synthesized MOFs has been increasing exponentially and given the large number of possible linkers and metal nodes and the various ways of combining them, the number of possible MOF structures is essentially limitless. This fact presents exciting opportunities, but it also imply a huge challenge. To address this challenge will be necessary two major supplementary tools: (i) High Throughput Computational screening to identify the potential candidates for a given structure-

property under investigation and (ii) High Throughput Combinatorial Screening of the candidate precursors to form the expected MOF with the desired property.

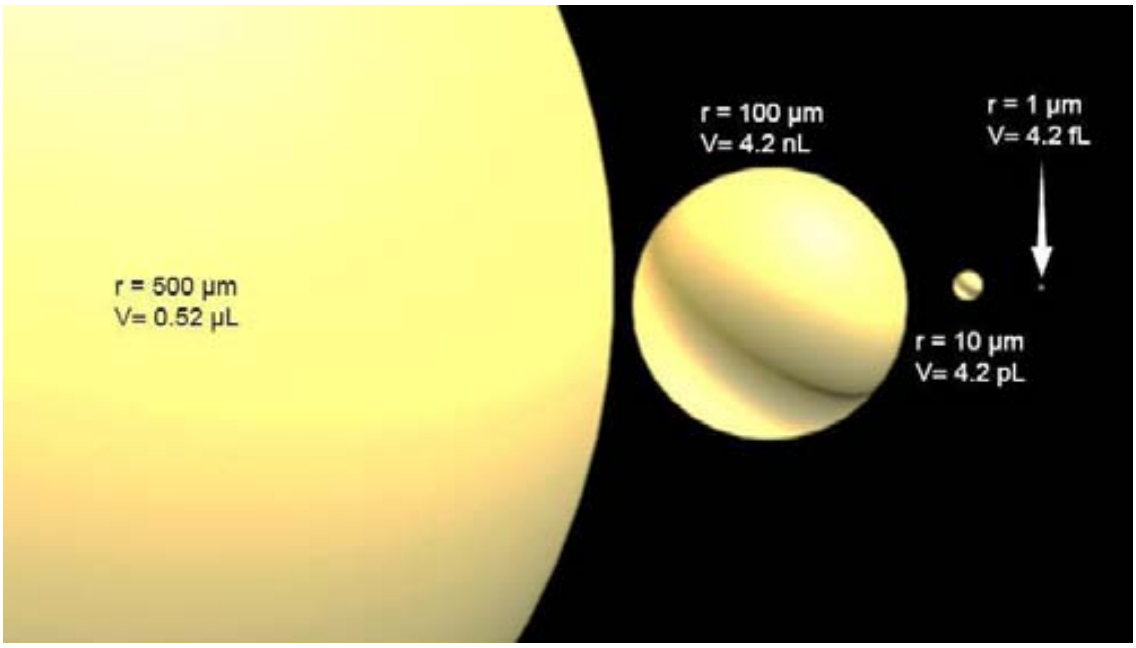

Figure 1 An increase of one order of magnitude in radius, is translated to 3 orders of magnitude in volume; scale representation of spheres from 1 µm to 500 µm radius, resulting from fL to µL volumes, respectively. The volume relationship between Sun and Earth is equivalent to the 1 µm radius sphere compared with the 100 µm one.

Although many efforts have been done for the computational high throughput screening of MOFs,[16-26] the use of High-Throughput methods in MOFs screening remains relatively unexplored. The first massive High-Throughput investigation of MOFs was performed by Yaghi et al.[17] Twenty five different ZIF crystals were synthesized from 9600 microreactions. 100 combination on 96-well plate as the reaction vessel and 0.3 mL reactant volume per well. The mixtures were prepared with a robotic programmed liquid handler and analised in a High Throughput PXRD machine. This nice job clearly shows the technological needs for a so complex task. Bein et al. investigated some synthetic parameters for the obtantion of MOF-5 and HKUST-1 in a self-made 24 cavities reactor block with a maximum volume of 3.4 mL per cavity.[27]

Nevertheless combinatorial chemistry is not exclusive for screening purposes but also can be very useful in patterning products of reactions. Femtoliter combinatorial chemistry with high precission positioning expands the scope of the possibilities described in chapter 3 where the mother solution containing both precursors was delivered on a desired place of a surface. If we can incorporate subsequent reagents or aditives to a prepatterned solution, would offer a significant increase on the variability of possible MOFs able to be micro-nanopatterned.

2. Our Results

The objective of our investigation is to expand the scope of the method presented in the Chapter 3 for structuring MOFs in surfaces. To achieve this, we propose the introduction of one step in the procedure to add femtoliter volume of reagents into selected, pre-delivered femtolitre droplets, also containing reagents, on a surface. This straightforward two-step Microfluidic Pen Lithography (MPL) process –Step #1: reagent A femtoliter droplet generation, and Step #2: reagent B femtoliter volume delivery addition (Figure 3.) will allow us to structure different MOFs on surfaces, but also opens a new avenue in general femtoliter chemistry and high throughput analysis. MPL overcomes the high-throughput limitations of vesicles and micelles and avoids the usually expensive step of fabricating microdevices and wells: it is capable to handle and mix femtoliter volumes with high registration accuracy over centimetre-scale regions, and use each mixture droplet to conduct an independent reaction. Keeping this in mind, we first studied the capabilities of the single writing (step #1) and mixing (step #2) using confocal microscopy study of fluorescent type samples. Once controlled each step, we reproducibly performed two control reactions - acid-base and enzymatic recognition. Demonstrating the versatility of the methodology, we finally performed the combinatorial synthesis of MOFs and NMOFs through careful selection of lithography conditions. We crystallized different desired MOFs into side-by-side patterned mixture droplets, thus creating combinatorial arrays, and we used this method to screen combinatorial reactions to rapidly evaluate the crystallization of novel peptide-based coordination networks. We believe that our method opens new avenues for rapid screening combinatorial reactions using very small amounts of usually costly reagents, and should be adopted by researchers as a desktop tool to synthesize and crystallize materials at desired locations on surfaces, fabricate arrays and study reactions at the femtoliter scale.

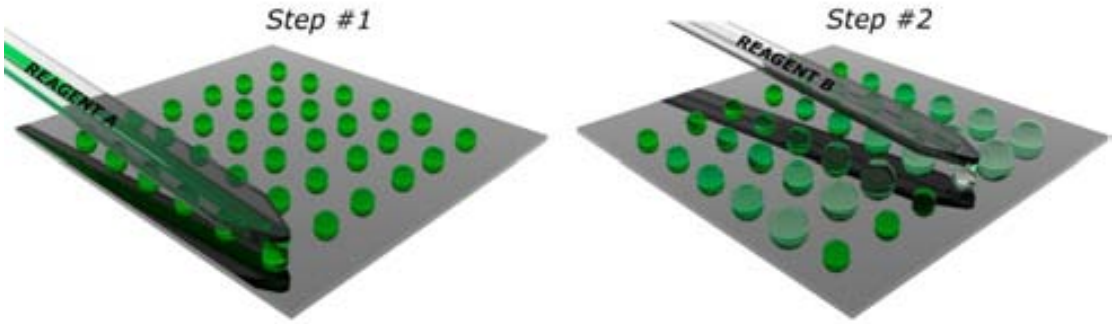

Figure 3. Scheme of the MPL process showing the reagent A femtoliter droplet generation (left) followed by the reagent B femtoliter volume addition (right).

2.1. MPL process

2.1.1. Writing Tools

We have previously demonstrated that conventional pen lithography technologies and tools, commonly used for molecular and material printing, and commercially available for many researchers, allow us to attain excellent conditions for structuring MOFs on surfaces. In this study, we have used Microfluidic pens (BioForce, USA; see Figure 4b) which offer high levels of uniformity and reproducibility on the deposition of femtoliter volumes combined with Dip-Pen Nanolithography (DPN) instrument (NLP-2000 platform, NanoInk Inc., USA) (see Figure 4a), which is equipped with a 5-axis stage system and commercial lithography software, offering ± 75 nm z precision and ± 25 nm positional precision over areas as large as square centimetre. This high accuracy enables the programmable positioning of microfluidic pens on top of selected, pre-patterned femtoliter droplets followed by their precise approach until reaching their contact surface area. Finally, an environmental humidity chamber included in the lithographic platform enables the realization of such reactions under controlled humidity or organic solvent vapour levels, and reduces droplet evaporation rate; a process that must be controlled in order to deliver the second reagent into the patterned droplets before they evaporate, and to give the reagents enough time to mix, react and crystallize.

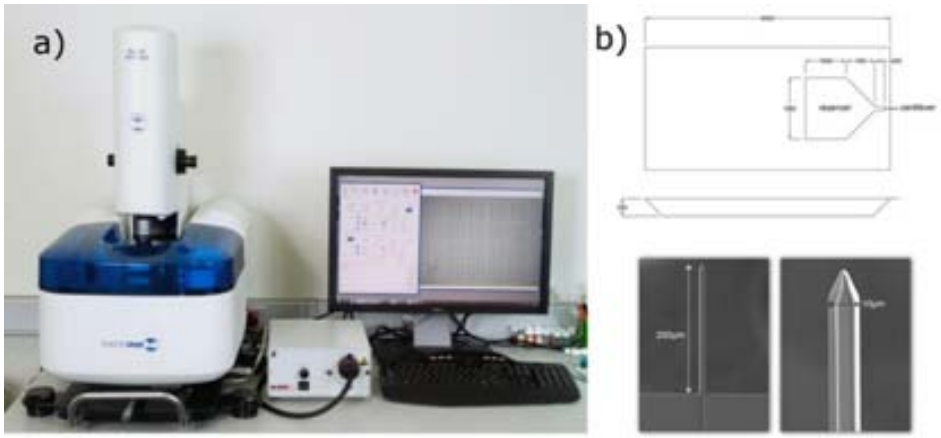

Figure 4 (a) NLP Dip-Pen Nanolithographic platform. **(b)** SPT scheme with some dimensions (up) and SEM images of the cantilever pen detail of one SPT (down)

2.1.2. Control of the Single Writing Process

In a first step, it will be necessary to determine certain control parameters for both, single and double writing approaches. These parameters are: the relationship between the dwell time (DT) with the volume of the delivered droplets, the writing reproducibility along one array and our capability to control premature evaporation. For this purpose we will create femtolitre droplet arrays of a sodium fluorescein (SoF) solution onto a SiO_2 surface and studied them by confocal microscopy.

The relationship between droplet volume and dwell time has to be determined in order to calibrate the delivered volume in function of the applied contact time which is the only parameter that we can control. The confocal microscopy study of the resulting arrays will give us also an idea of the writing homogeneity, stability and integrity of the arrays after a certain time.

2.1.2.1. Preparation of the array

Different Water, DMSO, DMF, EtOH, MeOH solutions prepared with different concentrations of SoF were prepared to test the writing viability. Every one of this solutions presented fast and incontrollable evaporation under ambient conditions. MeOH, EtOH and Water were evaporated already in the reservoir of the SPT even before mounting it into the instrument holder. DMF and DMSO solutions presented slower evaporation rates, but higher than the needed to achieve controllable patterning, manifested through the observation of condensed microdroplets in the substrate when the SPT was approached to the surface, making impossible to perform a delimited deposition of a droplet. Two different strategies were followed to overcome this evaporation problem: addition of some proportion of high boiling point solvents (mainly glycerol) and increasing the environmental relative humidity.

One array with different dwell times was prepared to evaluate both the DT-volume relationship and the reproducibility and premature evaporation, given by the DT-Mean Fluorescence Intensity. The standard supports used are Si/SiO_2 substrates which were subsequently sonicated for 10 min. in acetonitrile, ethanol and MilliQ water and dried with nitrogen gas flow. The microfluidic pen or SPT (SPT-10, Bioforce, USA) was cleaned in piranha solution (3:1 v/v solution of H_2SO_4 and 30 % H_2O_2) for 20 min., rinsed with MilliQ water and dried with slight N2 gas flow. **Caution: piranha solution is a strong acid and oxidizer and should be handled with extreme care.** Afterwards, the pen was introduced in an UV/ozone chamber (UV/Ozone Cleaner, Bioforce Inc., USA) for 20 min. The microfluidic pen was then loaded with 1.5 μl of a 0.01 M DMSO/glycerol (1:1 v/v) solution of NaF, and mounted onto the lithographic platform (NLP 2000, NanoInk

Inc, USA) at an acute angle of 10º. The instrument was programmed to pattern an array of 8 x 9 droplets (droplet separation = 28 μm), at DT1= 0.001, 0.1, 0.5, 1, 2, 3, 5 and 10 s (hereafter DT1: dwell time used in step #1) under a relative humidity of 60 % and at room temperature.

The resulting array were then characterized (Figure 5) by confocal fluorescence microscopy (Leica TCS SP5; see Figure 4.5.). The fluorescence images (310 × 310 μm^2) were registered in reflection mode, with a 50x objective (magnification = 0.15 μm/pixel) and at different heights by scanning in z-direction. Stacks comprising 30 fluorescence microscopy image slices (excitation wavelength (λexc) = 488 nm; emission wavelength (λem) = 500-575 nm) at different heights (Δz = 0.42 μm) were collected for each array.

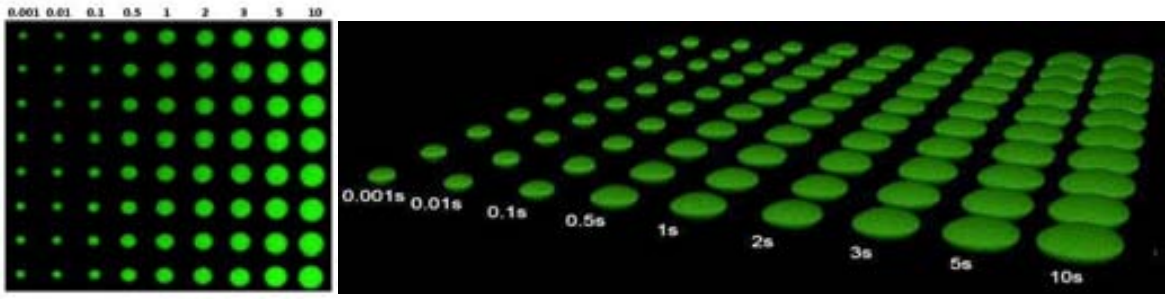

Figure 5 Confocal fluorescence microscopy image (λ_{exc} = 488 nm; λ_{det} = 500-575 nm) of the NaF droplet array (droplet distance = 28 μm) resulting from adding up all 30 collected fluorescence image slices. On the right, 3D reconstruction of the array using ImageJ software.

2.1.2.2. Determination of Dwell Time (DT1) *vs.* Volume relationship

The average contact diameter (d_1) was determined for each column of droplets patterned with the same contact time. Taking into account that contact angle values should be smaller than 90º we considered the top viewed diameter to be equal to the contact diameter. So, to determine d_1 values of each NaF droplet, the 30 confocal microscopy image slices were added up (Figure 6b), and a threshold was selected to define its contour in order to calculate area and diameter. All d_1 values determined from this threshold image were in fully agreement with those determined from the corresponding measured with optical microscopy (Figure 6c).

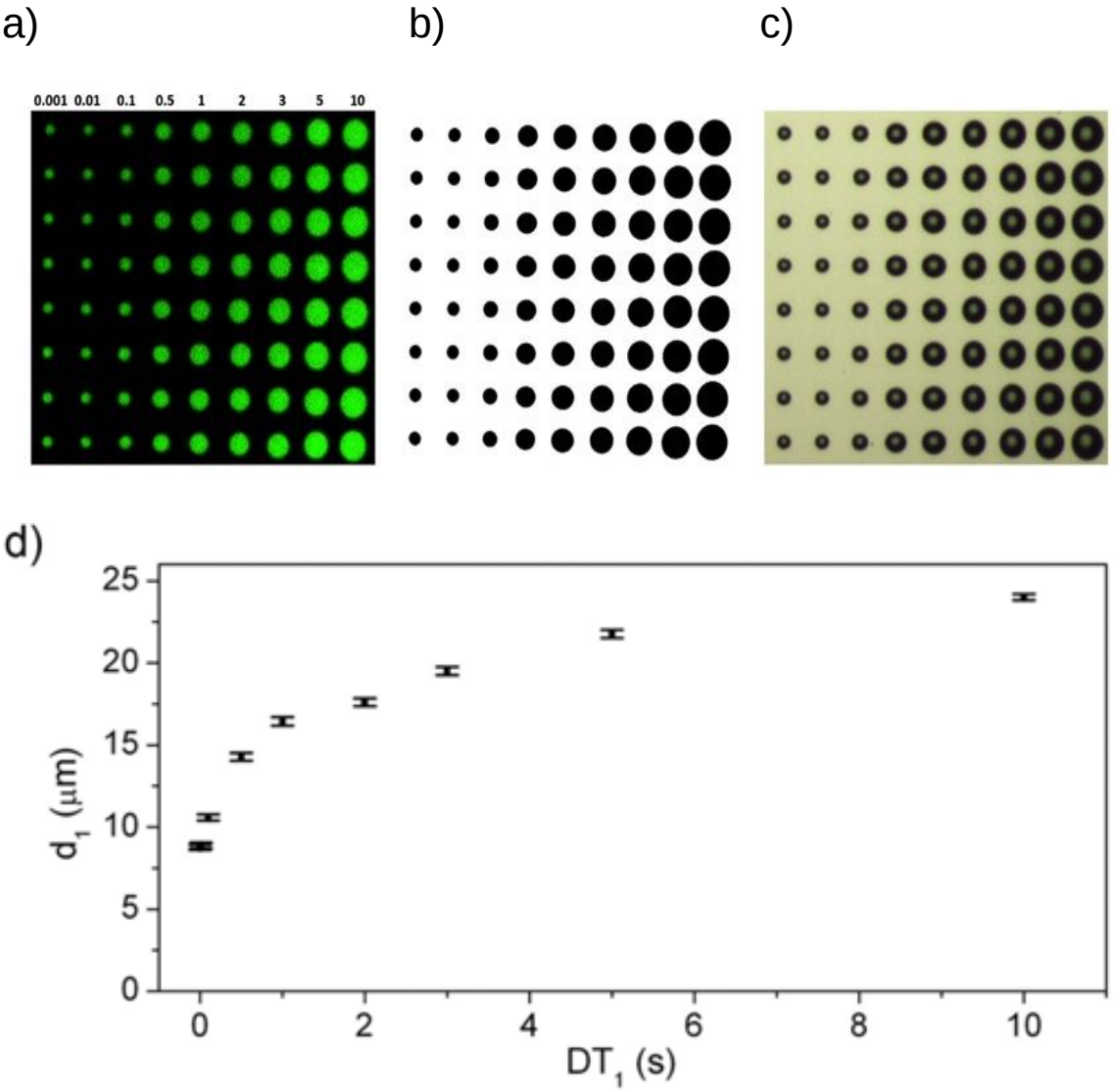

***Figure 6*. (a)** Confocal fluorescence microscopy image (λ_{exc} = 488 nm; λ_{det} = 500-575 nm) of the NaF droplet array (droplet distance = 28 µm) resulting from adding up all 30 collected fluorescence image slices. **(b)** Inverted image after filtering **a** using a background threshold. **c**, Corresponding optical microscopy image of the NaF droplet array.

As mentioned in chapter 3, we assume that droplets delivered on a surface can be considered as a sessile droplet having spherical cap geometry, one can then express their volume as:

$$V = \frac{\pi \cdot {r_b}^3}{3} \cdot \frac{2 - 3\cos\vartheta + \cos^3\vartheta}{\sin^3\vartheta} \quad (\textbf{\textit{Equation 1}})$$

where θ is the contact angle in degrees, and r_b is the contact radius in µm. This equation can be expressed in function of the height of the droplet instead of contact angle:

$$V = \frac{\pi \cdot h}{6} \cdot (3 \cdot {r_b}^2 + h^2) \qquad (\textbf{\textit{Equation 2}})$$

As we see in Equations 1 and 2, to determine the volume of a spherical cap geometry is necessary to know either the height and contact radius or the contact angle and contact radius. The contact angle θ was measured with a contact angle analyzer [Easy Drop Standard (Krüss, Germany)] depositing a 0.1 μL droplet of 0.01M NaF (in DMSO/glycerol, 1:1 v/v) on a SiO_2 surface giving a value of

$$\theta = 34.6 \pm 0.3$$

Following Equation 1, the estimated average volumes of the droplets forming each column for the measured macroscopic contact angle **34.6 ± 0.3º** are reported in the next table 1.:

DT_1 (s)	**d_1 (μm)**	**V_1 (fl)**
0.001	8.8 ± 0.2	43 ± 2
0.01	8.9 ± 0.2	44 ± 2
0.1	10.6 ± 0.2	75 ± 4
0.5	14.3 ± 0.2	184 ± 9
1	16.4 ± 0.3	281 ± 13
2	17.6 ± 0.2	345 ± 14
3	19.5 ± 0.2	470 ± 18
5	21.8 ± 0.3	652 ± 22
10	24.0 ± 0.1	873 ± 21

Table 1. Estimated Volumes calculated from the measured diameter and the calculated contact angle.

2.1.2.3. Dwell Time (DT1) – Mean Fluorescence Intensity relationship

During lithography, the solution present in the reservoir and cantilever could evaporate; this would cause an increase of the solute concentration in the solution. Besides, the surface to volume ratio of the liquid along the microchannel is much bigger than the reservoir, which would mean that variable writing rate will cause different concentration on droplets. Quantifying the fluorescence intensity of the droplets will allow us to determine any significant variation on the relative concentration of the droplets. The major evaporation problem, off course will occur once the droplets are patterned, but is expected to happen on the same way to the equivalent droplets. Thus, knowing the initial conditions (initial contact radius and

contact angle) we could determine the initial volume and so, the amount of dissolved solute that, when doing femtolitre chemistry, will be directly proportional to the amount of reagent.

The average of the fluorescence mean intensity per surface area (I/A, arbitrary units, a.u.) was measured for each droplet series patterned at a different DT_1. To determine the fluorescence mean intensity of each single droplet, the image slice in each z-stack corresponding to the droplet volume in contact with the surface was further analyzed. The exact location of such image slice within the z-stack was determined from the maximum background intensity.[28] It was observed that the maximum background intensity was different for different areas of the substrate, giving us information about the planarity degree of the surface. The I/A was then determined for every droplet in the image after subtracting the background signal of its surrounding area. The results obtained in this way were averaged over the droplets in the array delivered at equal DT_1 (Figure 7) The patterned droplets trend to an ultrafast evaporation due to its high surface to volume ratio. In order to overcome this problem it is necessary to equilibrate the vapor pressure by increasing the environmental vapor pressure.

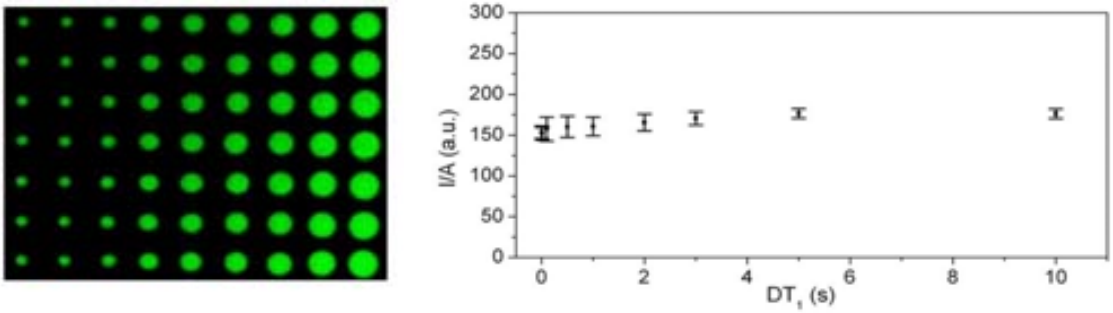

Figure 7. Confocal microscopy image of the mixture NaF/H_2O-glycerol droplet array resulting from adding up the 30 collected fluorescence image slices. **b**, Inverted image after filtering **a** using a background threshold. **c,** 3D reconstruction of the array from all the images data.

Significantly, less than 6 % deviation in I/A between droplet series was observed (Figure 7) once protected from fast evaporation.

2.1.3. Control of the Double Writing Process

First of all we studied the phenomena that comes to one's mind when propose to use a pen to deliver a certain volume into a pre-delivered droplet is the contamination of the pen with the liquid present in the droplet.

2.1.3.1. Preparation of the mixed array

To demonstrate the ability of controlling the deposition of a second femtoliter volume on top of the pre-patterned droplets (step #2), we delivered femtoliter volumes of a H_2O/glycerol (1:1) mixtures into pre-patterned H_2O/glycerol (1:1) droplets of NaF solution (d_1 = 9.4 ± 0.1 μm). The second liquid, H_2O/glycerol solution, was delivered at dwell times (hereafter DT_2: dwell time used in step #2) DT_2 = 0.001, 0.1, 0.5, 1.5, 2, 4, 6 and 8 seconds, starting from the second row (Figure 8) at 50 % humidity, forming an array of mixture droplets with diameters (d_2) from 10.5 ± 0.1 to 19.7 ± 0.4 μm, respectively. Figure 8a shows that the delivered volume increased with increasing DT_2.

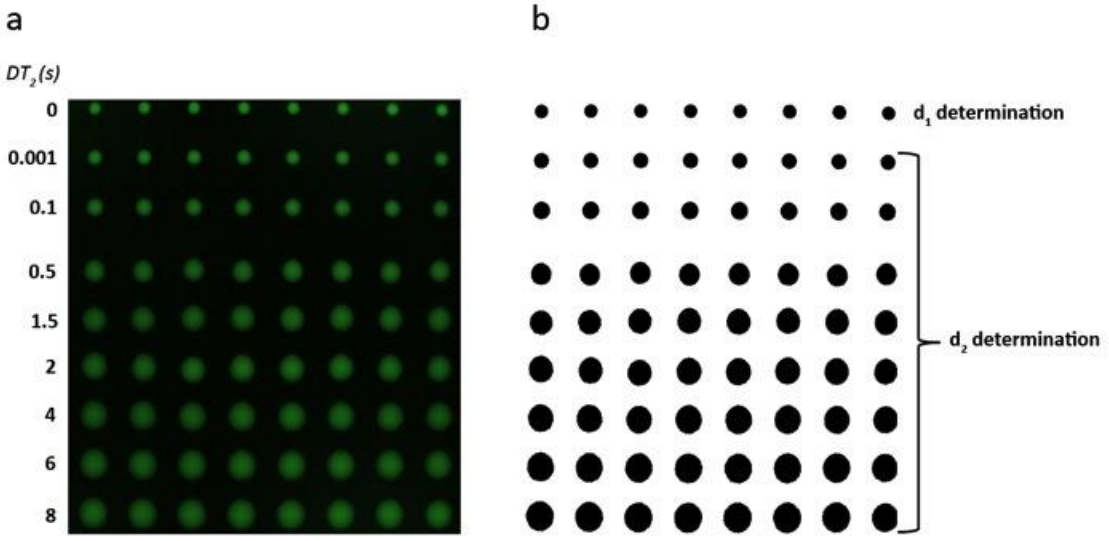

Figure 8. (a) Confocal microscopy image of the mixture NaF/H_2O-glycerol droplet array resulting from adding up the 30 collected fluorescence image slices. The first row, corresponds to the initial deposition without any addition of H_2O/Gly (DT_2=0 s) and with the initial diameter (d_1=9.4 ± 0.1 μm.) equal for all the droplets of the initial array. **(b)** Inverted image after filtering using a background threshold

The same procedure than the one explained in previous section was used to measure the fluorescence images, registered in reflection mode, with a 50x objective and at different heights (typically, 30 images for each z-stack, Δz = 0.42 μm). The corresponding threshold image was used to determine the d_1 (d_1 = 9.4 ± 0.1; 1st row) and d_2 values (from 2nd to 9th rows). From these values, the corresponding dilution

factors were calculated as: $V_2/V_1 = d_2^3/d_1^3$, considering that the θ of the pre-patterned NaF droplets (in H_2O/glycerol, 1:1 v/v) and the mixture droplets resulting from adding different volumes of a H_2O/glycerol (1:1 v/v) mixture do not change.

Dilution factor calculation:

Volum from DT_1 and DT_2;

$$V_1 = \frac{\pi \cdot r_1^3}{3} \cdot \frac{2 - 3\cos\vartheta + \cos^3\vartheta}{\sin^3\vartheta}$$

$$V_2 = \frac{\pi \cdot r_2^3}{3} \cdot \frac{2 - 3\cos\vartheta + \cos^3\vartheta}{\sin^3\vartheta}$$

Dilution Factor;

$$V_1/V_2 = \frac{\frac{\pi \cdot r_1^3}{3} \cdot \frac{2-3\cos\vartheta+\cos^3\vartheta}{\sin^3\vartheta}}{\frac{\pi \cdot r_2^3}{3} \cdot \frac{2-3\cos\vartheta+\cos^3\vartheta}{\sin^3\vartheta}}$$

Asuming $\theta_1 = \theta_2$;

$$V_1/V_2 = r_1^3/r_2^3 \rightarrow V_1/V_2 = d_1^3/d_2^3$$

DT_2 (s)	d_2(μm)	d_2^3/d_1^3
0.001	10.5 ± 0.1	1.4 ± 0.2
0.1	11.9 ± 0.1	2.0 ± 0.2
0.5	14.6 ± 0.2	3.8 ± 0.3
1.5	16.4 ± 0.5	5.4 ± 0.5
2	17.3 ± 0.5	6.3 ± 0.5
4	18.2 ± 0.5	7.3 ± 0.5
6	19.1 ± 0.4	8.5 ± 0.4
8	19.7 ± 0.4	9.2 ± 0.4

Table 2.

One important factor contributing to this ratio is cross-contamination, which affect the homogeneous mixing between mixture droplets. To evaluate the cross-contamination effect, an array of 1 × 8 droplets (droplet separation=35 μm) of 0.03 mM SoF (in H2O/glycerol, 1:1 v/v) was first patterned on a SiO2 surface at DT1=0.001 s at room temperature under a RH of 45%. Then, femtolitre volumes of an H2O/glycerol (1:1) mixture were delivered into the pre-patterned SoF droplets using a second microfluidic pen at DT2=0.001, 0.01, 0.1, 1, 3, 5, 8 and 10 s. In this case, after each one of these eight deliveries, eight consecutive droplets (droplet separation=35 μm) of the H2O/glycerol (1:1) mixture were patterned at a DT=2 s. (Figure 4.9. a) I/A was detected in the first three droplets for all cases: the average intensity values (relative to the initial SoF intensity) were ca. 6.0% (1st droplet), 2.8% (2nd droplet) and 1.2% (3rd droplet). 4^{th} droplet presented an intensity similar to the background in all the cases. Based on these values, we decided to introduce a cleaning step to prevent cross-contamination and ensure unadulterated reagent mixing. In the cleaning step, a few droplets are patterned outside the working area (that is, on a different surface) between each round of reagent delivery on top of the pre-patterned droplets. See Figure 9.

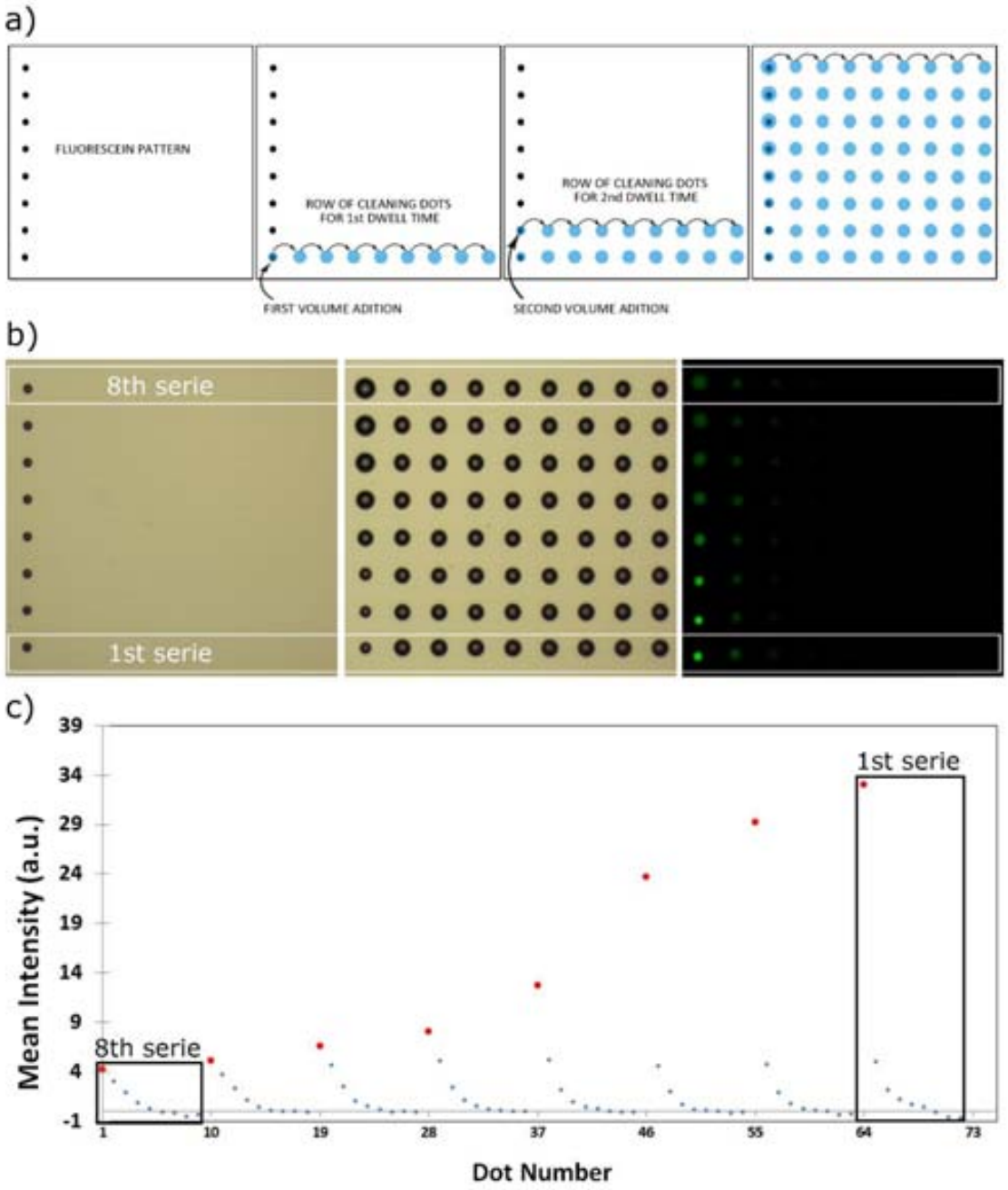

Figure 9. (a) Schematic illustration of the stepwise patterning of the array fabricated to ascertain any possible cross-contamination in the MPL method. (b) Optical microscopy image of the initial SoF droplet array (left) and the final array (middle) after the delivery of an H2O/glycerol (1:1) mixture into the pre-patterned droplets of SoF and the generation of the cleaning droplets. Confocal microscopy image of the resulting droplet array (right). (c) Mean intensity of every serie corresponding to every different DT_2 showing the similar values obtained for the cleaning droplets. Note that from the 4^{th} cleaning droplet, values are close to 0 in all cases.

Another confirmation, of the mixing capabilities results from analysing the confocal data: when DT_2 is increased, the NaF concentration into each mixture droplet, and therefore, I/A_N decrease according to the volumes of H_2O/glycerol added, following the expected behavior of a bulk NaF progressive dilution assuming that the decrease in fluorescence intensity is only due to dilution. (Figure 10b)

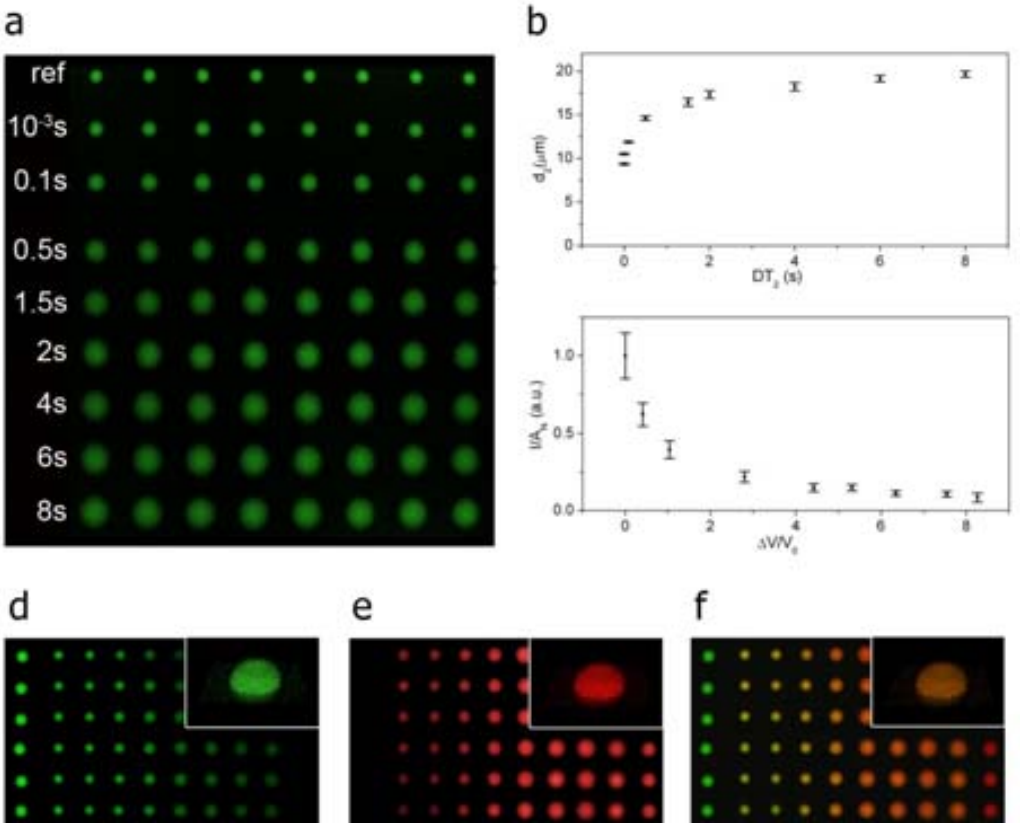

Figure 10. (a) Confocal fluorescence microscopy image of an array of NaF droplets (droplet distance = 35 μm), in which femtoliter volumes of a H_2O/glycerol solution were mixed by using different DT_2. Note that the top row correspond to bare NaF droplets without any addition. **(b)** DT_2 dependence of d_2. **(c)** Dilution factor dependence of I/A_N. Line represents the expected behavior of a bulk NaF solution assuming that the decrease in fluorescence intensity is only due to dilution. **(d-f)** Confocal fluorescence microscopy images (**d**, λ_{exc} = 488 nm; λ_{det} = 500-575 nm; **e**, λ_{exc} = 633 nm; λ_{em} = 600-785 nm; **f**, superimposed previous images) of an array of NaF droplets (droplet separation = 28 μm), in which femtoliter volumes of a solution of Nile Blue were mixed by using different DT_2. Note that left and right columns correspond to pure NaF and Nile Blue droplets, respectively, whereas the gradient of colors from yellow/orange to red (left to right) denotes the increase concentration of Nile Blue in comparison with NaF. In **b,c** error bars stand for the standard deviation of the average results obtained for different equivalent droplets in the array.

This dependence was reproducibly performed (see Figure 11.), demonstrating that DT_2 can effectively be used to control the ratio of reagents into the mixture droplets. As a further verification of the delivery capabilities of MPL and homogeneous mixing of solutions into each mixture droplet, we delivered a solution of Nile Blue at different DT_2 into pre-patterned NaF droplets and visualized their fluorescence signal co-localization (Figure 10 d-f).

Measured I/A values were subsequently normalized with respect to the maximum I/A of the non-diluted NaF droplets (i.e. droplets of the first row). Finally, the normalized emission intensities were plotted against the DT_2 and the dilution factor (Figure 11.)

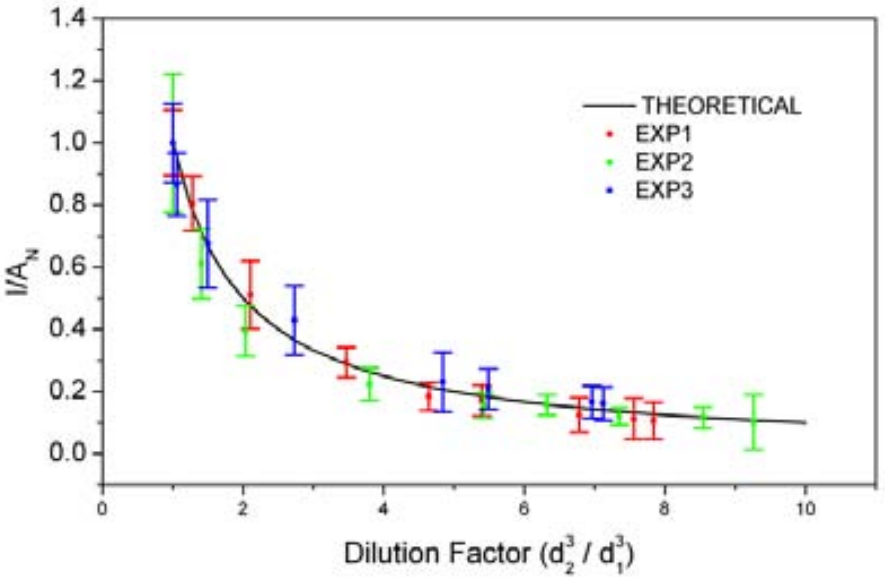

Figure 11. I/A_N plotted against the dilution factor for three independent different experiments. The solid line corresponds to the theoretical evolution assuming that the decrease in fluorescence intensity is only due to dilution upon addition of the H_2O/glycerol mixture. Error bars stand for the standard deviation of the average results obtained for different equivalent droplets in the array.

From such dependence we extracted that DT_2 can be used to control the volume delivered into the pre-patterned droplets, and therefore, to control the concentration of NaF into each mixture droplet.

2.1.4. Acid-Base Femtolitre Reaction

Once determined our ability to pattern and mix femtolitre volumes of two solutions containing two different reagents, we gave one step beyond. One of the heaviest limiting factors for femtolitre chemistry methods consists, not only on our ability to handle and mix femtolitre volumes, but also the lack of characterization techniques with micrometer scale resolution. The most recurring technique to characterize materials or substances confined on femtolitre volumes consist on fluorescence microscopy. Figure 12. shows an acid/base reaction between the non-fluorescent acidic and fluorescent basic state of fluorescein acid carried out at the femtoliter scale. To conduct the acid/base reaction, we delivered a H_2O/glycerol (1:1) solution of KOH into alternated pre-patterned H_2O/glycerol (1:1) droplets of fluorescein at 50% humidity (Figure 12.). Before KOH delivery, low fluorescence was detected from all fluorescein droplets, but a green fluorescence increase by about 30-fold corresponding to the deprotonation of fluorescein was observed at droplets in which KOH was mixed . Note that a large quantity of femtolitre reactions (400 replicas) over 750-μm^2 areas could be successfully made without the necessity of reloading the microfluidic pens (Figure 13).

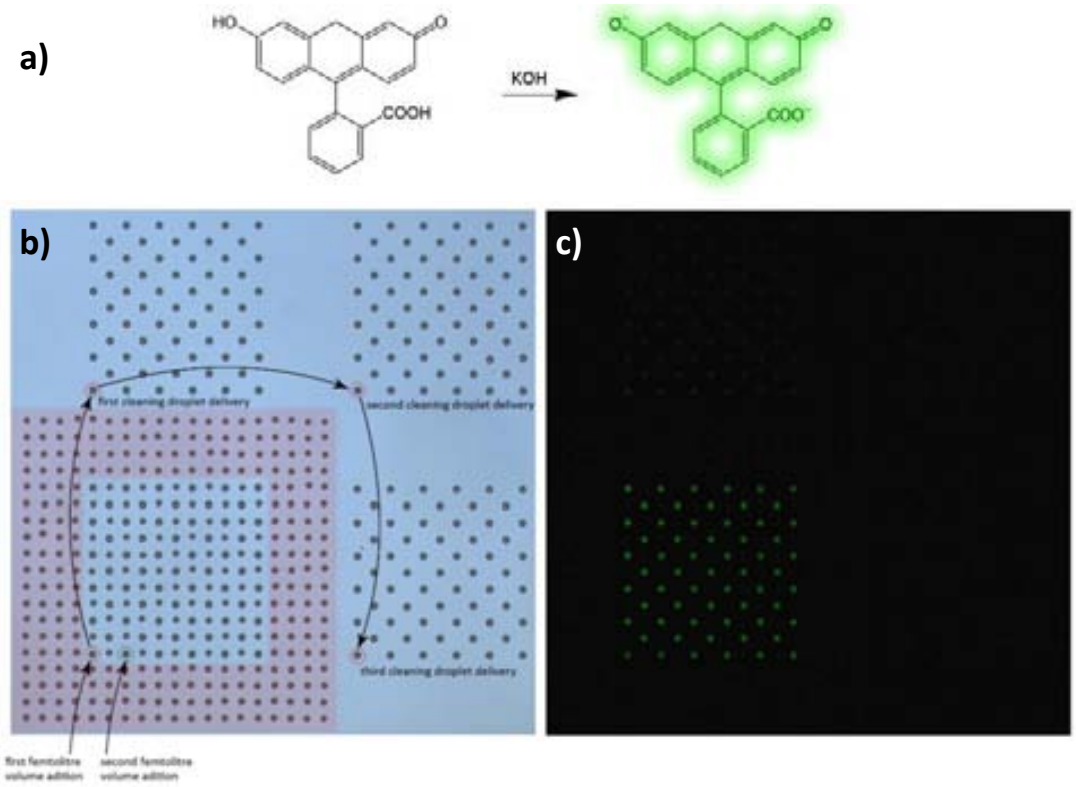

Figure 12. **a)**, Representation of the acid/base reaction between fluorescein acid and KOH. **b**) Optical Microscopy image of the area used to perform the acid-base reaction, including the cleaning step and the peripheral protecting areas. **c**) Fluorescence microscopy image of b) exciting at λ = 488 nm.

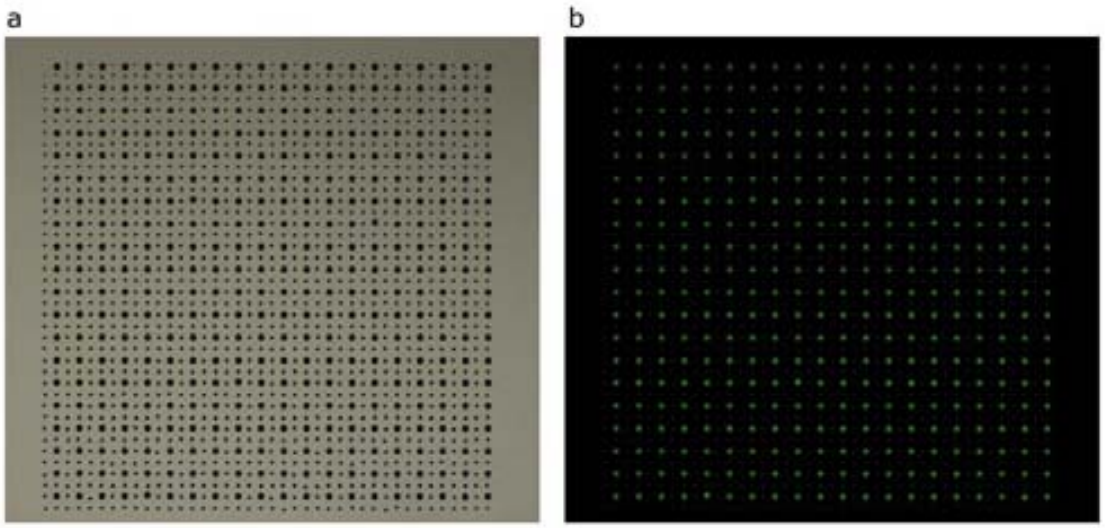

***Figure 13*. a**, Brightfield optical image of a 40 x 40 array of fluorescein acid droplets (droplet distance = 20 μm) covering an area of 760-μm², in which femtolitre volumes of KOH were mixed into alternated droplets. **b,** Fluorescence microscopy image of the droplet array after KOH addition, showing a green fluorescence increase at all alternated mixture droplets when excited at λ = 488 nm, thus confirming that femtolitre reactions can be homogenously made over large surface areas.

2.1.5. Alkaline Phosphatase Enzyme Recognition

When instead of simple organic molecules we used a biomolecule such as Alkaline Phosphatase, femtolitre reactions involving this enzyme were also performed with a high level of reproducibility. Alkaline phosphatase (ALP, ALKP) is a hydrolase enzyme responsible for removing phosphate groups from many types of molecules, including nucleotides, proteins, and alkaloids. The process of removing the phosphate group is called dephosphorylation. As the name suggests, alkaline phosphatases are most effective in an alkaline environment. It is sometimes used synonymously as basic phosphatase.

Figure 14. Diagram (rainblow colored, N-terminus = blue, C-terminus = red]) of the dimeric structure of bacterial alkaline phosphatase.

Calf-intestinal alkaline phosphatase (CIAP/CIP) is a type of alkaline phosphatase that catalyzes the removal of phosphate groups from the end of DNA strands.[29] This enzyme is frequently used in DNA sub-cloning, as DNA fragments that lack the phosphate groups cannot ligate.[30] This prevents recircularization of linearized vector DNA and improves the yield of vector containing the appropriate insert.

To detect this enzyme through the dephosphorilation of blue fluorescent 2'-[2-benzothiazoyl]-6'-hydroxybenzothiazole phosphate (BBTP) to green fluorescent 2'-[2-benzothiazoyl]-6'-hydroxybenzothiazole (BBT)[24] (see Figure 15a), a DEA/glycerol (7:3) droplet array of BBTP was created and femtolitre volumes of a DEA/glycerol (7:3) solution of AP were subsequent added only into alternated droplets within the array at 80 % humidity (Figure 15b). After mixing of both reagents, the substrate was incubated at 37 ºC and 80 % humidity for 15 min. The resulting array was first excited at 355 nm, and showed that all BBTP droplets were blue emissive, whereas all mixture droplets showed non fluorescence (Figure 15c). In contrast, all mixture droplets showed a green fluorescence increase by about 2-fold (even though they are

more diluted) in comparison to the BBTP droplets when excited at 488 nm (Figure 14d). These observations confirm the proper detection of AP through the complete dephosphorilation of BBTP, and that this approach show promise to do, localize and study biological reactions at femtolitre volumes.

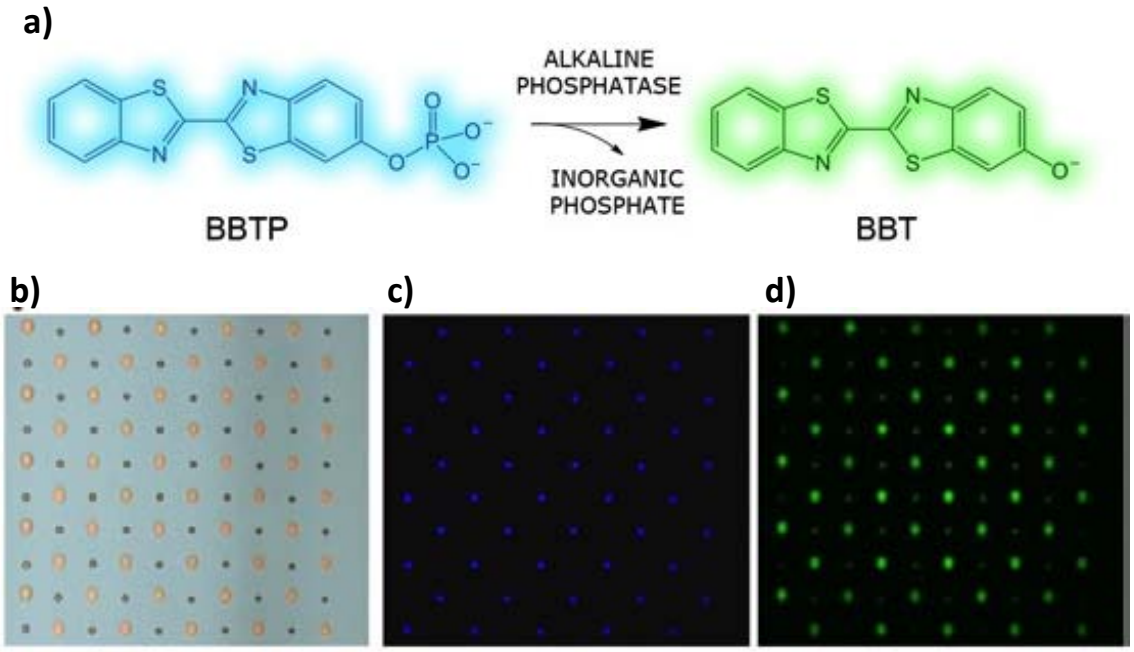

Figure 15. **a,** Representation of the detection of calf intestinal AP enzyme. **b,** Brightfield optical image of an array of BBTP droplets (droplet distance = 30 μm), in which femtolitre volumes of AP were mixed into alternated droplets. **c,** Fluorescence microscopy image (λ_{exc} = 359-371 nm; λ_{em} > 397 nm) of the corresponding array, showing the characteristic blue fluorescence of BBTP. **d,** Fluorescence microscopy image (λ_{exc} = 450-490 nm; λ_{em} > 515 nm) of the corresponding array, showing the characteristic green fluorescence of BBT when detected AP at all mixture droplets.

2.2. MOFs Synthesis

2.2.1. HKUST-1 Synthesis

The ability to use this MLP method to create well-defined mixture droplets and use them to confine the synthesis and crystallization of materials, rather than liquid reactions, on surfaces was evaluated. As a proof-of-concept, we reproducibly confined the crystallization of the chapter 3 studied archetypical HKUST-1. In this case, we first patterned (step #1) a 10x7 droplets array 20 μm separated and DT1=0.001s of a $Cu(NO_3)_2 \cdot 2.5(H_2O)$ [2.5 M, DMSO] solution and subsequent mixing (step 2#) of femtolitre volumes of trimesic acid [1 M, DMSO/glycerol (8.5:1.5)] with 0,1 s of DT2 on a SiO_2 surface, under 50% RH. The patterning was performed following the procedure, including cleaning step described in section 2.1. The resulting mixture droplet array was then placed in ambient conditions for two hours. After EtOH cleaning, the arrays where characterized by FESEM. (Figure 16). As shown in Figure 15, HKUST-1 nanocrystals islands were perfectly synthesized while placed in the desired position using the two steps MPL approach.

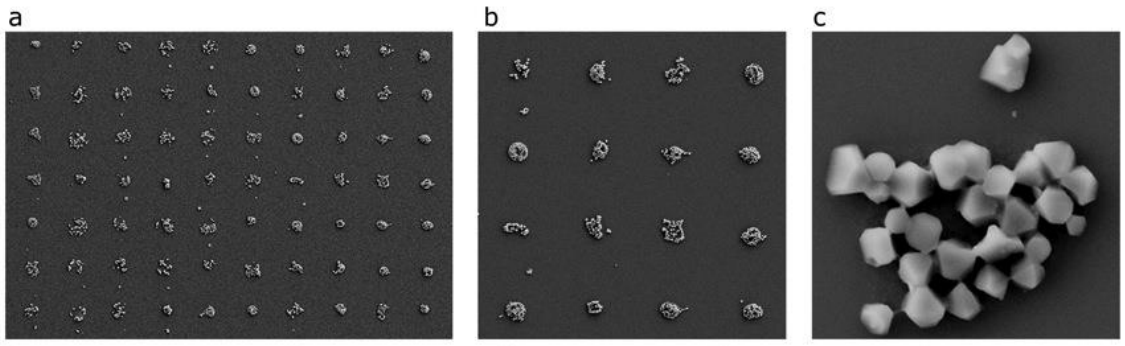

Figure 16. Femtoliter synthesis and controlled crystallization of MOFs. a-c, FESEM images of the synthesized HKUST-1 crystal array (feature distance = 20 μm), confirming the femtoliter droplet-by-droplet reaction reproducibility and showing the well-defined octahedral shape of the resulting HKUST-1 crystals.

2.2.2. Combinatorial PBA synthesis.

To increase the complexity and prove that one can use this MPL method to confine the synthesis of different materials into side-by-side mixture droplets within the same array, we created a combinatorial array of crystalline porous Prussian blue analogues (PBAs).[26,27] We selected four isostructural PBAs with general formula $M_3[Co(CN)_6]_2$, where M is Cd(II), Zn(II) and Mn(II), and $Ag_3[Co(CN)_6]$.

The combinatorial array was made by first creating a 40 μm separated 4 x 4 droplet array of a H_2O/glycerol (7.5:2.5) solution of $K_3Co(CN_6)$ either on SiO_2 or TEM grid surfaces and with a DT1 of 0,001s at 50% RH. Then, keeping the same RH, four different microfluidic pens, each one loaded with a different H_2O/glycerol (7.5:2.5) metal nitrate solution, $M(NO_3)_x \cdot yH_2O$ [M = Mn(II) (0.18 M), Cd(II) (0.18 M), Ag(I) (0.36 M) and Zn(II) (0.18 M) were used to deliver femtoliter volumes (DT2 = 0,5s) of each metal salt into four selected droplets composing the array, as shown in Figure 17. Mixing of both solutions into each one of the mixture droplets allowed the immediate formation of crystals that corresponded to the four desired PBAs, as confirmed by the positive matching between the interplanar distances extracted from electron diffraction patterns measured for each one of the synthesized PBAs and the distances derived from the literature (Figure 17 b-e).

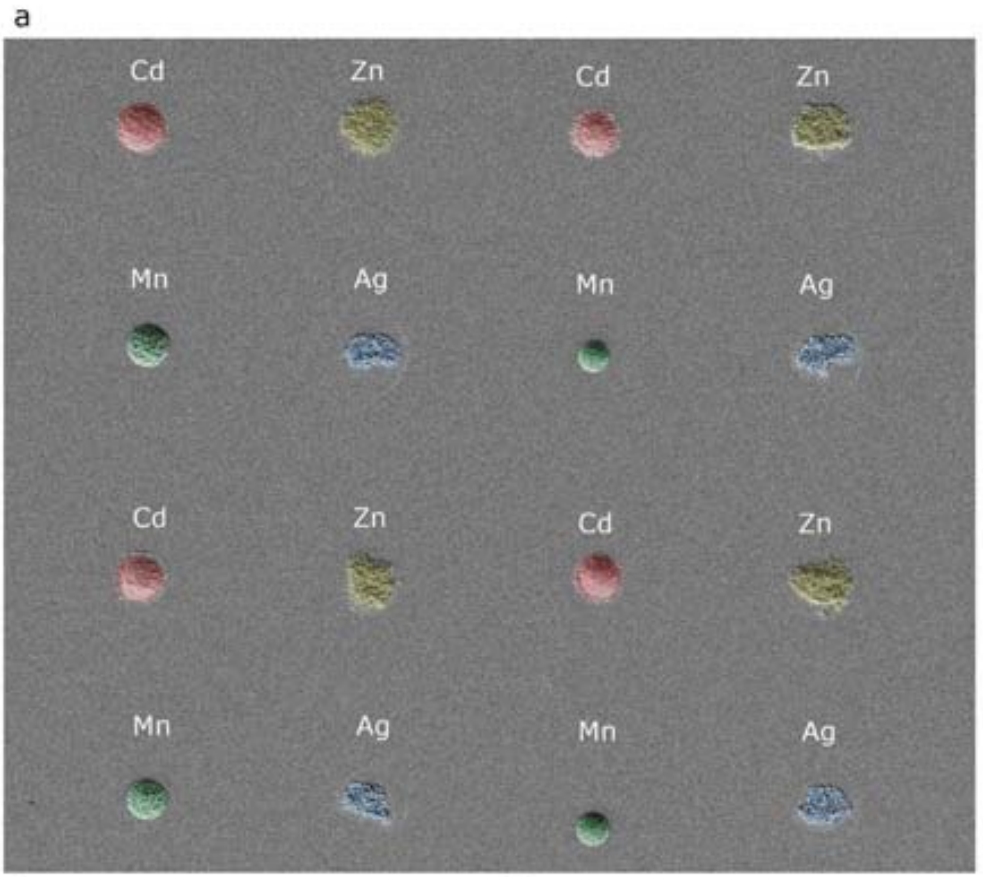

peak	d(Å)	d(Å) ref A
1	5.28	5.29
2	3.74	3.74
3	2.65	2.65
4	2.38	2.37

peak	d(Å)	d(Å) ref B
1	5.13	5.09
2	3.63	3.69
3	2.57	2.52

peak	d(Å)	d(Å) ref C
1	5.22	5.24
2	3.77	3.70
3	2.66	2.62
4	2.37	2.34

peak	d(Å)	d(Å) ref D
1	7.13	7.13
2	4.47	4.63
3	3.56	3.56
4	2.91	3.04

Figure 17. (a) Coloured FESEM images of the combinatorial 4 x 4 array of crystalline PBAs with general formula $M_3[Co(CN)_6]_2$, (PBA feature distance = 25 μm). **(b-e),** FESEM image of an individual island containing the synthesized Cd(II)-PBA (**b**), Zn(II)-PBA (**c**), Mn(II)-PBA (**d**), Ag(I)-PBA (**e**) nanocrystals (scale bars represents 2 μm), and their corresponding electron difraction patterns and tables that shows the comparison between measured interplanar distances (d) with the ones extracted from the literature: A, JCPDS No. 89-3740; B, JCPDS No. 32-1468; C, JCPDS No. 89-3735; and D, ICSD- 28501.

2.2.3. Bio-MOFs SCREENING

Bio-MOFs are MOFs in which the organic ligand used to link the nodes is a biomolecule. Bio-MOFs are a fascinating kind of materials as they can potentially offer biomedical applications, but also, morphology, bio-activity and the chemical particularity make biomolecules attractive candidates to construct the so called bio-MOFs. As a first proof-of-concept, this method was tested to discover new metal-peptide networks[28] made of a randomly selected, quite costly bio-organic ligand of the family of peptides, the Glycine-Histidine (GH).

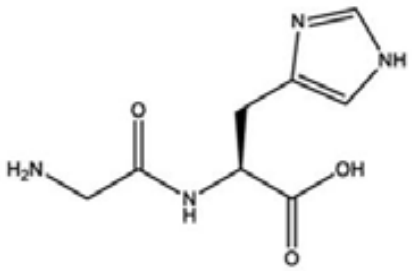

Figure 18. Glycine-histidine formula.

To proceed with the screening we selected 7 different transition metals because of their common use in MOF synthesis: Cr(III), Mn(II), Co(II), Ni(II), Cu(II), Zn(II), and Cd(II).

The patterning conditions (solvents, RH, DT_x, etc.) were determined after optimization one by one product. Once the optimal conditions were found, an array of 3x7 droplets of a 1M aqueous solution of GH with 30 μm of droplet distance was done over a SiO_2 clean surface at 85% RH. After the patterning of the biomolecule, we added one by one, the selected metal solutions. In this case, to further demonstrate the capabilities of the approach, we combined 3 different proportions of every metal in every one of the columns of GH droplets, by varying the dwell time DT_2 = 0.01, 0.1 and 0.2 s. Note that in general, dwell time used for the adition of the reagent in step 2# has to be bigger than the one used for the delivery of the first reagent in step #1 due to the cross-contamination that mainly occurs in the first instant of the mixing. The step #2 was performed with 0.3 M H_2O/diethyleneglycol (7:3) solutions of metal acetates [where metals were, from left to right, Cr(III), Mn(II), Co(II), Ni(II), Cu(II), Zn(II), and Cd(II)] at 85% humidity

Figure 19a shows the combinatorial 3 x 7 array after 2 hours of reaction at room temperature. Only droplets corresponding to Ni(II)-GH and Cu(II)-GH mixtures

showed the formation of crystals that were stable after cleaning with water. These screening results were confirmed by reproducing all these reactions in bulk (Figure 19b)

Bulk reactions:

0.35 mL of an aqueous solution of 0.3 M $M(CH_3COO)_x{\cdot}y(H_2O)$ [where M = Mn(II), Cd(II), Cu(II), Cr(III), Zn(II), Ni(II) and Co(II)] was added into 2 mL of an aqueous solution of GH (1 mmol) in a 5 mL glass vial. The resulting mixtures were left standing at RT or heated at 90 ºC for 2 hours. Under the studied conditions, only the reactions (both at RT and 90 ºC) between GH and $Cu(CH_3COO)_2{\cdot}(H_2O)$ and $Ni(CH_3COO)_2{\cdot}4(H_2O)$ gave rise dark blue (79 % yield) and blue crystals (62 % yield), respectively, suitable for single crystal analysis (see Table 3). Their phase purity was confirmed by XRPD (X'Pert PRO MPD diffractometer; Panalytical), IR (Tensor 27 FTIR spectrophotometer equipped with a Golden Gate diamond ATR cell; Bruker) and elemental analysis (see Figure 20). Interestingly, the reactions with the other metal ions did not showed the formation of any solid for over a week standing at room temperature.

$[Cu(GH)(H_2O)]{\cdot}H_2O$ and $[Ni(GH)_2]{\cdot}7H_2O$ networks were discovered after solving their crystal structures (See Suplementary Figures S7, S8 and S9 in the article). Thus, this MPL approach, with more elaborated control of the reaction conditions such as temperature, is likely to have important applications in biology, chemistry and materials science, and it will be ideal for fabricating arrays of complex structures that require to be synthesized through a reaction, such as crystals, making it also potentially useful in electronics and sensors as well.

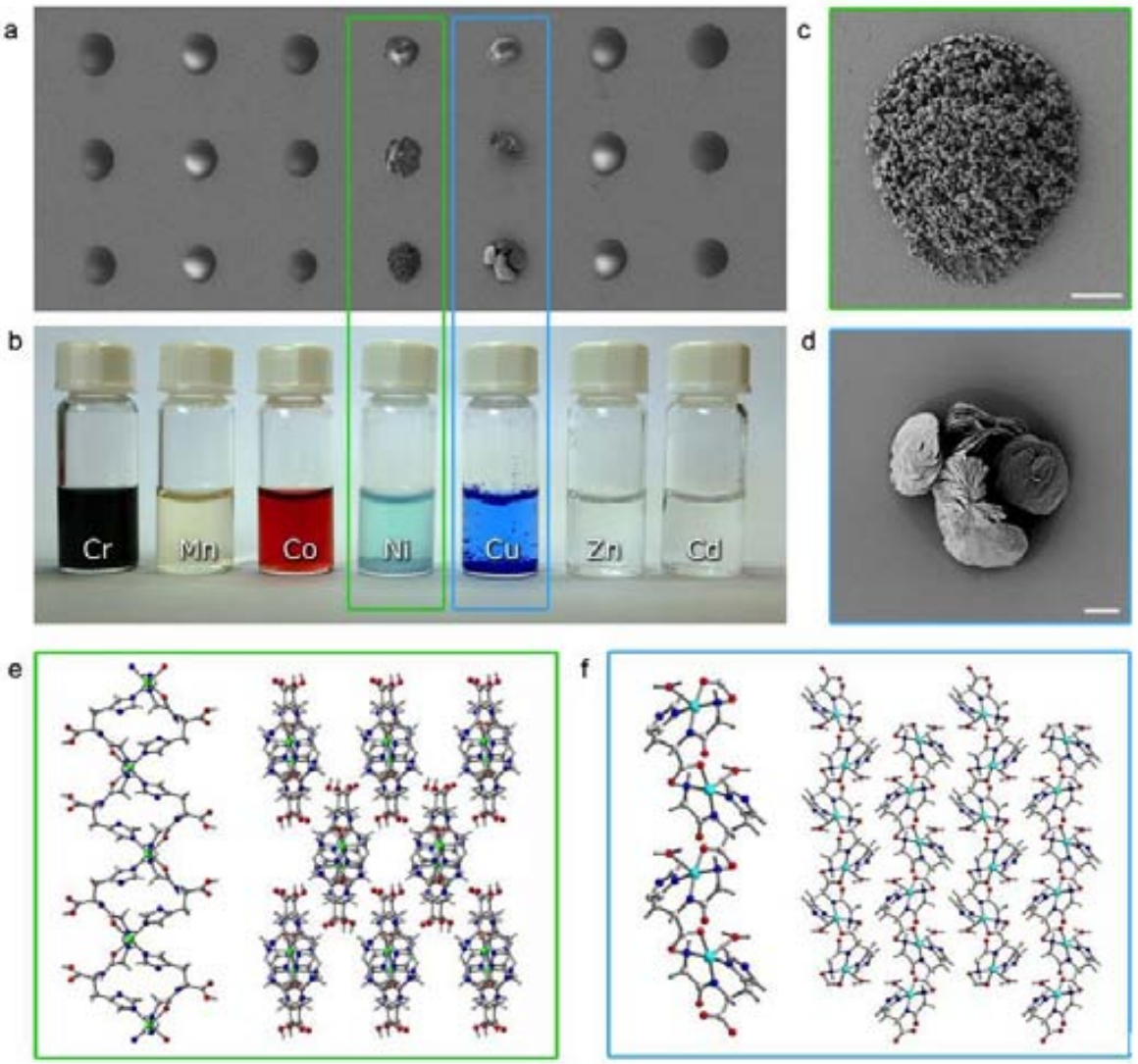

Figure 19. Screening the formation and crystallization of peptide-based coordination networks using MLP. **a,** FESEM image of a 3 x 7 droplet array in which each row is composed of droplets that contain mixtures of GH and seven metal acetates (droplet distance = 25 μm). Mixture droplets within each row were created by first patterning a droplet of an aqueous solution of 1M GH (contact time = 1 s), and then deliverying a H_2O:diethyleneglycol (7:3) solution of the corresponding 0.3 M metal acetate with different contact times depending on the row: 0.2 s (top), 0.1 s (middle) and 0.01s (bottom). **b**, Photograph that shows the bulk reproduction of all screened GH-metal acetate reactions, showing a perfect match on the formation of crystal when compared to the femtoliter reactions. **c,d**, Representative FESEM images of crystals obtained within the femtoliter mixture of Ni(II) (**c**) and Cu(II) (**d**) with GH dipeptide. **e,** Illustration of $[Ni(GH)_2]\cdot 7H_2O$, showing 1D chains along the *b*-axis. Ni(II) ion has an octahedral geometry coordinated to two imidazolate N atoms, two N atoms of NH_2 groups and two carbonyl O atoms of two consecutive GH ligands. Solvent molecules have been omitted for clarity. (green: Ni, grey: C, blue: N, and red: O). **f,** Ball and stick representation of $[Cu(GH)(H_2O)]\cdot H_2O$, showing 1D chains running along the *b*-axis. Cu(II) ion has a square pyramidal geometry coordinated to three N atoms (imidazolate N, NH_2 and NH groups), one carboxylate O atom of the GH ligand and one coordinated H_2O molecule. (blue: Cu, grey: C, blue:N, red: O, and white: H). **f,**

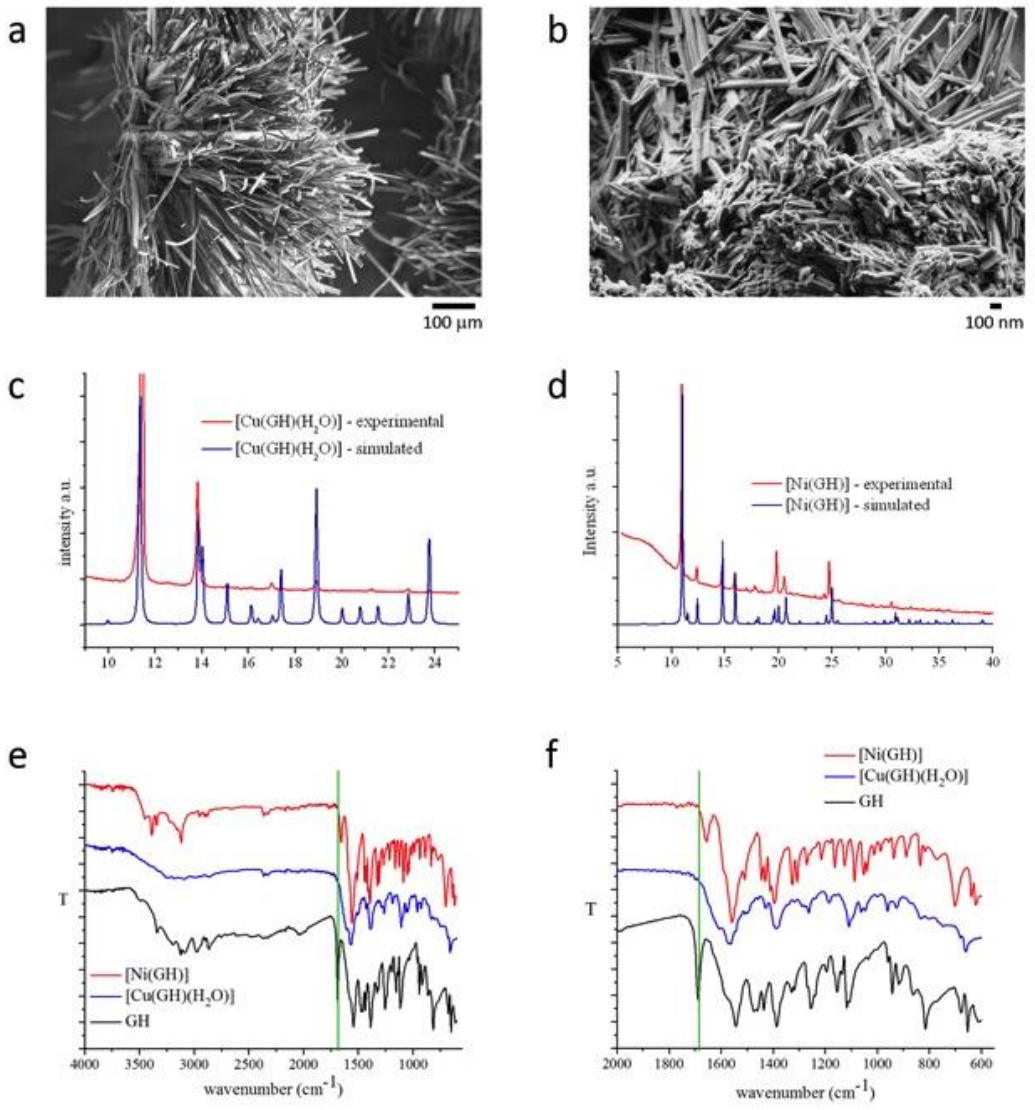

g

$[Cu(C_8H_{10}N_4O_3)(H_2O)]\cdot H_2O$	Calculated	C: 31.0 %	H: 4.6 %	N: 18.1 %
	Found	C: 31.4 %	H: 4.4 %	N: 18.0 %
$[Ni(C_8H_{11}N_4O_3)_2]\cdot(H_2O)_7$	Calculated	C: 31.7 %	H: 5.9 %	N: 18.5 %
	Found	C: 30.1 %	H: 5.7 %	N: 18.4 %

Figure 20. a,b, FESEM images of (**a**) $[Cu(GH)(H_2O)]\cdot H_2O$ and (**b**) $[Ni(GH)_2]\cdot 7H_2O$ synthesized in bulk. **c,d**, Comparison between the experimental and simulated XRPD patterns of (**c**) $[Cu(GH)(H_2O)]\cdot H_2O$ and (**d**) $[Ni(GH)_2]\cdot 7H_2O$, confirming the purity of both synthesized crystalline materials. **e,f**, IR spectra of free GH, $[Ni(GH)_2]\cdot 7H_2O$ and $[Cu(GH)(H_2O)]\cdot H_2O$. The C=O carboxylate band of the protonated GH is at 1687 cm^{-1}, whereas for $[Ni(GH)_2]\cdot 7H_2O$ and $[Cu(GH)(H_2O)]\cdot H_2O$ shifted to lower wavelength at 1641 cm^{-1} and 1596 cm^{-1}, respectively. The 46 cm^{-1} shift observed in the spectrum of $[Ni(GH)_2]\cdot 7H_2O$ confirms that the carboxylate moiety is not protonated but also that it is not coordinated to any Ni(II) atom. The bands corresponding to NH and NH_2 groups of GH at 2700-3300 cm^{-1} are all shifted for $[Ni(GH)_2]\cdot 7H_2O$ and $[Cu(GH)(H_2O)]\cdot H_2O$, showing that the peptide has coordinated to Ni(II) and Cu(II) *via* these groups. **g,** Comparison between the calculated and the experimental elemental analysis of $[Cu(GH)(H_2O)]\cdot H_2O$ and $[Ni(GH)_2]\cdot 7H_2O$.

Empirical formula	$CuC_8N_4O_5H_{12}$	$NiC_{16}N_8O_6H_{22}$, $7{\cdot}H_2O$
Formula weight	309.9	606.21
Temperature/K	293 K	150 K
Crystal system	Orthorhombic	Orthorhombic
Space group	$P2_12_12_1$	$P2_12_12_1$
a/Å	6.991(4)	8.768(5)
b/Å	10.778(4)	15.22(5)
c/Å	15.575(4)	18.86(5)
Volume/$Å^3$	1173.6(15)	2516.8(21)
Z	4	4
$\rho_{calc}mg/mm^3$	1.753	1.600
m/mm^{-1}	1.882	0.851
F(000)	636	1276
Crystal size/mm^3	0.2 × 0.2 × 0.2	0.4 × 0.1 × 0.1
2Θ range for data collection	5.2 to 57.4°	4.4 to 26.4º
Index ranges	-9 ≤ h ≤ 8, -13 ≤ k ≤ 12, -20 ≤ l ≤ 20	-10 ≤ h ≤ 10, -18 ≤ k ≤ 10, -23 ≤ l ≤ 10
Reflections collected	11380	6814
Independent reflections	2901[R(int) = 0.13]	4999 [R(int)=0.114]
Data/restraints/parameters	2901/0/175	4999/0/343
Goodness-of-fit on F^2	0.90	1.05
Final R indexes [I>=2σ (I)]	R_1 = 0.0675, wR_2 = 0.1432	R_1 = 0.1024, wR_2 = 0.2296
Final R indexes [all data]	R_1 = 0.1261, wR_2 = 0.1775	R_1 = 0.1635, wR_2 = 0.2653
Flack parameter	0.08(7)	0.06(5)

Table 3. Crystal data and structure refinement for [Cu(GH)(H2O)]·H2O and [Ni(GH)2]·7H2O. X-ray single-crystal diffraction data for [Ni(GH)2]·7H2O were collected on beamline I19 at Diamond Light Source, UK, on a Crystal Logic Kappa diffractometer with a Rigaku Saturn 724+ CCD detector (silicon 111 monochromated radiation, λ = 0.6889 Å). The applied absorption correction is based on multi-scans using REQAB within the d*TREK program[31]. The measurement for [Cu(GH)(H2O)]·H2O was done on a BRUKER SMART APEX CCD diffractometer using graphite-monochromated Mo Ka radiation (λ = 0.71073 Å). Both structures were solved by direct methods using the program SHELXS-97. The non-hydrogen atoms were refined anisotropically. The H atoms have been included in theoretical positions but not refined. The refinement and all further calculations were done using SHELXL-97. In both cases empirical absorption corrections were made, using SCALEPACK determination.[32]

.

3. References

1. D. S. Tawfik and A. D. Griffiths, *Nat Biotech*, 1998, **16**, 652-656.
2. D. T. Chiu and R. M. Lorenz, *Acc. Chem. Res.*, 2009, **42**, 649-658.
3. O. J. Miller, K. Bernath, J. J. Agresti, G. Amitai, B. T. Kelly, E. Mastrobattista, V. Taly, S. Magdassi, D. S. Tawfik and A. D. Griffiths, *Nat Meth*, 2006, **3**, 561-570.
4. K. Jensen, *Nature*, 1998, **393**, 735-737.
5. P. O. Brown and J. M. Trent, *Nature Genetics*, 1996, **14**, 3.
6. A. J. deMello, *Nature*, 2006, **442**, 394-402.
7. Y. Men, Y. Fu, Z. Chen, P. A. Sims, W. J. Greenleaf and Y. Huang, *Analytical Chemistry*, 2012, **84**, 4262-4266.
8. H. Song, D. L. Chen and R. F. Ismagilov, *Angew. Chem. Int. Ed.*, 2006, **45**, 7336-7356.
9. Y. Rondelez, G. Tresset, K. V. Tabata, H. Arata, H. Fujita, S. Takeuchi and H. Noji, *Nat Biotech*, 2005, **23**, 361-365.
10. P.-Y. Bolinger, D. Stamou and H. Vogel, *Angew. Chem. Int. Ed.*, 2008, **47**, 5544-5549.
11. D. Stamou, C. Duschl, E. Delamarche and H. Vogel, *Angew. Chem. Int. Ed.*, 2003, **42**, 5580-5583.
12. S. M. Christensen and D. Stamou, *Soft Matter*, 2007, **3**, 828-836.
13. D. M. Vriezema, P. M. L. Garcia, N. Sancho Oltra, N. S. Hatzakis, S. M. Kuiper, R. J. M. Nolte, A. E. Rowan and J. C. M. van Hest, *Angew. Chem. Int. Ed.*, 2007, **46**, 7378-7382.
14. D. T. Chiu, C. F. Wilson, F. Ryttsén, A. Strömberg, C. Farre, A. Karlsson, S. Nordholm, A. Gaggar, B. P. Modi, A. Moscho, R. A. Garza-López, O. Orwar and R. N. Zare, *Science*, 1999, **283**, 1892-1895.
15. S. M. Christensen, P.-Y. Bolinger, N. S. Hatzakis, M. W. Mortensen and D. Stamou, *Nat Nano*, 2012, **7**, 51-55.
16. C. Mellot Draznieks, J. M. Newsam, A. M. Gorman, C. M. Freeman and G. Férey, *Angew. Chem. Int. Ed.*, 2000, **39**, 2270-2275.
17. X. Kong, H. Deng, F. Yan, J. Kim, J. A. Swisher, B. Smit, O. M. Yaghi and J. A. Reimer, *Science*, 2013, **341**, 882-885.
18. M. Li, D. Li, M. O'Keeffe and O. M. Yaghi, *Chemical Reviews*, 2013, **114**, 1343-1370.
19. C. E. Wilmer, M. Leaf, C. Y. Lee, O. K. Farha, B. G. Hauser, J. T. Hupp and R. Q. Snurr, *Nat Chem*, 2012, **4**, 83-89.
20. S. Amirjalayer, M. Tafipolsky and R. Schmid, *The Journal of Physical Chemistry C*, 2011, **115**, 15133-15139.
21. S. Bureekaew and R. Schmid, *CrystEngComm*, 2013, **15**, 1551-1562.
22. R. Chakrabarty, P. S. Mukherjee and P. J. Stang, *Chemical Reviews*, 2011, **111**, 6810-6918.
23. B. J. Sikora, C. E. Wilmer, M. L. Greenfield and R. Q. Snurr, *Chemical Science*, 2012, **3**, 2217-2223.
24. K. E. Jelfs, E. G. B. Eden, J. L. Culshaw, S. Shakespeare, E. O. Pyzer-Knapp, H. P. G. Thompson, J. Bacsa, G. M. Day, D. J. Adams and A. I. Cooper, *J. Am. Chem. Soc.*, 2013, **135**, 9307-9310.

25. M. E. Briggs, K. E. Jelfs, S. Y. Chong, C. Lester, M. Schmidtmann, D. J. Adams and A. I. Cooper, *Crystal Growth & Design*, 2013, **13**, 4993-5000.
26. H. Hayashi, A. P. Cote, H. Furukawa, M. O/'Keeffe and O. M. Yaghi, *Nat Mater*, 2007, **6**, 501-506.
27. E. Biemmi, S. Christian, N. Stock and T. Bein, *Microporous and Mesoporous Materials*, 2009, **117**, 111-117.
28. M. Sundberg, A. Månsson and S. Tågerud, *Journal of Colloid and Interface Science*, 2007, **313**, 454-460.
29. P. H. Seeburg, J. Shine, J. A. Martial, J. D. Baxter and H. M. Goodman, *Nature*, 1977, **270**, 486-494.
30. A. Ullrich, J. Shine, J. Chirgwin, R. Pictet, E. Tischer, W. Rutter and H. Goodman, *Science*, 1977, **196**, 1313-1319.
31. J. Pflugrath, *Acta Crystallographica Section D*, 1999, **55**, 1718-1725.
32. Z. M. Otwinowski, W., *Methods Enzymol.*, 1997, **276**, 307-326.

PUBLICATION 3.

Femtolitre Chemistry assisted by microfluidic pen lithography

Carlos Carbonell, Kyriakos C. Stylianou, Jordi Hernando, Emi Evangelio, Sarah A. Barnett, Saju Nettikadan, Inhar Imaz and Daniel Maspoch

Nature Communications, **2013**, 4, 2173

nature COMMUNICATIONS

ARTICLE

Received 5 Jun 2013 | Accepted 19 Jun 2013 | Published 17 Jul 2013

DOI: 10.1038/ncomms3173 OPEN

Femtolitre chemistry assisted by microfluidic pen lithography

Carlos Carbonell[1], Kyriakos C. Stylianou[1], Jordi Hernando[2], Emi Evangelio[1], Sarah A. Barnett[3], Saju Nettikadan[4], Inhar Imaz[1] & Daniel Maspoch[1,5]

Chemical reactions at ultrasmall volumes are becoming increasingly necessary to study biological processes, to synthesize homogenous nanostructures and to perform high-throughput assays and combinatorial screening. Here we show that a femtolitre reaction can be realized on a surface by handling and mixing femtolitre volumes of reagents using a microfluidic stylus. This method, named microfluidic pen lithography, allows mixing reagents in isolated femtolitre droplets that can be used as reactors to conduct independent reactions and crystallization processes. This strategy overcomes the high-throughput limitations of vesicles and micelles and obviates the usually costly step of fabricating microdevices and wells. We anticipate that this process enables performing distinct reactions (acid-base, enzymatic recognition and metal-organic framework synthesis), creating multiplexed nanoscale metal-organic framework arrays, and screening combinatorial reactions to evaluate the crystallization of novel peptide-based materials.

[1]ICN2—Institut Catala de Nanociencia i Nanotecnologia, Esfera UAB, 08193 Bellaterra (Barcelona), Spain. [2]Departament de Química, Universitat Autònoma de Barcelona, 08193 Bellaterra, Spain. [3]Diamond Light Source, Harwell Science and Innovation Campus, Didcot, Oxfordshire OX11 0DE, UK. [4]NanoInk Inc., Illinois Science and Technology Park, Skokie, IL 60077 USA. [5]Institució Catalana de Recerca i Estudis Avançats (ICREA), 08100 Barcelona, Spain. Correspondence and requests for materials should be addressed to D.M. (email: daniel.maspoch@icn.cat).

Chemical reactions at volumes from femtolitres (10^{-15} litres) to attolitres (10^{-18} litres) are becoming increasingly necessary to study biological processes that occur in small volumes of cellular compartments[1–4] and liquid-phase reactions[5], to synthesize homogenous nanostructures[6] and to perform high-throughput assays and combinatorial screening[7,8]. To perform reactions on surfaces and at such dimensions, it is critical to manipulate and confine ultrasmall volumes of reagents and control their mixing into well-defined compartments. It is also important to control the dimensions and monodispersity of these reactors, their positioning to facilitate monitoring and the evaporation rate of all solvents used. To date, methods to conduct reactions at these ultrasmall dimensions can be classified into two types based on the use of micromachining techniques (mainly microfluidics and femtolitre wells[9–12]) and self-enclosed volume elements, including vesicles, micelles and oil/water-dispersed droplets[13–18].

We propose here an alternative approach to realize femtolitre reactions on a surface by handling and mixing femtolitre volumes of reagents using a microfluidic stylus. This approach, named microfluidic pen lithography (MPL), overcomes the high-throughput limitations of vesicles and micelles and obviates the usually costly step of fabricating microdevices and wells: it can be employed to mix reagents in isolated femtolitre droplets that can be used as reactors to conduct independent reactions and/or crystallization processes over centimetre-scale regions with high registration accuracy. In particular, we have found that conventional pen lithography technologies and tools[19–22], commonly used for molecular and material printing, and now available to many researchers, are ideal for running such reactions on surfaces. Microfluidic pens (BioForce, USA; see Supplementary Fig. S1) offer high levels of uniformity and reproducibility for depositing femtolitre volumes of liquids onto surfaces. Dip-Pen Nanolithography[19] NLP-2000 platform (NanoInk Inc., USA), equipped with a five-axis stage system and commercial lithography software, guarantees the control of the dwell time and the vertical and translational motion of the surface relative to the microfluidic pens (±75 nm z precision and ±100 nm positional precision over areas as large as 16 cm^2). This high accuracy enables the programmable positioning of microfluidic pens on top of selected, pre-patterned femtolitre droplets, followed by their precise approach up to the surface contact area. This straightforward MPL method comprises two steps: femtolitre droplet generation, and femtolitre volume delivery into these droplets (Fig. 1a; also see Supplementary Movie 1). It enables mixture of femtolitre volumes containing reagents directly on surfaces, thus forming well-defined mixture droplets in which individual femtolitre reactions can be conducted. Finally, an environmental humidity chamber included in the lithographic platform enables such reactions to be run under controlled atmospheres (that is, humidity or organic solvent vapour levels) and reduces droplet evaporation. This latter factor is crucial, as the second reagent must be delivered into the patterned droplets before they evaporate, and the resulting mixture droplet requires sufficient time to react and crystallize. Droplet evaporation can be also minimized by using reagent solutions containing high-boiling point, low-volatility solvents that do not affect the desired reaction. In this study, we demonstrate that MPL enables performing distinct reactions (acid-base, enzymatic recognition and metal-organic framework (MOF) synthesis), creating multiplexed nanoscale MOF arrays, and screening combinatorial reactions to evaluate the crystallization of novel peptide-based materials. We believe that this method could be adopted by researchers as a desktop tool to synthesize and crystallize nanomaterials at desired locations, fabricate arrays and devices, perform combinatorial screening and/or study reactions at the femtolitre scale.

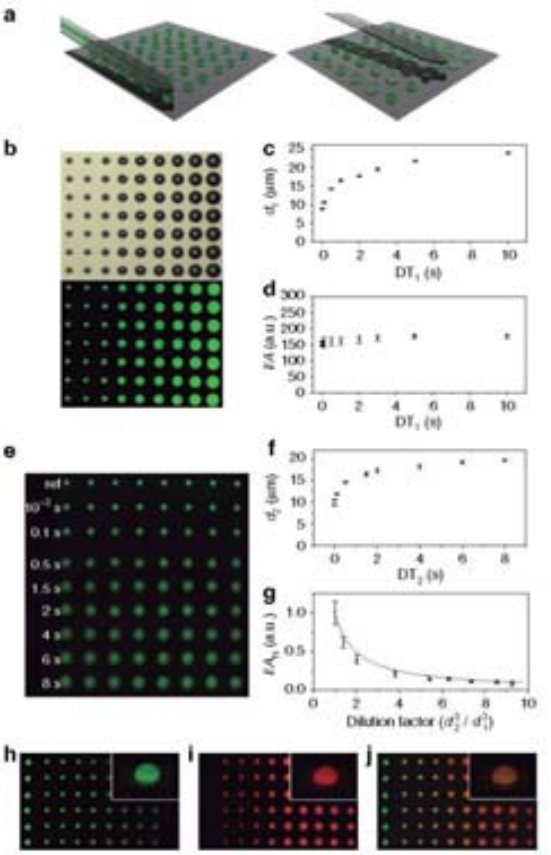

Figure 1 | Femtolitre delivery and mixing capabilities of MPL. (**a**) Schematic illustration of the two-step MPL method, showing the patterning of an array of SoF droplets (step 1), followed by precise delivery of different volumes of a solution into them (step 2). (**b**) Bright-field optical and corresponding confocal fluorescence microscopy images (λ_{exc} = 488 nm; λ_{em} = 500–575 nm) of an array of SoF droplets (droplet distance = 28 μm) created by using different DT_1. (**c**,**d**) DT_1 dependence of d_1 and of I/A measured for each droplet series. (**e**) Confocal fluorescence microscopy image of an array of SoF droplets (droplet distance = 35 μm), in which femtolitre volumes of an H_2O/glycerol solution were added at different DT_2. Note that the top row corresponds to bare SoF droplets. (**f**) DT_2 dependence of d_2. (**g**) Dilution factor dependence of I/A_{ref}. The line represents the expected behaviour of a bulk SoF solution (assuming that the decrease in fluorescence intensity is due only to dilution). (**h**–**j**) Confocal fluorescence microscopy images (λ_{exc} = 488 nm; λ_{em} = 500–575 nm (**h**); λ_{exc} = 633 nm; λ_{em} = 600–785 nm (**i**); and superimposed previous images (**j**)) of an array of SoF droplets (droplet separation = 28 μm), in which femtolitre volumes of a solution of Nile Blue were added at different DT_2. Note that the left and right columns correspond to pure SoF and Nile Blue droplets, respectively, whereas the gradient of colours from yellow/orange to red (left to right) denotes the increase in concentration of Nile Blue relative to SoF. In (**c**,**d**,**f**,**g**) the error bars represent the s.d. of the average results obtained for all equivalent droplets in the array.

Results

Patterning and mixing capabilities at the femtolitre scale. We evaluated the first step of this method—including, creation of femtolitre droplet arrays, reproducibility and homogenous

volume and reagent delivery—through delivery of a sodium fluorescein (SoF) solution onto a SiO_2 surface. In a typical experiment, the microfluidic pen was first loaded with a dimethylsulphoxide (DMSO)/glycerol (1:1) solution of SoF, mounted onto the lithographic platform at an acute angle of 10°, and used to fabricate an array of droplets by bringing it into contact with the surface for 0.001–10 s (hereafter, DT_1: dwell time used in step 1) at 60% relative humidity (RH; Fig. 1b; also see Supplementary Fig. S2 for a three-dimensional reconstruction of the droplet array). The patterned green fluorescent droplets had diameters (d_1) from 8.8 ± 0.2 to 24.0 ± 0.2 μm (Fig. 1c), confirming that DT_1 can be used to control the size (and therefore the estimated volumes, which vary from 42.7 ± 2.3 to 873.4 ± 20.9 fL, considering a measured macroscopic contact angle of $34.6 \pm 0.3°$; see also Supplementary Methods) of the initial droplets patterned by MPL. To demonstrate homogeneous concentration delivery, we measured the average of the fluorescence mean intensity per surface area (I/A—as a measure of dye concentration in the droplets, we analysed the fluorescence image slice corresponding to the droplet volume in direct contact with the surface, summed the intensity values for all fluorescent pixels of the droplet, and then divided by the droplet area in that image; also see Supplementary Methods) for each droplet series patterned at a different DT_1. Significantly, we observed <6% deviation in I/A among the droplet series (Fig. 1d).

To demonstrate the ability of controlling the deposition of a second femtolitre volume on top of the pre-patterned droplets (step 2), we delivered femtolitre volumes of an H_2O/glycerol (1:1) mixture into pre-patterned H_2O/glycerol (1:1) droplets of SoF ($d_1 = 9.4 \pm 0.1$ μm). The H_2O/glycerol solution was delivered at dwell times (hereafter DT_2: dwell time used in step 2) of 0.001 to 8 s at 50% RH, forming an array of mixture droplets with diameters (d_2) from 10.5 ± 0.1 to 19.7 ± 0.4 μm, respectively (Fig. 1e). Figure 1f shows that the delivered volume increased with increasing DT_2. Based on this finding, we concluded that DT_2 could be used to control the volume delivered into the pre-patterned droplets and, therefore, to control the concentration of SoF in each mixture droplet. This is demonstrated in Fig. 1g and Supplementary Fig. S3, in which the average I/A measured for each droplet series normalized to the average of the I/A measured for the initial SoF concentration (I/A_N) is plotted as a function of the dilution factor ($V_2/V_1 = d_2^3/d_1^3$) and of DT_2. When DT_2 is increased, the SoF concentration in each mixture droplet—and consequently, I/A_N—decreases according to the volumes of H_2O/glycerol added, following the expected behaviour of a bulk SoF solution (assuming that the decrease in fluorescence intensity is due only to dilution). This dependence was reproducibly obtained (see Supplementary Fig. S4), demonstrating that DT_2 can effectively be used to control the ratio of reagents in the mixture droplets.

Another factor contributing to this ratio is cross-contamination, which can affect the homogeneous mixing between mixture droplets. The influence of this phenomenon was evaluated by analysing the I/A of several droplets patterned at DT of 2 s after delivering an H_2O/glycerol (1:1) mixture into pre-patterned H_2O/glycerol (1:1) droplets of SoF ($d_1 = 8.7 \pm 0.2$ μm) at DT_2 of 0.001–10 s at 45% RH (see Supplementary Fig. S5). I/A was detected in the first three droplets for all cases: the average intensity values (relative to the initial SoF intensity) were *ca.* 6.0% (1st droplet), 2.8% (2nd droplet) and 1.2% (3rd droplet). Based on these values, we decided to introduce a cleaning step to prevent cross-contamination and ensure unadulterated reagent mixing. In the cleaning step, a few droplets are patterned outside the working area (that is, on a different surface) between each round of reagent delivery on top of the pre-patterned droplets. To further verify the delivery capabilities of MPL and homogeneous mixing of the solutions in each mixture droplet, we also delivered a solution of the red-fluorescent dye Nile Blue at different DT_2 into pre-patterned green-fluorescent SoF droplets, and then visualized their fluorescence signal co-localization (Fig. 1h–j).

Acid-base and enzymatic recognition reactions. Figure 2a–i show two chemical reactions performed at the femtolitre scale: an acid/base reaction between the non-fluorescent fluorescein acid and its fluorescent dianionic state (Fig. 2a), and a biologically-relevant reaction based on the detection of calf intestinal alkaline phosphatase (AP) enzyme (Fig. 2f). For the acid/base reaction, we delivered a H_2O/glycerol (7:3) solution of KOH into alternated pre-patterned DMSO/glycerol (7:3) droplets of fluorescein acid at 50% RH (Fig. 2b,d). Before the KOH delivery (Fig. 2c), low fluorescence was detected from all fluorescein droplets, but in the droplets in which KOH was mixed, a *ca.* 30-fold increase in green fluorescence (corresponding to the deprotonation of fluorescein) was observed (Fig. 2e). Note that numerous femtolitre reactions (400 replicas over 0.78 mm^2 area) were successfully run without the microfluidic pens having to be reloaded (Supplementary Fig. S6). Femtolitre reactions of the AP-detection reaction also were performed with a high level of reproducibility. To detect this enzyme through the dephosphorylation of blue fluorescent 2′-[2-benzothiazoyl]-6′-hydroxybenzothiazole phosphate (BBTP) to green fluorescent 2′-[2-benzothiazoyl]-6′-hydroxybenzothiazole (BBT), a diethanolamine (DEA)/glycerol (7:3) droplet array of BBTP was created, and then femtolitre volumes of a DEA/glycerol (7:3) solution of AP were added to alternating droplets in the array at 80% RH (Fig. 2g). After the two reagents were mixed, the substrate was incubated at 37 °C and 80% RH for 15 min. The resulting array was first excited at 355 nm: all the BBTP droplets fluoresced blue, whereas none of the mixture droplets fluoresced (Fig. 2h). In contrast, when excited at 488 nm (Fig. 2i) all the mixture droplets fluoresced green (even though they were more dilute), at approximately twice the intensity of the BBTP droplets. These observations confirmed the proper detection of AP through the complete dephosphorylation of BBTP, thus demonstrating the utility of the MPL method for studying biological reactions at the femtolitre scale.

Femtolitre crystallization of MOFs. We then evaluated the MLP method for creating well-defined mixture droplets and subsequently using them to confine the synthesis and crystallization of materials (rather than liquid reactions) on surfaces. As proof-of-concept, we reproducibly compartmentalized the crystallization of the archetypical MOF HKUST-1 (ref. 23) by mixing femtolitre volumes of two DMSO solutions of $Cu(NO_3)_2 \cdot 2.5(H_2O)$ and trimesic acid on a SiO_2 surface, and placing the resulting mixture droplet array in ambient conditions for 2 h (Fig. 3a–c). To increase the complexity and prove that this MPL method can be used to confine the synthesis of different materials into side-by-side mixture droplets in the same array, we created a multiplexed array of crystalline porous Prussian blue analogues (PBAs)[24,25]. We selected four PBAs with the general formula $M_3[Co(CN)_6]_2$, where M is Cd(II), Zn(II) and Mn(II), and $Ag_3[Co(CN)_6]$. The multiplexed array was made by first creating a 4×4 droplet array of an H_2O/glycerol (7.5:2.5) solution of $K_3Co(CN)_6$ either on SiO_2 or transmission electron microscopy-grid surfaces. Four different microfluidic pens, each one loaded with a different H_2O/glycerol (7.5:2.5) metal nitrate solution, were used to deliver femtolitre volumes of each metal salt into four selected droplets comprising the array, as shown in Fig. 3d. Mixing of the two solutions into each one of the mixture droplets enabled the immediate formation of nanocrystals corresponding to the four desired PBAs (Fig. 3e), as confirmed by the positive matching

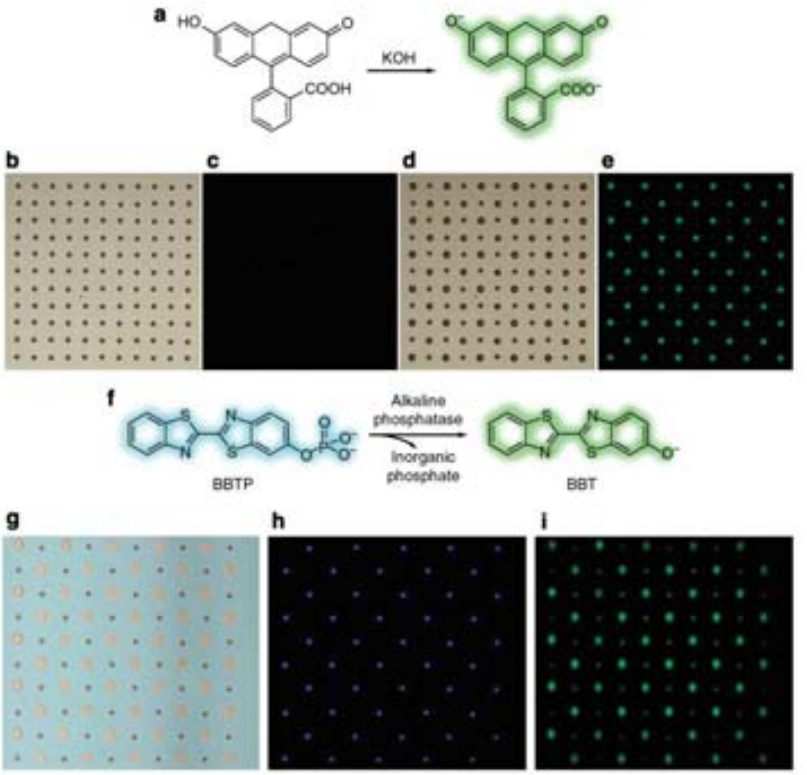

Figure 2 | MPL-assisted femtolitre reactions. (**a**) The acid/base reaction between fluorescein acid and KOH. (**b**,**c**) Bright-field optical and fluorescence microscopy (λ_{exc} = 450–490 nm; λ_{em} > 515 nm) images of an array of fluorescein acid droplets (droplet distance = 22 μm) before KOH addition, showing the absence of green fluorescence. (**d**,**e**) Bright-field optical and fluorescence microscopy images of the corresponding array after KOH addition, showing a *ca.* Thirty-fold increase in green fluorescence at all alternating mixture droplets. (**f**) Scheme of the detection of calf intestinal AP enzyme. (**g**) Bright-field optical image of an array of BBTP droplets (droplet distance = 30 μm), in which femtolitre volumes of AP were mixed into alternated droplets. (**h**) Fluorescence microscopy image of the corresponding array upon UV excitation (λ_{exc} = 359–371 nm; λ_{em} > 397 nm), showing the characteristic blue fluorescence of BBTP. (**i**) Fluorescence microscopy image of the corresponding array upon blue-light excitation (λ_{exc} = 450–490 nm; λ_{em} > 515 nm), showing the characteristic green fluorescence of BBT at all mixture droplets arising from AP-catalysed dephosphorylation of BBTP.

between the interplanar distances extracted from electron diffraction patterns measured for each synthesized PBAs and the corresponding literature values (Fig. 3f–i).

Screening new metal-peptide networks. Finally, as a first proof-of-concept, we tested our method to discover new metal-peptide networks[26] incorporating a randomly selected peptide ligand, glycine-histidine (GH). Figure 4a shows a 3 × 7 combinatorial array of droplets in which we mixed different femtolitre volumes of an aqueous solution of GH with H_2O/diethyleneglycol (7:3) solutions of various metal acetates (the metals were, from left to right, Cr(III), Mn(II), Co(II), Ni(II), Cu(II), Zn(II) and Cd(II)) at 85% RH. After 2 h of reaction at room temperature, only the droplets corresponding to Ni(II)-GH and Cu(II)-GH mixtures showed the formation of crystals that were stable after cleaning with water (Fig. 4c,d). These screening results were confirmed by reproducing all these reactions in bulk (Fig. 4b), from which two $[Cu(GH)(H_2O)] \cdot H_2O$ and $[Ni(GH)_2] \cdot 7H_2O$ networks were discovered after solving their crystal structures (Fig. 4e,f; also see Supplementary Figs S7–S10 and Supplementary Tables S1–S5). Thus, this MPL approach, once enhanced to enable greater control over reaction conditions such as temperature, will likely have important applications in biology, chemistry and materials science. Furthermore, it will be ideal for fabricating arrays of complex structures that can only be prepared via chemical synthesis (for example, crystals), thus making it potentially useful for electronics and sensors.

Discussion

We have reported a new, highly versatile lithographic method, MPL, for doing femtolitre chemistry on surfaces by handling and mixing femtolitre volumes of reagents. Albeit this nascent form of MPL includes only a microfluidic single pen, it can reproducibly perform a broad range of femtolitre reactions in water and organic solvents, and enables the confined crystallization of nanomaterials at precise locations on surfaces in a spatially ordered and combinatorial manner. We are confident that MPL could be greatly enhanced in scope and capability through the introduction of microfluidic multi-pens, analogously to the evolution recently undergone by other nanolithography methods that began with a single pen (for example Dip-Pen Nanolithography). Furthermore, method development to optimize crucial

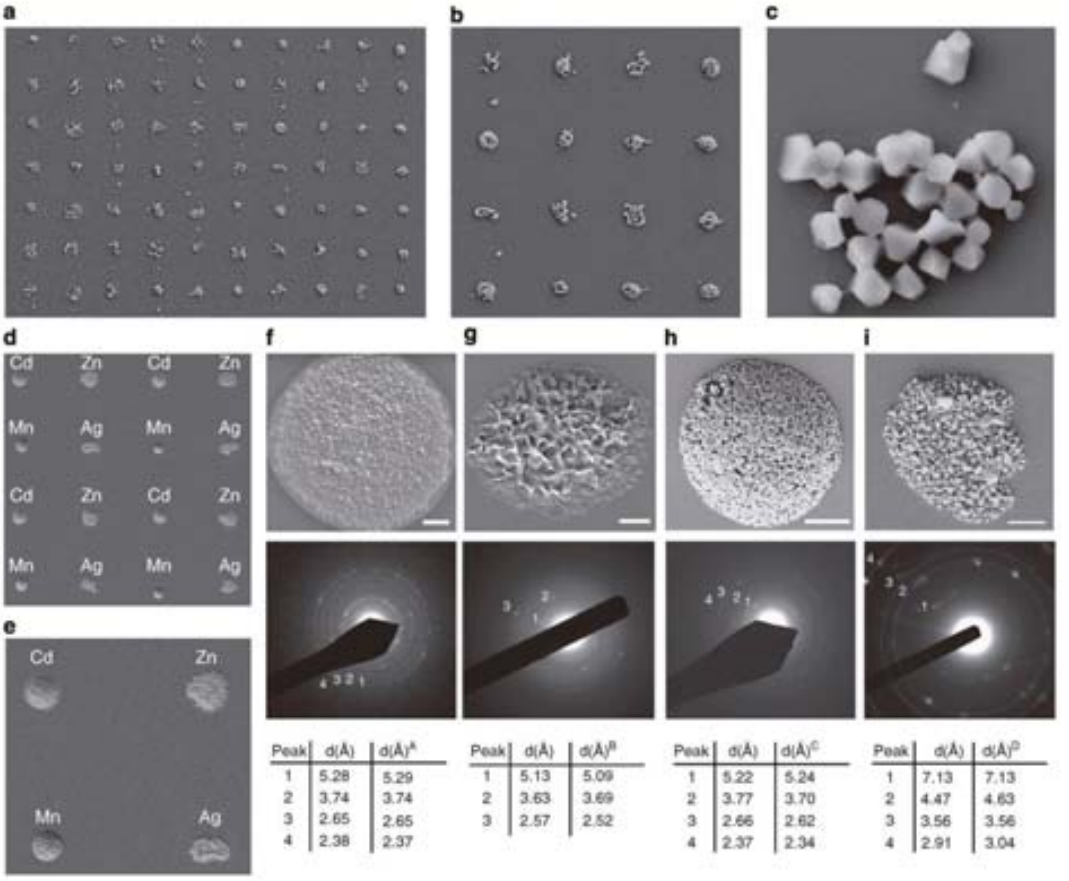

Peak	d(Å)	d(Å)^{A}
1	5.28	5.29
2	3.74	3.74
3	2.65	2.65
4	2.38	2.37

Peak	d(Å)	d(Å)^{B}
1	5.13	5.09
2	3.63	3.69
3	2.57	2.52

Peak	d(Å)	d(Å)^{C}
1	5.22	5.24
2	3.77	3.70
3	2.66	2.62
4	2.37	2.34

Peak	d(Å)	d(Å)^{D}
1	7.13	7.13
2	4.47	4.63
3	3.56	3.56
4	2.91	3.04

Figure 3 | Femtolitre synthesis and controlled crystallization of MOFs. (**a**–**c**) FESEM images of the synthesized HKUST-1 crystal array (feature distance = 25 μm), confirming the reproducibility of the femtolitre droplet-by-droplet reaction and showing the well-defined octahedral shape of the resulting HKUST-1 crystals. (**d**,**e**) FESEM images of the multiplexed 4 × 4 array of crystalline PBAs with general formula $M_3[Co(CN)_6]_2$, where M is Cd(II), Zn(II) and Mn(II), and $Ag_3[Co(CN)_6]$ (PBA feature distance = 25 μm). (**f**–**i**) FESEM image of an individual island containing the synthesised Cd(II)-PBA (**f**), Zn(II)-PBA (**g**), Mn(II)-PBA (**h**), Ag(I)-PBA (**i**) nanocrystals (scale bars, 2 μm), and their corresponding electron diffraction patterns, plus tables comparing the measured interplanar distances (d) with the corresponding literature values: A, JCPDS No. 89-3740; B, JCPDS No. 32-1468; C, JCPDS No. 89-3735; and D, ICSD- 28501.

reaction parameters (for example, humidity, temperature, surface type, evaporation rate, possible cross-contamination and so on), should provide access to an ever widening scope of femtolitre reactions and crystallizations on diverse surfaces. Finally, we are cautiously optimistic that as MPL matures and becomes more sophisticated, it will ultimately enable researchers to run high-throughput assays and combinatorial screening, perform femtolitre-scale biological studies, and even discover novel materials based on expensive building blocks.

Methods

Substrate preparation and microfluidic pen lithography. Si/SiO_2 substrates were subsequently sonicated for 10 min. in acetonitrile, ethanol and MilliQ water, and dried with N_2 gas flow. Each microfluidic pen was cleaned in piranha solution (3:1 v/v solution of H_2SO_4 and 30% H_2O_2) for 20 min., rinsed with MilliQ water and dried with slight N_2 gas flow. Caution: piranha solution is a strong acid and oxidant and should be handled with extreme care. Afterwards, each pen was introduced in an UV/ozone chamber for 20 min., and was then loaded with the corresponding reagent solutions by adding 1.5 μl of the appropriate solutions into the reservoir via micropipette. MPL-assisted femtolitre reactions were run on an NLP-2000 Nanolithography Platform at room temperature and at relative humidities of 50–85%.

Array of SoF droplets delivered at different DT_1. An array of 7 × 9 droplets (droplet separation = 28 μm) of 0.01 M SoF (in DMSO/glycerol, 1:1 v/v) was patterned on a SiO_2 surface at DT_1 = 0.001, 0.01, 0.1, 0.5, 1, 2, 3, 5 and 10 s at room temperature under a RH of 60%.

Mixture droplet arrays. An array of 8 × 9 droplets (droplet separation = 35 μm) of 0.01 mM SoF (in H_2O/glycerol, 1:1 v/v) was first patterned on a SiO_2 surface at DT_1 = 0.001 s at room temperature under a RH of 60%. Femtolitre volumes of an H_2O/glycerol (1:1) mixture were then delivered into the pre-patterned SoF droplets using a second microfluidic pen at DT_2 = 0.001, 0.1, 0.5, 1.5, 2, 4, 6 and 8 s, starting from the second row. To evaluate the cross-contamination effect, an array of 1 × 8 droplets (droplet separation = 35 μm) of 0.03 mM SoF (in H_2O/glycerol, 1:1 v/v) was first patterned on a SiO_2 surface at DT_1 = 0.001 s at room temperature under a RH of 45%. Then, femtolitre volumes of an H_2O/glycerol (1:1) mixture were delivered into the pre-patterned SoF droplets using a second microfluidic pen at DT_2 = 0.001, 0.01, 0.1, 1, 3, 5, 8 and 10 s. In this case, after each one of these eight deliveries, eight consecutive droplets (droplet separation = 35 μm) of the H_2O/glycerol (1:1) mixture were patterned at a DT = 2 s. An SoF/Nile Blue mixture droplet array was fabricated by first patterning an array of 10 × 6 droplets (droplet separation = 28 μm) of 0.01 M SoF (in H_2O/glycerol, 1:1 v/v) on a SiO_2 surface at DT_1 = 0.01 s at room temperature under a RH of 52%. Femtolitre volumes of 0.014 mM Nile Blue (in H_2O/glycerol, 1:1 v/v) were then delivered into the pre-patterned droplets using a second microfluidic pen at DT_2 = 0.001, 0.01, 0.1, 0.5, 2, 4, 8 and 10 s.

aqueous solution of GH (1 mmol) in a 5-ml glass vial. The resulting mixtures were left standing at RT or heated at 90 °C for 2 h. Under the studied conditions, only the reactions (both at RT and 90 °C) between GH and $Cu(CH_3COO)_2 \cdot H_2O$ or $Ni(CH_3COO)_2 \cdot 4H_2O$ afforded crystals suitable for single crystal analysis: dark blue (79% yield) and blue (62% yield), respectively (see Supplementary Tables S1–S5). Their phase purity was confirmed by XRPD (X'Pert PRO MPD diffractometer; Panalytical), IR (Tensor 27 FTIR spectrophotometer equipped with a Golden Gate diamond ATR cell; Bruker) and elemental analysis (see Supplementary Fig. S10). Interestingly, no formation of solid was observed in any of the reactions with the other metal ions, even after 1 week left standing at room temperature.

22. Carbonell, C., Imaz, I. & Maspoch, D. Single-crystal metal-organic framework arrays. *J. Am. Chem. Soc.* **133,** 2144–2147 (2011).
23. Chui, S. S.-Y., Lo, S. M.-F., Charmant, J. P. H., Guy Orpen, A. & William, I. D. A chemically functionalizable nanoporous material $[Cu_3(TMA)_2(H_2O)_3]_n$. *Science* **283,** 1148–1150 (1999).
24. Verdaguer, M. *et al.* Molecules to build solids: high T_C molecule-based magnets by design and recent revival of cyano complexes chemistry. *Coord. Chem. Rev.* **190–192,** 1023–1047 (1999).
25. Chapman, K. W., Southon, P. D., Weeks, C. L. & Kepert, C. J. Reversible hydrogen gas uptake in nanoporous Prussian Blue analogue. *Chem. Commun.*

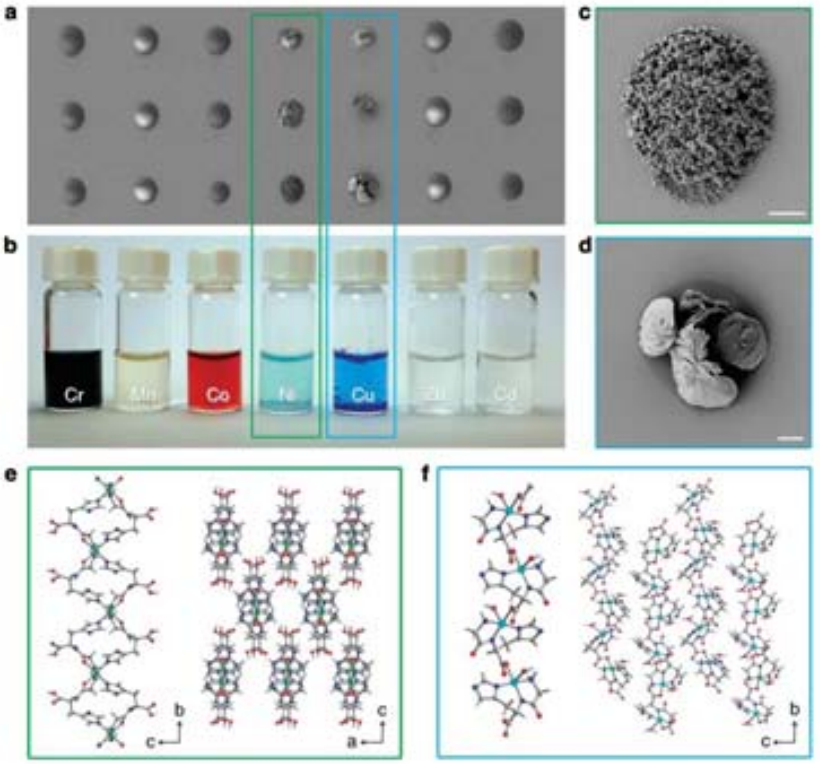

Figure 4 | Formation and crystallization of peptide-based coordination networks using MLP. (**a**) FESEM image of a 3 × 7 droplet array in which each row comprises droplets of a mixture containing the GH ligand and one of seven metal acetates (droplet distance = 25 μm). Mixture droplets within each row were created by first patterning a droplet of an aqueous solution of 1 M GH (contact time = 1 s), and then delivering a solution of the corresponding metal acetate (0.3 M in 7:3 H_2O/diethyleneglycol) for different contact times per row: 0.2 s (top), 0.1 s (middle) and 0.01 s (bottom). (**b**) Photograph showing the bulk reproduction of all screened GH-metal acetate reactions, revealing that the occurrence of crystal formation matched perfectly to the corresponding femtolitre reactions. (**c**,**d**) Representative FESEM images of crystals obtained within the femtolitre mixture of Ni(II) (**c**) and Cu(II) (**d**) with GH dipeptide. Scale bars: 2 μm. (**e**,**f**) X-ray crystal structures of the new $[Ni(GH)_2] \cdot 7H_2O$ and $[Cu(GH)(H_2O)] \cdot H_2O$.

MPL-assisted femtolitre reactions. In a typical experiment, an array of droplets of a solution containing a reagent (R_1) was first patterned onto a SiO_2 surface at a certain DT_1. Then, femtolitre volumes of a second solution containing another reagent (R_2) were delivered into the pre-patterned droplets using another microfluidic pen at an optimized DT_2. This two-step process was performed at a certain RH. Unless otherwise noted, all resulting mixture droplets were then kept at RT under the same RH for a certain time (t) in order to conduct the intended reactions. Following this protocol, optimal reaction conditions were studied for the acid/base reaction and the enzymatic recognition reaction, as well as for the synthesis of HKUST-1, PBAs and metal-peptide coordination networks. The conditions used to perform these femtolitre reactions were: Acid-base reaction. R_1: Fluorescein acid [2 mM, DMSO/glycerol (7:3)]; DT_1: 0.001 s; 11 × 11 droplet array (droplet distance = 25 μm); R_2: KOH [0.34 M, H_2O/glycerol (7:3)]; DT_2: 0.1 s; RH: 50%; t: 1 min. Enzymatic recognition reaction. R_1: BBTP [14 mM, AttoPhos buffer—Promega AttoPhos AP Fluorescent Substrate System, Technical Bulletin. http://www.promega.com, (2.4 M DEA, 0.057 mM $MgCl_2$, 0.005% NaN_3)]; DT_1: 0.5 s; 10 × 10 droplet array (droplet distance = 30 μm); R_2: AP [1 unit 6 μl^{-1} (1 unit: amount of enzyme required to catalyse the hydrolysis of 1 μmol of 4-nitrophenyl phosphate per minute at 37 °C in 1 M DEA, 10.9 mM 4-nitrophenyl phosphate and 0.5 mM $MgCl_2$ (pH = 9.8))]; DT_2: 0.5 s; RH: 75%; t: 15 min. at 37 °C. HKUST-1 synthesis. R_1: $Cu(NO_3)_2 \cdot 2.5H_2O$ [2.5 M, DMSO]; DT_1: 0.001 s; 30 × 30 droplet array (droplet distance = 20 μm); R_2: Trimesic acid [1 M, DMSO/glycerol (8.5:1.5)]; DT_2: 0.1 s; RH: 50%; t: 4 h. Combinatorial PBA synthesis. R_1: $K_3Co(CN)_6$ [0.1 M, H_2O/glycerol (7.5:2.5)]; DT_1: 1 s; 4 × 4 droplet array (droplet distance = 20 μm); R_2: $M(NO_3)_x \cdot yH_2O$ [M = Mn(II) (0.18 M), Cd(II) (0.18 M), Zn(II) (0.18 M) and Ag(I) (0.36 M), H_2O/glycerol (7.5:2.5)]; DT_2: 0.5 s; RH: 50%; t: 0.5 h. Screening the formation/crystallization of metal-peptide networks. R_1: GH [1 M, H_2O]; DT_1: 1 s; 3 × 7 droplet array (droplet distance = 30 μm); R_2: $M(CH_3COO)_x \cdot y(H_2O)$ (where M = Mn(II), Cd(II), Cu(II), Cr(III), Zn(II), Ni(II) and Co(II), 0.3 M, H_2O:diethyleneglycol (7:3)); DT_2: 0.01, 0.1 and 0.2 s; RH: 85%; t: 0.5 h.

Array characterization. SoF and mixture (SoF/H_2O-glycerol and SoF/Nile Blue) droplet arrays were characterized by confocal fluorescence microscopy (LEICA TCS SP5). Stacks comprising 30 fluorescence microscopy image slices (λ_{exc} = 488 nm; λ_{em} = 500–575 nm for SoF and λ_{exc} = 633 nm; λ_{em} = 600–785 nm for Nile Blue) at different heights (Δz = 0.42 μm) were collected for each array. Confocal microscopy images were then used to determine the average droplet diameter (d_1 and d_2), and therefore, the estimated average volumes of each droplet series, as further described in Supplementary Methods, Supplementary Figs S11,S12 and Supplementary Tables S6, S7. Moreover, the same images were used to determine the average of the fluorescence mean intensity (I/A; defined as the sum of the intensities of all fluorescent pixels in a droplet divided by its area) for each droplet series, as detailed in Supplementary Methods. The data were analysed using ImageJ software. Importantly, d_1 and d_2 values determined from confocal microscope images were in full agreement with those determined from optical microscopy images. Acid-base and enzymatic recognition reactions, both involving fluorescent compounds, were followed by fluorescence optical microscopy (Zeiss Axio Observer Z-1). FESEM (Zeiss Merlin) and Energy Dispersive X-Ray (Oxford INCA X-Max) analysis were used to study the formation of the different MOF crystals. To confirm the formation of the desired PBA phases, electron diffraction analysis (Hitachi H-7000) was also performed on each one of the sixteen individual crystalline islands of the multiplexed array.

Bulk reactions between metal salts and the dipeptide GH. A quantity of 0.35 ml of an aqueous solution of 0.3 M $M(CH_3COO)_x \cdot y(H_2O)$ (where M = Cr(III), Mn(II), Co(II), Ni(II), Cu(II), Zn(II) and Cd(II)) was added into 2 ml of an

Supplementary Information

Supplementary Figure S1. **a,b**, Schematic of the microfluidic pen used in MPL. **c,d**, FESEM images of the microfluidic pen used to run the femtolitre reactions on surfaces.

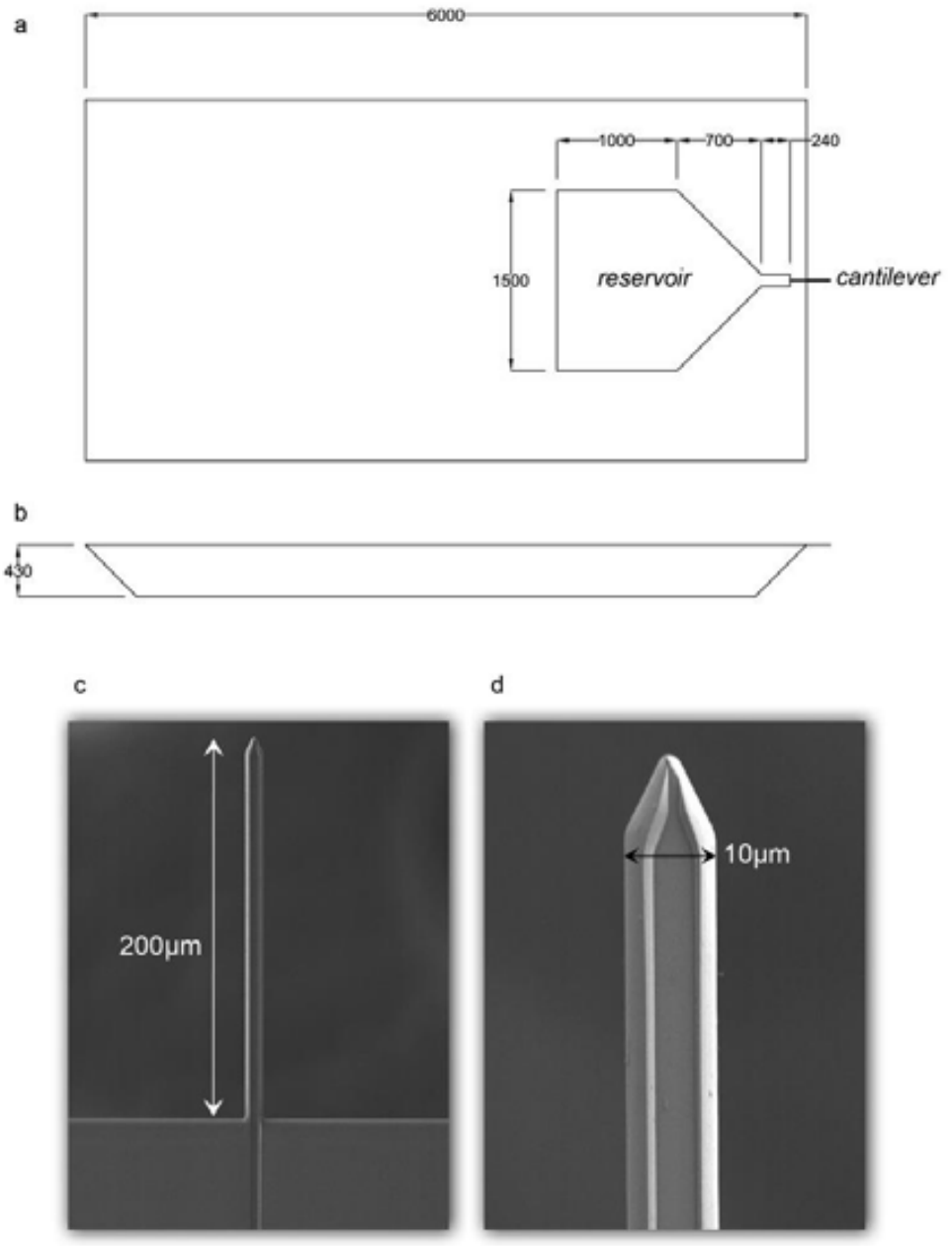

Supplementary Figure S2. Confocal 3D image reconstructions from confocal image stacks of the array of SoF droplets delivered at different DT_1.

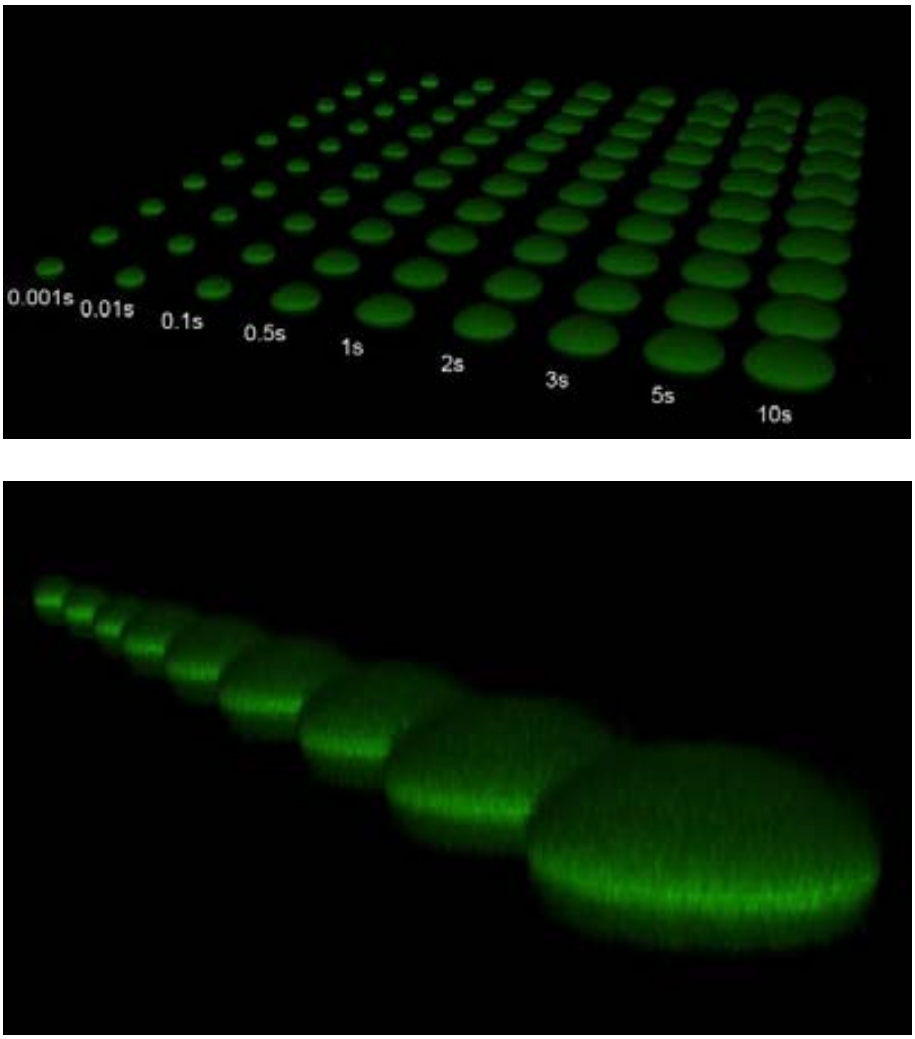

Supplementary Figure S3. DT_2 dependence of I/A_N. Error bars stand for the standard deviation of the average results obtained for all equivalent droplets in the array.

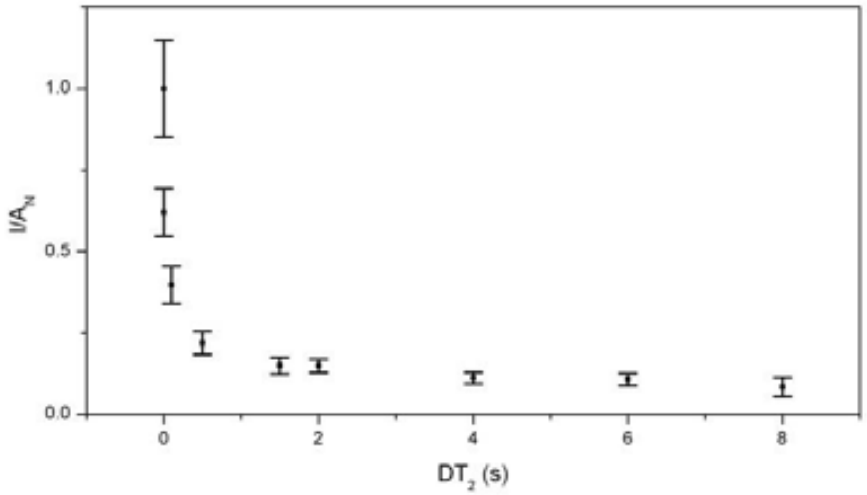

Supplementary Figure S4. I/A_N plotted against the dilution factor for three independent different experiments (red, green and blue). The solid black line corresponds to the expected behaviour of a bulk SoF solution assuming that the decrease in fluorescence intensity is due only to dilution upon addition of the H_2O/glycerol mixture. The error bars represent the standard deviation of the average results obtained for all equivalent droplets in the array.

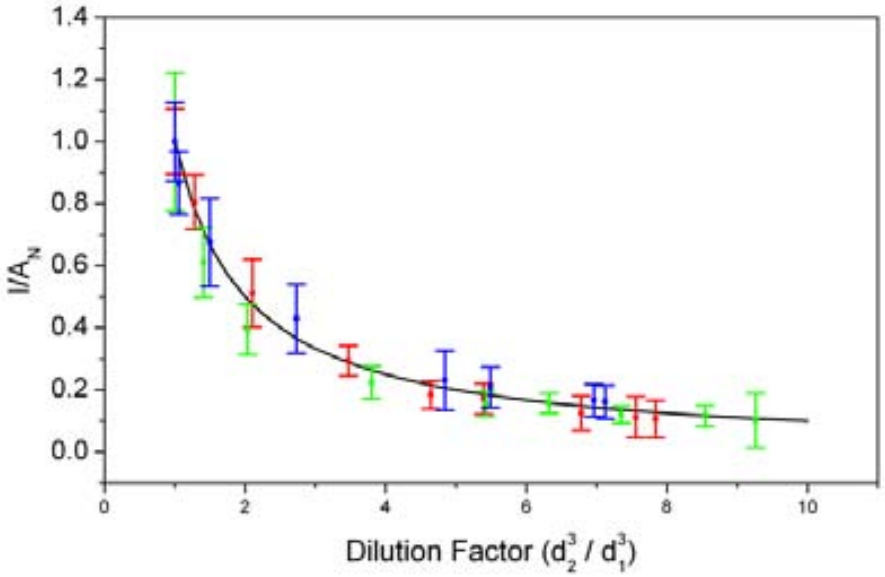

Supplementary Figure S5. a, Schematic illustration of the stepwise patterning of the array fabricated to ascertain any possible cross-contamination in the MPL method. **b,** Optical microscopy image of the initial SoF droplet array (left) and the final array after the delivery of an H_2O/glycerol (1:1) mixture into the pre-patterned droplets of SoF, and the generation of the cleaning droplets (middle). Confocal microscopy image of the resulting droplet array (right).

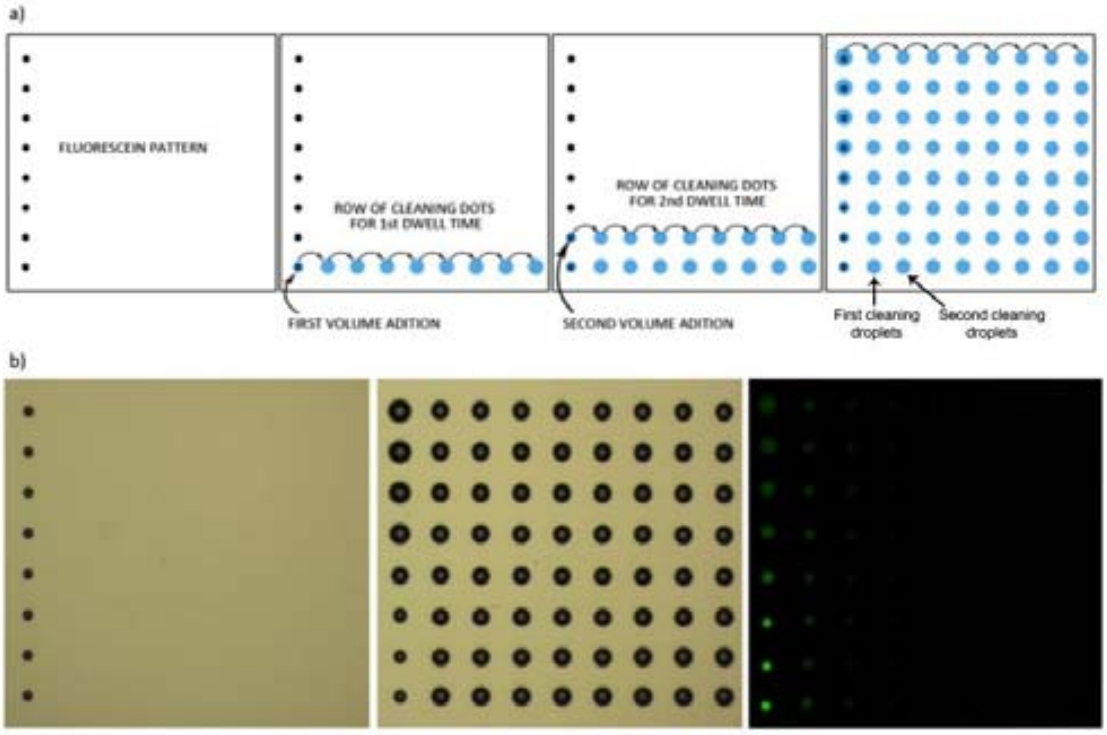

Supplementary Figure S6. a, Bright-field optical image of a 40 x 40 array of fluorescein acid droplets (droplet distance = 20 μm) covering an area of 0.61 mm^2, in which femtolitre volumes of KOH were mixed into alternating droplets. **b,** Fluorescence microscopy image of the droplet array after KOH addition, showing an increase in green fluorescence at all alternating mixture droplets when excited at λ = 488 nm, thus confirming that femtolitre reactions can be homogenously run over large surface areas.

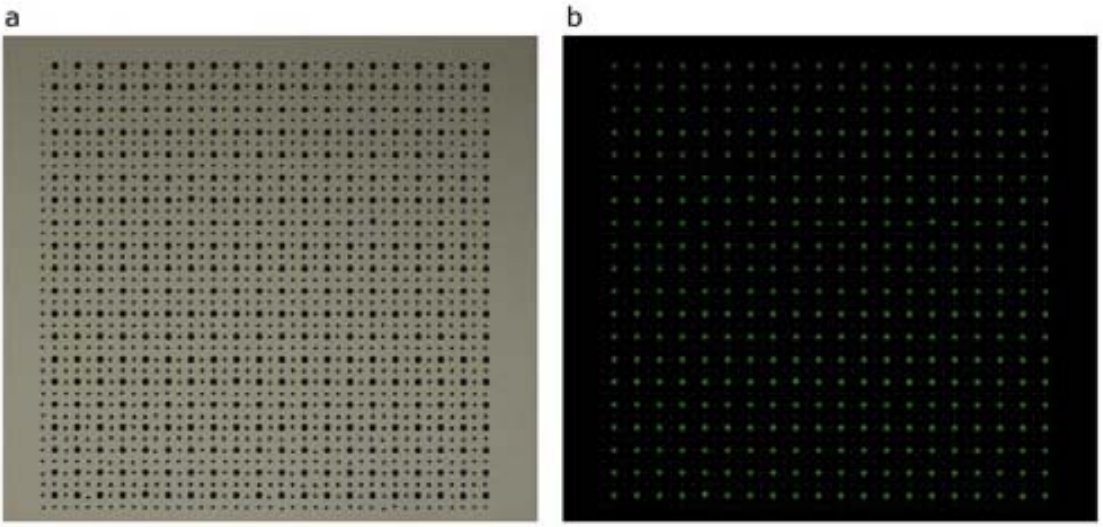

Supplementary Figure S7. a, Representation of the glycil-histidine (H-Gly-His-OH - $C_8H_{12}N_4O_3$, GH) peptide, which contains –COOH, -NH_2 and imidazole functional groups that can coordinate to metal ions. **b,** Ball and stick representation of [Cu(GH)(H_2O)]·H_2O, showing the presence of 1D chains along *b*-axis. The Cu(II) ion has a square pyramidal geometry and is coordinated to three N atoms (imidazolate N [N2], NH_2 [N4] and NH [N3] group), one carboxylate O (O1) atom (from the GH ligand), and one coordinated H_2O (O4) molecule, in the axial position. **c and d,** Intermolecular hydrogen-bonding interactions (represented by dashed lime and pink lines) between the neighbouring 1D chains – N4-H4B···O3 / 1.954(1) Å and O4-H2A···O3 / 1.703(0) Å. (navy blue: Cu; grey: C; blue: N; red: O; and white: H)

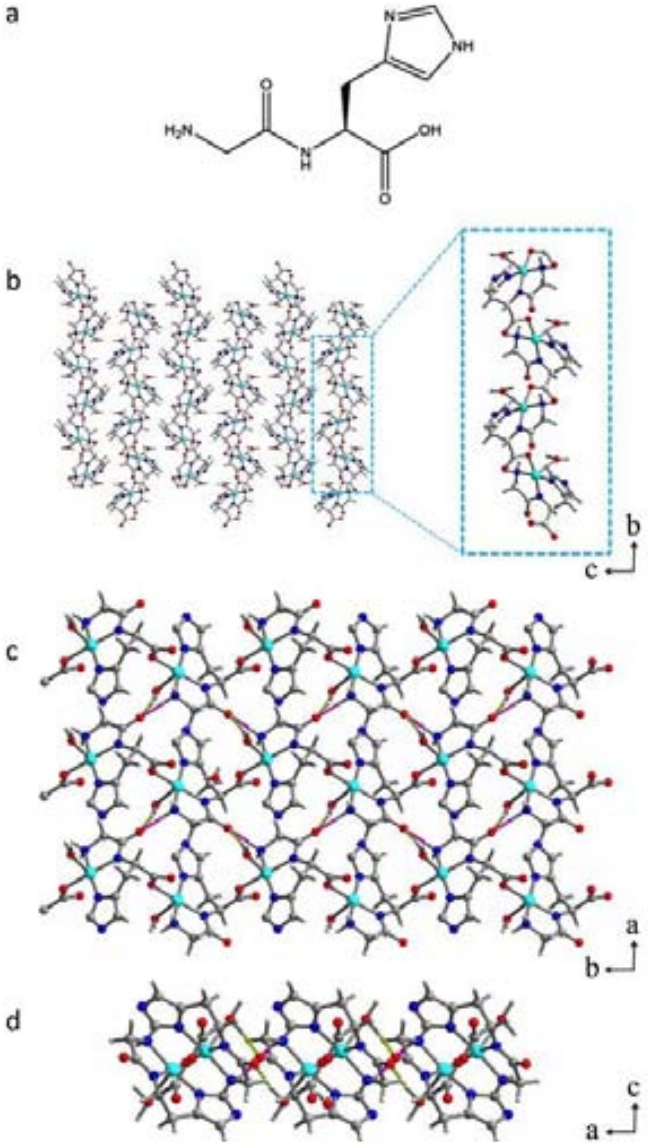

Supplementary Figure S8. **a,** Ball and stick illustration of $[Ni(GH)_2]\cdot 7H_2O$, showing the packing of the 1D chains along the *a*- and *b*-axes. Ni(II) has an octahedral geometry coordinated to two imidazolate N atoms (N11 and N1), two amino N atoms (N4 and N14) and to two carbonyl O atoms (O3 and O13) from two consecutive GH ligands. The carboxylic acid function of the GH is not involved in any metal bonding, and thus, it is not deprotonated. Each Ni atom is coordinated to four consecutive GH ligands, extending the structure in one dimension. The guest H_2O molecules are omitted for clarity. The Ni-Ni distance between two parallel chains is 8.768(0) Å, whereas the closest distance between these chains is 4.023(8) Å (H2B – H14B), thus preventing any interactions between them. **b,** Illustrations showing the packing of these chains, which reveals the presence of interlocked chains. **c,** Illustrations showing that between the interlocked chains there are several intermolecular hydrogen bonding interactions; with the most-important to be observed between the carboxylate function of the GH and the neighbouring chain (N2 ⋯ H2c / 2.037(2) Å - coloured in pink and N-H7⋯O4 / 2.013(4) Å – coloured in lime). (green: Ni, grey: C, blue: N, red: O and white: H).

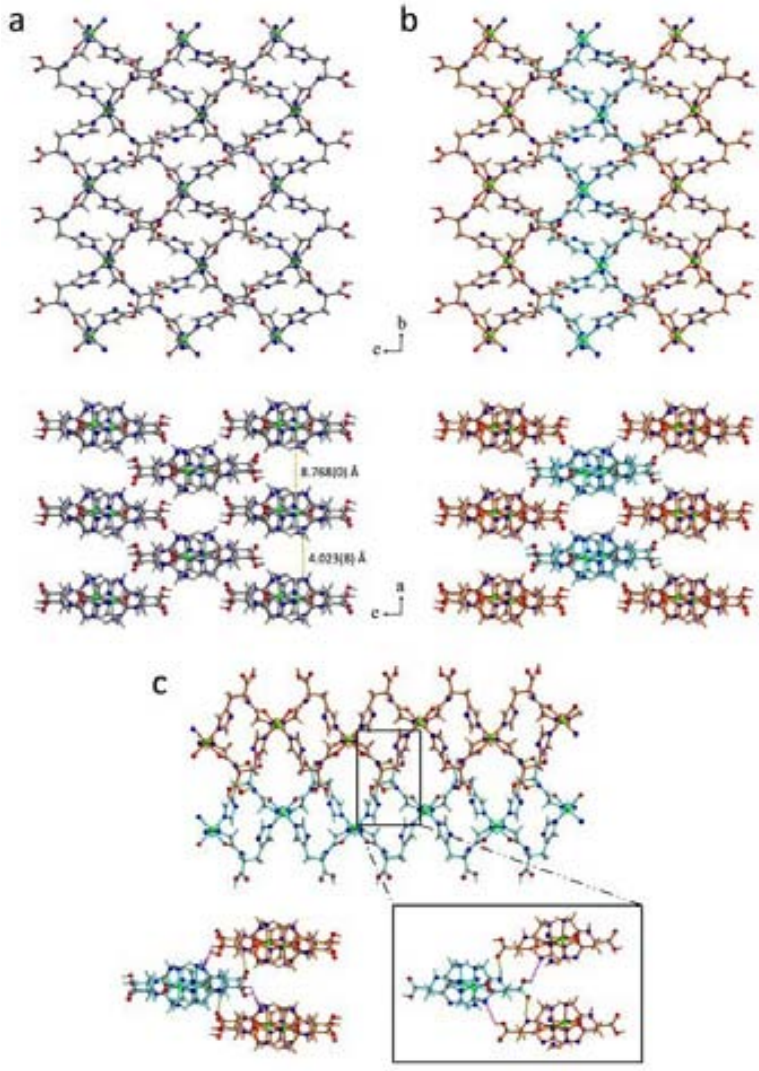

Supplementary Figure S9. a,b, ORTEP representation of the asymmetric unit of $[Cu(GH)(H_2O)]\cdot H_2O$ (**a**) and $[Ni(GH)_2]\cdot 7H_2O$ (**b**). Ellipsoids displayed at 30% probability.

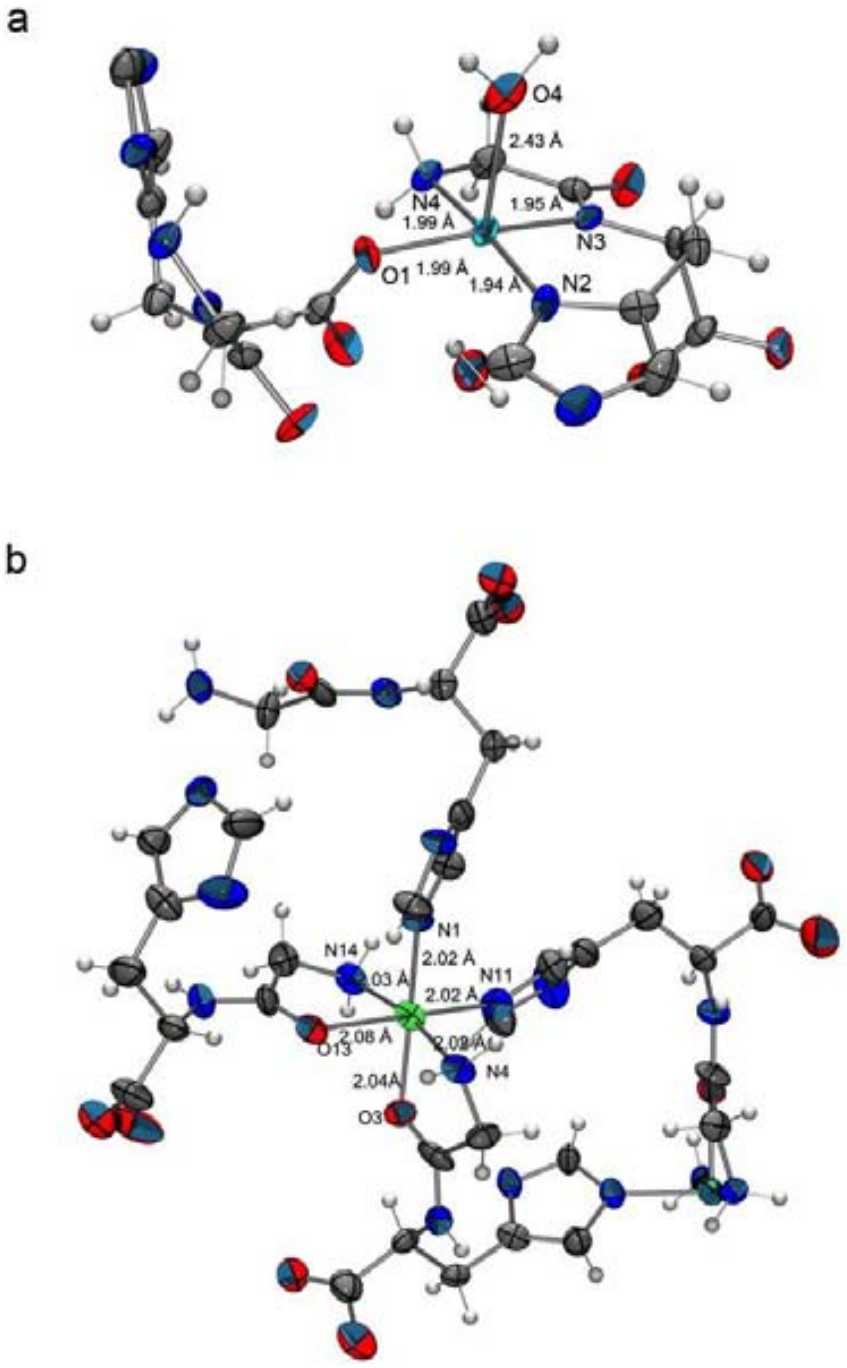

Supplementary Figure S10. a,b, FESEM images of (**a**) $[Cu(GH)(H_2O)]\cdot H_2O$ and (**b**) $[Ni(GH)_2]\cdot 7H_2O$ synthesised in bulk. **c,d**, Comparison between the experimental and simulated XRPD patterns of (**c**) $[Cu(GH)(H_2O)]\cdot H_2O$ and (**d**) $[Ni(GH)_2]\cdot 7H_2O$, confirming the purity of both synthesised crystalline materials. **e,f**, IR spectra of free GH, $[Ni(GH)_2]\cdot 7H_2O$ and $[Cu(GH)(H_2O)]\cdot H_2O$. The C=O carboxylate band of the protonated GH is at 1687 cm^{-1}, whereas for $[Ni(GH)_2]\cdot 7H_2O$ and $[Cu(GH)(H_2O)]\cdot H_2O$ shifted to lower wavelengths, at 1641 cm^{-1} and 1596 cm^{-1}, respectively. The 46 cm^{-1} shift observed in the spectrum of $[Ni(GH)_2]\cdot 7H_2O$ confirms that the carboxylate moiety is protonated and not coordinated to any Ni(II) atom. The bands corresponding to NH and NH_2 groups of GH at 2700-3300 cm^{-1} are all shifted for $[Ni(GH)_2]\cdot 7H_2O$ and $[Cu(GH)(H_2O)]\cdot H_2O$, showing that the peptide has coordinated to Ni(II) and Cu(II) via these groups. **g,** Comparison between the calculated values and the experimental elemental analysis values for $[Cu(GH)(H_2O)]\cdot H_2O$ and $[Ni(GH)_2]\cdot 7H_2O$.

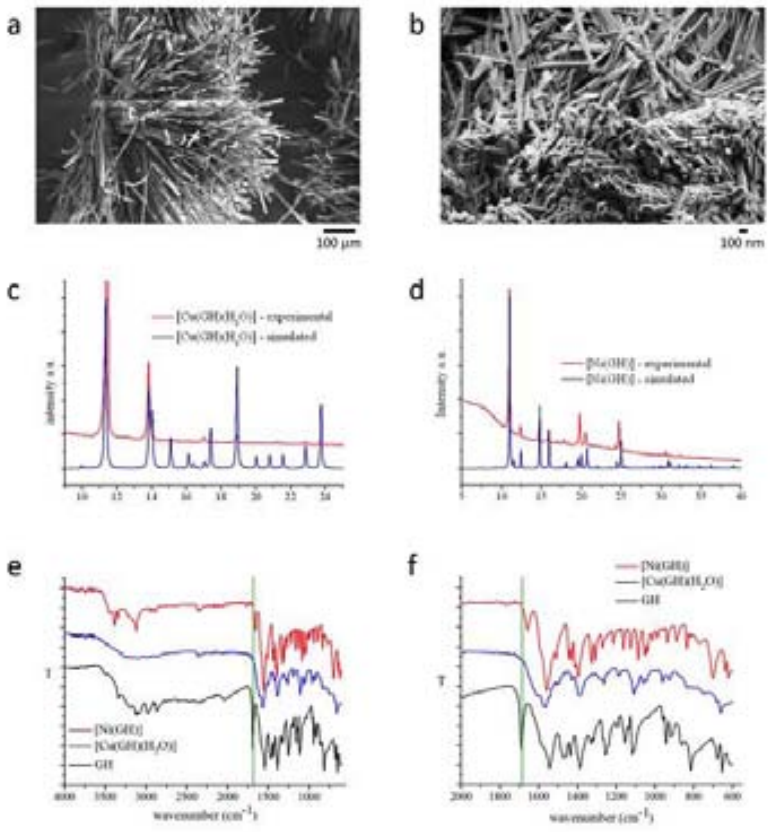

g

$[Cu(C_8H_{10}N_4O_3)(H_2O)]\cdot H_2O$	Calculated	C: 31.0 %	H: 4.6 %	N: 18.1 %
	Found	C: 31.4 %	H: 4.4 %	N: 18.0 %
$[Ni(C_8H_{11}N_4O_3)_2]\cdot(H_2O)_7$	Calculated	C: 31.7 %	H: 5.9 %	N: 18.5 %
	Found	C: 32.1 %	H: 5.7 %	N: 18.4 %

Supplementary Figure S11. a, Confocal microscopy image of the SoF droplet array resulting from summing all 30 collected fluorescence image slices. **b**, Inverted image after filtering the image in **a** using a background threshold. **c**, Corresponding optical microscopy image of the SoF droplet array.

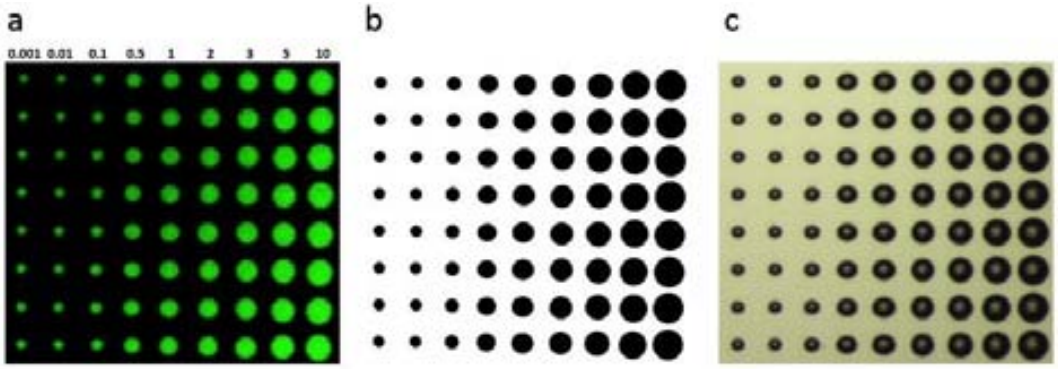

Supplementary Figure S12. a, Confocal microscopy image of the SoF/H_2O-glycerol mixture droplet array resulting from summing the 30 collected fluorescence image slices. **b**, Inverted image after filtering the image in **a** using a background threshold.

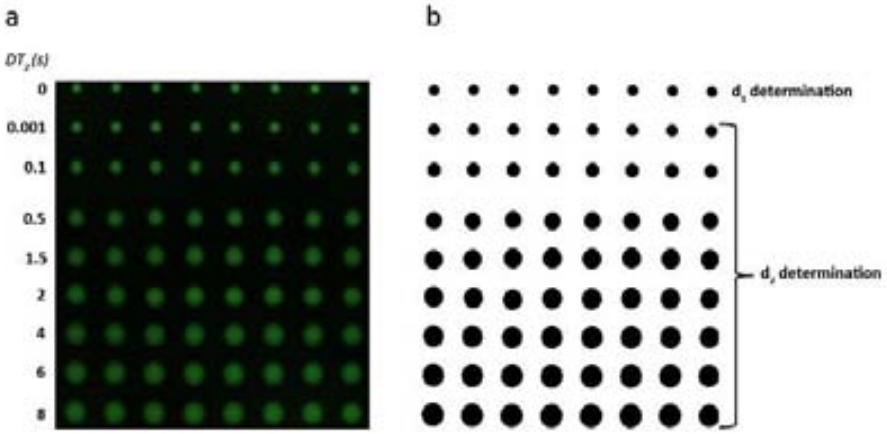

Supplementary Table S1. Crystal data and structure refinement for $[Cu(GH)(H_2O)]\cdot H_2O$ and $[Ni(GH)_2]\cdot 7H_2O$. X-ray single-crystal diffraction data for $[Ni(GH)_2]\cdot 7H_2O$ were collected on beamline I19 at Diamond Light Source, UK, on a Crystal Logic Kappa diffractometer with a Rigaku Saturn 724+ CCD detector (silicon 111 monochromated radiation, λ = 0.6889 Å). The applied absorption correction is based on multi-scans using REQAB within the d*TREK program.[27] The measurement for $[Cu(GH)(H_2O)]\cdot H_2O$ was done on a *BRUKER SMART APEX CCD* diffractometer using graphite-monochromated Mo *K*a radiation (λ = 0.71073 Å). Both structures were solved by direct methods using the program SHELXS-97. The non-hydrogen atoms were refined anisotropically. The H atoms have been included in theoretical positions but not refined. The refinement and all further calculations were done using SHELXL-97.[28] In both cases empirical absorption corrections were made, using SCALEPACK determination.[29] Crystal data for $[Ni(GH)_2]\cdot 7H_2O$ and $[Cu(GH)(H_2O)]\cdot H_2O$ were deposited as CCDC references: 912266 and 912870, respectively.

Empirical formula	$CuC_8N_4O_4H_{10}$, H_2O	$NiC_{16}N_8O_6H_{22}$, $7H_2O$
Formula weight	309.9	606.21
Temperature/K	293 K	100 K
Crystal system	Orthorhombic	Orthorhombic
Space group	$P2_12_12_1$	$P2_12_12_1$
a/Å	6.991(4)	8.768(13)
b/Å	10.778(4)	15.22(2)
c/Å	15.575(4)	18.86(3)
Volume/Å^3	1173.6(15)	2516(6)
Z	4	4
ρ_{calc}mg/mm^3	1.753	1.600
m/mm^{-1}	1.882	0.851
F(000)	636	1276
Crystal size/mm^3	0.05 × 0.1 × 0.45	0.04 × 0.01 × 0.01
2Θ range for data collection	5.2 to 57.4°	4.4 to 26.4°
Index ranges	$-9 \le h \le 8$, $-13 \le k \le 12$, $-20 \le l \le 20$	$-10 \le h \le 10$, $-18 \le k \le 10$, $-23 \le l \le 10$
Reflections collected	11380	6814
Independent reflections	2901[R(int) = 0.13]	4999 [R(int)=0.114]
Data/restraints/parameters	2901/0/175	4999/0/343
Goodness-of-fit on F^2	0.90	1.05
Final R indexes [I>=2σ (I)]	R_1 = 0.0675, wR_2 = 0.1432	R_1 = 0.1024, wR_2 = 0.2296
Final R indexes [all data]	R_1 = 0.1261, wR_2 = 0.1775	R_1 = 0.1635, wR_2 = 0.2653
Flack parameter	0.08(7)	0.06(5)

Supplementary Table S2. Bond lengths (Å) for $[Cu(GH)(H_2O)]\cdot H_2O$.

Atoms	Distances (Å)	Atoms	Distances (Å)
Cu1-O1	1.991(6)	N3-C5	1.440(10)
Cu1-O4	2.434(7)	N3-C7	1.295(10)
Cu1-N2	1.938(7)	N4-C8	1.475(11)
Cu1-N3	1.951(6)	N4-H4A	0.9000
Cu1-N4	1.992(6)	N4-H4B	0.9000
O1-C6	1.257(11)	C2-C3	1.340(12)
O2-C6	1.241(11)	C3-C4	1.479(12)
O3-C7	1.245(9)	C4-C5	1.495(11)
O4-H2B	1.0200	C5-C6_a	1.551(11)
O4-H2A	1.0200	C7-C8	1.500(12)
O5-H9B	0.6600	C2-H2	0.9300
O5-H9A	0.8200	C4-H4B	0.9700
N1-C1	1.326(12)	C4-H4A	0.9700
N1-C2	1.360(13)	C5-H5	0.9800
N2-C3	1.387(11)	C8-H8B	0.9700
N2-C1	1.318(11)	C8-H8A	0.9700

Supplementary Table S3. Bond angles (º) for $[Cu(GH)(H_2O)]\cdot H_2O$.

Atoms	Angles (º)	Atoms	Angles (º)
O1-Cu1-O4	92.1(2)	Cu1-N4-H4B	109.00
O1-Cu1-N2	90.8(3)	H4A-N4-H4B	108.00
O1-Cu1-N3	171.1(3)	N1-C1-N2	109.0(8)
O1-Cu1-N4	90.4(3)	N1-C2-C3	106.5(9)
O4-Cu1-N2	92.3(3)	N2-C3-C4	120.7(7)
O4-Cu1-N3	95.6(2)	C2-C3-C4	131.3(9)
O4-Cu1-N4	95.9(2)	N2-C3-C2	107.8(7)
N2-Cu1-N3	93.4(3)	C3-C4-C5	115.3(7)
N2-Cu1-N4	171.6(3)	N3-C5-C4	111.7(7)
N3-Cu1-N4	84.3(3)	N3-C5-C6_a	113.8(6)
Cu1-O1-C6	115.1(5)	C4-C5-C6_a	109.8(7)
Cu1-O4-H2B	150.00	O2-C6-C5_b	116.2(8)
H2A-O4-H2B	105.00	O1-C6-C5_b	118.9(7)
Cu1-O4-H2A	89.00	O1-C6-O2	124.9(8)
H9A-O5 -H9B	91.00	O3-C7-N3	125.9(7)
C1-N1-C2	109.3(8)	O3-C7-C8	116.9(7)
Cu1-N2-C3	124.1(5)	N3-C7-C8	117.2(7)
C1-N2-C3	107.4(7)	N4-C8-C7	111.7(7)
Cu1-N2-C1	128.4(6)	C3-C2-H2	127.00
Cu1-N3-C7	115.8(5)	N1-C2-H2	127.00
Cu1-N3-C5	127.4(5)	C3-C4-H4B	108.00
C5-N3-C7	116.5(6)	C5-C4-H4A	108.00
C5-C4-H4B	108.00	C3-C4-H4A	109.00
N3-C5-H5	107.00	H4A-C4-H4B	107.00
C6_a-C5-H5	107.00	N4-C8-H8B	109.00
C4-C5-H5	107.00	C7-C8-H8B	109.00
N4-C8-H8A	109.00	H8A-C8-H8B	108.00
Cu1-N4-C8	110.7(5)	C7-C8-H8A	109.00
C8-N4-H4B	109.00		
Cu1-N4-H4A	110.00		
C8-N4-H4A	109.00		

a = [4746.00] = 2-x,-1/2+y,3/2-z
b = [4756.00] = 2-x,1/2+y,3/2-z
c = [1655.00] = 1+x,y,z
d = [2755.00] = 5/2-x,-y,1/2+z
e = [4746.00] = 2-x,-1/2+y,3/2-z
f = [4646.00] = 1-x,-1/2+y,3/2-z
h = [4656.00] = 1-x,1/2+y,3/2-z
i = [3556.00] = 1/2+x,1/2-y,1-z
j = [2754.00] = 5/2-x,-y,-1/2+z
k = [2654.00] = 3/2-x,-y,-1/2+z
l = [2655.00] = 3/2-x,-y,1/2+z
m = [3456.00] = -1/2+x,1/2-y,1-z

Supplementary Table S4. Bond lengths (Å) for $[Ni(GH)_2]\cdot 7H_2O$.

Atoms	Distance (Å)	Atoms	Distance (Å)
Ni1-O3	2.042(6)	N11-C11	1.279(19)
Ni1-O13	2.079(7)	N12-C11	1.325(16)
Ni1-N1	2.020(9)	N12-C13	1.338(15)
Ni1-N4	2.019(8)	N13-C15	1.391(14)
Ni1-N11	2.019(9)	N13-C17	1.295(13)
Ni1-N14	2.030(8)	N14-C18	1.455(13)
O1-C6	1.233(16)	N3-H3	0.8600
O2-C6	1.259(16)	N4-H2B	0.9000
O3-C7	1.200(15)	N4-H2A	0.9000
O11-C16	1.211(16)	N13-H13	0.8600
O12-C16	1.248(17)	N14-H14B	0.9000
O13-C17	1.198(14)	N14-H14A	0.9000
O40-H40B	0.9400	O44-H44A	1.1000
O40-H40A	0.8000	O44-H44B	0.9300
O41-H41B	0.9100	O45-H45A	1.1800
O41-H41A	0.9400	O45-H45B	1.0900
O42-H42A	1.0300	O46-H46A	1.0400
O42-H42B	1.0500	O46-H46B	0.8500
O43-H43B	0.7900	C2-C3	1.315(14)
O43-H43A	1.0100	C3-C4	1.448(11)
N1-C1	1.302(15)	C4-C5	1.515(13)
N1-C2	1.334(12)	C5-C6	1.477(12)
N2-C1	1.307(12)	C7-C8	1.522(16)
N2-C3	1.336(14)	C12-C13	1.319(16)
N3-C5	1.419(14)	C13-C14	1.456(14)
N3-C7_b	1.298(13)	C14-C15_a	1.503(16)
N4-C8	1.458(13)	C15-C16	1.481(12)
N11-C12	1.339(13)	C17-C18	1.533(16)
C1-H1	0.9300	C11-H11	0.9300
C2-H2	0.9300	C12-H12	0.9300
C4-H4A	0.9700	C14-H14A	0.9700
C4-H4B	0.9700	C14-H14B	0.9700
C5-H5	0.9800	C15-H15	0.9800
C8-H8A	0.9700	C18-H18B	0.9700
C8-H8B	0.9700	C18-H18A	0.9700

Supplementary Table S5. Bond angles (º) for $[Ni(GH)_2]\cdot 7H_2O$.

Atoms	Angles (º)	Atoms	Angles(º)
O3-Ni1-O13	86.9(3)	Ni1-N11-C12	128.4(8)
O3-Ni1-N1	174.7(4)	C11-N11-C12	105.4(9)
O3-Ni1-N4	80.1(3)	C11-N12-C13	107.2(11)
O3-Ni1-N11	90.2(3)	C15-N13-C17	123.9(10)
O3-Ni1-N14	91.5(3)	Ni1-N14-C18	110.8(6)
O13-Ni1-N1	89.9(3)	C5-N3-H3	120.00
O13-Ni1-N4	91.7(3)	C7_b-N3-H3	120.00
O13-Ni1-N11	173.1(4)	H2A-N4-H2B	108.00
O13-Ni1-N14	81.3(3)	C8-N4-H2B	110.00
N1-Ni1-N4	95.8(4)	Ni1-N4-H2A	110.00
N1-Ni1-N11	93.5(3)	Ni1-N4-H2B	110.00
N1-Ni1-N14	92.2(3)	C8-N4-H2A	110.00
N4-Ni1-N11	93.9(4)	C15-N13-H13	118.00
N4-Ni1-N14	169.4(3)	C17-N13-H13	118.00
N11-Ni1-N14	92.6(4)	H14A-N14-H14B	108.00
Ni1-O3-C7	115.1(7)	Ni1-N14-H14A	110.00
Ni1-O13-C17	112.0(6)	Ni1-N14-H14B	109.00
H40A-O40-H40B	117.00	C18-N14-H14A	110.00
H41A-O41-H41B	159.00	C18-N14 -H14B	110.00
H42A-O42-H42B	95.00	H44A-O44-H44B	102.00
H43A-O43-H43B	134.00	H45A-O45-H45B	71.00
Ni1-N1-C2	127.2(8)	H46A-O46-H46B	148.00
C1-N1-C2	104.4(9)	N1-C1-N2	110.8(9)
Ni1-N1-C1	125.9(7)	N1-C2-C3	
C1-N2-C3	108.3(9)	N2-C3-C2	104.9(8)
C5-N3 -C7_b	119.6(10)	N2-C3-C4	122.4(9)
Ni1-N4 -C8	110.1(6)	C2-C3-C4	
Ni1-N11-C11	123.6(8)	C3-C4-C5	114.4(7)
N3-C5-C4	108.9(8)	N1-C2-H2	124.00
C4-C5-C6	109.1(7)	C3-C2-H2	124.00
N3-C5-C6	114.0(10)	H4A-C4-H4B	108.00
O1-C6-O2	122.9(9)	C3-C4-H4B	109.00
O1-C6-C5	120.5(12)	C3-C4-H4A	109.00
O2-C6-C5	116.1(11)	C5-C4-H4A	109.00
N3_a-C7-C8	114.8(11)	C5-C4-H4B	109.00

Atoms	Angles (°)	Atoms	Angles(°)
O3-C7-N3_a	125.6(11)	C6-C5-H5	108.00
O3-C7-C8	119.6(9)	C4-C5-H5	108.00
N4-C8-C7	107.9(9)	N3-C5-H5	108.00
N11-C11-N12	111.2(11)	N4-C8-H8A	110.00
N11-C12-C13	110.6(11)	N4-C8-H8B	110.00
C12-C13-C14	130.9(11)	C7-C8-H8A	110.00
N12-C13-C12	105.5(9)	C7-C8-H8B	110.00
N12-C13-C14	123.5(11)	H8A-C8-H8B	108.00
C13-C14-C15_a	113.5(9)	N11-C11-H11	124.00
N13-C15-C14_b	109.4(9)	N12-C11-H11	124.00
N13 -C15-C16	114.7(10)	N11-C12-H12	125.00
C14_b-C15-C16	110.0(8)	C13-C12-H12	125.00
O11-C16-O12	121.2(9)	C15_a -C14-H14B	109.00
O11-C16-C15	119.7(12)	C13-C14-H14A	109.00
O12-C16-C15	119.1(11)	C13-C14-H14B	109.00
N13-C17-C18	113.7(10)	H14A-C14-H14B	108.00
O13-C17-N13	123.3(10)	C15_a-C14-H14A	109.00
O13-C17-C18	123.1(9)	N13-C15 -H15	108.00
N14-C18-C17	107.7(8)	C16-C15-H15	108.00
N1-C1-H1	125.00	C14_b-C15-H15	107.00
N2-C1-H1	125.00	N14-C18-H18A	110.00
N14-C18-H18B	110.00	C17-C18-H18B	110.00
C17-C18-H18A	110.00	H18A-C18-H18B	109.00

a = [4646.00] = 1-x,-1/2+y,3/2-z
b = [4656.00] = 1-x,1/2+y,3/2-z
c = [2565.00] = 1/2-x,1-y,1/2+z
d = [3467.00] = -1/2+x,3/2-y,2-z
e = [3467.00] = -1/2+x,3/2-y,2-z
g = [3567.00] = 1/2+x,3/2-y,2-z
h = [3466.00] = -1/2+x,3/2-y,1-z
i = [2664.00] = 3/2-x,1-y,-1/2+z
j = [2664.00] = 3/2-x,1-y,-1/2+z
k = [1455.00] = -1+x,y,z
l = [2665.00] = 3/2-x,1-y,1/2+z
m = [2665.00] = 3/2-x,1-y,1/2+z
n = [3566.00] = 1/2+x,3/2-y,1-z
o = [2664.00] = 3/2-x,1-y,-1/2+z
q = [3466.00] = -1/2+x,3/2-y,1-z
r = [2565.00] = 1/2-x,1-y,1/2+z
s = [2564.00] = 1/2-x,1-y,-1/2+z
t = [2665.00] = 3/2-x,1-y,1/2+z
w =[2564.00] = 1/2-x,1-y,-1/2+z

Supplementary Table S6. Measured droplet diameters and estimated average volumes for each DT_1.

DT_1 (s)	d_1 (μm)	V_1 (fL)
0.001	8.8 ± 0.2	43 ± 2
0.01	8.9 ± 0.2	44 ± 2
0.1	10.6 ± 0.2	75 ± 4
0.5	14.3 ± 0.2	184 ± 9
1	16.4 ± 0.3	281 ± 13
2	17.6 ± 0.2	345 ± 14
3	19.5 ± 0.2	470 ± 18
5	21.8 ± 0.3	652 ± 22
10	24.0 ± 0.1	873 ± 21

Supplementary Table S7. Measured droplet diameters and calculated dilution factors for each DT_2.

DT_2 (s)	d_2 (μm)	d_2^3/d_1^3
0.001	10.5 ± 0.1	1.4 ± 0.2
0.1	11.9 ± 0.1	2.0 ± 0.2
0.5	14.6 ± 0.2	3.8 ± 0.3
1.5	16.4 ± 0.5	5.4 ± 0.5
2	17.3 ± 0.5	6.3 ± 0.5
4	18.2 ± 0.5	7.3 ± 0.5
6	19.1 ± 0.4	8.5 ± 0.4
8	19.7 ± 0.4	9.2 ± 0.4

Supplementary Methods S1: Determination of the diameter, contact angle and calculus of volume of the patterned droplets.

An array of 8 x 9 droplets of 0.01 M SoF (in DMSO/glycerol, 1:1 v/v) was generated on a SiO_2 surface under a relative humidity of 60% and at room temperature. In this array, we controlled the droplet size of each column by systematically increasing DT_1 (from 0.001 to 10 s, corresponding to the first to ninth columns, respectively; see Fig. 1b in the manuscript; also see Supplementary Figure S11a).

Assuming that droplets delivered on a surface can be considered as a sessile droplet having spherical cap geometry,[30,31] one can then express their volume (in fL) as:

$$V = \frac{\pi \cdot {r_b}^3}{3} \cdot \frac{2-3\cos\vartheta+\cos^3\vartheta}{\sin^3\vartheta} \quad \text{(S1)}$$

where θ is the contact angle in deg, and r_b is the contact radius in μm. The contact angle θ ($\theta = 34.6 \pm 0.3$) was measured with a contact angle analyser (Easy Drop Standard [Krüss, Germany]) by depositing a 0.1 μL droplet of 0.01 M SoF (in DMSO/glycerol, 1:1 v/v) onto a SiO_2 surface. The average contact radius r_b ($r_b = d_1/2$) for each column of droplets was calculated by determining the d_1 value of each SoF droplet. To determine these d_1 values, the 30 confocal microscopy image slices were summed (see Supplementary Fig. 1a), and a threshold was selected to discriminate between the fluorescent areas and the background (see Supplementary Figure S11b). All d_1 values determined from this threshold image were in full agreement with those determined from the corresponding optical microscopy image (see Supplementary Figure S11c).

Following *Equation S1*, the average volumes of the droplets forming each column were estimated (see Supplementary Table S6):

We followed the same methodology to determine the d_1 and d_2 values of the SoF/H_2O-glycerol mixture droplet array. This array was generated by first patterning an array of 9 x 8 droplets of 0.01 mM SoF (in H_2O/glycerol, 1:1 v/v) on a SiO_2 surface at DT_1 = 0.001 s at room temperature under a relative humidity of 60%. Femtolitre volumes of a H_2O/glycerol (1:1 v/v) mixture were then delivered into the pre-patterned SoF droplets at DT_2 = 0.001, 0.1, 0.5, 1.5, 2, 4, 6 and 8 s, starting from the second row (see Supplementary Figure S12a).

The corresponding threshold image was used to determine d_1 ($d_1 = 9.4 \pm 0.1$; 1st row) and d_2 values (from the second to ninth rows). From these values, the corresponding dilution factors were calculated as: $V_2/V_1 = {d_2}^3/{d_1}^3$, considering that the θ of the pre-patterned SoF droplets (in H_2O/glycerol, 1:1 v/v) and the mixture droplets resulting from adding different volumes of a H_2O/glycerol (1:1 v/v) mixture do not change.

Supplementary Methods S2: Determination of mean fluorescence intensities per unit of surface area (I/A).

An inverted confocal fluorescence microscope (Leica TCS SP5) was used to measure the fluorescence images (310 × 310 μm^2) of fluorescein droplets arrays patterned onto SiO_2 surfaces (see Supporting Figure S11a). The fluorescence images of these arrays were registered in reflection mode, with a 50x objective (magnification = 0.15 μm/pixel) and at different heights by scanning in z-direction (typically, 30 images were measured for each z-stack by scanning within a Δz = 0.42 μm). The dimensions and mean emission intensities of each droplet in the fluorescence images were determined using the software ImageJ.

To investigate the variation in fluorescence intensities along the arrays, the image slice in each z-stack corresponding to the droplet volume in contact with the surface was further analysed. The exact location of the image slice within the z-stack was determined from the maximum background intensity.[32] The I/A was then determined for every droplet in the image after subtracting the background signal. The results were averaged over the droplets in the array delivered at equal DT_1 (for the array of SoF droplets delivered at different DT_1; see Fig. 1d in the manuscript for a plot of I/A against DT_1) and with equal SoF concentration (for the array of SoF/H_2O-glycerol mixture droplets). For the last array, the measured I/A values were subsequently normalised relative to the maximum I/A of the non-diluted SoF droplets (*i.e.* the droplets of the first row). Finally, the normalised emission intensities were plotted against the dilution factor and DT_2 (see Fig. 1g and Supplementary Figure S3; also see Supplementary Figure S4 for reproducible data from three independent experiments). In the cross-contamination experiment, the I/A value for each cleaning droplet was normalised relative to the maximum I/A of the initial, non-diluted SoF droplets. As no significant variation in the I/A_N (less than 2%) was observed between the equivalent cleaning droplets from different dilutions (*i.e.* all first droplets, all second droplets, all third droplets, etc., see Supplementary Figure S5), the resulting values were then averaged over the droplets corresponding to the same iteration (*e.g.* average I/A_N of all first droplets, etc.).

Supplementary references

27. J.W. Pflugrath, *Acta Cryst*., **D55**, 1718-1725 (1999)

28. G. M. Sheldrick, SHELXL-97, Program for refinement of crystal structures, University of Göttingen, Germany (1997)

29. [Otwinowski, Z., Minor, W. *Methods Enzymol.* **276**, 3017 (1997)]

30A. K. Panwar, S. K. Barthwal, S. Ray, *J. Adhes. Sci. Technol.* **17**, 1321 (2003).

31. C. Bourgks-Monnier, M. E. R. Shanahan, *Langmuir* **11**, 2820 (1995).

32. M. Sundberg, A. Manson, S. Tagerud, *Journal of Colloid and Interface Science* **313**, 454-460 (2007).

Conclusions

Conclusions

The development of a novel and versatile pen-type lithography approach for growing HKUST-1 crystals on supports has been described in the first stage of this PhD Thesis. Although there are previous works describing the patterning of MOFs on surfaces, this is the first time that a serial patterning method has been used to pattern on an arbitrary way, HKUST-1 single crystals on the desired position of a surface.

Playing with the interaction forces of the substrate and patterning tools, the different results obtained confirm not only that MOFs can be grown on surface but also that the number and size of the crystals can be controlled. Thus HKUST-1 single crystals 500 nm have been structured with high homogeneity and reproducibility using this novel approach.

Since many functional MOFs have been synthesized, it is likely that this approach can be expanded for controlling the growth of many other MOFs at the single-crystal level on several surfaces. Such capabilities will expand the scope of application for MOFs in sensors, magnetic and electronic devices, etc., where such control opens new opportunities to integrate them in specific locations of devices.

On the second part of the thesis, we have reported a highly versatile and effective soft-lithographic method based on the first Chapter approach, to mix femtoliter volumes on surfaces, having nanometre precision on their position. We have been able to perform acid-base, enzymatic recognition and MOFs synthetic reactions and furthermore, we have discovered two new peptide based frameworks by using this new approach to femtolitre chemistry.

This strategy enables the programmable realization of a broad range of combinatorial femtoliter reactions and crystallization processes on surfaces, and offers a unique opportunity for performing high-throughput assays and combinatorial screenings while consuming ultrasmall reagent volumes, which for example might be of great interest for discovering novel materials. Thus, this MPL approach, with more elaborated control of the reaction conditions such as temperature, is likely to have important applications in biology, chemistry and materials science, and it will be ideal for locating complex structures that require to be synthesized through a reaction, such as crystals, making it also potentially useful in electronics and sensors as well.